



THE UNIVERSITY *of* EDINBURGH

This thesis has been submitted in fulfilment of the requirements for a postgraduate degree (e.g. PhD, MPhil, DClinPsychol) at the University of Edinburgh. Please note the following terms and conditions of use:

- This work is protected by copyright and other intellectual property rights, which are retained by the thesis author, unless otherwise stated.
- A copy can be downloaded for personal non-commercial research or study, without prior permission or charge.
- This thesis cannot be reproduced or quoted extensively from without first obtaining permission in writing from the author.
- The content must not be changed in any way or sold commercially in any format or medium without the formal permission of the author.
- When referring to this work, full bibliographic details including the author, title, awarding institution and date of the thesis must be given.

High-Pressure X-ray Diffraction Studies of light Lanthanides



Shaun Russell Evans

A thesis submitted in fulfilment of the requirements
for the degree of Doctor of Philosophy
to the
University of Edinburgh
2010

Abstract

The (trivalent) lanthanides exhibit a common sequence of phases upon the application of pressure: $hcp \rightarrow dhcp \rightarrow fcc \rightarrow$ “distorted-fcc”. The “distorted-fcc” phase (d - fcc), observed in the light lanthanides is known to be related by geometric distortions to the fcc unit cell, yet the d - fcc phase has been reported to comprise of one or two structures, with no prevailing consensus as to the solution(s). This thesis contains a detailed study of the d - fcc phase of the light lanthanides Pr and Nd.

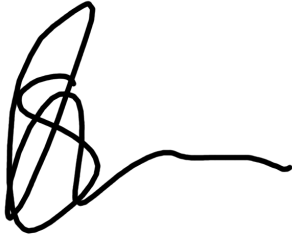
High-pressure angle-dispersive powder-diffraction techniques were employed to systematically study the phases adopted by Pr (up to 25GPa) and Nd (up to 44GPa). Particular attention was paid to solving the d - fcc of each of these elements, the structure of which is very unclear in published work. In Pr, the d - fcc between 7 and 20GPa is shown to comprise of two phases, the solutions of which are shown to be $hR24$ ($R\bar{3}m$) and $oC16$ ($Ibam$) for the regions 7-14GPa and 14-20GPa, respectively. The pressure-dependence of each of these structures over their stability range is presented. Revisions to previously-published volume vs. pressure data are made, with a different value for the volume collapse at the $4f$ electron delocalisation transition reported.

Similarly, the d - fcc phase of Nd, stable over the pressure range 16-40GPa, is studied in detail. Nd differs from Pr by undergoing a further transition, to a $hP3$ ($P6_3$) structure, on pressurisation above 40GPa, before transforming to a α -Uranium phase. The distorted-fcc phase is shown, like that of Pr, to comprise of two phases, $hR24$ ($R\bar{3}m$) and $oC16$ ($Ibam$) for the pressure regions 16-26GPa and 26-40GPa, respectively. Data on Nd are presented up to the maximum pressure achieved, 44GPa.

Data from a preliminary study of La are also presented, along with a brief report on attempts to prepare a single crystal of Pr within a diamond anvil cell, by laser annealing of a powder of Pr.

Declaration

I do hereby declare that this thesis was composed by myself and that the work described within is my own, except where explicitly stated otherwise.

A handwritten signature in black ink, consisting of a large, stylized initial 'S' followed by a horizontal line.

Shaun Evans
March 2010

Acknowledgements

The author would like to thank the following people for their assistance provided to the author during the preparation of and work carried out during this thesis, without which the completion of this would not have been possible.

For guidance, support, and supervision Prof. Malcolm McMahon of The University of Edinburgh. Dr. Lars Lundegaard, Dr. Clivia Hejny, Dr. Olga Degtyareva and Dr. Ingo Loa for their assistance and guidance during many of the experiments performed whilst collecting the data for this thesis. The beamline scientists responsible for the synchrotron stations used to collect data, Dr. Mark Roberts of Station 9.1 of Daresbury SRS, Dr. Alistair Lennie of Station 9.5 HPT of Daresbury SRS, Dr. Micheal Hanfland of ID09A of the ESRF.

For assistance with the laser annealing attempts with Pr, Dr. John Proctor and Dr. Eugene Gregoryanz of The University of Edinburgh.

Colleagues at The University of Edinburgh for moral support Dr. Helen Maynard, Dr. Miriam Marques, Dr. Graham Stinton, Ms. Jenny Jeppsson, Dr. Christophe Guillame and Mr. Gaeton Girat.

For moral, financial and general support Mr. Russell Evans, Mrs. Gaynor Evans, Mr. Adam Evans, Mr. Ivor Thomas and Ms. Elizabeth Evans.

Dedicated to the family members who will be sorely missed, Mrs. Jean Evans, Mr. Clifford Evans and Mrs. Kathleen Thomas.

Contents

Abstract	i
Declaration	iii
Acknowledgements	v
Contents	vii
List of figures	xi
List of tables	xxiii
1 Introduction	1
1.1 Extreme Conditions	1
1.2 Lanthanides	3
1.3 Motivation	5
1.4 Thesis Outline	7
2 Experimental Techniques	9
2.1 Introduction	9
2.2 Diffraction	9
2.2.1 Single-Crystal Diffraction	14
2.2.2 Powder Diffraction	15
2.2.3 Synchrotron Radiation	16
2.2.3.1 Angle Dispersive X-ray Diffraction	20
2.2.3.2 Energy Dispersive X-ray Diffraction	22
2.3 Accurate data	23
2.4 Pressure Cells and High-Pressure Techniques	25
2.4.1 Basic Principles	25
2.4.1.1 Diamond Anvil Cells	25
2.4.2 Pressure Media	28
2.4.3 Pressure Calibration	30
2.4.4 Preferred Orientation	32
2.5 Experimental Setup and Data Analysis	36
2.5.1 Detectors	36
2.5.1.1 MD Image Plate	36
2.5.1.2 Mar345	37

2.5.1.3	Comparison of Beamlines 9.1/9.5 and Detectors	37
2.5.2	Station 9.1 at Daresbury SRS	37
2.5.2.1	Alignment of Station 9.1	38
2.5.3	Station 9.5	39
2.5.3.1	Alignment of Station 9.5	40
2.5.4	Comparison of Stations 9.1 and 9.5	42
2.5.5	Data Processing	42
2.5.6	Data Analysis - Indexing and Refinement	43
2.5.6.1	Indexing	43
2.5.6.2	Refinement	44
2.6	Concluding Remarks	46
3	Literature Reviews	47
3.1	Introduction	47
3.2	Review of Lanthanides	47
3.3	Review of Praseodymium	57
3.4	Contaminants	63
3.5	Conclusions	66
4	Studies of Praseodymium	67
4.1	Introduction	67
4.2	Experimental Details	67
4.3	Contaminant Phases	69
4.3.1	Introduction	69
4.4	Praseodymium at relatively low pressures (0 - 7GPa)	73
4.5	<i>d-fcc</i> of Praseodymium from 7-14GPa	79
4.6	Pressure dependence of <i>hR24</i> 7-14GPa	87
4.7	Transition at 14GPa	92
4.8	Structure of Praseodymium from 14-20GPa	96
4.9	Structure of the α -Uranium phase	106
4.9.1	Single Crystal Growth Attempts	111
4.10	Discussion and conclusions	115
5	Studies of Neodymium and Lanthanum	121
5.1	Introduction	121
5.2	Brief review of Neodymium and Lanthanum	121
5.3	Experimental Details	123
5.3.1	Loadings	123
5.4	Contaminants	123
5.5	Structures of Neodymium below 16GPa	127
5.6	Structure of <i>d-fcc</i> Neodymium	133
5.7	Pressure Dependence of <i>hR24</i> Neodymium	140
5.7.1	Comparison to Praseodymium	146
5.7.2	Comment on quality of collected data	146
5.8	New phase of Neodymium?	148
5.9	Structure of Neodymium from 25-40GPa	153

5.9.1 Comparison to Praseodymium	156
5.10 <i>hP3</i> Phase of Neodymium	158
5.10.1 Comparison to Praseodymium	162
5.11 Preliminary Studies of Lanthanum	162
5.12 Discussion and Conclusions	168
6 Conclusions	173
6.1 Conclusions	173
A Appendix Title	181
Bibliography	182
Publications	189

CONTENTS

List of Figures

1.1	Diagram illustrating the scale of the variation in pressure observable within nature. Here, atmospheric pressure is used as a relatable lower reference pressure, it is not the lowest pressure attainable. Reproduced with permission [Ingo Loa 07].	2
1.2	Common phase diagram of the regular lanthanide series, reproduced from Johansson [Johansson 75] sources contained in references therein. .	4
2.1	Adjacent planes of atoms will give constructive interference only when Braggs' Law is satisfied.	10
2.2	Diagram illustrating planes of different $h k l$ in a cubic cell in real space. Illustrated is possible permutations of index 1, higher indices lie parallel to the index 1 plane. The directions h, k and l are labelled for (001) only.	12
2.3	Diagram illustrating a vector map showing a scattering event in (i) real space and (ii) reciprocal space. The wavevectors k_i, k_f and Q represent the incident beam, diffracted (final) beam and scattering vector respectively. The vectors q_i and q_f represent the projection of k_i, k_f onto Q in (ii).	14
2.4	A 2D diffraction image of Si at ambient pressure collected on ID09A at ESRF, using a wavelength of $\lambda = 0.44397\text{\AA}$. Image is screen captured from Fit2D [Hammersley 98]. Collected intensity is shown in inverse grey-scale, with darker regions being of higher intensity. The white circle at the centre of the image is the absence of collected intensity corresponding to the location of a lead beamstop.	17
2.5	(a) A graph showing the characteristic spectrum of a synchrotron radiation source (b) A plot showing how the maximum attainable brilliance (defined as number of photons / s / mm ² / mrad / 0.1% of bandwidth) vs. time of global synchrotron sources, increasing brilliance is shown with the building of new synchrotrons. (b) reproduced from <i>XFEL</i> comparison site [XFEL 09].	18
2.6	Two schematic diagrams showing (i) the layout and components of a typical optics hutch (in this case for Beamline I04 of Diamond Light Source, in Didcot, UK) and (ii) how an optics hutch is positioned relative to the other hutches (experimental hutch and control hutch) in a typical beamline (in this case from the ESRF, Grenoble, France). Images taken from (i) Diamond Light Source [Source 10] and (ii) ESRF [ESRF 10]. .	21

2.7	Diagram showing a schematic of the MB type DAC, with an enlarged section showing the sample chamber.	26
2.8	Diagram showing the two means of supporting diamond anvils (a) using standard Be backing discs and (b) using Bholer-Almax tungsten carbide seats	27
2.9	Schematic diagram of a DAC showing an exploded view of a Merrill-Basset DAC, how the two halves fit together and location of sample chamber is shown in 2.7. Separate sections and components are labeled. Image from [Website 10].	28
2.10	Labelled schematic diagram of pressure measuring system available within the Edinburgh High Pressure group, at Daresbury SRS. A green ($\lambda = \text{\AA}$) laser is used to excite the ruby fluorescence. The laser light passes through half silvered mirrors (grey rectangles) which, if in place direct the light coming from the sample (reflected and fluorescence) to either the video monitor or spectrometer. The video monitor is used during alignment of the laser radiation on the ruby pressure calibrant within the sample chamber. The spectrometer is connected to a PC, to allow collection, analysis and archival of spectra.	31
2.11	Schematic diagram showing how the orientation of crystallites within a perfect powder (a), and (b) a powder with pronounced preferred orientation, could look.	32
2.12	Example of the effect of preferred orientation on a powder pattern collected on Station 9.5 HPT of Daresbury SRS from a “powder” sample of Pr at 20.3 GPa. Contrast has been adjusted to highlight the effect preferred orientation has upon the intensity distribution around a powder ring. Arrows indicate the positions of highest intensity on the ring. . .	33
2.13	Simplified diagram to show the preferred orientation direction (POD), preferred orientation axis (POA) and how each relates to the scattering vector (h_j), diffracted spot (P), incident beam (IB) and diffracted beam (DB). Diagram reproduced from [mim]	35
2.14	Labelled schematic diagram of Station 9.5, Daresbury SRS. Position of the optics relative to the setup is noted. Telescope used for alignment and online pressure measurement is shown in dotted line, indicating the position of this device is out of the path of the incident x-ray beam when not in use. The rectangle labelled “pinhole” contains at the detector-side a pinhole for defining the x-ray beam, and on beam-pipe side collumator and slits for providing initial definition of beam.	40
3.1	Figure reproduced from Johansson and Rosengren [Johansson 75]. The top graph (referred to as (a) in [Johansson 75]) shows experimentally derived Wigner Seitz ratio and ionic radius variation across the lanthanide series. The lower graph, (b) shows how the ratio F (defined in figure and previously in Equation 3.1, with r_{ws} defined in Equation 3.2) varies across the series.	50

3.2	Figure reproduced from Johansson and Rosengren [Johansson 75]. Figure shows the constructed general phase diagram for the regular (trivalent) lanthanides constructed by Johansson and Rosengren from references contained within [Johansson 75]	51
3.3	Diagram showing the relationship between the closed packed structures adopted by the regular lanthanides on pressure increase. Hexagonal layers, labelled A, B and C can be used to describe each of the <i>fcc</i> (a), <i>hcp</i> (b), <i>dhcp</i> (c) and (d) Sm-type structures. Diagram reproduced from [tay]	55
3.4	Electrical resistance measurement as a function of pressure for (3 isotherms of) Pr reproduced from Figure 2 of Stager and Drickhammer [Stager 64]	58
3.5	Diagram of the α -Uranium structure, <i>oC4</i> (space group <i>Cmcm</i>) which is adopted by Pr after the delocalisation of <i>4f</i> electrons on compression above 20GPa [Smith 84]. Atoms are located in the <i>4c</i> Wyckoff positions (which correspond to atomic positions within the unit cell of $(0, y, \frac{1}{4})$ and $(0, -y, \frac{3}{4})$ with $y = 0.1$), here the unit cell parameters of $a = 2.7330$, $b = 5.4665$ and $c = 4.8769\text{\AA}$ for Pr in α -Uranium phase at 27GPa are taken (along with the atomic position, y) from [Baer 03]. Figure drawn using the crystal visualisation program Vesta [Momma 08].	60
3.6	Diffraction pattern from the <i>d-fcc</i> phase of Pr, collected at 10.4GPa. Additional peaks arising from contamination are identified with arrows. Inset shows an enlarged segment of the 2D diffraction image, with contrast adjusted to illustrate the texture (spottiness) of the contaminant rings, which are identified with arrows. These peaks do not correspond to gasket peaks.	65
4.1	Diffraction pattern from the <i>d-fcc</i> phase of Pr, collected at 10.4GPa on Station 9.5 of Daresbury SRS, using a wavelength of $\lambda=0.44397\text{\AA}$. Additional peaks arising from contamination are identified with arrows. Inset shows an enlarged segment of the 2D diffraction image, with contrast adjusted to illustrate the texture (spottiness) of the contaminant rings, which are identified with arrows. These peaks do not correspond to gasket peaks. Reproduced from Figure 3.6.	70
4.2	Plot of the lattice parameters (\AA) with respect to pressure (GPa) for the contaminant phases. Open symbols represent data collected on pressure decrease, and solid on pressure increase. Shown for comparison are the ambient pressure lattice parameters for PrO, PrO ₂ and PrH ₂ , along with the measured and calculated contaminant lattice parameters from Hamaya <i>et al.</i> [Hamaya 96] (\times and $+$). The calculated lattice parameter from the study of Chesnut and Vohra [Chesnut 00b], which was incorrectly identified as a sample reflection is denoted with a Δ . Figure modified from Evans <i>et al.</i> [Evans 09].	71

4.3	Plot of cubic lattice parameter (\AA) with respect to pressure (GPa) for the first contaminant phase. Shown for comparison is the dashed line, which represents the fitted EoS for the contaminant. Error bars are plotted on all points, but only visible for three, the size of the symbols use to plot the data points obscure the error bars for the other points.	72
4.4	Integrated diffraction patterns collected from Pr loaded in a MB DAC, with dry mineral oil pressure medium, plotted as I vs. 2θ . Diffraction patterns are stacked in increasing pressure, with pressures indicated on the left hand side of each plot, the phase name is displayed on the right hand side of the figure, with arrow heads indicating where the transition occurs (on pressure increase). Data were collected using MB DACs with culets of $300\mu\text{m}$ Station 9.5 of Daresbury SRS, using a wavelength of $\lambda=0.44397\text{\AA}$	74
4.5	Example refinement of Pr in the <i>dhcp</i> phase, collected at 1GPa on Station 9.1 of Daresbury SRS using $\lambda = 0.4654\text{\AA}$, mineral oil pressure transmitting media. A MB DAC with $300\mu\text{m}$ culets was used to collect the data.	75
4.6	Plot of diffraction patterns for Pr between 1.7 and 7.0GPa. The transition pressure from <i>dhcp</i> to <i>fcc</i> is shown to occur between 1.7 and 5.4 GPa, with the shown intermediary pressure (5.2GPa) showing a mixed phase. The phase of each integrated diffraction pattern is noted on the left of the figure.	77
4.7	Example Rietveld refinement of Pr in the <i>fcc</i> phase. The sample pressure is 7.1(2)GPa, diffraction pattern was collected on Station 9.5 of Daresbury SRS using $\lambda = 0.44397\text{\AA}$ at room temperature. A MB-type cell with culets of size $300\mu\text{m}$, ruby sphere manometer and mineral oil pressure medium were used. Peaks labeled with asterisks correspond to contaminant peaks.	78
4.8	Comparison of the (111) reflection from (i) <i>fcc</i> pattern, collected at 6GPa and (ii) <i>d-fcc</i> pattern collected at 7.4GPa. Shown in (ii) is the reflection that splits from the (111) <i>fcc</i> upon pressurisation into the <i>d-fcc</i> phase, the maximal splitting is shown here, which is approximately 0.1° . Both patterns were collected from the same sample on pressure increase, at Station 9.5HPT of Daresbury SRS with a wavelength of $\lambda=0.44397\text{\AA}$	80
4.9	Comparison of the <i>hP6</i> , <i>hR24</i> and <i>mC4</i> structures which have been suggested as solutions for the <i>d-fcc</i> phase with the precursor <i>fcc</i> phase. Shown in (i) is the <i>hP6</i> structure, in (ii) the <i>hR24</i> structure and in (iii) the <i>mC4</i> structure. The <i>fcc</i> unit cells are shown with smaller, black circles joined by solid black lines, the respective proposed <i>d-fcc</i> solutions have atoms in their unit cell shown with larger, grey circles, joined by dashed lines. The crystallographic axes (a, b and c) for the <i>fcc</i> and <i>d-fcc</i> are noted on each diagram.	81

- 4.10 Rietveld refinement of Pr in *d-fcc* phase at 10GPa using the *hR24* structure. From Rietveld refinement, the unit cell parameters are given as: $a=6.6284(1)$, $c=16.3991(6)\text{\AA}$, $\text{Vol./atom}=25.9990(11)\text{\AA}^3$. Atomic positions: $z_1=0.2698(3)$, $x_2=0.5053(3)$, $y_2=-x_2$, $z_2=0.2444(4)$. Data was collected on Station ID09A of ESRF using a wavelength of $\lambda=0.414412\text{\AA}$. 82
- 4.11 Refinement of Pr in *d-fcc* phase at 10GPa using the *hP6* structure. From the refinement the unit cell parameters are given as: $a=6.6295(8)\text{\AA}$ and $c=16.4045(5)\text{\AA}$. Data collected on ID09A of ESRF, Grenoble using a wavelength of $\lambda=0.414412\text{\AA}$. Contaminant peaks are observed and labelled in the figure with asterisks. 83
- 4.12 Figure showing a refinement of *C2/m* to a sample of Pr collected at 15GPa on ID09a of the ESRF, Grenoble. Upper tick marks correspond to the refined peak positions from Ta (pressure calibrant), the lower tick marks to refined peak positions from Pr. Figure is reproduced from Syassen *et al.* [Syassen 00]. 84
- 4.13 Refinement of Pr at 10GPa using the *C2/m* structure. Unit cells parameters are given as: $a = 5.7510(2)$, $b = 3.2924(2)$ and $c = 5.6817(3)\text{\AA}$. Data was collected on Station 9.5 of Daresbury SRS using a wavelength of $\lambda=0.44397\text{\AA}$ 85
- 4.14 Plot showing variation of atomic volume vs. pressure for the stability range of the *hR24 d-fcc* structure of Pr. Errors bars corresponding to errors in volume and pressure (estimated) are omitted, as they are obscured by the symbols used to plot the data. Filled symbols represent data collected on pressure increase, open symbols represent data collected on pressure decrease. Different symbol shapes represent data collected during different experiments at Station 9.5 HPT of Daresbury SRS. A wavelength of $\lambda=0.44397\text{\AA}$ was used for collection of this data. 88
- 4.15 Axial ratio, c/a , plotted as a function of pressure for the *hR24* structure between 7 and 14GPa in Pr. Datapoints for this graph originate from multiple datasets, collected at different times on different beamlines. Error bars are plotted on this figure, but are obscured by the size of the data points. The straight line represents the c/a ratio for the *fcc* unit cell transformed into the hexagonal setting. Open symbols represent data collected on pressure decrease, filled symbols represent data collected on pressure increase with the different filled symbols corresponding to data collected during different experiments. 89
- 4.16 Plot of relative displacements of atomic positions in *hR24* away from *fcc* positions as a function of pressure. Labels ϵ , δ_1 and δ_2 are used, as from Hamaya *et al.* [Hamaya 93]. Error bars are too small to be seen. 91
- 4.17 Waterfall plot showing the switching in relative intensities of (i) the $8\text{-}10^\circ$ doublet, and (ii) the doublet around $17\text{-}18^\circ$, between which an additional peak appears. Data for (i) and (ii) were collected on pressure increase at Station 9.5 of Daresbury SRS, using a wavelength of $\lambda=0.44397\text{\AA}$ 92

4.18	Rietveld refinement made to Pr diffraction pattern collected at 19GPa on Station 9.5HPT of Daresbury SRS using the <i>mC16</i> structure reported as the solution to the <i>d-fcc</i> phase by Dmitriev <i>et al.</i> Dots are experimental points, upper line is calculated diffraction pattern, lower line is the difference plot between calculated and observed data and tick marks are the locations of peaks in the model structure. [Dmitriev 00]. A wavelength of $\lambda=0.44397\text{\AA}$ was used for the collection of this data. . . .	94
4.19	Rietveld refinement made to Pr diffraction pattern collected at 19GPa on Station 9.5HPT of Daresbury SRS using the <i>mC16</i> structure reported as the solution to the <i>d-fcc</i> phase by Dmitriev <i>et al.</i> [Dmitriev 00] with the <i>b</i> and <i>c</i> lattice parameters switched relative to those refined in Figure 4.18. A wavelength of $\lambda=0.44397\text{\AA}$ was used for the collection of this data.	95
4.20	Diagram showing the relationship between the <i>fcc</i> and <i>Ibam</i> structures. In this 3D view a single <i>Ibam</i> unit cell is drawn (comprises of all atoms, with basis vectors, a, b and c shown). Atoms within the <i>Ibam</i> unit cell are shown as grey circles, atoms within the <i>fcc</i> unit cell are shown by red circles, with the <i>fcc</i> unit cell shown by dashed black lines, the <i>Ibam</i> unit cell is not drawn.	99
4.21	Rietveld refinement of Pr using the <i>Ibam</i> , the 1D integrated pattern made from file 260 of the HS3109 run, collected at Station ID09A of the ESRF, Grenoble. Where $\lambda=0.41146\text{\AA}$, pressure= 19GPa. Fit parameters are as follows $a=8.8955\text{\AA}$, $b=6.3809\text{\AA}$; $c=6.2011\text{\AA}$. $x_1=0.2673(5);y_1=0.0405(6);y_2=0.2310(6)$	101
4.22	Plot of variation of the <i>Ibam</i> <i>c/a</i> ratio with respect to pressure. Error bars are plotted, but are obscured by the plotted symbols.	102
4.23	Plot of of the <i>Ibam</i> atomic volume with respect to pressure. Error bars are plotted, but are obscured by the plotted symbols.	103
4.24	Diagram how the <i>Ibam</i> structure fails to account for the splitting of a peak (440) located at 18.27° . Here, dots represent the observed data, the upper line represents the refined model, the lower line is the difference plot between the observed and refined data. Lower tick marks are the peak positions as predicted by the <i>Ibam</i> model, the upper tick marks were added to highlight the positions of the observed peak centroids. The small peak splitting, 0.05° was only observed in the x-ray diffraction data collected at beamline ID09a of the ESRF, which offered both higher resolution and higher flux compared to Station 9.5 of Daresbury SRS. $\lambda = 0.414412\text{\AA}$, $P = 19\text{GPa}$	105
4.25	Waterfall plot showing the transition from the <i>Ibam d-fcc</i> phase to the α -U phase in Pr. Pressures of each data set are noted on the right side of the diffraction pattern. The pattern at 19.6GPa is predominantly <i>Ibam</i> , 20.3 and 20.5GPa are mixed-phase patterns, 20.6GPa is a predominantly α -U pattern.	107

4.26	Part of a 2D diffraction image of Pr at 21GPa taken at beamline ID09a of the ESRF. This figure highlights the pronounced texture visible in the diffraction rings, which is observed in all samples upon transition to the α -Uranium phase.	108
4.27	Rietveld refinement made to a sample of Pr, at 21GPa, in the α -Uranium phase. Data collected on Station 9.5 of Daresbury SRS using a wavelength of $\lambda = 0.44397\text{\AA}$. Refined lattice parameters are given in Table 4.8 $R_{wp}=4.79\%$	110
4.28	Schematic diagram of the sample chamber used for laser annealing trials. A thin NaCl barrier is highlighted. Location of Pr sample, ruby sphere pressure calibrant and tungsten gasket are labeled.	112
4.29	Section of 2D diffraction image from the laser annealed Pr sample in Boehler-Almax style DAC. Diffraction pattern collected on Station 9.5 HPT at Daresbury SRS, with a wavelength of $\lambda = 0.44397\text{\AA}$, $P = 19\text{GPa}$. Spots originating from contaminants are labelled with (\star), from ruby manometer with (+), remaining diffraction rings originate from the laser annealed Pr sample.	114
4.30	Plot of the atomic volume vs. pressure for the pressure range investigated in Pr. Alternating black and grey points are used to differentiate between data collected in different phases. The determined phase transition pressures are represented on the figure with dashed vertical lines, phases are labelled. The <i>d-fcc</i> phase is labelled as <i>hR24</i> and <i>Ibam</i> , representing the respective solutions for the structure of the phase. On the right of the figure the volumes before and after the transition to the α -U phase are noted, a volume difference of 11% is observed at this transition. Data was collected on Station 9.5 of Daresbury SRS using a wavelength of $\lambda=0.44397\text{\AA}$	117
4.31	Plot of the atomic volume vs. pressure for the pressure range investigated in Pr with a fitted 3 rd order Birch-Murnaghan equation of state (EoS) shown in black. The EoS, fitted using EOSFIT [Angel 01], has least-squares refined values of $k_0=31.81761\text{ GPa}$, $k'=2.29268$, $k''=-0.16018$ and $V_0=33.81656\text{ \AA}^3$. The EoS was fitted from zero (ambient pressure) to 20GPa, owing to the volume discontinuity which occurs at 20GPa. Data collected from Station 9.5 of Daresbury SRS using a wavelength of $\lambda=0.44397\text{\AA}$. Errors plotted, but obscured by the size of the datapoints.	118
5.1	High-pressure and high-temperature phase diagram of Nd, reproduced from Tonkov [Tonkov 05].	122
5.2	Integrated 1D diffraction profile of Nd collected at 11.6 GPa from a sample in a DXR6 type DAC on Station 9.5 of Daresbury SRS, using a wavelength of $\lambda=0.44397\text{\AA}$. Contaminant peaks are highlighted with asterisks in the main diffraction profile. The inset shows an enlarged region of the diffraction profile, between 8 and 12° in 2θ , with contaminant peaks indicated by crosses.	125

5.3	Waterfall plot of integrated 1D diffraction profile representative of the phases observed on compression of Nd from 1.7-42GPa. Pressures of the individual patterns are listed to the right of each diffraction pattern. Data were collected on Station 9.5 of Daresbury SRS using a wavelength of $\lambda=0.44397\text{\AA}$	128
5.4	Rietveld refinement of a Nd <i>dhcp</i> pattern collected at 1.7GPa on Station 9.5 of Daresbury SRS, using a wavelength of $\lambda=0.44397\text{\AA}$. A mineral oil pressure transmitting medium was used. $R_{wp} = 11.16\%$. The unit cell parameters are: $a = 3.5394(2)\text{\AA}$ and $c = 11.5867(1)\text{\AA}$. An asterisk indicates the position of the contaminant peak within the sample. . . .	129
5.5	Rietveld refinement of the <i>fcc</i> phase of Nd collected at 12.3GPa on Station 9.5 of Daresbury SRS, using a wavelength of $\lambda=0.44397\text{\AA}$. A mineral oil pressure medium was used, with ruby spheres as a pressure manometer within the sample chamber. The unit cell parameters are $a = b = c = 4.74309(5)\text{\AA}$, $R_{wp}=4\%$	131
5.6	Plot showing the atomic volume plotted against pressure for the <i>fcc</i> phase of Nd. Data were collected on Station 9.5 of Daresbury SRS, on both pressure increase and pressure decrease, during different experiments. Errors in the volume at each pressure are of the order $\times 10^{-4} \text{\AA}^3$ and as such are not visible on the plot. A guide to the eye (fitted using a linear least squares routine) is also shown.	132
5.7	Diagram illustrating the hysteresis observed in the <i>fcc</i> to <i>d-fcc</i> transition on pressure increase and decrease. The data shown were collected from a single sample during an experiment on Station 9.5 of Daresbury SRS, using a wavelength of $\lambda=0.44397\text{\AA}$. Open squares represent data collected on pressure decrease, filled squares represent data collected on pressure increase.	133
5.8	Two integrated diffraction patterns from Nd, collected at (i) 12.6GPa and (ii) 15.4GPa. The pattern in (i) is within the <i>fcc</i> phase, while that of (ii) is in the <i>d-fcc</i> phase. Note the splitting of the <i>fcc</i> (111) and (200) peaks and additional peaks appearing in (ii). This splitting is highlighted (by tick marks below the diffraction patterns) in the inset, which shows an the region around the <i>fcc</i> (111) reflection for both the 12.6GPa and 15.4GPa diffraction pattern shown in main body of the figure. The pattern presented in (ii) is shifted by -0.27° in 2θ , such that the main peaks are approximately aligned in both patterns. Data for this figure were collected on Station 9.5 of Daresbury SRS, using a wavelength of $\lambda=0.44397\text{\AA}$	135
5.9	Background-corrected <i>d-fcc</i> Nd pattern collected at 22.4GPa on Station 9.5 of Daresbury SRS, using a wavelength of $\lambda=0.44397\text{\AA}$	136
5.10	LeBial refinement of a Nd <i>d-fcc</i> pattern collected at 22.4GPa on Station 9.5 of Daresbury SRS using the $C2/m$ structural solution. Refined lattice parameters are $a = 5.5010(2)\text{\AA}$, $b = 3.1328(2)\text{\AA}$, $c = 5.4232(3)\text{\AA}$, and $\beta = 109.295(5)^\circ$. $R_{wp} = 5.69\%$ for this LeBial refinement. A wavelength of $\lambda=0.44397\text{\AA}$ was used to collect this data.	137

- 5.11 Refinement made to a Nd *d-fcc* pattern collected at 22.4GPa from Station 9.5 of Daresbury SRS using the *P2/m* structural solution. Refined lattice parameters are $a = 5.4988(2)\text{\AA}$, $b = 3.1373(2)\text{\AA}$, $c = 5.4198(2)\text{\AA}$, and $\beta = 109.217(4)^\circ$. $R_{wp} = 4.28\%$ for this LeBial refinement. A wavelength of $\lambda=0.44397\text{\AA}$ was used to collect this data. 138
- 5.12 Refinement made to a Nd *d-fcc* pattern collected at 22.4GPa from Station 9.5 of Daresbury SRS using the *hR24* structural solution. Refined lattice parameters are $a = b = 6.2640(1)\text{\AA}$, $c = 15.5776(3)\text{\AA}$. $R_{wp} = 5.14\%$ for this LeBial refinement. A wavelength of $\lambda=0.44397\text{\AA}$ was used to collect this data. 139
- 5.13 Rietveld refinement of Nd *d-fcc* phase using the *hR24* structure to an x-ray diffraction pattern collected at 22.4GPa at Station 9.5 of Daresbury SRS, with a wavelength of $\lambda=0.44397\text{\AA}$. Refined lattice parameters are $a = b = 6.61396(9)\text{\AA}$, $c = 16.2340(3)\text{\AA}$. Atomic positions are $x_1 = -y_1 = 0.4909(2)$, $z_1 = 0.2575(2)$, $x_2 = y_2 = 0$, $z_2 = 0.2277(2)$. $R_{wp} = 7.63\%$ for this refinement. 141
- 5.14 Variation of the *c/a* ratio for the *hR24* phase of Nd, between 12.3 and 22.4GPa on both pressure decrease (open squares) and pressure increase (all filled symbols). The *c/a* ratio of the precursor *fcc* phase for comparison is $\sqrt{6}$, or 2.449. Data were collected on Station 9.5 of Daresbury SRS using a wavelength of $\lambda=0.44397\text{\AA}$ 142
- 5.15 Variation of the atomic volume Nd in the stability range of the *hR24* phase (between 12.3 and 22.4GPa), on both pressure decrease (open squares) and pressure increase (all filled symbols). Different filled symbols correspond to data collected from different loadings of Nd. Data was collected on Station 9.5 of Daresbury SRS using a wavelength of $\lambda=0.44397\text{\AA}$ 143
- 5.16 Variation of the refinable atomic positions Nd in the stability range of the *hR24* phase, between 12.3 and 22.4GPa (a data point at 24GPa is shown for comparison of the atomic position in the following phase). The refinable atomic position x_1 , z_1 and z_2 are shown in different plots, for clarity. Filled square and triangle data points are collected on pressure increase, open squares on pressure decrease. Data was collected on Station 9.5 of Daresbury SRS using a wavelength of $\lambda=0.44397\text{\AA}$ 145
- 5.17 Comparison of a section of two datasets, collected from a DAC containing Nd and a mineral-oil pressure medium at 17.5GPa (lower diffraction pattern) and 22.4 GPa (upper diffraction pattern). The upper pattern has been offset in 2θ to better illustrate the effect of pressure on the observed peak widths. Some additional peak separation is evident in the upper diffraction pattern, which is expected from the pressure dependence of the lattice parameters. Data was collected on Station 9.5 of Daresbury SRS using a wavelength of $\lambda=0.44397\text{\AA}$ 147

5.18	Comparison of a sample of Nd within a DXR6 DAC before (i), and after (ii) annealing in a furnace for 4 hours at 200°C. Diffraction patterns collected on Station 9.5 of Daresbury SRS. $\lambda = 0.44397\text{\AA}$, $P = 23.9$ GPa. Insert shows an enlarged section of the diffraction pattern, which illustrates the increase in resolution gained from annealing. Patterns are offset in 2θ for clarity.	149
5.19	Comparison of diffraction patterns obtained from a sample of Nd within a DXR6 DAC (i) before, and (ii) after annealing in a furnace for 4 hours at 200°C. Diffraction patterns are the same as those used in Figure 5.18, but focused on a section of the 2D diffraction pattern, exemplifying how “fuzzy” diffraction rings become sharper and resolved into distinct rings.	150
5.20	Comparison of the (i) 9.0 - 11.0° and (ii) 19.2 - 20.4° 2θ range for patterns collected from Nd in a DXR6 DAC at 18.9, 22.4, 25.6 and 26.6 GPa at Station 9.5 of Daresbury SRS during a single experiment. In (i) the (202) and (006) peaks are visible, in (ii) the (0 0 12) and (404) are seen. The appearance of a peak between the (0 0 12) and (404) peaks on pressure increase is highlighted in (ii) with an arrow. Data were collected using a DXR6 type DAC, $\lambda = 0.44397\text{\AA}$, and a mineral-oil pressure-transmitting medium.	151
5.21	Graph of relative intensities of the (006) and (202) reflections for the <i>d-fcc</i> phase of Nd between 15 and 27GPa. Open squares represent data collected on pressure decrease, filled squares represent data collected on pressure increase. Dashed lines represent linear least-squares fits made to the data, in the case of increasing pressure, back extrapolated to 20GPa to better highlight the intersection point at 22.06GPa. The data were collected on Station 9.5 of Daresbury SRS, a wavelength of $\lambda=0.44397\text{\AA}$ was used.	152
5.22	Rietveld refinement of a sample of Nd collected at 26.6(2) GPa on Station 9.5 of Daresbury SRS using a wavelength of $\lambda=0.44397\text{\AA}$. Refinement made using the <i>Ibam</i> structure in Jana2000, refined lattice parameters are $a = 8.7511(26)$, $b = 6.2325(9)$, $c = 6.1036(11)\text{\AA}$. Preferred orientation effects are present in the sample and account for the difference in intensity of observed and predicted diffraction pattern.	154
5.23	Plot of the pressure-dependence of the atomic volume for the <i>hR24</i> and <i>Ibam</i> solutions to the <i>d-fcc</i> phase of Nd. Points below 25 GPa (which correspond to the atomic volume of the <i>hR24</i> solution) are shown for comparison. A dashed vertical line indicates the boundary of the two phases on pressure increase. The lack of discontinuity in the plot indicates a 2nd-order transition between the two structures. Different symbols represent data collected from different loadings of Nd, all on pressure-increase.	155
5.24	Plot of the pressure-dependence of c/a ratio for the <i>Ibam</i> solution to the <i>d-fcc</i> phase of Nd. Errors are too small to be seen with the plotted symbol size. Different symbols represent data collected from different loadings of Nd, all on pressure-increase. Data was collected on Station 9.5 of Daresbury SRS using a wavelength of $\lambda=0.44397\text{\AA}$	156

- 5.25 Figure showing the splitting of the (440) *Ibam* reflection, into the (440) and the peak identified with an arrow above it. The data for this integrated diffraction pattern was collected at 26.6(2)GPa on Station 9.5 of Daresbury SRS with a wavelength of $\lambda=0.44397\text{\AA}$. Dots correspond to the observed (integrated) data, the upper line to the refined *Ibam* model, the lower line is the difference plot between observed and modelled data. Tick marks represent the positions of peaks in the refined model. . . . 157
- 5.26 LeBail fit of a *hP3* model to the post-*Ibam* phase, using unit cell values derived from the *hP3* structure reported by Akella *et al.* ([Akella 99]) as the solution to the structure of Nd before transformation to α -Uranium structure. Data was collected on Station 9.5 of Daresbury SRS using a wavelength of $\lambda=0.44397\text{\AA}$ 159
- 5.27 Waterfall-plot of integrated diffraction profiles collected from Nd on pressure increase from 34.7 to 43.1 GPa during a single experiment at Station 9.5 of Daresbury SRS, using a wavelength of $\lambda=0.44397\text{\AA}$. For clarity, successive patterns are shifted by 0.5° in 2θ . The pressure of each dataset is indicated at the right of each plot. 160
- 5.28 Enlarged section of the $17\text{-}21^\circ$ region in 2θ of Figure 5.27 for the patterns collected at 36.7, 38.9 and 41.3 GPa, thus illustrating the changes occurring during the transition from an *Ibam* structure (36.7GPa), a mixed (*hP3+Ibam*) phase (38.9GPa), to a *hP3* phase (41.3GPa). Data was collected on Station 9.5 of Daresbury SRS using a wavelength of $\lambda=0.44397\text{\AA}$ 161
- 5.29 Waterfall plot showing data collected on La at Station 9.5 of Daresbury SRS using monochromatic x-rays of wavelength $\lambda=0.44397\text{\AA}$. The sample pressure, measured by ruby fluorescence, is displayed on the right hand side of each diffraction pattern. Pressures shown are from 5.2 to 38.6GPa in uneven steps. 164
- 5.30 Waterfall plot showing data collected on La at Station 9.5 HPT of Daresbury SRS using monochromatic x-rays of $\lambda=0.44397\text{\AA}$. Successive plots are shifted by 0.1° in 2θ for clarity. A switching in the relative intensities of the first (006) and second (202) peaks in the doublet occurs at about 16GPa on pressure increase. 165
- 5.31 Refinement of La with *hR24* structure made to a *d-fcc* diffraction pattern collected at 19.8GPa from Station 9.5 of Daresbury SRS. Refined lattice parameters are $a = 6.66112(9)\text{\AA}$, and $c = 16.2280(1)\text{\AA}$ 166
- 5.32 Refinement of La with *Ibam* structure made to a *d-fcc* diffraction pattern collected at 28GPa from Station 9.5 of Daresbury SRS, using a wavelength of $\lambda=0.44397\text{\AA}$. Refined lattice parameters are $a = 9.1734(4)\text{\AA}$, $b = 6.4914(3)\text{\AA}$ and $c = 6.3557(3)\text{\AA}$. $R_{wp} = 4.65\%$ 167

5.33 A plot of the variation of atomic volume with pressure for the entirety of the pressure range studied within Nd. Transition pressures between structures are indicated by dashed vertical lines, the respective phases are labelled on the diagram. Data were collected on multiple separate experiments on Station 9.5 of Daresbury SRS, using a wavelength of $\lambda=0.44397\text{\AA}$. Some scatter exists on within the *fcc* region due to a mixture of data collected on pressure increase and decrease being plotted. Atomic volume derived from volume calculated using Rietveld refined lattice parameters for patterns at each pressure point. 169

5.34 Plot of the atomic volume vs. pressure for the pressure range investigated in Nd (0-40GPa) with a fitted 3rd order Birch-Murnaghan equation of state (EoS) shown in black. The EoS, fitted using EOSFit[Angel 01], has least-squares refined values of $k_0=31.96464$ GPa, $k'=2.82263$, $k''=-0.12820$ and $V_0=34.16375 \text{\AA}^3$. The EoS was fitted from zero (ambient pressure) to 40GPa. Data collected from Station 9.5 of Daresbury SRS using a wavelength of $\lambda=0.44397\text{\AA}$. Errors plotted, but obscured by the size of the datapoints. 170

6.1 Plot of the atomic volume vs. pressure for the pressure range investigated in Pr. Alternating black and grey points are used to differentiate between data collected in different phases. The determined phase transition pressures are represented on the figure with dashed vertical lines, phases are labelled. The *d-fcc* phase is labelled as *hR24* and *Ibam*, representing the respective solutions for the structure of the phase. On the right of the figure the volumes before and after the transition to the α -*U* phase are noted, a volume difference of 11% is observed at this transition. . . . 176

6.2 Plot of the atomic volume vs. pressure for the pressure range investigated in Nd. Alternating black and grey points are used to differentiate between data collected in different phases. The determined phase transition pressures are represented on the figure with dashed vertical lines, phases are labelled. The *d-fcc* phase is labelled as *hR24* and *Ibam*, representing the respective solutions for the structure of the phase. The maxima of pressure included in this diagram is 40GPa. 177

List of Tables

2.1	Summary of a hydrostaticity of pressure transmitting media commonly used during high-pressure x-ray diffraction experiments. The results of Angel <i>et al.</i> and Klotz <i>et al.</i> differ substantially for the Argon pressure transmitting medium, with Angel quoting a hydrostatic limit 5x smaller than Klotz. The difference is attributable to the method used for determining the loss of hydrostaticity. Angel <i>et al.</i> used diffraction line-broadening (at a high-resolution synchrotron source) to determine the approach to the hydrostatic limit, and state that the 10GPa value often quoted was discovered using ruby luminescence broadening. . . .	29
3.1	Summary of a selection of papers on Pr comments regarding presence of contaminant within their data.	64
4.1	Table showing the Rietveld refined unit cell parameters for the <i>dhcp</i> phase of Pr, data corresponds to the refinement shown in Figure 4.5 at a pressure of 1GPa, collected using a wavelength of $\lambda = 0.4654\text{\AA}$ on Station 9.1 of Daresbury SRS.	75
4.2	Table showing the Rietveld refined unit cell parameters for the <i>fcc</i> phase of Pr, data corresponds to the refinement shown in Figure 4.7 at a pressure of 7GPa, collected using a wavelength of $\lambda = 0.44397\text{\AA}$ on Station 9.5 of Daresbury SRS. Atomic positions refined, but round to regular <i>fcc</i> values.	76
4.3	Table showing the Rietveld refined unit cell parameters for the <i>hR24</i> phase of Pr, data corresponds to the refinement shown in Figure 4.10 at a pressure of 10GPa, collected using a wavelength of $\lambda = 0.414412\text{\AA}$ on Station ID09A of ESRF.	86
4.4	Table showing the degree of overlap encountered in the structure proposed by Dmitriev [Dmitriev 00] for a peak at 13° in 2θ . Locations of the peak in 2θ and index assigned by Jana2000 during refinement. Values from a Rietveld refinement made to data collected at 13GPa at Station 9.5 HPT of Daresbury SRS using a wavelength of $\lambda=0.44397\text{\AA}$. .	96
4.5	Subset of the peaks from a diffraction pattern of Pr, used for indexing the <i>d-fcc</i> phase. Data was collected on Station 9.5 of Daresbury SRS using a wavelength of $\lambda=0.44397\text{\AA}$	97
4.6	Table showing the orthorhombic trial cell found by DicVol when indexing the peaks from Table 4.5.	98

4.7	Structural information gained from a Rietveld refinement of Pr diffraction data collected at 19.0GPa using the <i>Ibam</i> structure. Data collected at Station ID09A of the ESRF, Grenoble with a wavelength of $\lambda=0.41146\text{\AA}$	101
4.8	Table showing the structural parameters of the α -U phase of Pr, as refined from patterns collected at 21GPa	110
5.1	Table showing the structural parameters of the <i>dhcp</i> phase of Nd, as refined from a pattern collected at 1.7GPa on Station 9.5 of Daresbury SRS, using a wavelength of $\lambda=0.44397\text{\AA}$. Rietveld refinement is shown in Figure 5.4.	127
5.2	Table showing the structural parameters of the <i>fcc</i> phase of Nd, as refined from a pattern collected at 12.3GPa on Station 9.5 of Daresbury SRS, using a wavelength of $\lambda=0.44397\text{\AA}$. Rietveld refinement is shown in Figure 5.5.	130
5.3	Table showing the structural parameters of the <i>fcc</i> phase of Nd, as refined from a pattern collected at 12.3GPa on Station 9.5 of Daresbury SRS, using a wavelength of $\lambda=0.44397\text{\AA}$. Rietveld refinement is shown in Figure 5.5.	140
5.4	Table showing the structural parameters of the <i>Ibam</i> phase of Nd, as refined from a pattern collected at 26.6GPa on Station 9.5 of Daresbury SRS, using a wavelength of $\lambda=0.44397\text{\AA}$. Rietveld refinement is shown in Figure 5.22.	154
5.5	Table of peak positions extracted from a 40GPa pattern of Nd run on Station 9.5 of Daresbury SRS, using a wavelength of $\lambda=0.44397\text{\AA}$. Peaks location, together with associated intensity were extracted using DatLab [Syassen 08b], then indexed using DicVol [Louer 04].	159

Chapter 1

Introduction

1.1 Extreme Conditions

Pressure, as a thermodynamic variable, has the largest observable range within nature. The pressure scale within the universe ranges from 1×10^{-15} Pa, the pressure within the vacuum of space (the non-equilibrium pressure of H_2 gas in intergalactic space), to 1×10^{16} Pa, the pressure within a neutron star. This pressure range is shown in Figure 1.1. Pressure, defined as

$$Pressure = \frac{Force}{Area} \quad (1.1)$$

, is applied to systems being studied using relatively simple apparatus. In the case of small sample volumes (volumes of the order $50 \mu\text{m}^3$) used for x-ray diffraction studies, diamond anvil cells are employed (as is the case in this work). Larger volumes require larger apparatus, such as those used for neutron diffraction studies, where the samples need to be orders of magnitude larger (typically of the order mm^3) than those used for x-ray diffraction studies .

X-ray diffraction allows an insight into the novel atomic structures adopted by materials when subjected to the extreme conditions of pressure (and temperature) found in nature. Applying pressure changes the density, crystal structure and electronic configuration of materials, and the effect of the latter can be pronounced enough to transform materials which, at ambient conditions are insulators, into semiconductors or metals at pressure [McWhan 72]. Similarly, the compression of elements can lead “simple” elements, such as the alkali-earth metals, to behave as $3d$ transition metals, which can cause these “simple” conductive metals to superconduct at low temperatures [McWhan 72]. High pressure experiments work towards the modelling of astronomical processes in the outer planets (Uranus and Neptune) [Cavazzoni 99]; the formation and behaviour of minerals within the Earth’s surface [Davis 64]; the behaviour of

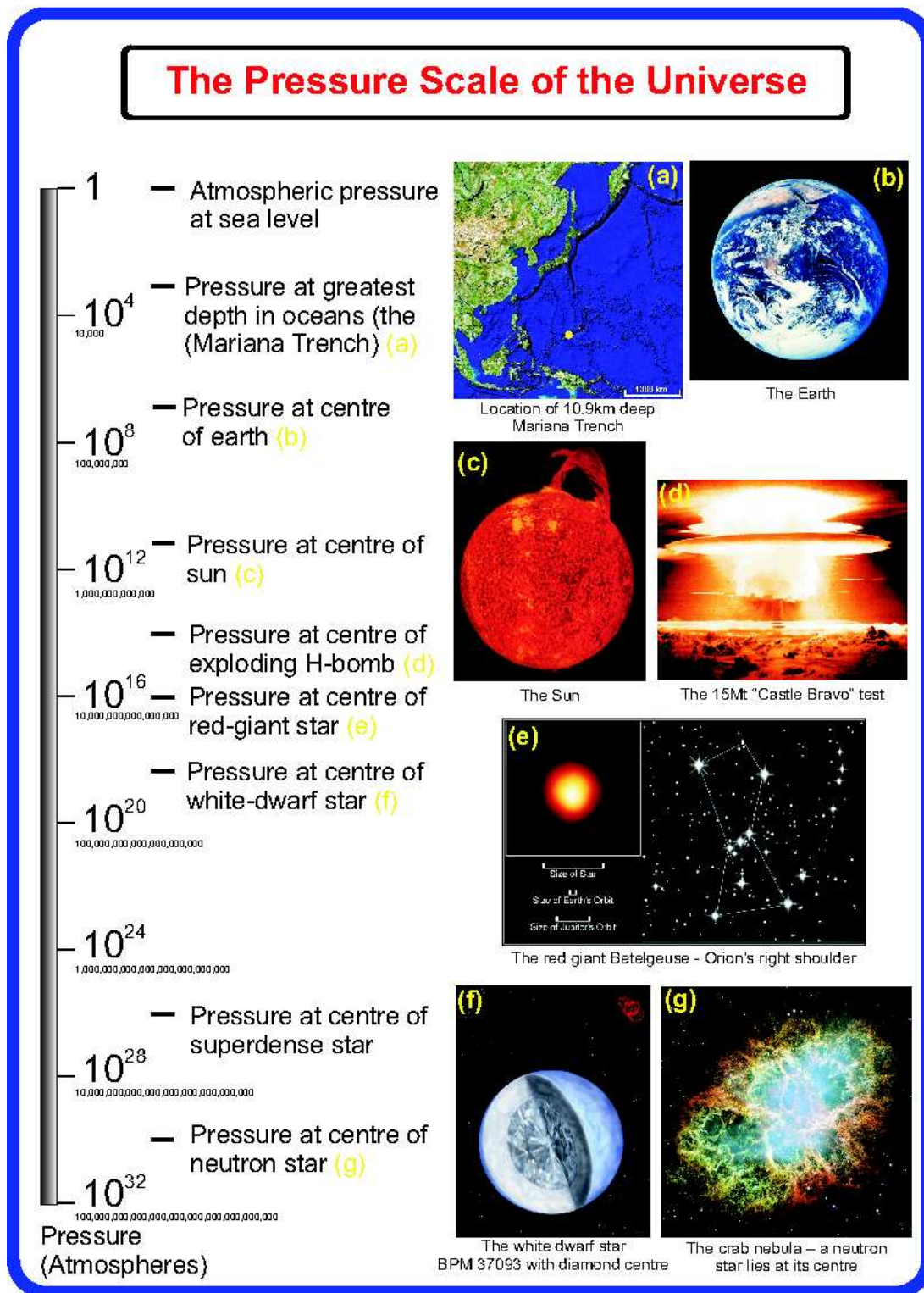


Figure 1.1: Diagram illustrating the scale of the variation in pressure observable within nature. Here, atmospheric pressure is used as a relatable lower reference pressure, it is not the lowest pressure attainable. Reproduced with permission [Ingo Loa 07].

mechanised or industrial components (such as drill bits for deep sea drilling, concrete for wells, fault propagation in fuselage); the novel biological systems (extremeophiles) [Anurag Sharma 02]; and military research [Davidson 07].

1.2 Lanthanides

In traversing the lanthanide group of elements, the $4f$ electronic shell is filled with increasing atomic number, Z . The $4f$ shell is a partially-filled shell buried within the atom, shielded from outside influences (and partially shielded from the electrostatic influence of the nucleus) by the $5s$ and $5p$ electronic shells [Cotton 91]. A similar valence shell electronic structure of 3 valence ($5d$) electrons throughout the lanthanide group (with the exception of the divalent lanthanides Europium and Ytterbium) yields the expectation of similar chemical and physical properties. Indeed, it can be expected that this similarity in properties of the lanthanides will be repeated at high pressure, at least until the effects of pressure increase the energy of the unfilled $4f$ orbital to above that of the valence $5p$ electrons (thus making the $4f$ shell the valence).

It is worth noting that the distinction between the lanthanide and actinide series, while a similarity persists in the electronic structure between the two series with localised f orbitals gaining electrons as Z increases. Actinides have differing $5f$ orbital occupancy and a filled $4f$ orbital. Quantum mechanics dictates that the $4f$ and $5f$ orbitals have differing spatial extent (required by the different energy of the electrons constrained within each) and be mutually orthogonal. Thus, the $5f$ orbital, with electrons of higher energy, must have a larger spatial extent, extending beyond the “screening” influence of the core, making the behaviour of the (lower Z) actinides like those of $6d$ transition metals with itinerant $5f$ electrons [Johansson B. 81]. Increased screening at high Z yields behaviour more akin to lanthanides, as the $5f$ orbital becomes confined to occupy space bound by the d orbital, effectively preventing the participation of the $5f$ electrons in bonding. Lanthanides are also distinctively different from the transition metal series, which is also characterised by filling of a d orbital. For the transition metals, however, the spatial extent of the d orbital is larger, and, as such, is deformed by a greater extent under the influence of neighbouring atoms [Johansson 75].

The chemical similarity of the lanthanides, as stated earlier, is indeed known to extend to high pressure [Johansson 75]. Such is the similarity that the term “regular lanthanide series” (or variations thereof) is used in the literature to describe the series of crystal structures adopted at high pressure by the regular (trivalent) lanthanides. Johansson’s [Johansson 75] common phase diagram (Figure 1.2) exemplifies this similarity, showing

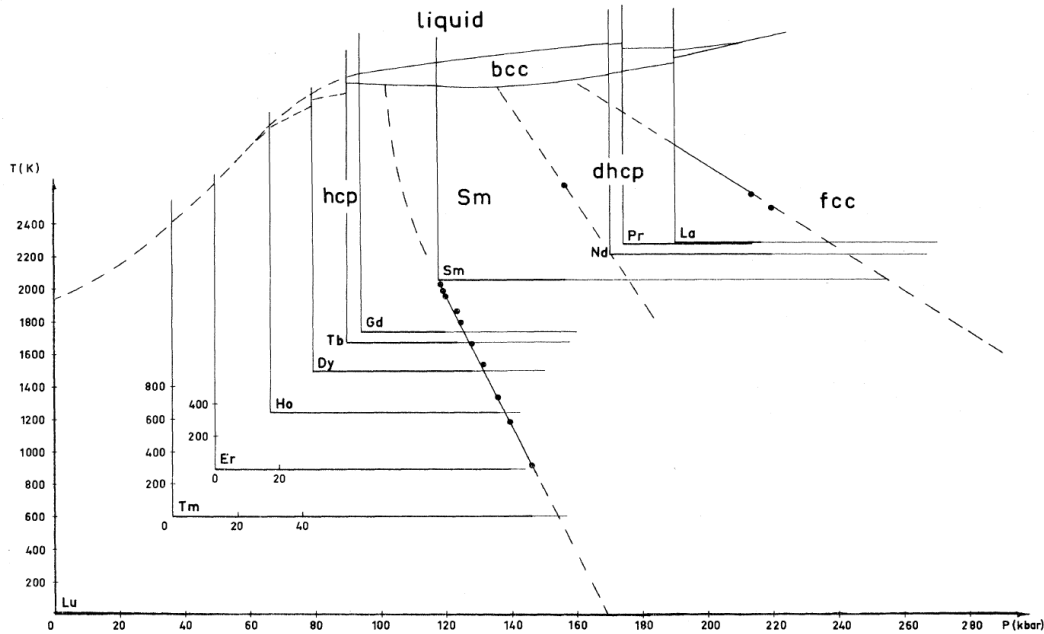


Figure 1.2: Common phase diagram of the regular lanthanide series, reproduced from Johansson [Johansson 75] sources contained in references therein.

that given the similar electronic arrangement of the valence shell, and the addition of electrons to the $4f$ orbital changes the size of the atom. At ambient pressure the low- Z lanthanides (La, Pr, Nd) adopt high-pressure (high- Z lanthanide) crystal structures. Thus, members of the lanthanide series can act as analogues for one another, thus, enabling the experimentalist to use high-pressure (HP) low- Z lanthanides as an analogue to very high pressure (perhaps outside of the ranges accessible with techniques currently available) high- Z lanthanides.

Having established a similarity in the pressure-induced structure of the lanthanides, a closer look at the phase transition sequence shows a succession of second order phase transitions through close-packed structures, $hcp \rightarrow dhcp \rightarrow fcc \rightarrow d\text{-}fcc$, before reaching an open-packed α -Uranium type structure.

Until the $d\text{-}fcc$ phase, the pressure-induced phase transitions are all second order, as transitions are observed to be gradual (occurring, with the co-existence of pre- and post-transition phases over a few GPa) and there are no volume discontinuities in volume vs. pressure plots. However, the $d\text{-}fcc$ to α -Uranium transition marks a first order close-

packed to open-packed transition, with an associated discontinuity in atomic volume of about 10 % [Mao 81]. The mechanism underlying the volume collapse relates to the pressure-induced delocalisation of the $4f$ electrons (the rising of the energy of the $4f$ orbital as pressure decreases the overall volume of each atom leads to the $4f$'s energy surpassing that of the $5d$, thus changing the valence orbital).

1.3 Motivation

Much of the work on the lanthanides under extremes of pressure and temperature conducted after 1980 takes advantage of the high-brilliance synchrotron x-ray radiation sources available globally.

Before 1993 much of this work used energy dispersive x-ray diffraction techniques (EDX) (refer to Section 2.2.2, in Chapter 2 for more information on the techniques employed). However, EDX is a method which is seldom used at present, foregone in favour of the higher-resolution angle-dispersive x-ray diffraction methods (ADX) using 2-dimensional image plates (IP) [McMahon 94, Shimomura 92] or CCDs. These detectors are capable of yielding the accurate intensities required for determination of atomic positions within the unit cell using Rietveld refinement.

This higher resolution offered by ADX at current (3rd / 4th) generation synchrotron sources enabled a plethora of complex [mim], counter-intuitive [Loa 07] and novel [Lundegaard 06] structures to be discovered in elemental systems at high pressure.

The close-packed transition sequence of the lanthanides described in the previous section is accepted in the literature. However, ambiguity persists in the reports of the structure of one of the phases in this sequence. The “*d-fcc* phase” in Pr has been reported as comprising one, or two (similar) phases, and 8 different spacegroups have been presented as the solution to this phase. These problems raise the following questions. In the Pr *d-fcc* pressure range of 7-20GPa is there a transition between two similar structures? What is (are) the structure(s) of the *d-fcc* phase? What is the degree of volume collapse at the *d-fcc* to α -Uranium phase transition?

Further to the study of the *d-fcc* phase of Pr, the *d-fcc* phase of Nd will be investigated, as the structures reported for this phase in the literature are similar to those reported

for Pr, some suggestions for the structure made by analogy. This led the author to question, by analogy, the nature of the structure of the *d-fcc* phase of Nd; will it too exhibit evidence of a phase transition within what is referred to in the literature as a single phase? And, what is the structure of the Nd *d-fcc* phase?

The author will address each of these questions within this thesis. As the literature suggests that the different models for the *d-fcc* structures are differentiated by weak peaks, the use of synchrotron radiation will be required, to be able to observe the subtle differences between the reported structures. Angle-dispersive powder x-ray diffraction, using monochromatic synchrotron radiation will be used to collect the data required for this thesis. The author intends to attempt to encourage crystallisation of powder samples into single crystals to further aid in the disambiguation of the *d-fcc* phase.

1.4 Thesis Outline

Below, an outline of this thesis is presented, with a brief summary for each chapter, of this thesis.

Experimental techniques This chapter describes the angle-dispersive x-ray diffraction techniques used in the experimental chapters of the thesis. The principles of x-ray diffraction, crystallography and high-pressure techniques will be introduced to the reader. Pressure generation, calibration and experimental setup will be covered, including a comparison of the stations used for the majority of this work at Daresbury SRS.

Literature review A review of the publications in the literature, comprising two sections, one on the high pressure behaviour of the lanthanide metals in general, and the other on Pr, specifically is presented in this chapter. In familiarising the reader with the large body of published work, the structures suggested for the *d-fcc* phase, and problems associated with previous studies, are discussed. Reports of sample contamination in the literature will be briefly presented.

Studies of Praseodymium Data are presented on the high-pressure phase transitions of Pr, collected using angle-dispersive x-ray diffraction on Stations 9.1 and 9.5 HPT of Daresbury SRS and ID09A of the ESRF. The data encompasses the pressure range of 0-24GPa, with the focus of study being the *d-fcc* phase between 7 and 20GPa. Detailed analysis of this 7-20GPa pressure range is presented, with the author providing a revised solution to the structure within this pressure range, which differs to those present in the literature.

Studies of Neodymium and Lanthanum Details of studies made at high pressure on Nd in the 0-44GPa pressure range, using angle-dispersive x-ray diffraction techniques are presented in this chapter. Like the preceding chapter, the *d-fcc* of Nd is the focus, existing between 16-40GPa on pressure increase. Refinements made on the data and structural solutions for this pressure range are shown, and the pressure dependence of the unit cell and atomic positions are discussed. Initial studies performed on the light lanthanide La are also presented.

Conclusions The conclusions from the previous chapters are concisely summarised, and the author makes suggestions for further studies.

Chapter 2

Experimental Techniques

2.1 Introduction

In this chapter the author will introduce the experimental techniques used within chapters 4 and 5. This chapter will begin with a brief review of the theoretical background to x-ray diffraction, a technique used to ascertain the atomic structures of materials. The considerations and methods employed to reach the high-pressure phases of the samples under investigation will then be discussed, along with the data collection, processing and analysis methods/tools used. This chapter will give the reader the background information required to understand the author's techniques and methodology.

2.2 Diffraction

Atoms in crystals are arranged in a regular periodic manner, forming a regular lattice (in an ideal single crystal). This lattice, through symmetry, can be considered as a series of planes, a distance d apart (assumed infinite in length, to negate end effects). Electromagnetic (EM) radiation incident on a crystal will illuminate a series of parallel planes, and be scattered elastically (or inelastically) from the electrons within the atoms. Elastic scattering, that is the scattering of radiation which leaves the wavelength of the radiation unchanged (no energy is lost or gained), occurs when the tightly-bound electrons oscillate in response to the magnetic field of the incident EM wave, radiating the same wavelength as was incident upon them. For inelastic scattering, however the energy of the scattered beam is altered by the diffraction process. In some cases, *part* of the energy of incident EM radiation is used in electronic transitions within the atom (Stokes scattering), or creation of a phonon, so the energy emitted by the electrons after transition will have a longer wavelength (lower energy) than the initial incident radiation [Cullity 78]. Conversely, energy can be imparted to the diffracted beam by the sample, on the annihilation of a phonon (anti-Stokes scattering).

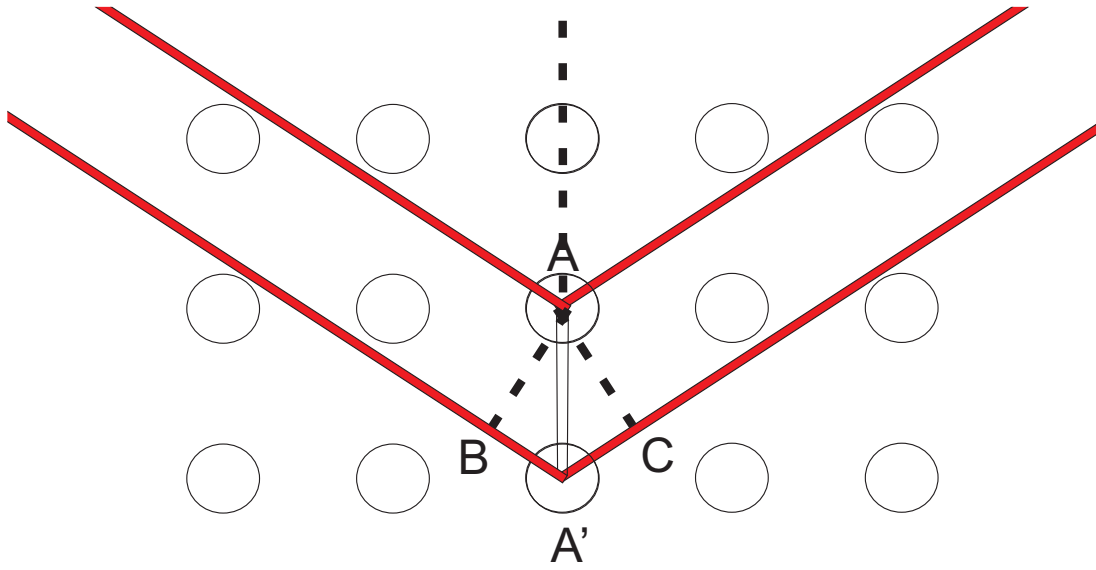


Figure 2.1: Adjacent planes of atoms will give constructive interference only when Bragg's Law is satisfied.

Parallel planes will scatter the incident radiation in the same direction, albeit with some path difference introduced between the radiation scattered from adjacent planes, which, seen in Figure 2.2, is defined geometrically as $2d \sin(\theta)$ (restated in Equation 2.2). Radiation scattered elastically from atoms (equally, planes of atoms) within a crystal will be coherent with radiation scattered elastically from all other atoms within the crystal. This enables radiation scattered from different locations within a crystal to interfere, constructively, or destructively, upon reaching a detector. The path difference between scattered waves, which forms the basis of Bragg's Law, defines when it will be possible for constructive interference to occur between radiation scattered from adjacent planes.

Bragg's Law (Equation 2.2) provides the basis for all diffraction based studies, by stating, the condition necessary for a series of planes or atoms to diffract a photon beam that is incident upon it at some arbitrary angle.

$$(2.1) \quad n\lambda = 2d \sin \theta$$

Parallel rays scattered from points on parallel planes will constructively interfere when Bragg's Law is satisfied; that is, when the path difference for an incident beam at an angle θ to some planes, with wavelength λ , for planes with interplanar spacing of d is equal to a multiple of λ (or a phase difference of $2n\pi$). Another formulation of Bragg's Law is presented later in Equations 2.5, which use vectors to state the conditions required for constructive interference from radiation scattered from a series of planes.

Bragg's law can be proven geometrically. For example, in 2D Figure 2.2 shows how Bragg's law is formulated, where the path difference between radiation scattered from points A and A', $BA' + A'C$, can be determined geometrically as $2d\sin\theta$, this leads to the condition for constructive interference, $2d\sin\theta = n\lambda$, as the scattered radiation from the different points must arrive at the detector with a difference in phase of $2n\pi$ or difference in path length of $n\lambda$ (where n is an integer) [Woolfson 97]. This 2D form of Bragg's Law is readily extensible to 3D, by replacing d (the separation between planes in 2D) with d_{hkl} , the separation between planes of indices (hkl) . Thus, from Bragg's Law, the position of Bragg peaks in a diffraction pattern tells the observer of the size and shape of the unit cell that is diffracting. Bragg's Law, however, does not describe the intensity of the diffracted beam, which is dependent on the positioning of atoms within the layers comprising a unit cell.

The intensity of a diffracted beam is dependent on the position of atoms within the unit cell and their atomic number (i.e. number of electrons scattering coherently) [Cullity 78]. The term f , the atomic scattering factor, describes how the intensity of radiation from a single atom varies with λ and θ . In the most basic form, f can be seen as the ratio of scattered photons from an atom to a single electron, as indicated below:

$$f = \frac{\text{amplitude of wave scattered by atom}}{\text{amplitude of wave scattered by a single electron}} \quad (2.2)$$

The structure factor, f has an angular dependence, simply put, f starts at a maxima for $\theta=0$ and decreases as θ increases. This can be stated as occurring due to the photons being scattered from individual electrons within the atom becoming more out of phase as θ increases [Cullity 78].

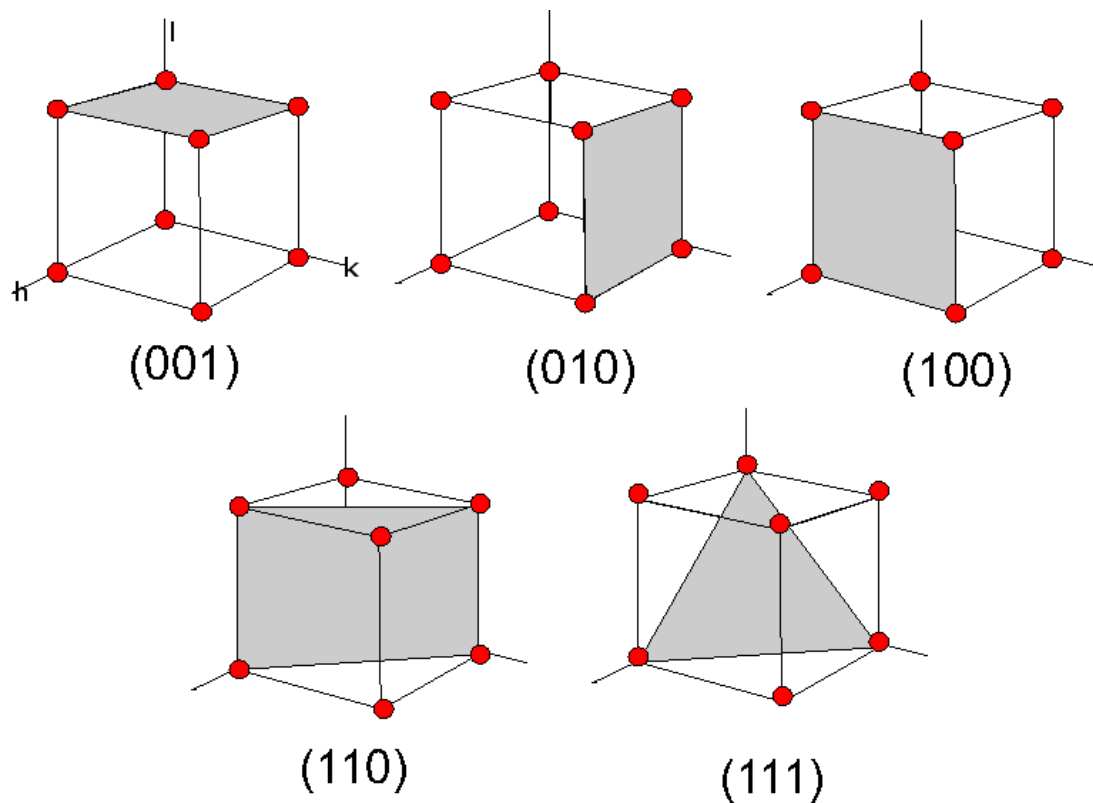


Figure 2.2: Diagram illustrating planes of different $h k l$ in a cubic cell in real space. Illustrated is possible permutations of index 1, higher indices lie parallel to the index 1 plane. The directions h , k and l are labelled for (001) only.

$$F_{hkl} = \sum_1^N f_n e^{2\pi i(hu_n + kv_n + lw_n)} \quad (2.3)$$

Planes of atoms (and hence directions within a crystal lattice) are labeled with the Miller indices ($h k l$), where h , k , l represent the base orthogonal directions in a cartesian coordinate system. The plane (001) is defined as the plane 1 reciprocal unit along the l axis that is perpendicular to c (exemplified in Figure 2.2).

A crystal lattice, as it is periodic can be described in reciprocal space, by a reciprocal lattice, which has dimensions of inverse length. In reciprocal space a spatial frequency, such as the distance between planes within a real-space (direct) lattice (described by the indices (hkl)), will be points (labeled with corresponding (hkl)) within the reciprocal lattice. The direct and reciprocal lattice can be related by the following equations

$$a^* = 2\pi \frac{b \times c}{a \cdot b \times c} \quad (2.4)$$

where a^* , b^* and c^* are the reciprocal lattice basis vectors.

The reciprocal lattice is imaged in 2D diffraction patterns collected from a crystal ¹. Transformations made on the crystal in real-space, such as rotations, also rotate the reciprocal lattice.

Points within a reciprocal lattice define the end points of a scattering vector (difference between the incident k_i and scattered k_f wavevectors), \mathbf{q} , from a series of planes of label (hkl), where $q = ha^* + kb^* + lc^* = k_i - k_f$. A scattering event is shown in Figure 2.3 (i) in real space and (ii) for reciprocal space. In Figure 2.3 the general case for a scattering event is shown, where the wavevectors k_i and k_f are not necessarily equal. The size of a wavevector in reciprocal space is defined by the wavelength of the radiation it represents, thus, for elastic scattering where there is no change in energy upon scattering, $k_i = k_f = k = \frac{1}{\lambda}$. In real space, the diffraction conditions in vector notation are given by the Laue equations 2.5, which state that constructive interference from will occur when the dot product of the scattering vector \mathbf{Q} (which has a defined length and orientation) with each of the three lattice basis vectors (a , b and c) is equal to an integer number (h , k , l) which define the indices of the reflection. The Laue equations can be restated as Bragg's Law.

$$\mathbf{a} \cdot \mathbf{Q} = h$$

¹A direct transformation of the reciprocal lattice imaged in a 2D diffraction pattern, to a real space lattice is not possible directly (through a Fourier transform). This is because the intensity of diffracted x-rays is recorded in a diffraction pattern. Intensity is defined as $|F|^2$, where F is defined in Equation 2.3, as such, information on the relative phase of diffracted x-rays from reflections of different (hkl) are lost, preventing the electron density, and thus atomic position being determined within the real-space unit cell.

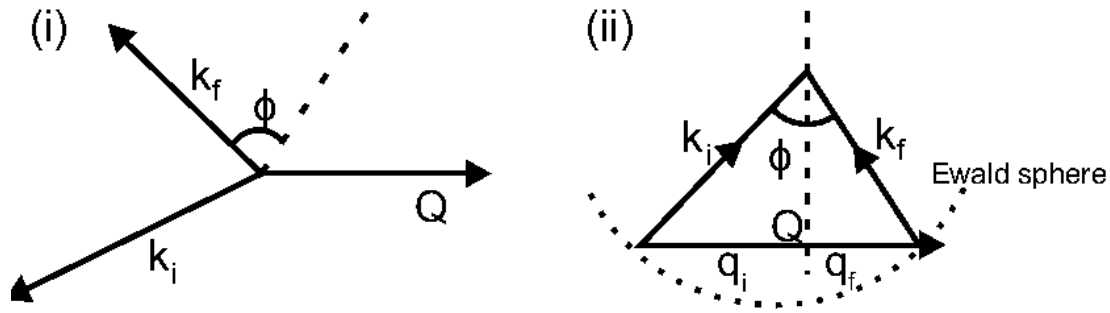


Figure 2.3: Diagram illustrating a vector map showing a scattering event in (i) real space and (ii) reciprocal space. The wavevectors k_i , k_f and Q represent the incident beam, diffracted (final) beam and scattering vector respectively. The vectors q_i and q_f represent the projection of k_i , k_f onto Q in (ii).

$$\mathbf{b} \cdot \mathbf{Q} = k$$

$$\mathbf{c} \cdot \mathbf{Q} = l$$

Equation 2.1: Vector representation of the diffraction requirements in terms of mutually orthogonal basis vectors (\mathbf{a} , \mathbf{b} and \mathbf{c}), scattering vector (\mathbf{Q}) and crystallographic indices (h , k and l) (2.5)

The dashed circular arc shown in Figure 2.3 (ii) represents a section of the Ewald sphere, a geometrical construction in reciprocal space, of radius $\frac{1}{\lambda}$, centered on the crystal in real space. The diffraction condition is met when the end points of scattering vectors intersect the surface of the Ewald sphere (i.e. a reciprocal lattice point lies on the surface of the sphere). This is equivalent to the real space diffraction condition given by Bragg's Law.

2.2.1 Single-Crystal Diffraction

Single-crystal x-ray diffraction techniques yield direct information on the position of atoms within the unit cell and the crystal structure independently (through the intensity and position of Bragg), allowing the experimenter to gain a powerful insight into the behaviour of materials under the application of high pressure. Single-crystal diffraction techniques are, however, reliant upon the sample loaded within the pressure cell being, and then remaining, a single crystal upon increase of pressure to desired level, which itself poses two problems. Pressure increase can cause samples to undergo first-order

phase transitions, which, if accompanied by a large change in volume (a pressure induced volume reduction of $\approx 10\%$ is reported for a first order phase transition in Pr [Mao 81]), will cause the single crystal to shatter into many crystallites (a powder). The other problem is that samples may not be available as a single crystal for ambient pressure loading, prohibiting the increase of pressure to some level below a first order transition; or a method for encouraging the growth of a single crystal at a desired pressure may not be known, or achievable for the sample being studied. A common method to grow a single crystal from a powdered sample is to encourage growth from the melt, heating to the melting point at the desired pressure and allowing to cool. This method relies on the P-T phase diagram of the sample being known at elevated pressure (or time to explore the P-T phase diagram), along with equipment to heat the sample to the necessary level. Neither of those is always possible, leading experimentalists to use powder-diffraction techniques, which, can be viewed as having a number of advantages over single crystals from a perspective of ease of handling and use. For example, not strictly requiring (though is beneficial from the standpoint of data accuracy) a truly hydrostatic pressure medium for the entirety of the P-T region to be explored, and not having to worry about the sample undergoing first order phase transitions. This is especially useful for studying the structure of a sample around a first-order phase transition.

2.2.2 Powder Diffraction

A powder can be considered as an (infinitely) large number of small single crystals (crystallites) each randomly orientated with respect to one another [Warren 90]. A beam incident upon a powder will observe multiple diffracted peaks from all observable hkl , as there will be some large, finite, number of crystallites orientated such that the diffraction condition will be met. Diffracted photons will be observed in discrete spots at calculable positions in three dimensional (3D) space, the position of these spots governed by the orientation of the crystallographic planes that meet the diffraction condition. Typically a two dimensional detector is used to observe the diffracted x-rays, the 3D pattern of diffracted x-rays will be projected onto the 2D detector necessitating geometric corrections to be made to the observed 2D pattern. The discrete spots that appear on a two dimensional (2D) diffraction image will appear as rings (Debye-Scherrer rings) of fixed d -spacing from the central beam, as if a single crystal was to be rotated in many different directions about the central beam. Diffraction rings from a powdered sample can appear textured where the presence of some large crystallites causes concentration of intensity in some positions on the ring, or when preferred orientation (where the alignment of crystallites along a particular direction is

statistically preferred relative to the other possible directions). Powder diffraction can thus give accurate values for the unit cell parameters, with the width of the powder rings being defined by the spread of wavelength about the value of the monochromated beam, strain distribution within the crystallites exposed by the incident beam (or degree of homogeneity of the pressure media) and the instrument parameter (error inherent in the measurement apparatus used) [Warren 90].

A typical angle dispersive x-ray (ADX) powder-diffraction pattern for an face centered cubic (*fcc*) Si sample is shown in Figure 2.4. The dark rings present in the figure are the Debye-Scherrer rings, the first three (moving outwards from the central white spot to edge) are (111) and (220). The white spot at the center of the image and filled black circle surrounding it are the beamstop (a lead disk which prevents the direct x-ray beam illuminating the detector, as this could cause damage) and air-scattering respectively.

2.2.3 Synchrotron Radiation

Charged particles experiencing an acceleration will emit radiation. Synchrotrons utilise this by magnetically confining an electron to a plane, in which it is confined to move in a circular trajectory by a force directed radially inwards. Radiation is emitted, conically, in the plane of motion in the direction of the instantaneous velocity of the electron (tangentially, in plane). When such a particle is moving in the relativistic limit (v tending towards c), this radiation is referred to as synchrotron radiation, SR, and is characterised by a high frequency, small opening angle and clear polarization [Hofmann 04]. At ultra-relativistic velocities (where $pc > mc^2$, that is the momentum term in the total energy, $E = m^2c^4 + p^2c^2$, of the electrons in the storage ring is dominant over the mass energy. Or when $v \approx 0.99c$) the high frequency of the radiation places it within the x-ray region of the EM spectrum.

Realising synchrotron radiation in practice requires a multi faceted polygon comprising a number of straight sections of confinement magnets and bending magnets which alter the direction of the electron travel, providing the radial force required to change the direction of motion. It is at each point in which the motion is changed that radiation is emitted, allowing for beam-lines (such as Station 9.5, of Daresbury SRS or ID09A at

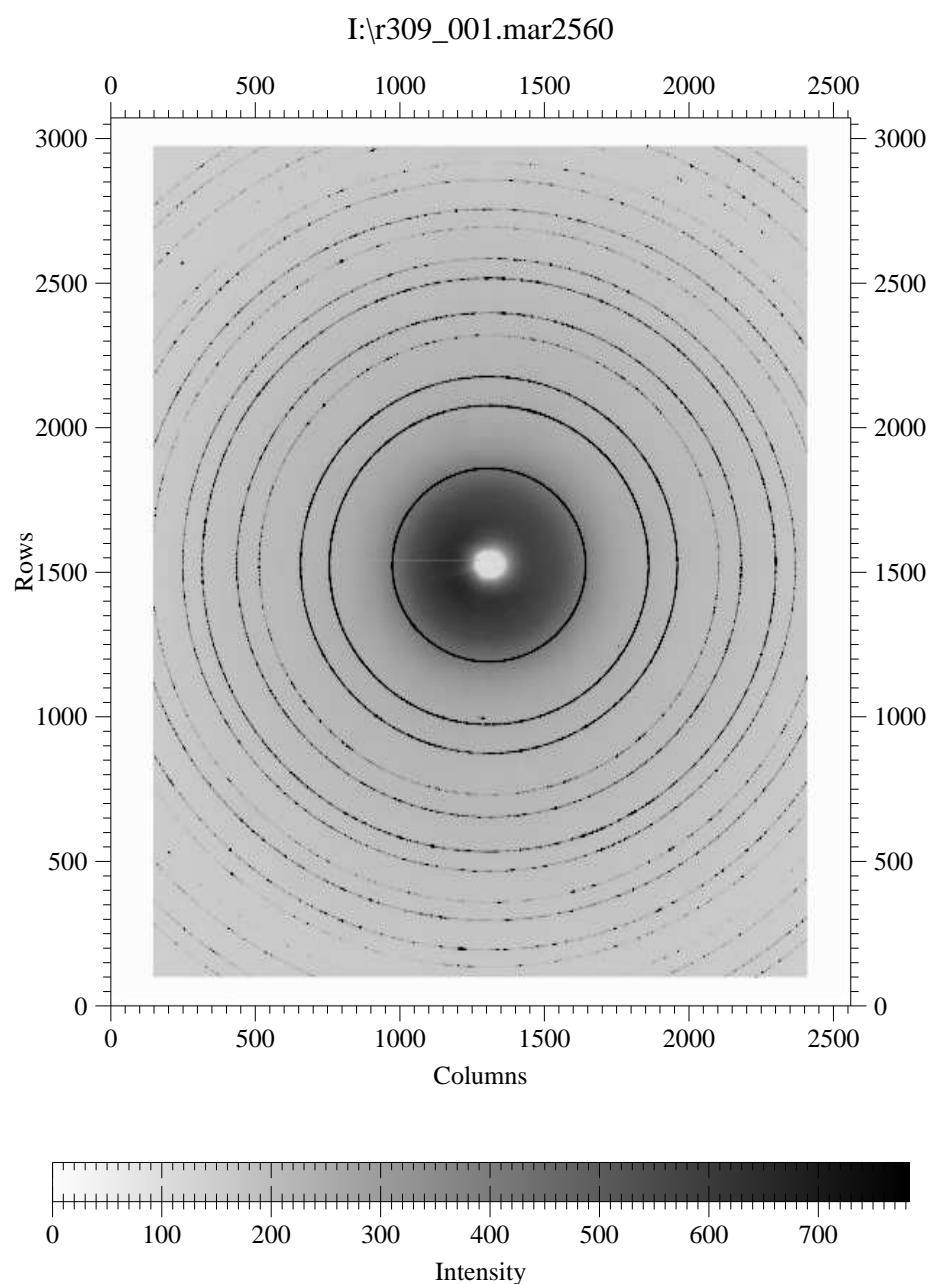


Figure 2.4: A 2D diffraction image of Si at ambient pressure collected on ID09A at ESRF, using a wavelength of $\lambda = 0.44397\text{\AA}$. Image is screen captured from Fit2D [Hammersley 98]. Collected intensity is shown in inverse grey-scale, with darker regions being of higher intensity. The white circle at the centre of the image is the absence of collected intensity corresponding to the location of a lead beamstop.

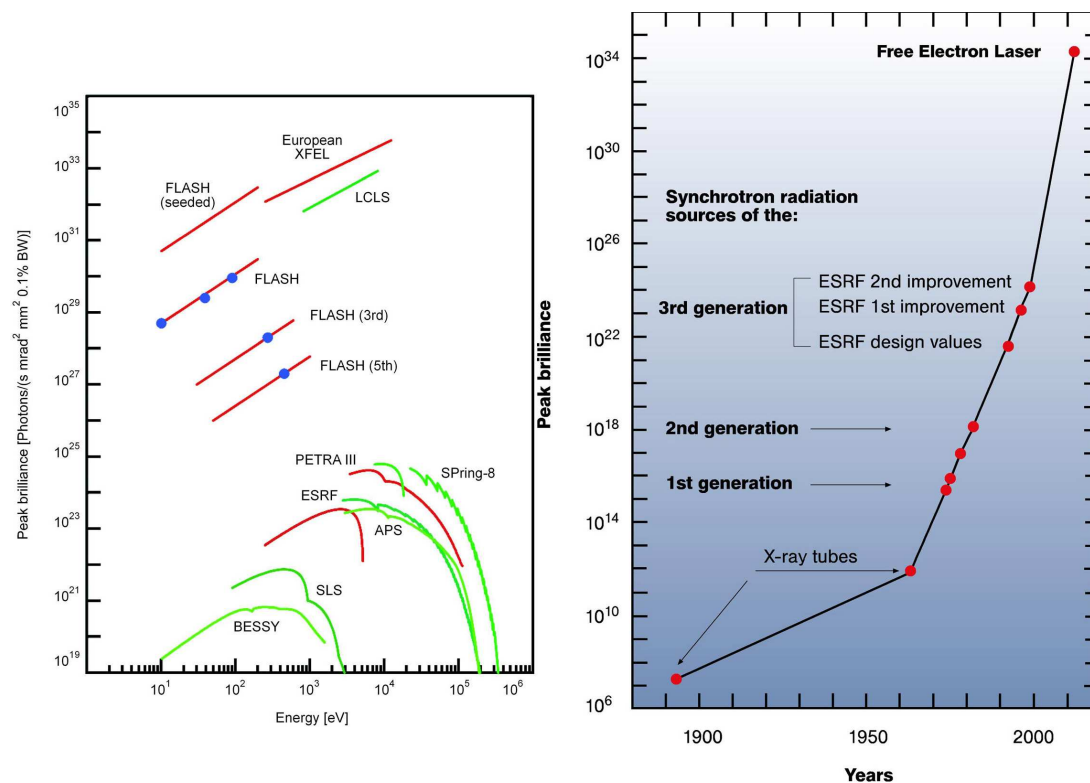


Figure 2.5: (a) A graph showing the characteristic spectrum of a synchrotron radiation source (b) A plot showing how the maximum attainable brilliance (defined as number of photons / s / mm² / mrad / 0.1% of bandwidth) vs. time of global synchrotron sources, increasing brilliance is shown with the building of new synchrotrons. (b) reproduced from *XFEL* comparison site [XFEL 09].

the ESRF[†]) to utilise this intense radiation.

Insertion device is the collective term which refers to wigglers and undulators. These are arrays of magnets which perturb the motion of the electrons to tailor the emitted radiation to specific needs. These are located in the straight sections of the synchrotron ring, and operate so as not to affect the overall orbit of the electrons around the synchrotron storage ring. Each magnetic element within an insertion device changes the path of the electron beam, an array of oppositely aligned magnetic fields such as that found in an insertion device determines the wavelength of the radiation emitted. Adjusting the field strength of the magnets within the insertion device and the separation of the magnets within the insertion device alters the intensity of the emitted radiation and allows "tuning" to constructive interference at harmonics of the x-ray beam.

Laboratory based x-ray sources are electrically driven cathode devices, relying on the emission of x-rays from electrons striking a metal target (known as bremsstrahlung, German for breaking-radiation) as they travel through an electric potential of the order 10 - 100 kV. The metal chosen for the target (in conjunction with the potential) dictates the wavelength of the emitted x-rays, with Cu or Mo commonly being used as target materials giving x-ray wavelengths of $\lambda=1.54056\text{\AA}$ and $\lambda=0.70930\text{\AA}$ (for the $K_{\alpha 1}$ x-ray emission). The flux of these sources is limited by practicalities in design and use. Laboratory sources require a constant supply of coolant water during operation, owing to the large heat load on the target from inefficiencies in conversion of electron kinetic energy to usable radiation.

Compared to laboratory-based sources, synchrotron radiation facilities provide a number of distinct advantages to high-pressure science, where the nature of the experiments dictate a number of constraints upon the data collected and apparatus used. Synchrotron radiation facilities allow access to smaller wavelength, without the loss of flux expected from tuning the laboratory source away from an emission line, or even allowing access to wavelengths that are not accessible using a conventional source. This enables reflections which would otherwise be obfuscated by the limited opening angle of the DACs to be observed. When solving a structure using either single-crystal or powder-diffraction techniques, the largest possible access to reflections in reciprocal

[†]Station 9.5 HPT of Daresbury SRS (referred to as Station 9.5) was a dedicated powder diffraction beamline designed for use at high pressures and temperatures, located in Daresbury, UK. ID09A, of the ESRF (European Synchrotron Radiation Facility), is a dedicated high pressure/high temperature station located in Grenoble, France

space is of the upmost importance. High-pressure experiments, use sample sizes of the order $50 \times 50 \mu\text{m}$ (discussed in Section 2.4.1.1). To overcome the small scattering volume of the sample a large incident photon flux is required for the diffraction experiments to observe subtle details in the resulting diffraction patterns. Necessitated by the small sample size is a beam size of the same order of magnitude as the sample chamber size. Conventional, laboratory-based sources (rotating anode) illuminate the sample with a beam of approximate size $0.8 \times 0.8 \text{mm}$, synchrotron sources routinely use beam sizes of $30 \times 30 \mu\text{m}$ (ID09A and Station 9.5) down to $10 \times 10 \mu\text{m}$ (ID27), achieved through focusing and beam definition at the pinhole. Conventional sources lack the photon flux required to perform adequate data collections in a reasonable time and sufficient focussing of the x-ray beam to ensure that, for sample volumes typically used for high pressure studies, only the sample is illuminated by the x-rays (as opposed to sample *and* materials surrounding it). The intensity of incident photons on synchrotron beamlines is approximately 10 orders of magnitude higher than that achievable with a laboratory source ($\approx 10^{17}$ c.f. $\approx 10^7$ photons/s [Oliveira 09]).

Briefly summarizing, a beamline consists of an optics hutch (located next to the synchrotron storage ring) and an experimental hutch (situated downstream from the optics hutch). The whitebeam (polychromatic x-ray beam) is emitted from the storage ring (at a vertex) and enters the optics hutch (in vacuu), where it is monochromated, focussed and defined (in vacuu) by the optical components, before being passed, in vacuu, to the experimental hutch. Upon entering the experimental hutch, the monochromated x-ray beam has its shape further defined, by beam-slits and a pinhole, before reaching the sample and being diffracted to a detector. The optical components of a beamline are shown in Figure 2.6, which shows in (i) a schematic diagram of an optics hutch and (ii) the optics hutch in relation to the rest of a beamline.

2.2.3.1 Angle Dispersive X-ray Diffraction

Angle-dispersive x-ray diffraction (ADX) utilises the angular dependence of Bragg's Law when an beam of monochromatic radiation is incident on a crystalline sample. Diffraction will thus occur only when Bragg's law, as stated in Equation 2.2, is satisfied.

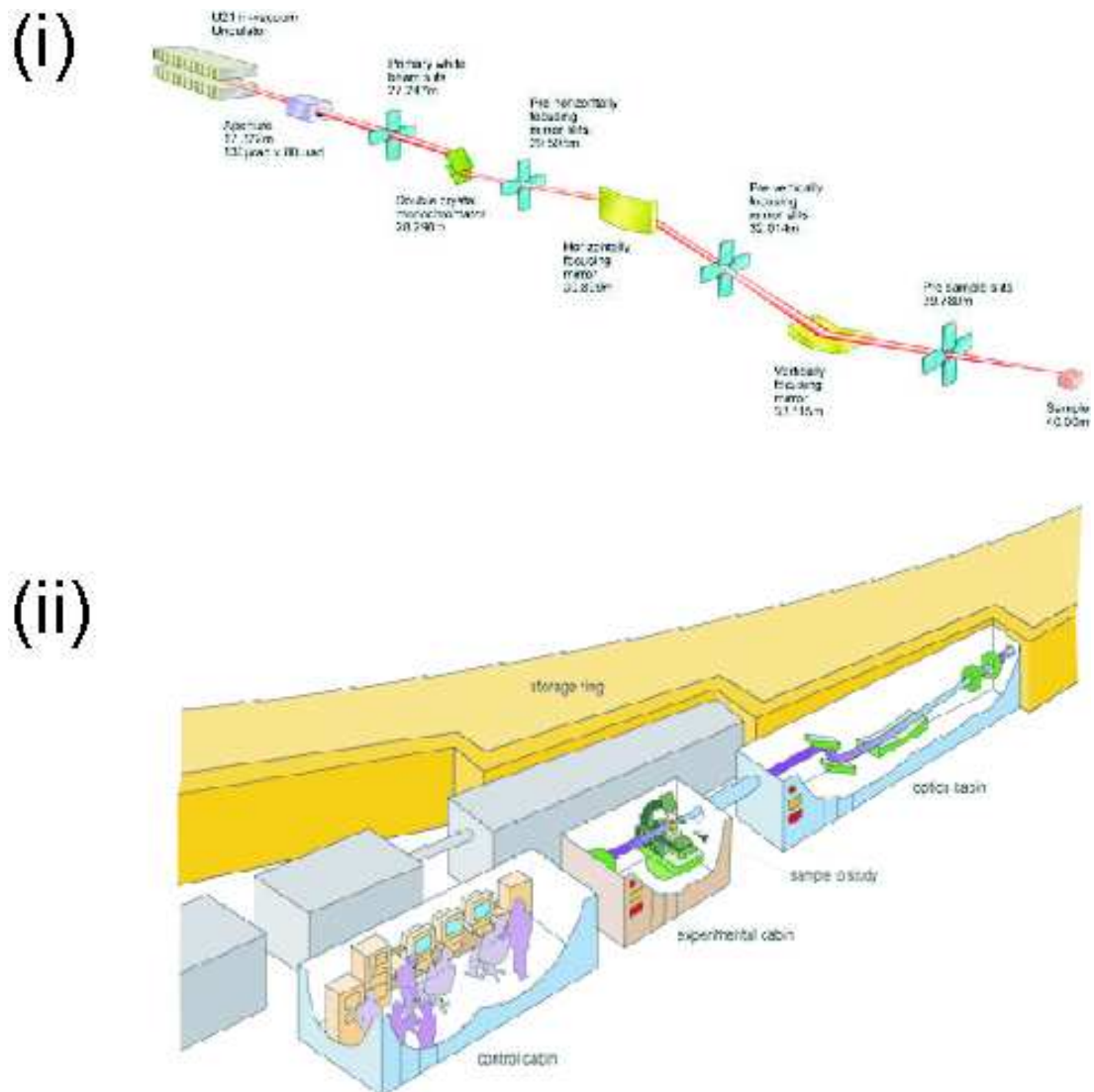


Figure 2.6: Two schematic diagrams showing (i) the layout and components of a typical optics hutch (in this case for Beamline I04 of Diamond Light Source, in Didcot, UK) and (ii) how an optics hutch is positioned relative to the other hutches (experimental hutch and control hutch) in a typical beamline (in this case from the ESRF, Grenoble, France). Images taken from (i) Diamond Light Source [Source 10] and (ii) ESRF [ESRF 10].

2.2.3.2 Energy Dispersive X-ray Diffraction

An alternative method (for structural analysis) to angle-dispersive x-ray diffraction is energy-dispersive x-ray diffraction (EDX). EDX utilises a “white beam”, an x-ray beam which has not been monochromated and as such contains a large energy bandwidth. As the diffraction condition in Equation 2.2 can be rewritten in terms of energy by substituting for wavelength (Equation 2.6).

$$(2.6) \quad E = h\nu = \frac{hc}{\lambda} = \frac{hc}{2d \sin \theta}$$

a fixed experimental setup (i.e. fixed angle of x-ray beam incidence upon a sample, θ and fixed location of detector, 2θ) with a detector capable of energy (wavelength) discrimination can record the d -spacings of all planes able to diffract within the energy range of the detector and incident beam [Cullity 78]. Each set of planes within the fixed sample illuminated by the incident beam will diffract different energies (wavelengths) from the incident beam. The historical significance of this technique is that it allowed for rapid data collection (of the order of a couple of minutes at a time where angle dispersive techniques would have required many hours) and neglected the need for (costly) monochromation of the x-ray beam (which had the positive side effect of increasing the number of incident photons).

EDX typically has a lower “intrinsic resolution” than ADX (because of the discrete ranges in energy able to be sampled by the detector), being unable to resolve fine details such as closely spaced diffraction lines in energy space. By comparison, ADX, which uses a monochromated beam, and so does not require energy discrimination within the detector, has its resolution limited by the pixel size (size of the detector array and maximum 2θ by detector’s size/distance ratio) and point spread function.

2.3 Accurate data

This section will present the prerequisites to ensure the highest-possible quality of powder-diffraction data within the experimental constraints is presented.

A high signal-to-noise ratio is necessary in the diffraction profiles to be analysed. Background noise, being random in nature, has the potential to obfuscate weak peaks if the noise is of a level equivalent to that of the sample reflections. Noise of a systematic nature, arising from spurious scattering, can be minimised through shielding of the x-ray source at points where the beam travels through air (this minimises spurious scatter from materials in the vicinity of the beam). Oscillation of the sample about an axis of rotation in the x-ray beam (which would average each discrete crystallite reflection over a number of pixels) maximises the number of crystallites exposed to the x-ray beam (in theory sampling more crystallites increases the likelihood of sampling over more crystallite orientations in reciprocal space, increasing the quality of “powder averaging” around the diffraction rings). Radial integration of the 2D diffraction images also acts to minimise the effect of a non-uniform distribution of crystallite orientations through all possible orientations, thus reducing the effects of a number of large crystallites upon 1D slices taken through the 2D image.

Sharp, well-resolved peaks are of utmost importance in a diffraction pattern, as they help eliminate the potential for ambiguity to arise when a sample has many, closely-spaced Bragg reflections in a diffraction profile. Sharp, well-resolved peaks can be realised through the minimisation of strain and pressure gradients within the sample chamber. Strain / pressure inhomogeneities in the sample act to broaden the width of diffracted peaks. Detrimental effects, such as broadening to a degree whereby two closely-spaced peaks overlap, forming a poorly-resolved doublet, could occur in the presence of strain. Incorrect analysis of data could ensue. In single-crystal diffraction patterns an unstrained sample should have sharp diffraction spots. On the 2D powder-diffraction pattern, smooth, sharp, well defined circular rings should be observed. More will be discussed on strain minimisation in Section 2.4.2.

Impurities on the sample surface also need to be minimised. A common problem with reactive metallic samples (such as the lanthanide metals) is the oxidation process, which results in thin films of metal-oxide on the surface of the sample. If improperly

considered, the data collected from such samples will be a superposition of the metal and metal-oxide diffraction patterns. Cleaning of the surface can be performed by scraping away lackluster regions in a protected, oxygen free, environment (such as a glovebox). Impurities within the sample must also be considered. Steps should be taken to source samples of the highest feasible purity from commercial sources (such as Alfa-Aesar) or research facilities (some of the samples sourced for this work were provided by Ulrich Schwarz of the MPI, Dresden), as facilities to refine reactive, metallic substances are not available within the research group in Edinburgh. Steps should also be taken to limit the exposure of samples to other potential sources of contamination at the sample preparation stage as this will have the same effect on the diffraction pattern as impurities. Contamination can also arise from improper cleaning of tools, workspace and cell (equipment used to house the sample during an experiment). Discrimination of contaminant peaks from sample peaks can be extremely difficult and can result in erroneous data being published.

Finally, steps can be taken at the data collection stage of the experiment to ensure accuracy of data. Oscillation of the sample about an axis in the x-ray beam ensures maximisation of the number of diffracting crystallites within a powder, oscillation about a small angle in the x-ray beam (a value of $\pm 3^\circ$ was used during this body of work) maximises the powder averaging statistics on integration of the 2D powder-diffraction image. Care should be taken during the alignment of the sample within the x-ray beam to ensure that only the sample is illuminated by the x-rays and thus the sample is the only contribution to the diffraction pattern. Appropriate choice of x-ray beamsize (ultimately defined by the size of the pinhole/soller slits before the sample), so as to be of comparable size to the sample, but less than the sample chamber, will help to ensure that only the sample is illuminated by the x-ray beam, not surrounding equipment. The appearance of gasket lines (powder diffraction rings from the gasket) at extremely high pressures can become unavoidable, as curtailing the beamsize reduces intensity, a tradeoff between beamsize, data collection time and beam intensity needs to be made at some point.

Random orientation of crystallites is required, as powder diffraction relies upon the sample consisting of small, randomly orientated crystallites. Dramatic variance of the size of crystallites within a "powder" sample leads to profound preferred orientation effects and pronounced texture within the powder diffraction rings on a 2D diffraction image, this can lead to poor powder averaging at the data processing stage, by yielding

intensities in the integrated 1D diffraction pattern which differ markedly from that which is expected based on the positions of atoms within the unit cell. Preferred orientation must therefore be taken into account when modeling the structure at the refinement stage to be able to determine the positions of atoms within the unit cell effectively.

A low background, which smoothly varies over the angular range that is studied in an experiment, is required to maximise the quality of the diffraction image. This allows for diffraction peaks from the sample studied to be easily differentiated from the background, enabling the Bragg peaks to be fitted using a Rietveld refinement package such as Jana2000 [Petricek 00].

2.4 Pressure Cells and High-Pressure Techniques

2.4.1 Basic Principles

To realise the extreme pressure conditions eluded to in the Chapter 1.1 the sample needs to be contained within a device (pressure cell) capable of exerting large forces uniformly over a small area. In this section the Diamond Anvil Cell (DAC) will be reviewed.

2.4.1.1 Diamond Anvil Cells

Pressure cells required for use on x-ray beamlines, or x-ray diffractometers, require that there be a viewing window that is x-ray transparent, above the requirements that the cell windows can withstand the mechanical stresses involved in pressurisation of a sample and be of suitable size (both size of the cell and the volume of the sample chamber) for the required experiment. These requirements can met by using diamond anvils. Diamond acts as a transparent window for optical and hard x-ray regions of the EM spectrum and through its high hardness it is capable of being used for exerting the forces required.

Opposed anvil cells have been used throughout this work, of DXR, MB and Bohler-Almax design. Each utilises the same principle, having two sections (one of which

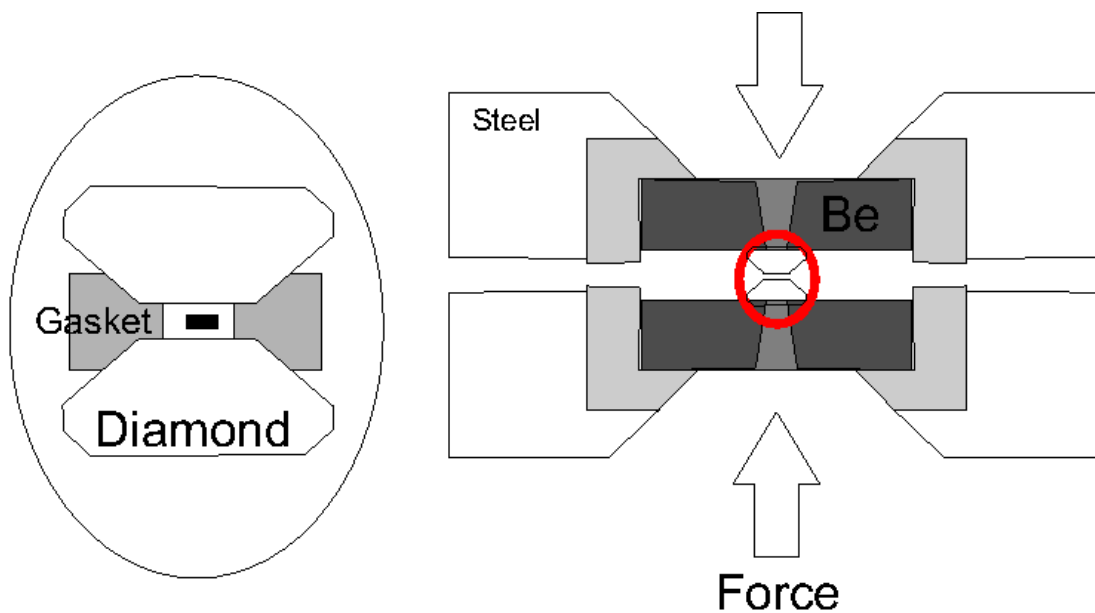


Figure 2.7: Diagram showing a schematic of the MB type DAC, with an enlarged section showing the sample chamber.

is shown in Figure 2.9), each with a diamond anvil, of culet size approximately 300 microns, secured to a seat, held in place within the larger cell body by a backing disc of beryllium (or tungsten-carbide for the Bohler-Almax design). Pressure is applied mechanically in each of these designs by the tightening of threaded screws which pull together the two sections of the cell body, forcing the diamond anvils to compress the sample within the sample chamber. For the case of standard anvil designs which use beryllium backing discs, support is provided conically to the back of the diamond anvils (see Figure 2.8 (a)). Bohler-Almax seats (2.8 (b)) support the diamond anvils base at an angle, which allows for a much greater effective "opening angle" (the opening angle is defined as the half angle about an axis perpendicular to rear of the diamond through which diffracted x-rays can pass without impinging on the diamond supports), due to their tapered design, of supporting the diamond anvils on beveled rear, compared to conventional Be seats which support on a flat rear (conventional Be seats typically give diffraction from the Be when the DAC is rotated to angles greater than $\pm 10^\circ$ in the x-ray beam, Bohler-Almax allow for the DAC to be rotated by 20° without substantial contamination, above this angle however "shadowing" from the DAC body will obscure part of the diffracted image).

The two sections of the cell fit together to create a sample chamber (Figure 2.7 shows sample chamber), containing the sample within some inert media, sandwiched between

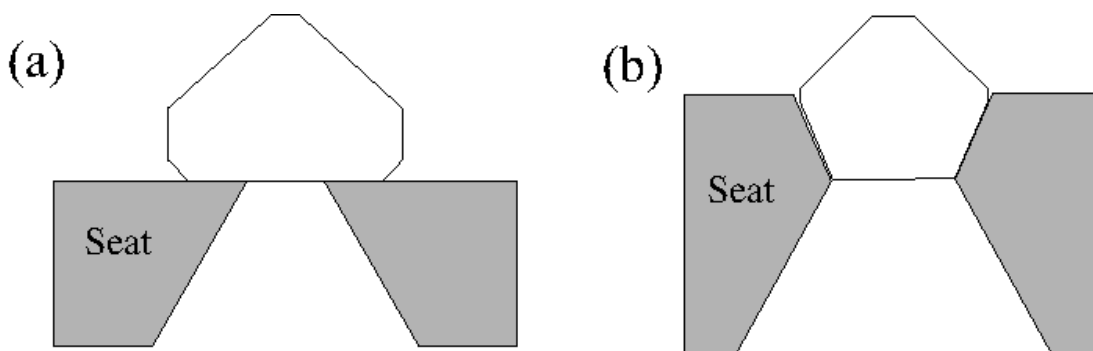


Figure 2.8: Diagram showing the two means of supporting diamond anvils (a) using standard Be backing discs and (b) using Bholer-Almax tungsten carbide seats

the two anvils. By tightening the screws shown in Figure 2.9, the diamonds are forced closer together, a pressure is so generated on the sample chamber as

$$P = \frac{F}{A}$$

. Thus, using a small area ($A = 6.89 \times 10^{-8} \text{m}^2$ when 16 sided, $300 \mu\text{m}$ culets are used), and a modest mechanical force applied by hand-tightening of the screws on the DAC, a large force is generated at the diamond culets ($F \approx 2000 \text{N}$). This large force confers a large pressure ($P = 30 \text{GPa}$) to the sample.

As shown in Figure 2.7, the gasket provides the outer walls of the sample chamber. It therefore must be able to undergo plastic deformation under the application of pressure and be non reactive with respect to the materials contained within the chamber. An inability to deform plastically (a brittle gasket) would lead to the gasket shattering on compression. Typical materials used for gaskets include tungsten, spring-steel and rhenium. Once the cell is closed, the gasket deforms around the diamond facets creating an air tight seal, preventing sample oxidation (of particular importance when dealing with reactive metals such as Lanthanides) and supporting the diamond culets.

The choice of cell, and size of diamonds used, governs the maximum attainable pressure. Smaller diamond culets allow for higher achievable pressures, but limit the size of the sample chamber, and hence the size of sample studied. This lowers the amount of scattered intensity from the sample, necessitating the use of synchrotron radiation sources for high-pressure studies and/or increasing the exposure time of the sample to the x-ray radiation. To reach the maximum attainable pressures with a DAC the distortion of the diamond culets in response to the high pressures being exerted on

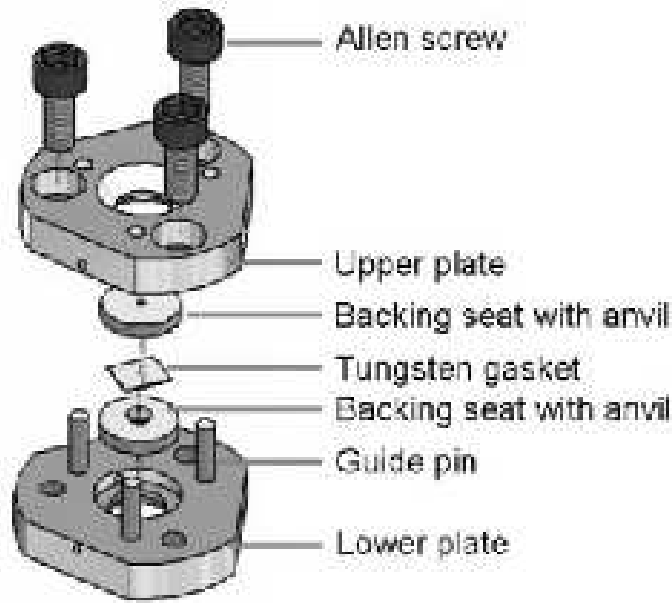


Figure 2.9: Schematic diagram of a DAC showing an exploded view of a Merrill-Basset DAC, how the two halves fit together and location of sample chamber is shown in 2.7. Separate sections and components are labeled. Image from [Website 10].

the sample must be taken into account, as the culets warp to become concave at their maximum pressure. Finite-element analysis of the distortion of the culet at a particular pressure (the desired pressure to be reached) can be used to model the culet shape required to produce a “flat” culet at a particular pressure, culets with bevelled tips (with a bevel degree of 8°) and culet tip size of $40\mu\text{m}$ can be used to reach pressures in excess of 1.5 MBar (150 GPa) [Gregoryanz 03]. Bevelled tipped diamonds were not used during the work within this thesis.

2.4.2 Pressure Media

Opposed-anvil type cell designs apply a force to the sample chamber uniaxially, along a direction perpendicular to the diamond culets. The sample, in this configuration, if free, would extend outwards (parallel to the diamond culets) under compression. Samples are contained in a sample chamber, filled with an inert media. This inert media acts to transmit pressure uniformly, or hydrostatically (uniform application of pressure from all directions) to the sample. Under compression, a filled sample chamber will have its walls and height contract uniformly (provided it is circular, of constant thickness, and properly centered on the diamond culet). Uniform contraction compresses the sample

P. Media	Hydrostatic Limit (GPa)	Ref.
4:1 Methanol - Ethanol	10.5(5)	[Klotz 09], [Angel 07]
Mineral Oil	0.9	[Angel 07]
Argon	$\approx 10 / 1.9$	[Klotz 09] / [Angel 07]
Helium	40	[Klotz 09]

Table 2.1: Summary of a hydrostaticity of pressure transmitting media commonly used during high-pressure x-ray diffraction experiments. The results of Angel *et al.* and Klotz *et al.* differ substantially for the Argon pressure transmitting medium, with Angel quoting a hydrostatic limit 5x smaller than Klotz. The difference is attributable to the method used for determining the loss of hydrostaticity. Angel *et al.* used diffraction line-broadening (at a high-resolution synchrotron source) to determine the approach to the hydrostatic limit, and state that the 10GPa value often quoted was discovered using ruby luminescence broadening.

chamber in the plane of the gasket as well as in the plane of the applied force.

The choice of pressure medium is dependant on:

- the sample under investigation,
- pressures expected to be obtained in the experiment,
- and temperature expected to be reached.

A pressure medium needs to be inert with respect to the sample under investigation. Reactivity with the sample would lead to undesirable contaminants becoming present in the sample chamber, which could lead to misinterpretation of the data collected. An example of this would be Si reacting with H₂ pressure transmitting medium. The pressure medium must also be inert with respect to the gasket and diamonds. Failure to take this into consideration will result in the sample chamber failing at high pressure.

The desired conditions (of P and T) to be explored for the experiment is a deciding factor in choosing pressure medium. In reality pressure media are hydrostatic over a limited range of pressure, all will become non-hydrostatic (due to solidification) at some point. The point at which this occurs is dependant upon the pressure transmitting medium used. Table 2.1 details the hydrostatic pressure limit of a number of common pressure transmitting media. Above these pressures hydrostaticity will be lost, it should then be assumed the pressure applied will be largely uniaxial, leading to pronounced effects on Bragg peak width (a strain based effect) and preferred orientation.

Hydrostaticity can be returned to a sample through the relief of internal stresses within

the sample chamber by mild heating of the cell, causing recrystallisation of the pressure medium.

2.4.3 Pressure Calibration

The pressure within a sample is measured through the change in a physical property of a calibrated manometer standard [Mao 86, Datchi 97, Hanfland 02, Dewaele 04] which can be measured through optical fluorescence or x-ray diffraction. The ruby fluorescence method [Mao 86] is a convenient for both “on-line” (on the beam line) “off-line” pressure measurement. Small ($\approx 5 \mu\text{m}$), single crystal ruby chips or spheres (typically 2 at spatially distinct locations within the sample chamber) are loaded into the sample chamber along with pressure medium and sample. The pressure calibrant (e.g. ruby spheres) must be positioned away from the chamber walls to prevent the walls impinging on the calibrant during pressurisation and “pinching” (trapping the calibrant between the gasket and diamond, which will cause excessive broadening of the ruby fluorescence signal). The ruby manometers should also be placed away from the center of the sample chamber, to minimise diffraction from the ruby during exposure of the sample chamber to x-rays. Ruby peaks are, however, easily identifiable and can be removed from 2D diffraction images during data processing. Multiple manometers are loaded to overcome potential loss of a manometer upon adding pressure medium to the cell and can be used to measure the inhomogeneity in pressure within the sample chamber. Use is made of the characteristic fluorescence of ruby when stimulated by laser light of wavelength $\lambda=532 \text{ nm}$ (green laser light). Two R fluorescence peaks are excited, having ambient pressure wavelengths of $R_1= 694.23$ and $R_2= 692.86 \text{ nm}$. The variation of the R_1 line with pressure has been studied comprehensively by numerous authors and summarised by Syassen [Syassen 08a], and follows the form shown in Equation 2.7.

Equation 2.7 shows a non-linear increase in the wavelength shift, $\Delta\lambda$, with respect to pressure. This can be assumed as being accurate to $\approx 50\text{GPa}$ (and useful to 100GPa , above which the intensity of the R_1 emission line becomes difficult to measure), as the ruby pressure scale equations are calibrated to data of measured lattice parameters of gold and platinum [Syassen 08a] from x-ray diffraction.

$$P = 380.8\left[\left(\frac{\Delta\lambda}{694.2} + 1\right)^5 - 1\right] \quad (2.7)$$

A schematic of the pressure measurement apparatus used at Daresbury SRS (for data collected on both Station 9.1 and 9.5) is presented in Figure 2.10. A He-Cd laser

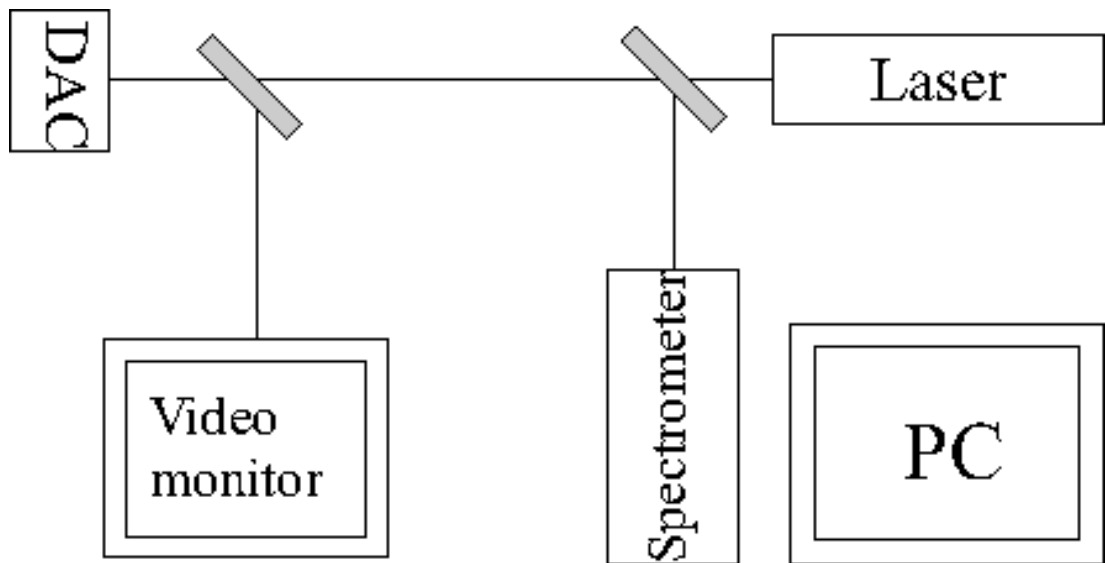
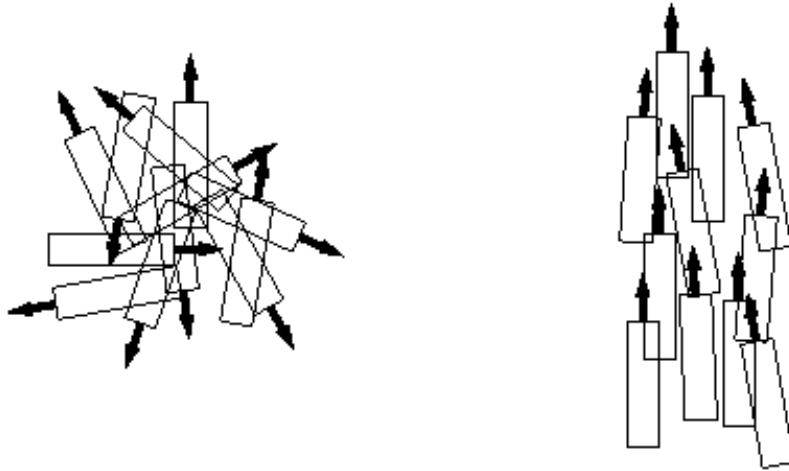


Figure 2.10: Labelled schematic diagram of pressure measuring system available within the Edinburgh High Pressure group, at Daresbury SRS. A green ($\lambda = \text{\AA}$) laser is used to excite the ruby fluorescence. The laser light passes through half silvered mirrors (grey rectangles) which, if in place direct the light coming from the sample (reflected and fluorescence) to either the video monitor or spectrometer. The video monitor is used during alignment of the laser radiation on the ruby pressure calibrant within the sample chamber. The spectrometer is connected to a PC, to allow collection, analysis and archival of spectra.



(a) Random Orientation **(b) Preferred Orientation**

Figure 2.11: Schematic diagram showing how the orientation of crystallites within a perfect powder (a), and (b) a powder with pronounced preferred orientation, could look.

is focussed through an optical fiber onto the sample using a 10X optical lens. A Dilor spectrometer, connected to a PC, records the spectra of light leaving the cell. Background noise and the R-fluorescence peaks can be removed, and fitted, respectively in the software package LabSpec.

2.4.4 Preferred Orientation

Earlier, it was noted that for optimum results from powder diffraction, the powdered sample should have crystallites that are small and randomly orientated. In high-pressure experiments, where the the pressure medium is not capable of providing a truly hydrostatic sample environment, the crystallites, due to their shape (if fibrous or plate-like shaped crystallites are present) or an applied uniaxial pressure gradient to the sample chamber, can exhibit a tendency to orientate preferentially along a particular axis within the sample chamber. This is effect is known as preferred orientation. A tendency of a powdered sample, which at low pressures has smooth diffraction rings (and so randomly orientated crystallites), when pressured to exhibit preferred orientation after undergoing a high-pressure phase transition within a DAC is not uncommon [mim]. A diagram schematically illustrating this effect is shown in Figure 2.11.

Orientation of crystallites along a particular axis causes deviation from the assumed

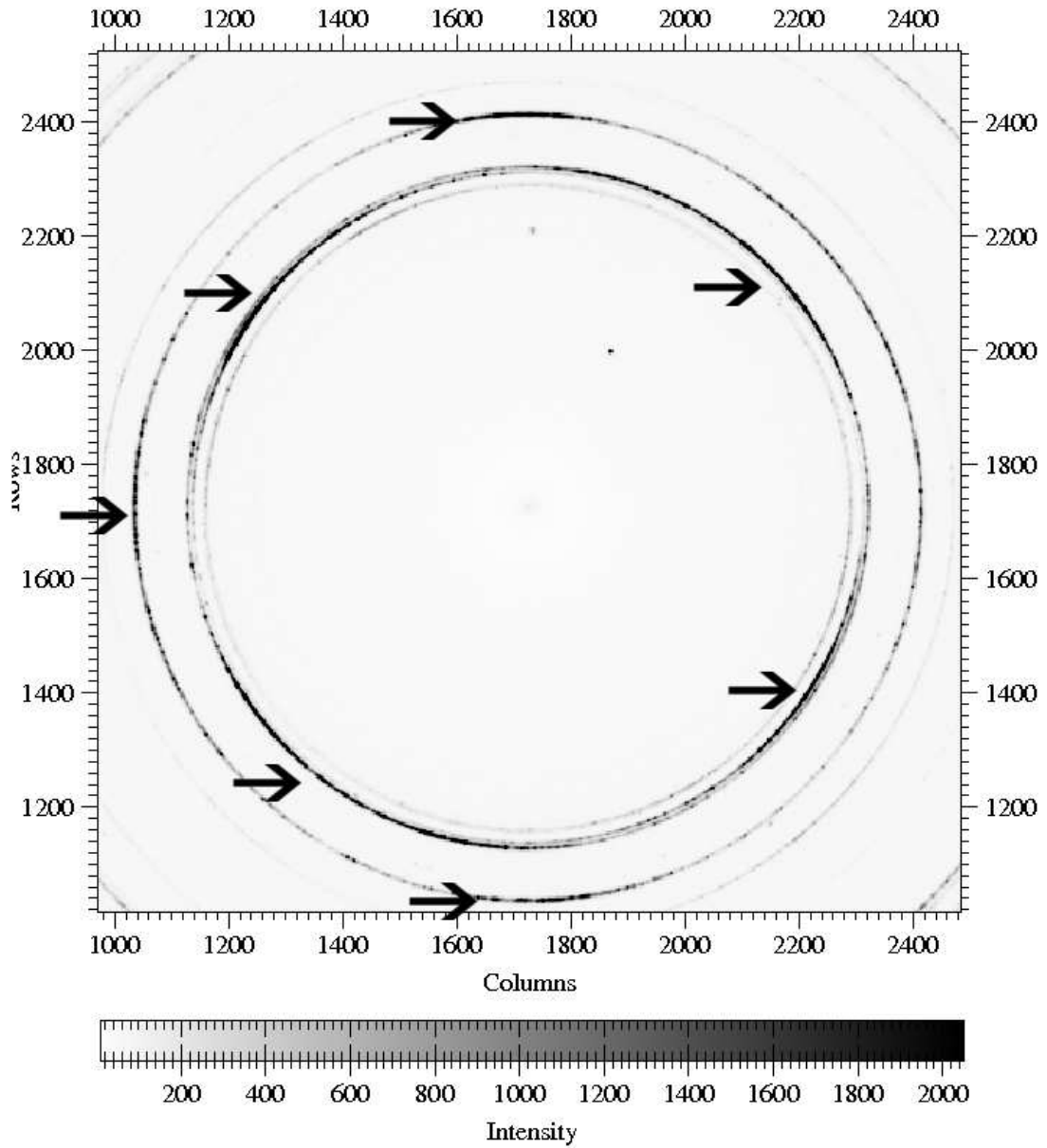


Figure 2.12: Example of the effect of preferred orientation on a powder pattern collected on Station 9.5 HPT of Daresbury SRS from a “powder” sample of Pr at 20.3 GPa. Contrast has been adjusted to highlight the effect preferred orientation has upon the intensity distribution around a powder ring. Arrows indicate the positions of highest intensity on the ring.

random distribution of crystallites expected in a “perfect” powder pattern, and so, the smooth powder rings (from a powder sample with random orientation of crystallites) to diffraction rings which show texture around the circumferential intensity distribution of a Debye-Scherrer ring (evident as regions of high and low intensity around the circumference of a Debye-Scherrer ring). An example of this effect on a diffraction pattern is shown in Figure 2.12.

If the direction in which the unique cell axis is aligned with (approximately coincident with) z (assuming the crystallites are disc or fibrous), there will be a probability of finding crystallites aligned at some angle α away from z . This probability decreases as the angle α increases. The direction z is chosen in this example as the preferred orientation axis (POA), the direction within the sample chamber along which the crystallites align, to be coincident with the direction of applied uniaxial pressure within the DAC. Another direction can be defined as the direction within the sample chamber along which the crystallites are approximately orientated with some external axis, the preferred orientation direction (POD), the (crystallographic) direction about which the crystallites orientate with respect to each other. These two axes are shown in Figure 2.13, which is taken from ??, which shows the relation between the POA, POD, incident beam and diffracted beam. The scattering vector, h_j , is shown at some small angle to the POD. h_j is, for crystallites meeting the reflection condition, the fixed value about which the POD sweeps out a cone around in 3D. The base of, or locus of this cone defines the boundary of the intensity distribution from the scattered intensity, which, by virtue of the probability density with respect to α will be non-uniform, containing regions of high and low probability. A Debye-Scherrer ring will be constructed from the POD cone sweeping out a path on the Ewald sphere, leading to the ring having regions of high and low intensity characteristic of preferred orientation [mim].

Rietveld refinement software packages are capable of correcting for the effect of preferred orientation effects in integrated 1D diffraction patterns using functions such as the March-Dollase model (Equation 2.8) which describe the probability distribution for observing a preferred orientation direction (POD) of the crystallites at an angle of α with respect to the preferred orientation angle (POA) [mim].

$$F\alpha = (G^2 \cos^2 \alpha + G^{-1} \sin^2 \alpha)^{\frac{1}{2}} \quad (2.8)$$

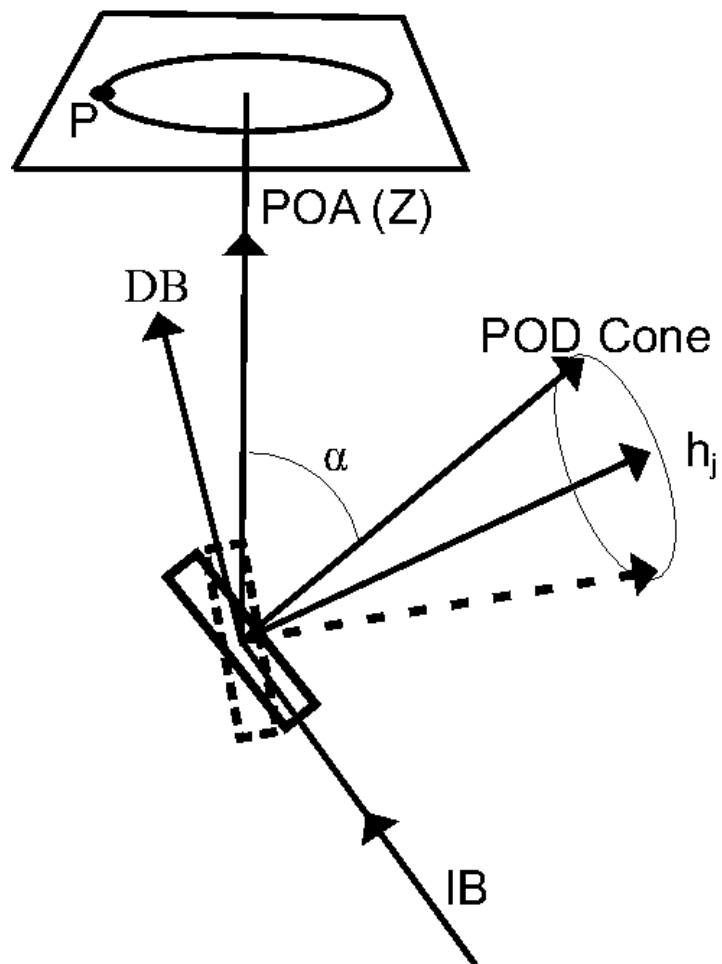


Figure 2.13: Simplified diagram to show the preferred orientation direction (POD), preferred orientation axis (POA) and how each relates to the scattering vector (h_j), diffracted spot (P), incident beam (IB) and diffracted beam (DB). Diagram reproduced from [mim]

Corrections for preferred orientation made using the March-Dollase equation shown in Equation 2.8 do not properly account for experimental geometry used in high pressure experiments, as simplifications are made to limit computational time within the refinement process (P.O corrections being one of a number of variable corrections made at refinement), typically assuming Bragg-Brentano and Debye-Scherrer diffraction geometries. While not directly applicable to high pressure experiments in these geometries, the correction made for P.O. seems to work [mim]. These corrections are made, (when enabled in software) during the Rietveld refinement, in Jana2000 [Petricek 00] where the preferred orientation axis must be given to the program for it to be modeled in the refinement.

2.5 Experimental Setup and Data Analysis

2.5.1 Detectors

2.5.1.1 MD Image Plate

Data collected at the start of this work was collected using a Molecular Dynamics 400A PhosphorImager IP (Image Plate) reader at Station 9.1 of Daresbury SRS. This reader is based on a rastering He-Ne laser which was capable of scanning the A4 sized image plates in ≈ 11 minutes. This IP reader provided a resolution of 2800x2000 pixels, with an approximate pixel size of 88x88 μm .

The image plates for this instrument were rectangular, of size 20 x 25cm, giving an area of 500 cm^2 . Image plates and detectors in this system are distinct devices, with the reader (due to its size and weight) housed away from the x-ray source. Image plates housed in 'light tight' or light proof container need to be moved from experimental area to the IP reader, then later to an erasing lamp to be prepared for reuse.

2.5.1.2 Mar345

A Mar345 Image Plate Detector System became available in on Station 9.5 HPT of Daresbury SRS in 2006. The Mar345 is an integrated image plate, scanner and eraser, mounted in the experimental area and remotely operable over a LAN. No action other than computer driven commands (scan/erase) are required. A circular image plate of diameter 345mm is employed in this system, with 150 or 100 μ mpixel size, yielding a maximum resolution of 3450 x 3450 pixels scanned and read out in less than 2 minutes. The area of the IP in this system is $\approx 935 \text{ cm}^2$. The physical size of the detector system (50 x 40 x 30cm) with all necessary IP components into a single unit enables mounting within the experimental area.

2.5.1.3 Comparison of Beamlines 9.1/9.5 and Detectors

A transition from using the Molecular Dynamics IP system to the Mar345 was made during the data collection for this work. The Mar345 gave a number of advantages over the Molecular Dynamics system, most notably the integration of all components into a single system capable of scanning data in approximately $\frac{1}{10}^{\text{th}}$ the time of the MD system.

In real terms, the Mar345 reduced the time for a data collection procedure from 90 to 20 minutes (full alignment, exposure and scanning of the IP data). The Mar345 does have a larger pixel size than the MD system, but, the larger area of the IP in the Mar345 system allows for greater resolution in the diffraction profile by enabling the IP system to be placed further away from the sample. Increasing sample-to-IP distance can allow for the separation of closely spaced features on the diffraction profile to be increased. Conversely, at a fixed sample to IP distance, a larger IP allows for collection of diffraction data to higher angles.

2.5.2 Station 9.1 at Daresbury SRS

Station 9.1 is a flexible beamline intended for use in either high-pressure IP configuration or a conventional x-ray diffraction from a 2-circle diffractometer configuration. For the experiments performed for this work, the high-pressure IP configuration was used.

Situated approximately 15m from the 5T, Line 9 wiggler at Daresbury SRS, Station 9.1 uses a channel cut silicon monochromator (double-bounce, utilising the (111) Si reflection) to provide wavelengths from 0.4 - 1.7Å. A wavelength of 0.4654Å (Cd edge) was used on this station to minimise the x-ray beam harmonics ($\lambda/3$) from the Si monochromator. Beamsize is defined on this station by tungsten carbide slits, reducing beam to 0.5mm x 0.5mm, before a platinum pinhole further reduces the beamsize to 75 μ m (and further attenuating the $\lambda/3$ beam harmonics at this wavelength).

2.5.2.1 Alignment of Station 9.1

The alignment process used for the IP setup on Station 9.1 was developed by previous members of the Edinburgh High-Pressure group [Bovornratanaraks 01], based on the extension of the alignment procedure developed by Shimomura *et al.* [Shimomura 92] for use at the Photon Factory, Tsukuba, Japan.

The station is prepared with components placed upon the support beam (with the exception of the telescope being positioned in place of the beamstop). Upon the sample stage the pressure cell is placed, and telescope focused upon the sample (assumed perpendicular to the x-ray beam for simplicity), with the cross-hairs from the telescope view-piece centered on the sample to be studied. The telescope's position is noted from a digital display (connected to the micrometers used to position the telescope, which reads), and the sample is replaced by a piece of x-ray sensitive paper, mounted on an additional, small traveling stage placed at a position corresponding to the sample location within the DAC (taking the high refractive index of diamond into account). When exposed to the x-ray beam (for ≈ 2 minutes) the paper blackens, allowing for the telescope to be aligned on the blackened spot in two mutually orthogonal directions perpendicular to the x-ray beam (without the focal point of the telescope being altered). With the telescope crosshairs aligned to the beam position, the DAC is placed on the sample stage, and moved so as to be in focus and centered on the crosshairs.

Due to the removable nature of the IP detector on Station 9.1, the DAC placed upon the beamline must be aligned so that the diamond back is perpendicular to the x-ray beam (for consistency between successive measurements). This is achieved using optical methods, employing a low power (< 1 mW) laser diode, already aligned to the x-ray beam. Back-reflection of the laser onto the laser diode is utilised to ensure the x-ray beam and diamond face are perpendicular. This is extremely important as it also ensures that the telescope and the diamond back are perpendicular, otherwise the high refractive index of the diamond (3.42) will complicate optical alignment of the

sample. If back reflection does not reflect onto the laser diode the diamond facet is not perpendicular, and must be “shimmed” using spacers until the appropriate deviation away from vertical is found. This laser based optical alignment is also used to align the telescope to be parallel to the x-ray beam (in which case a mirror replaces the objective lens in the telescope). The laser is aligned to be parallel the x-ray beam using pieces of x-ray sensitive paper placed near the pinhole and the other near the laser. The x-ray beam path is marked at these two end points, thus, if the laser can travel through holes made at the darkend spots on both papers then it is aligned along the x-ray beam.

This alignment process takes approximately 15 minutes to complete as each exposure of the x-ray sensitive paper/IP requires going through the safety procedure and sealing of the experimental area of the beamline, exposure, opening the beamline then exposing the x-ray sensitive paper to white light to increase contrast of the darkened spot. The accuracy of this alignment procedure is highly dependant on the accuracy of the telescope and degree of care taken during the alignment procedure, yet is sufficient to allow a $75\mu\text{m}$ diameter beam to pass through a $100\mu\text{m}$ diameter sample chamber without hitting the gasket.

2.5.3 Station 9.5

Station 9.5 is approximately 30m from the 5T, Line 9 wiggler (which is also used by Station 9.1). A Laue focusing monochromator comprising a horizontally bent Si single crystal, focuses and monochromates the white beam [Lienert 98]. Radiation is focused in the vertical direction down to $\approx 85\mu\text{m}$ from $450\mu\text{m}$. After focusing the monochromated x-ray beam travels through an evacuated beam tube (4m long) to a platinum pinhole of $70\mu\text{m}$ aperture. This pinhole acts to define the beamsize (just before the beam impinges on the sample) and to attenuate the $\lambda/3$ harmonics of the x-ray beam (as the wavelength of $\lambda/3$ for typically used λ of 0.4646\AA is approaching the value of the K absorption edge of Pt). The radiation that passes through the pinhole will still contain some $\lambda/3$ contamination. A collimator and soller slits reduce the scatter and define the size of the unfocused horizontal component of the beam [Lennie 07]. A schematic diagram of the experimental hutch part of the beamline is shown in Figure 2.14, the design is essentially the same as for Station 9.1 (although Station 9.1 lacked computer driven rotation and translation stages).

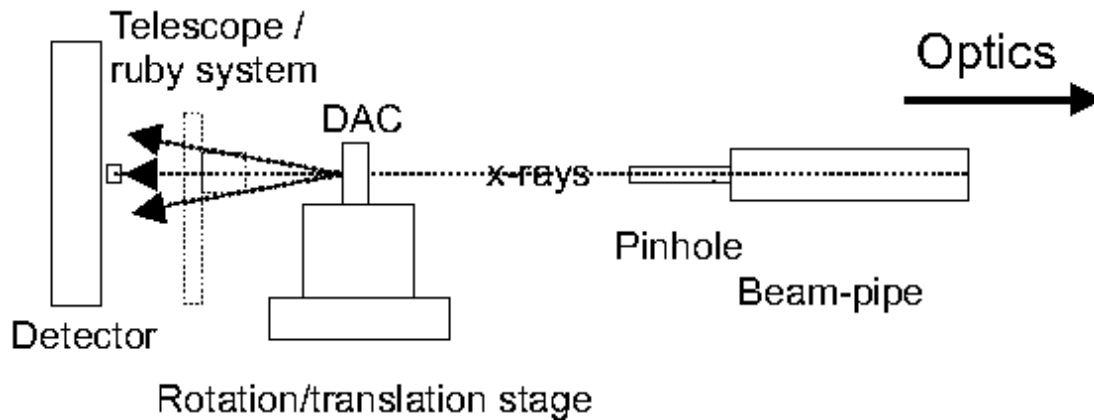


Figure 2.14: Labelled schematic diagram of Station 9.5, Daresbury SRS. Position of the optics relative to the setup is noted. Telescope used for alignment and online pressure measurement is shown in dotted line, indicating the position of this device is out of the path of the incident x-ray beam when not in use. The rectangle labelled “pinhole” contains at the detector-side a pinhole for defining the x-ray beam, and on beam-pipe side collimator and slits for providing initial definition of beam.

2.5.3.1 Alignment of Station 9.5

Samples are mounted on the sample stage within a “tombstone”. Initial alignment is performed using a telescope, previously focused on an object laying in the beam and coincident with center of rotation of the sample stage. The sample is brought into focus and aligned by adjusting the sample stage. Once aligned optically, a more accurate alignment procedure is made using the x-ray beam and motorised sample stage. The sample is stepped in $\approx 0.01\text{mm}$ steps for 2mm along two directions perpendicular to the beam, with the beam intensity recorded at each step with a photodiode placed in front of the beamstop. The stepped scans rely on differing x-ray absorption of the sample chamber’s components. The gasket material (of similar thickness to the sample when the DAC is pressurised) will absorb more x-rays than the pressure transmitting media (and sometimes the sample) resulting in a larger attenuation compared to the contents of sample chamber. Thus the resulting scan will appear as a gaussian like profile, corresponding to the convolution of the x-ray beam cross-section (gaussian) with the sample chamber (assumed to be a “top hat” owing to low absorption of x-rays by the pressure transmitting medium), with a dip corresponding to the location of the sample. The intensity on either side of the gaussian will be relatively low (orders of magnitude lower) owing to much greater absorption of the incident x-ray beam by the gasket compared to absorption from the sample chamber. Motor positions are set to the sample location, as read off from a plot of beam intensity vs. motor position. The sample is now centered in the two directions perpendicular to the beam.

The sample stage is motorised not only in 3 perpendicular directions for translation of the DAC, but rotationally, allowing for rotation and oscillation of the sample about an axis perpendicular to the monochromated beam. Centering of the sample on the axis of rotation of the sample stage must also be performed, to ensure that upon rotation about an axis perpendicular to the incident x-ray beam (to maximise powder averaging statistics), the sample remains upon the rotation axis. Alignment of the sample is performed by rotation of the sample by 3° in the positive direction, scanning (as above) in the horizontal direction, noting the sample location. This is repeated for 3° in the negative direction, again the sample position is noted. The offset of the sample from the axis of rotation is determined using equation 2.9. Rotation of the sample in the x-ray beam was not possible on Station 9.1.

$$(2.9) \quad \Delta y = \frac{1}{2} \frac{\Delta x}{\tan \alpha}$$

This rotation axis alignment procedure should be repeated at higher angles, $\pm 5^\circ$ (or at least the angle used for the cell oscillation) for greater accuracy in the alignment.

The DAC alignment procedure on Station 9.5 is inherently more accurate than that used on Station 9.1. The latter is heavily dependant on the accuracy of the optical alignment. On Station 9.5, the optics are used only as an initial guide (and could be viewed as redundant beyond an initial alignment, if cells of similar size are used) with the majority of the alignment being carried out using the x-ray beam, and with more precise control over changes made to the sample/cell position (as stepping motors are capable of smaller adjustments to the position of the DAC). The step size of the stepping motors used by the sample stage ($\approx 0.005\text{mm}$) is the limiting factor here.

Gasket holes of $75\mu\text{m}$ can be routinely aligned without contamination from the gasket in the diffraction image. Alignment to this degree of precision is attainable in ≈ 5 minutes, comparing favourably to the ≈ 15 minutes for alignment on Station 9.1.

2.5.4 Comparison of Stations 9.1 and 9.5

2.5.5 Data Processing

This section introduces the software packages EDIPUS [Belmonte 98] and Fit2D [Hammersley 98] which are used for processing the Image Plate scans. EDIPUS, written by Drs S.A. Belmonte and R. Piltz, previously members of the Edinburgh HP Group. It takes the .gel format generated by the Molecular Dynamics IP Reader from datasets collected on Station 9.1 as input. Fit2D is capable of reading the .mar345 file format output from the Mar345 detector used on Station 9.5 (and ID09A of the ESRF). Both of these software packages display 2D diffraction patterns, apply geometric corrections and azimuthally integrate 2D diffraction patterns. A brief review of the corrections made follows, as both programs perform the same corrections this generalised review applies to both packages unless one is explicitly stated.

Powder-diffraction data is analysed through considering 1D powder diffraction profiles, of the form scattering angle (2θ) vs. diffracted intensity. Azimuthal integration (the averaging of diffracted intensity in direction of increasing angle around Debye-Scherrer rings) of the IP data yields profiles of radial distance (pixels) vs. integrated intensity. Conversion from pixel number to 2θ requires that the IP to sample distance is known accurately. For accurate integration the beam center (where the “straight through” x-ray beam strikes the detector, forming the center of the diffraction image) must be known precisely.

The IP used in an experiment will not be truly perpendicular to x-ray beam. The degree of obliquity of the IP manifests itself as the tendency of an (expected) circular Debye-Scherrer ring towards an ellipse. Using a calibrant of finely-powdered Si at ambient pressure, known to produce sharp, smooth Debye-Scherrer rings, the tilt can be refined at the start of the experiment. In EDIPUS, the diffraction image is split into 60 equally segments of equal angular size [Belmonte 98]. Comparison of the radial position of the ring segments about the beam center is made, then the tilt adjusted until each segment lines to form a circle. This method is dependant on the beam center having been specified through user selection on a GUI or refined along with the tilt (as the center of a diffraction ellipsoid).

Fit2D requires the user to select a number of points within the first diffraction ring of the Si calibrant, from which the ring is traced by the software, and least-squares refined to ensure an accurate representation of the true shape. The tilt is determined from deviation of the ring away from circular. The beam center is automatically refined from the centroid of the diffraction ring. Requiring the user select the (111) powder ring from the Si diffraction image, Fit2D can determine the radial distance of the ring from the refined beam center. The locations of the subsequent FCC diffraction rings are predicted (within bounds) and least-squares refined to give their radial separation. Knowing the radial separation and wavelength of incident radiation, the sample to plate distance can be precisely determined from $n\lambda = 2d\sin\theta$.

The sample to plate distance in EDIPUS is refined similarly, locations of the diffraction rings and beam center must be passed to an external program which returns the sample to plate distance to EDIPUS.

2.5.6 Data Analysis - Indexing and Refinement

This section describes the process of determining the structure of an unknown phase of a substance; how one indexes a powder pattern to find the unit cell; how the space group is determined and how the atomic positions are found and refined.

2.5.6.1 Indexing

Indexing in crystallography is the process of assigning (hkl) values to reflections observed in a diffraction pattern, and thereby find the cell (and space group) of the sample being studied. In powder diffraction studies, the information available from 2D diffraction images is limited to the d -spacing of the Bragg peak and its intensity. The loss of full, 3D coordinates of the Bragg peaks in 3D space means, for any given d -spacing, the intensity can comprise the summation of a number of distinct overlapping reflections, each with different (3D) hkl indices (such as (340) and (500) in a cubic material) . Powder diffraction indexing programs take account of this during their operation, but, for optimal results peaks at high 2θ angles are preferable [mim].

The indexing software used, DicVol [Louer 04], requires accurate angular positions of diffraction peaks, in 2θ to be able to find a unit cell. DicVol uses the dichotomy method, whereby trial cells have their dimensions and internal angles varied within user specified bounds in an attempt to exhaustively search parameter space for cells which have diffraction peaks at the locations supplied to the program as input. From

an integrated, 1D diffraction profile peak locations are determined accurately using the program DatLAB [Syassen 08b], a graphing program capable of fitting a range of functions to a supplied dataset (in this case a powder diffraction pattern). Specifying the approximate location of the centroid and width of a diffraction peak, a pseudo-Voigt curve is fitted to the diffraction peak. From the fitted curve position, the intensity and full width half maximum (FWHM) are recorded, along with an estimation of the error in each, supplied as a χ^2 value.

Having prepared an input file for DicVol, which contains the 2θ locations of the Bragg peaks to be indexed (along with corresponding uncertainty in position of each peak), the upper and lower bounds on volume to be searched through for solutions and the type of solutions to search for (cell type: cubic, hexagonal, orthorhombic, tetragonal, monoclinic and triclinic). The output file generated by DicVol then contains, for each of the cell types, a number of possible solutions. These possible solutions state the unit cell parameters, some figures of merit (for internal comparison on the relative merit of each solution) and for each 2θ peak location supplied a hkl index, corresponding calculated 2θ (calculated based of the cell parameters) and difference between observed and calculated positions.

Cell types provided by DicVol are judged based upon a number of criteria. If all of the peaks supplied to the program can be indexed (this assumes that all of the peaks supplied to the indexing software are coming from the sample, rather than contaminants), how close the predicted peak locations are to the measured peak locations in 2θ (within $\approx 0.01\text{deg}$ is appropriate), and if it is a high-symmetry solution (high symmetry solutions are favorable at high pressure over the rarely-occurring triclinic solution type [mim]).

2.5.6.2 Refinement

Once the data has been corrected for tilt and beam center location, integrated azimuthally and the 1D diffraction pattern saved in a compatible format, the measured data can be used within a refinement package to determine the structure of the sample.

Rietveld refinement [Rietveld 69] is a means of least-squares refinement, used on integrated 1D powder diffraction patterns, to progressively refine a structural model

from a set of starting values against the supplied diffraction pattern, by means of minimising the difference between the calculated intensity for the model (y_{calc}) and observed intensity (y_{obs}) of a diffraction pattern. Equation 2.10 is used within the Rietveld refinement process, with χ^2 as the parameter that is minimised during the refinement process; w_i is the weighting placed on each point, i , in the 1D integrated diffraction pattern; y_{obsi} is the intensity in the measured diffraction pattern at point i ; y_{calci} is the intensity in the calculated diffraction pattern (from the model being refined during the Rietveld refinement process) at point i .

$$\chi^2 = \sum_i w_i (y_{obsi} - y_{calci})^2 \quad (2.10)$$

Refinable parameters within the model include, but are not limited to, the unit cell parameters, peak shape, variation of peak shape with 2θ , background intensity and preferred orientation. Additional phases (or contaminants) within samples need to be accounted for when performing Rietveld refinements, so as to avoid the refinement software attempting to fit the additional phases during the refinement. This can be achieved by either masking regions of the diffraction pattern (i.e. instructing the software to ignore specific 2θ ranges where non-sample reflections occur) or through the addition of extra phases in the refinement (essentially instructing the software that there are 2 samples present, each with different refinable parameters). The latter method for dealing with additional phases requires more detailed knowledge of the additional phase than the former method, as well as being more computationally demanding.

The Rietveld refinement program Jana2000 [Petricek 00] was used throughout this work for structural refinement. Jana2000 allows the user to perform both Le Bail (fits to 1D diffraction data in which only the unit cell parameters, peak shape and background are modelled and fitted) and Rietveld refinements. Le Bail refinements ignore the effect of atomic position on the intensity of Bragg peaks. Thus, as each peak is treated as having a variable maxima, and this allows for trial cells to be tested against the integrated diffraction pattern in cases where the position of atoms within the unit cell are not known. In judging the quality of a Le Bail fit close attention must be made to the difference plot (output by default in Jana2000), as a poor Le Bail fit is indicative of a bad choice of unit cell and/or spacegroup. Initial structure models were tested using this Le Bail refinement method, the unit cell parameters gained from Le Bail refinements were used as a starting values for Rietveld Refinements, this minimises the number of initial refined parameters during the Rietveld refinement, helping prevent

the refinement becoming stuck in a local minima or spend too long making small, incremental changes to a large number of parameters as parameter space is searched for a minima. Using Jana2000 corrections can be applied to the model prior to refinement, allowing (for example) preferred orientation to be considered.

2.6 Concluding Remarks

This chapter presented the background information required for the reader to understand the principles behind the experimental setup required for high pressure x-ray diffraction from samples within DACs. The majority of the datasets collected and analysed during the work presented in this thesis was carried out at Daresbury SRS, with early work being carried out on Station 9.1, before Station 9.5 became available for use with high pressure DAC diffraction. Comparisons made within this chapter (2.5.1.3, 2.5.4) show the benefits gained from switching from Station 9.1 to Station 9.5 of Daresbury SRS. Some work was performed at beamline ID09A of the ESRF, a more powerful synchrotron. Access to the ESRF was more limited, reflected in the proportion of data collected from it being an order of magnitude lower than the amount collected from Daresbury SRS. As such, and due to the principle of operation of beamlines at the two synchrotron facilities (Station 9.5 of SRS being an analogue to ID09A at ESRF) being the same, the alignment procedure for Daresbury SRS, Station 9.5 has been presented.

Chapter 3

Literature Reviews

3.1 Introduction

This chapter presents two reviews of work published to date in the literature. The first is concerned with the physics and high-pressure behaviour of the lanthanide series of elements, highlighting the importance of praseodymium as a key member of that series. The second review is focused on praseodymium, critically evaluating the last 25 years of high-pressure studies conducted on this element. The chapter concludes with the identification of the main discrepancies found, the resolution of which forms the major part of this thesis.

3.2 Review of Lanthanides

As a function of increasing $4f$ occupancy the ambient-pressure and temperature structures of the trivalent lanthanide elements are observed to follow a sequence of close packed crystal structures, $fcc \rightarrow dhcp \rightarrow Sm\text{-type} \rightarrow hcp^*$. Early studies of the lanthanides, in the decade following the introduction of the high pressure (diamond anvil) cell by Weir *et al.* [Weir], were limited to electrical resistivity measurements [Stager 64] and unit cell measurements [Perez-Albuerne 66]. These early studies provided accurate transition pressures (later confirmed by McWhan *et al.* [McWhan 72], Mao *et al.* [Mao 81], Holzapfel *et al.* [Holzapfel 95] for example) for each of the lanthanides, to approximately 50GPa for 11 of the lanthanides, without detailing the structural transition sequence. Indeed, the work of [Perez-Albuerne 66] (an early x-ray diffraction study) was stated as being limited by the Mo x-ray tube

*The author uses the abbreviations *fcc* for face-centered-cubic structure, *dhcp* for double-hexagonal close-packed structure, *Sm-type* for the α -Sm type structure, *hcp* for hexagonal close-packed and *d-fcc* for distorted-*fcc* structures

used for the experiments, which gave few usable diffraction peaks, the “100, 101, and at lower pressures the 110”. The small number of usable diffraction peaks in Perez *et al.*’s study [Perez-Albuerne 66], as commented by the authors, was sufficient to observe a splitting of the (101) reflection of the *hcp* phase, and suggest a transition to be *hcp* \rightarrow *dhcp*, but not sufficient to “be definite about it”.

An attempt was made at explaining the underlying cause for the regular lanthanide phase transition sequence in the late 1960s by Gschneider and Valletta [Gschneider 68]. At the time of publication by Gschneider, the regular lanthanide phase transition sequence was known up to and including the *fcc* phase which had been observed in La, Pr and Nd. Prior to Gschneider, the relation between phases adopted at high pressure and ambient within the lanthanides was made through observation of the *c/a* ratio of the unit cells with pressure, Jayaraman and Sherwood [Jayaraman 64] likening *c/a* ratio for Sm-type and *dhcp* structures at HP and ambient. However, this approach was later refuted, with McWhan and Stevens [McWhan 67] stating that the *c/a* ratio changes slightly with the application of pressure and can not be correlated with transition pressures between phases. Gschneider [Gschneider 68] presented an alternate theory, in which the participation of the *4f* electrons in the metallic bonding dictates the structure adopted. Qualitative measurements of the *4f* electron participation in bonding could be gained from the ratio of metallic radius to the *4f* electron radius of the lanthanide element (or alloy), here, the metallic radius was an indirectly measurable quantity gained from atomic volume data. The radius of the *4f* wavefunctions used was based on those obtained from calculations performed on 8 of the lanthanides, with the remaining members of the series having their wavefunctions spatial extent interpolated/extrapolated from neighbouring elements. Gschneider assumed that the spatial extent of the *4f* electrons is pressure independent and that the metallic radius decreases with pressure. These two assumptions corroborate a suggestion made in the paper (and shown to be true later by [Wittig 80]) that pressure increases the *4f* contribution to bonding within the lanthanides, from a constant negligible amount in heavy lanthanides (Gd-Lu) to a larger fraction (although still small at <10%) for light lanthanides (La-Sm), which Gschneider uses to explain the adoption of the *fcc* structure under pressure “These calculations show that any *4f* contribution to the bonding favours *fcc* over the *hcp* structure” [Gschneider 68]. Pressure induced changes in the occupancy of orbitals as the driving force behind the phase transitions observed in the lanthanides would later be addressed by McMahan *et al.* [McMahan 84].

An empirical attempt at relating the properties and structure adopted by the

lanthanides under pressure was made by Johansson and Rosengren [Johansson 75]. Noting work carried out prior to this study (such as that by McWhan [McWhan 72] and Gschneider [Gschneider 68]) Johansson and Rosengren assumed that the Sm-type structure was a common member of lanthanide's phase transition sequence, a view the authors suggest was not broadly accepted at this point, due to only a few, tentative reports in the literature of the observation of $hcp \rightarrow$ Sm-type transition in high-Z lanthanides on the application of pressure).

Furthering the idea proposed by Gschneider and Valletta [Gschneider 68] that the atomic volume of the lanthanides is not directly correlated to the structures adopted in the lanthanide transition sequence, Johansson and Rosengren sought to explain the sequence of close-packed structural transitions in terms of a parameter F, where, F is defined as the variation of the Wigner-Seitz radius r_{ws} , with ionic radius r_{ionic} , i.e.

$$F = \frac{r_{ws}}{r_{ionic}} \quad (3.1)$$

where the Wigner-Seitz radius is the radius of a sphere which encompasses the entire atom [Wigner 34] (is inversely proportional to the cube root of the electron density, i.e.

$$r_{ws} = \left(\frac{3}{4\pi n}\right)^{\frac{1}{3}} \quad (3.2)$$

where n is the number of valence electrons of the atom, divided by atomic volume) and ionic radius is the radius of the electrons bound to the atomic core only. Figure 1 of Johansson's paper (reproduced in Figure 3.1) shows how r_{ws} , r_{ionic} and F vary linearly (to first order) for the trivalent lanthanides at ambient pressure and temperature. It was then postulated that, as applying pressure decreases r_{ws} without decreasing r_{ionic} (which causes F to increase) pressure allows the simulation of heavy lanthanide behaviour in pressurised light lanthanides.

To construct a generalised phase diagram of the trivalent lanthanides, phase diagrams of each of these elements were collated and overlaid by Johansson and Rosengren from the literature [Jayaraman 64, McWhan 65, McWhan 67, Bucher 69]. Heavy lanthanides, starting with thulium (Tm) being used as the origin, transition pressures between phases were used as reference points to align overlaid phase diagrams of erbium and holmium (when properly scaled) atop of thulium. Successive phase diagrams

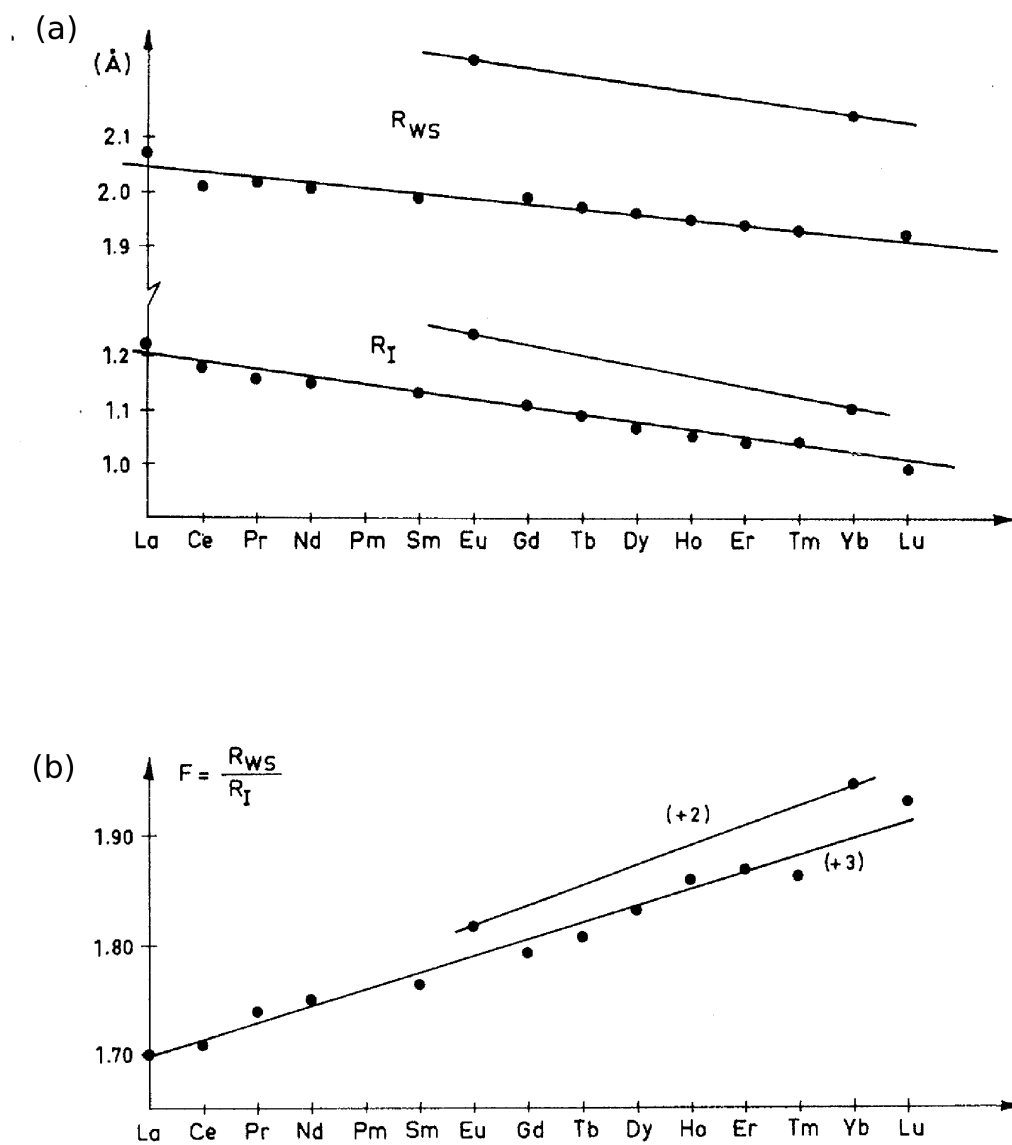


Figure 3.1: Figure reproduced from Johansson and Rosengren [Johansson 75]. The top graph (referred to as (a) in [Johansson 75]) shows experimentally derived Wigner Seitz ratio and ionic radius variation across the lanthanide series. The lower graph, (b) shows how the ratio F (defined in figure and previously in Equation 3.1, with r_{ws} defined in Equation 3.2) varies across the series.

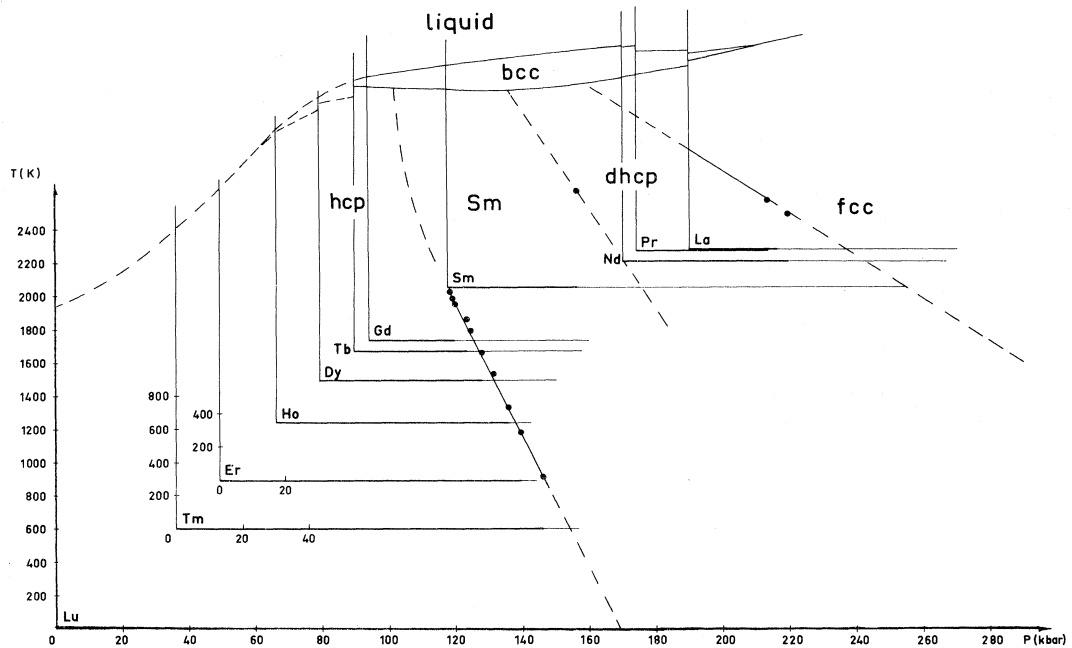


Figure 3.2: Figure reproduced from Johansson and Rosengren [Johansson 75]. Figure shows the constructed general phase diagram for the regular (trivalent) lanthanides constructed by Johansson and Rosengren from references contained within [Johansson 75]

were scaled and positioned to keep continuous phase boundaries between transitions, resulting in the diagram shown in Figure 2 of their paper [Johansson 75] (reproduced in Figure 3.2). Lu was added to the diagram in Figure 3.2 after the addition of the light lanthanides, its inclusion (despite not being a member of the lanthanide series) was based on the prediction of a transition to Sm-type from *hcp* at 17GPa. This prediction was made by Johansson and Rosenberg in the theoretical modelling section of their 1975 paper [Johansson 75]. Promethium and cerium are not present in this general phase diagram. Promethium is absent from Figure 3.2, owing to its radioactivity: at the time of publication few articles described the HP behaviour of Pm. Cerium's absence is due to the delocalisation of $4f$ electrons occurring at low T and ambient pressure [Johansson 75], as such, the authors state it is not possible to place the room-temperature phase diagram on Figure 3.2. Discontinuities in the generalised phase diagram exist around the HP-HT phase boundary between the regular lanthanide transition sequence and the *bcc* phase for Nd, Pr and La, the author gives no reason for this discontinuity, which could have arisen from incorrect scaling or limitations (accuracy, precision) in the data used to construct and collate the figure.

Similarities thus became evident in the behaviour of individual lanthanides under the influence of pressure and temperature. Such comparisons [Johansson 75] later culminated in Holzapfel's [Holzapfel 95] 1995 paper, which presented a series of equation of state (EoS) diagrams for the trivalent lanthanides ([Holzapfel 95] will be addressed later in this chapter). The phase-transition sequence shown in Figure 3.2 became known as the regular lanthanide phase transition sequence. When Johansson and Rosengren's paper was published, this sequence was verified up until the *fcc* phase (it is now speculated that the phase transition sequence includes additional post-*fcc* phase/phases). Compression beyond the final member of this sequence, the *fcc* phase yields phases not found at ambient conditions within the lanthanide series. The first of which, the distorted-*fcc* (*d-fcc*) phase, is so called because of a close resemblance (in its measured x-ray diffraction pattern) with the precursor *fcc* phase, albeit with distortions to the unit cell atomic positions which yield superlattice reflections in addition to a regular *fcc* pattern [Mao 81].

Indirect evidence of the mechanism behind the volume collapse transition in Pr came from electrical resistivity measurements was made by Wittig [Wittig 80] (shortly followed by the acceptance of more direct, x-ray diffraction measurements by Mao *et al.* [Mao 81]). Wittig's experiments detailed the temperature dependence of resistivity of Pr at fixed pressures (9-23GPa in 9 uneven steps). A large drop (30%) in the measured resistivity of Pr was observed at the transition from the *d-fcc* phase (referred to by Wittig as the low-P phase) to the α -Uranium phase (referred to as the high-P phase), and an anomalously large temperature dependence on resistivity in the low-P phase, both of which are characteristic of the $\gamma \rightarrow \alpha$ phase transition in cerium. This led the author to draw parallels between the *d-fcc* \rightarrow α -U transition in Pr and the $\gamma \rightarrow \alpha$ transition in Ce, as, at this time, it was known that the $\gamma \rightarrow \alpha$ Ce transition was caused by delocalisation of the $4f^1$ to an itinerant $4f$ band. Later resistivity experiments performed by Velisavljevic *et al.* [Velisavljevic 04b] confirm the large sharp decrease in electrical resistivity measured by Wittig, but show a larger measured drop in resistivity (59%).

On compression above 20GPa (beyond the *d-fcc* phase) a large decrease in volume, reported to be of the $\approx 19\%$ of unit cell volume for Pr, was observed by Mao *et al.* [Mao 81]. Until 1981, the mechanism behind the large volume decrease had not been verified through diffraction methods. A similar large volume decrease had been previously observed in Ce [Stager 64] ($\alpha \rightarrow \gamma$ Ce) and it was postulated that the driving mechanism, already accepted by consensus in the literature to be the result of pressure-

induced electronic transfer, is analogous to the $\alpha \rightarrow \gamma$ transition in Ce [Wittig 80, Mao 81]. The work of Wittig [Wittig 80] provided indirect evidence for $4f$ electron delocalisation, suggesting x-ray diffraction experiments would provide more conclusive evidence, which came with the study (he) performed with Mao *et al.* [Mao 81] a year later. Thus it became accepted that the $4f$ electrons, previously not participating in bonding within the crystal structure, become itinerant and participate in the metallic bonding, greatly reducing the volume of the atom, and so the unit cell. The volume collapse associated with the phase transition from d - fcc to post- d - fcc phase (α -Uranium structure, space-group $Cmcm$ or $oC4$ in Pearson notation) is responsible for the coining of the term “collapsed” phases, which is used to refer to phases that exist after the $4f$ delocalisation unit-cell volume collapse.

Steps began to be made to identify the structure adopted in the d - fcc phase within the light lanthanides, with work focusing on Pr (a more detailed synopsis is given in 3.3) and other light lanthanides. Mao *et al.* [Mao 81] suggested, based on diffraction photographs (x-ray film techniques), an orthorhombic unit cell for the collapsed phase, suggesting a maximum space group symmetry of $P2/m 2/m 2/m$. The authors noted limitations of their technique, notably an inability to gather fractional coordinates of the atoms within the unit cells.

Grosshans *et al.* [Grosshans 82], building upon the earlier work performed on Pr [Wittig 80, Mao 81] performed high-pressure diffraction experiments on Pr, La and Y, in order to establish a basis for explaining the distortion seen to occur to the fcc structure. The distortion, Grosshans *et al.* reasoned, could be described by a soft phonon mode, \mathbf{q} , shown in Equation 3.3.

$$(3.3) \quad \mathbf{q} = \frac{2\pi}{a_0} \left(\frac{1}{2}, \frac{1}{2}, \frac{1}{2} \right),$$

Using \mathbf{q} , the additional diffraction lines that appear on distortion of the fcc structure can be indexed with $\Delta\mathbf{k} = \mathbf{G} = \mathbf{G}_{fcc} \pm \mathbf{q}$. Here, \mathbf{q} corresponds to the L zone-boundary point in the Brillouin zone (along the $\langle 111 \rangle$ in cubic setting, or c axis in hexagonal

setting) [Grosshans 82]. The phonon softening is thus responsible for the distortion along the hexagonal- c axis (in the fcc cell), which doubles the length of this axis upon transition to the d - fcc phase.

McMahan and Young [McMahan 84], considered the structures of the rare-earth transition sequence as a series of stacked hexagonal layers, which were labeled A, B and C depending on the positions of the atoms within the layers relative to the other layers. Extending this idea further, reducing ABC repeat pattern to be denoted “c”, for cubic and the ABA repeat to be “h” shorthand for hexagonal, simplifies the rare-earth transition sequence (third column in Figure 3.3, making it apparent, according to McMahan and Young, that missing from the sequence (reproduced in Figure 3.3) is an intermediary step, cchcch, or triple-hcp ($thcp$). Theoretical calculations performed on the band stability of the d -band (valence band) for trivalent systems (approximating the rare-earth metals) [McMahan 84] indicate a region of stability for this $thcp$ structure within the rare-earth transition sequence. The calculations place the stability region *between* the $dhcp$ and fcc phases, confirming their logical reasoning. However, within the same journal (paper published immediately after McMahan and Young’s), Smith and Akella [Smith 84] state they are able to, provide a fit to the Pr(III) (nomenclature for d - fcc in their paper) pattern of Mao *et al.* [Mao 81] using the $thcp$ structure which is as good as the other models suggested prior to this time [Mao 81]. It was noted by the authors [Smith 84] that the $thcp$ solution is unable to account for all of the observed peaks within the data.

Three lanthanide elements, Ce, Eu and Yb, the latter two of which have a half-filled and filled $4-f$ shell are considered “irregular” lanthanide metals, also referred to as divalent lanthanide metals owing to the dominance of the (II) oxidation state in their compounds. These “irregular” lanthanide elements do not have share the phase transition sequence under application of pressure common to the other, trivalent lanthanide elements [Grosshans 92], and so do not appear in the diagram presented in Figure 3.2. Instead, beyond the fcc phase, complex and as yet unidentified phases occur. As this study of lanthanides focusses on the low- Z lanthanides, which are trivalent, the behaviour of divalent lanthanides will not be considered in this review.

Duthie and Pettifor [Duthie 77] built upon the idea of a correlation between the ionic radius and crystal structure adopted by the lanthanide series presented by Johansson and Rosengren [Johansson 75], postulating that the previous authors’ failure to model the correlation (using pseudopotentials) arose because the ionic radius was itself an indirect measurement of the mechanism driving the transitions, the changing d -band

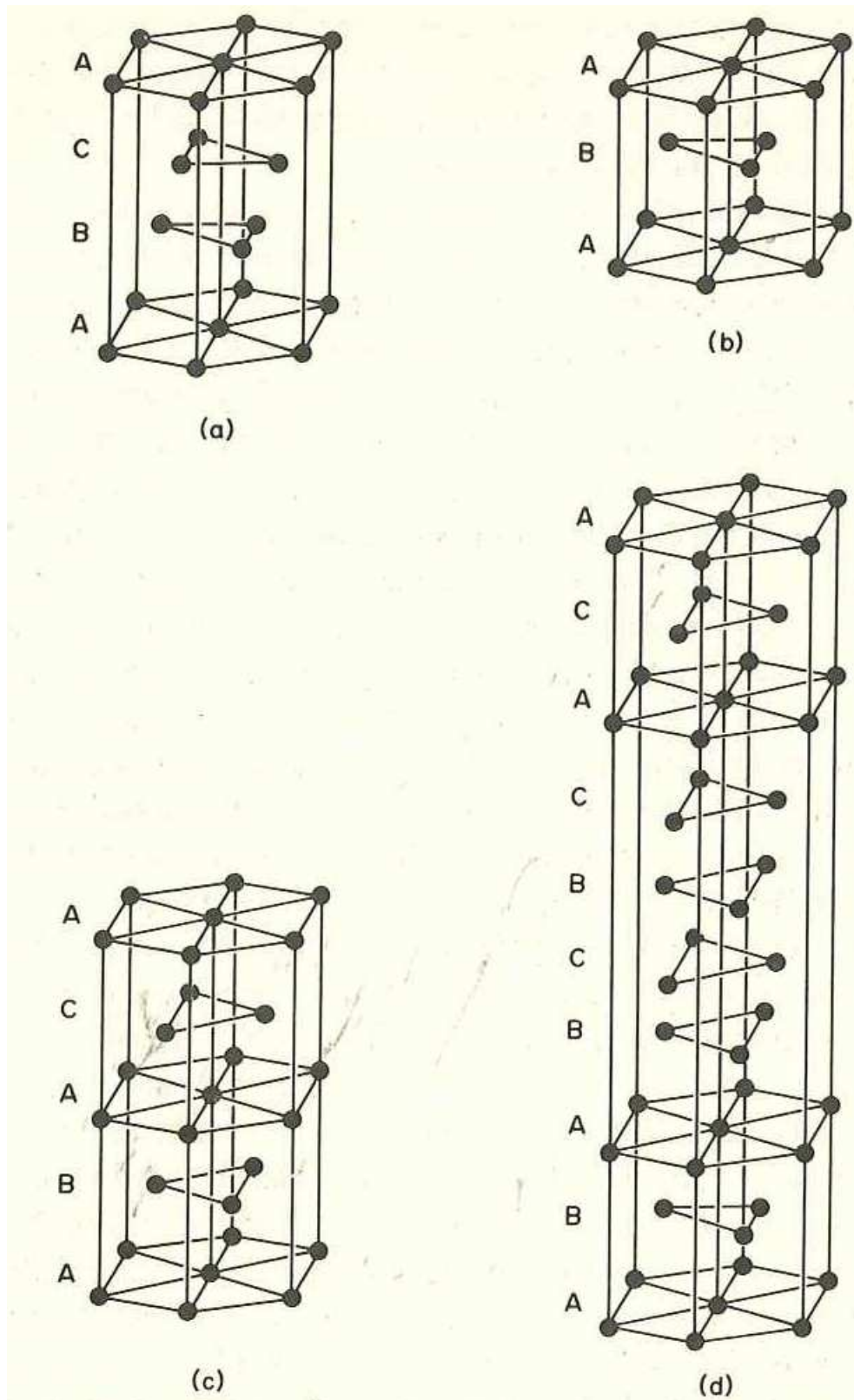


Figure 3.3: Diagram showing the relationship between the closed packed structures adopted by the regular lanthanides on pressure increase. Hexagonal layers, labelled A, B and C can be used to describe each of the *fcc* (a), *hcp* (b), *dhcp* (c) and (d) Sm-type structures. Diagram reproduced from [tay].

occupancy of the lanthanides upon pressurisation. The d -band occupancy is shown to change from about 1.5 to 2.5 during the regular lanthanide structure sequence, which itself affects the energy contribution of the d -band to the total energy of the crystal lattice. An increase in the d -band occupancy increases the total energy of the crystal lattice.

The mechanism driving the phase transitions at pressure in lanthanides accounts for the similarities observed in the phase diagrams. It was known in the early 1980s (following the work of Johansson and Rosengren [Johansson 75], and Duthie and Pettifor [Duthie 77]) that, like in the alkaline and alkaline-earth metals, the mechanism driving the phase transitions within the lanthanides is electron transfer from $s \rightarrow d$ states, resulting from the relative lowering in the energy of the d states with pressure. As the energy of the d states increases under pressure, at a slower rate than the s and the p electronic states, the s and p states eventually surpass the energy of the d states, which causes electron transfer from the s to the d electronic states. This was proved by observation of the phase transitions occurring in yttrium, Y, under pressure by Vohra *et al.* [Vohra 81]. Yttrium, a $4d$ transition metal, displays the transition sequence $hcp \rightarrow \text{Sm-type} \rightarrow dhcp$, with $dhcp$ tending towards fcc (shown by c/a ratio tending towards 1.633). As a consequence of this observation in Y, the regular lanthanide transition sequence can be shown by inference to be driven by the increasing number of d -electrons in the lanthanides (changing d -band occupancy), on increasing Z , or simulated by increasing pressure on single member. The regular lanthanide phase transition sequence is thus independent of $4f$ electron behaviour [Vohra 81]. Vohra *et al.* postulate that structural anomalies within Eu, Ce, Yb and Pr are related to the Fermi surface of these elements having f -electron character. However, the elements stated as having structural anomalies consist of Pr and the divalent lanthanides, the former is later shown to have a post- fcc phase, the transition to which is driven by delocalisation of the $4f$ electrons, the authors here must have mistakenly attributed the (at this point) unresolved d - fcc phase as a structural anomaly caused by “ f electron character in the Fermi surface”.

The study of Grosshans and Holzapfel [Grosshans 92] presents EoS diagrams for all of the lanthanides up to $\approx 40\text{GPa}$, some of which collate data from other studies with the authors' data. Using energy-dispersive techniques, the authors state a typical precision of $1 \times 10^{-3} \text{\AA}$ in the lattice parameters used to determine the EOS using Birch-Murnaghan type equation, although the dominant error source in the EOS curves

came from uncertainties in the measured pressure for some, particularly in the upper region of the pressure range. Inaccuracies in the measured pressure, in this study, like others originates from strain induced broadening of the calibrant's characteristic signal (pressure inhomogeneity within the sample chamber). Evident in the plots (Figures 1-15 in Grosshans *et al.* [Grosshans 92]) is a consistency in the behaviour of the trivalent lanthanides under pressure, in progressing through the regular transition sequence to a post-*fcc* phase, which the authors present as being (in line with other studies made, up to the early 90s [Mao 81]) as a trigonal structure.

The late 1990s (1995-1999) represented a resurgence in the study of lanthanides, prompted by the adoption of angular dispersive x-ray diffraction techniques developed in the early 1990s [Shimomura 92, McMahon 94]. Angle dispersive techniques allowed the collection of accurate intensity values for reflections and reliable angular position, the former required for determining the position of atoms within a unit cell, the latter for unit cell/space-group. Used in conjunction with synchrotron radiation sources, high pressure x-ray diffraction studies were performed on members of the lanthanide series.

3.3 Review of Praseodymium

The importance of praseodymium (Pr) within the Lanthanide series has been alluded to in Section 3.2; the *fcc* \rightarrow *d-fcc* \rightarrow collapsed-phase sequence of the regular lanthanide transition sequence occurs within low-*Z* lanthanides at lower pressures compared to the high-*Z* lanthanides. Within Pr these transitions occur at pressures of approximately 7 and 14GPa. Thus, a large body of work on Pr, focusing on the *fcc* \rightarrow *d-fcc* \rightarrow collapsed-phase transition sequence, has been contributed to the literature, which form the basis for subsequent experiments performed on higher-*Z* lanthanides, and some members of the actinide series. This is important as the understanding of the high pressure behaviour of Pr is vital to interpret the data from, and understand, the higher-*Z* lanthanides behaviour under pressure.

Some of the earliest high-pressure studies of Pr were performed by Stager and Drickhammer [Stager 64] and comprised of electrical resistivity measurements of Pr as a function of pressure at 3 discreet isotherms (296K, 197K and 77K). Whilst no diffraction data were provided to accompany these experiments (due to the technical limitation of the time), changes in electrical resistivity at approximately 4GPa, 7GPa

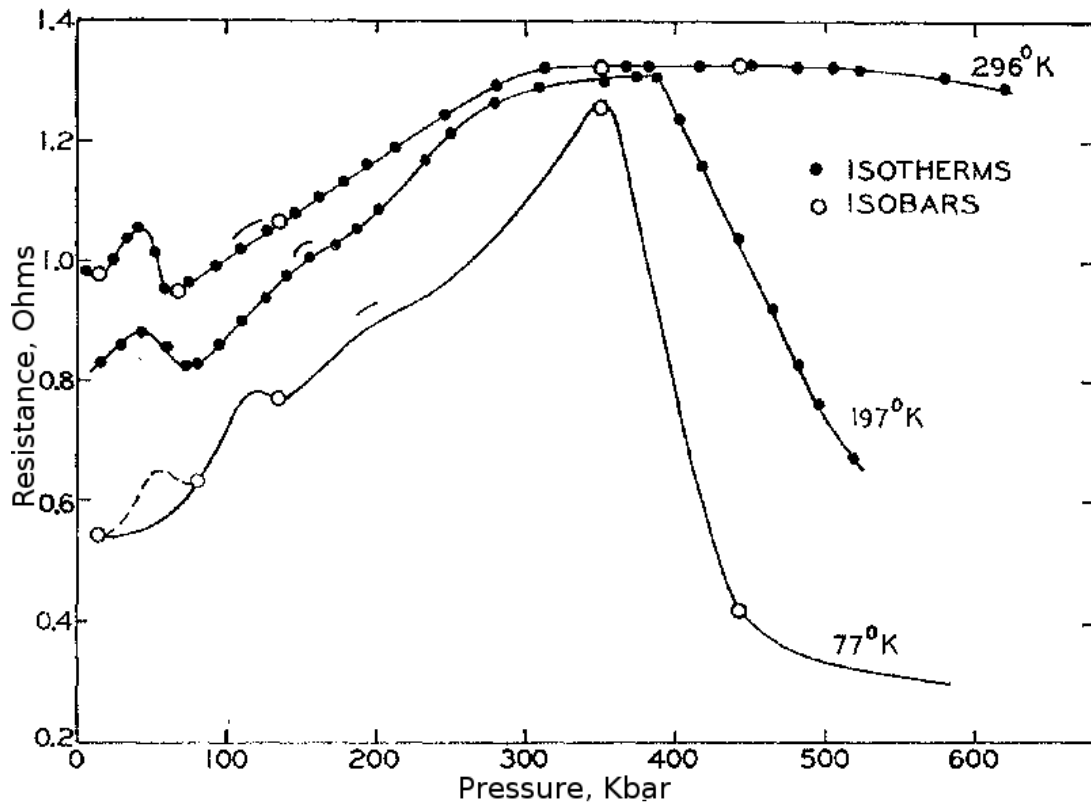


Figure 3.4: Electrical resistance measurement as a function of pressure for (3 isotherms of) Pr reproduced from Figure 2 of Stager and Drickhamer [Stager 64]

and 14GPa are evident from their data for the 296K isotherm in Figure 3.4. The points at which the resistivity changes were noted by the authors to be indicative (indirectly) of phase transitions occurring within the compressed metal. At this time the phase transition sequence of Pr was not known, but, was shown from later experiments [Johansson 75, Dmitriev 00], that these indirect measurements of the transition pressures within Pr are accurate. It is interesting to note this early discovery of a subtle change in resistivity at 14GPa, one which is more pronounced (albeit at slightly higher pressure) at 197K. This feature at 14GPa will be commented upon at a later point, as the story of Pr unfolds.

Mao *et al.* [Mao 81], using an angle-dispersive (x-ray sensitive) film based technique, were the first to use angle-dispersive measurements to investigate the *d-fcc* \rightarrow collapsed phase transition (indeed, Mao *et al.*'s study was the first to provide a structural solution

to the *d-fcc* phase). The focus of this study concerns parallels between the γ to α transition in Ce and that of the *d-fcc* to collapsed transition in Pr, the former by the point in time was accepted to be caused by the delocalisation of $4f$ electrons from the constituent atoms under pressurisation (indeed, it is referred to as “collapsed” phase due to the large volume difference between it and the *d-fcc* phase).

Mao *et al.*'s data shows 19 observed diffraction lines for a powdered sample of Pr collected at 14.4GPa. As expected, a close relationship to an *fcc* unit cell is evident, with 8 of the diffraction lines capable of being indexed with an *fcc* unit cell (stated $a_{fcc}=4.5\text{\AA}$). Indexing 18 of these 19 observed diffraction lines was performed using an orthorhombic unit cell, distorted from the precursor phase *fcc* unit cell and comprising 16 atoms in the unit cell (this solution will be referred to as oP16, following Pearson notation [Villars 91]). The comparison of reported observed and calculated peak positions (d-spacings) tabulated in Table 1 of Mao *et al.* [Mao 81] show a favourable agreement for this solution, although, I_{obs} (expressed as a %, relative to most intense peak) shows no peaks below 10% relative intensity were observed. As Mao notes, for each observed phase in the study (*d-fcc* and collapsed-phase) there remains a peak which is not capable of being indexed by the proposed models for each phase. For the *d-fcc* phase at 14.4GPa this peak is stated as having an intensity, $I = 30\%$, and d-spacing of $d = 2.87\text{\AA}$, for the collapsed phase the unidentified peak is at $d = 2.717\text{\AA}$ with an I of $<10\%$. Mao *et al.* identified the phase following the *d-fcc* phase as a *d-hcp* (distorted hcp) phase, with a volume difference of $(\frac{\Delta V}{V_{trans}})$ of 19% at the *d-fcc* to collapsed phase transition.

Mao *et al.*'s (in [Mao 81]) data was re-indexed by Smith and Akella [Smith 84], who identified the collapsed phase to be isostructural with the orthorhombic α -Uranium structure (*Cmcm* or *oC4* in Pearson notation). A diagram of the α -Uranium is presented in Figure 3.5. This re-indexing of the collapsed phase revised the volume collapse at the transition between *d-fcc* and collapsed-phase to $\approx 9.5\%$ [Smith 84]. Further to the re-indexing of the collapsed phase, Smith and Akella provided a revised solution to the *d-fcc* phase, tentatively suggesting the *d-fcc* phase has a triple hexagonal close packed (*thcp*) structure [Smith 84]. This *thcp* structure was considered an energetically favourable structure in a theoretical study published in 1984 by McMahan and Young [McMahan 84], who proposed the *thcp* structure as a solution to the *d-fcc* phase as it follows the transition sequence through open packed structures related by stacking of hexagonal planes.

Hamaya *et al.* [Hamaya 96] performed the first angle-dispersive study (a technique

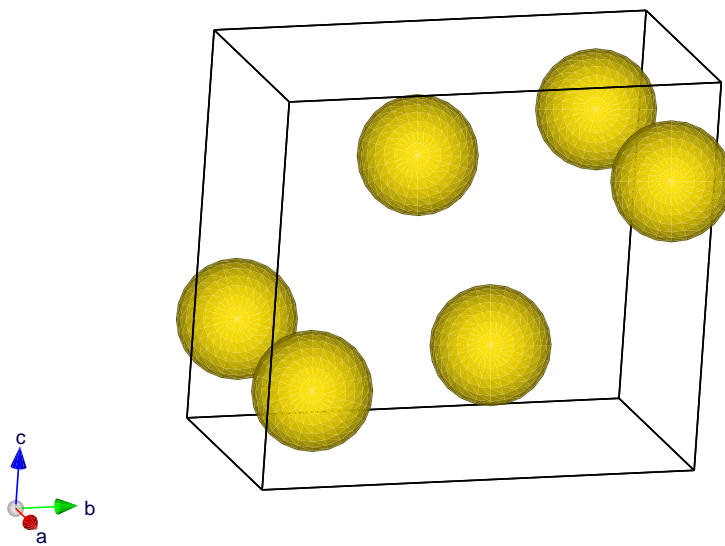


Figure 3.5: Diagram of the α -Uranium structure, $oC4$ (space group $Cmcm$) which is adopted by Pr after the delocalisation of $4f$ electrons on compression above 20GPa [Smith 84]. Atoms are located in the $4c$ Wyckoff positions (which correspond to atomic positions within the unit cell of $(0, y, \frac{1}{4})$ and $(0, -y, \frac{3}{4})$ with $y = 0.1$), here the unit cell parameters of $a = 2.7330$, $b = 5.4665$ and $c = 4.8769\text{\AA}$ for Pr in α -Uranium phase at 27GPa are taken (along with the atomic position, y) from [Baer 03]. Figure drawn using the crystal visualisation program Vesta [Momma 08].

developed in Japan in the early 1990s [Shimomura 92]) of Pr at a synchrotron radiation source. The use of synchrotron radiation, coupled with a monochromatic beam, angle-dispersive technique and an image-plate detector afforded Hamaya *et al.* resolution superior to that of previous studies [Johansson 75, Mao 81, Grosshans 82]. Numerous additional, low-intensity reflections were observed by Hamaya *et al.* in the *d-fcc* phase, which could not be accounted for by the *oP16* solution proposed by Mao *et al.* Hamaya indexed and was able to account for each observed reflection using a rhombohedral structure, with 24 atoms in the unit cell (in hexagonal setting, giving this structure the Pearson notation *hR24*) and spacegroup $R\bar{3}m$, and in doing so showed the first Rietveld refinement of the *d-fcc* phase. This *hR24* structure (in the hexagonal setting) can be related to the precursor *fcc* phase through the relationships $\vec{a} = -\vec{a}_{fcc} + \vec{b}_{fcc}$ and $\vec{c} = 2(\vec{a}_{fcc} + \vec{b}_{fcc} + \vec{c}_{fcc})$, where \vec{a} and \vec{c} are the *a* and *c* of the *hR24* unit cell.

Following Hamaya *et al.*'s study, Porsch and Holzapfel [Porsch 94a] reconsidered the *fcc* \rightarrow *d-fcc* transition, based upon the symmetry relationship between the *fcc* and *d-fcc* phases if the transition is first-order, and if it is second-order. Porsch and Holzapfel state that if the transition is second-order, a single orthorhombic structure exists which accounts for the x-ray diffraction patterns in [Hamaya 96], a *Cmmm*, with 8 atoms in the unit cell (*oC8* or *oS8* in Pearson notation[†]). This *oS8* structure can be related to the *fcc* by the relations $\vec{a} = 2\vec{a}_{fcc}$, $\vec{b} = \vec{b}_{fcc} + \vec{c}_{fcc}$ and $\vec{c} = -\frac{1}{2}\vec{b}_{fcc} + \frac{1}{2}\vec{c}_{fcc}$. If the transition is second-order, Porsch and Holzapfel report 3 possible structures; the orthorhombic *Cmma*, the triclinic $P\bar{1}$ and the rhombohedral spacegroup $R\bar{3}m$ (the *hR24* structure of Hamaya *et al.* [Hamaya 96]).

The *hR24* structure from Hamaya *et al.*, was later questioned by Syassen *et al.* [Syassen 00], who, after conducting a high-resolution diffraction study, reported an alternate, monoclinic solution to the *d-fcc* phase. This monoclinic solution, with 4 atoms in the unit cell and spacegroup $C2/m$ (*mC4* in Pearson notation), provided a good fit to the high resolution data shown in their report (a Rietveld refined pattern at 15GPa is shown) [Syassen 00], and is stated as having a good quality of fit in Rietveld refinements above 13GPa (Hamaya *et al.* show a refinement performed at 13.8GPa). The proposed *mC4* solution is directly relatable to the *fcc* precursor phase through subgroup relations (vector relationship is: $\vec{a} = \frac{1}{2}\vec{a}_{fcc} + \frac{1}{2}\vec{b}_{fcc} - \vec{c}_{fcc}$, $\vec{b} = -\frac{1}{2}\vec{a}_{fcc} + \frac{1}{2}\vec{b}_{fcc}$ and $\vec{c} = \frac{1}{2}\vec{a}_{fcc} + \frac{1}{2}\vec{b}_{fcc} + \vec{c}_{fcc}$), and had already been observed as a high pressure structure of Ce. However, upon close observation of the Rietveld refinement shown in

[†]the convention of using *oC* for a centered orthorhombic structure was, in 1985 changed, such that *oS* is now used [de Wolff 85]. This is to prevent confusion between the "C" referring to centered cell and the unique axis in cell choice for orthorhombic and monoclinic systems.

Syassen *et al.*'s report, a number of weak peaks are evident which are not accounted for by a $mC4$ structure, and not attributed to contaminants.

The studies of Hamaya *et al.* and Syassen *et al.*, who propose a $hR24$ and a $mC4$ structure, respectively, as the unique solution to the d - fcc phase, were followed by a paper by Chesnut and Vohra [Chesnut 00b]. Chesnut and Vorha, interestingly, reported observation of both the $hR24$ and $mC4$ structures in the d - fcc pressure range of Pr (which they report as 7-20GPa). This study was the first to suggest a phase transition occurring in what was previously thought of as a single phase between 7 and 21GPa. The $hR24$ from Hamaya *et al.* was observed as stable from 7-10GPa by Chesnut and Vorha [Chesnut 00b], the $mC4$ from 10-20GPa, and upon further pressurisation the α -U phase was observed. No volume discrepancy was observed by Chesnut and Vorah at the $hR24$ to $mC4$ transition. At the d - fcc ($mC4$) to α -U transition a volume change, ($\frac{\Delta V}{V_{trans}}$) of 16.7% is observed [Chesnut 00b].

The phase diagram of Pr was studied in 2003 by Baer *et al.* [Baer 03], who, noted difficulty in refining patterns with the $hR24$ structure when collected near the d - fcc to α -Uranium transition pressure. The authors show the $hR24$ structure fails to adequately describe the d - fcc phase (from 7-20GPa), in agreement with Syassen *et al.* [Syassen 00] and Chesnut and Vorah [Chesnut 00b]. However, Baer disagrees that the $mC4$ structure is a solution to the d - fcc phase of Pr, stating that it leads to an unfeasible volume change at the d - fcc to α -U phase transition, as $mC4$ has a larger volume than that of the $hR24$ solution proposed for these pressures. Baer *et al.*, in probing the high-temperature, high-pressure regions of the phase diagram, discovered a new phase, between the d - fcc and α -U phases. This new phase, which exists at high-temperature (above 700K, between 10 and 20GPa), was labelled Pr-VI. Baer *et al.* provide no solution to the structure of Pr-VI, stating simply that the $mC4$ structure does not fit.

Dmitriev *et al.* [Dmitriev 00] note the difficulty of other authors to adequately refine structures towards the upper limit in pressure of the d - fcc [Baer 03] pressure range. Enlargements of the 1D diffraction patterns around the doublet at $\approx 16^\circ$ in 2θ provided in Figure 5 of Dmitriev *et al.* [Dmitriev 00] show the authors' recognition of a potential new phase existing in the d - fcc pressure range as being the cause for the inability of previous authors to get adequate refinements in this pressure range.

Dmitriev *et al.* conducted their experiments on Pr, sourced commercially from GoodFellow, at stations ID30 and BM1A (Swiss Norwegian Beamline) of the ESRF,

at wavelengths $\lambda=0.3738\text{\AA}$ and $\lambda=0.72\text{\AA}$ respectively. While the authors state a maximum pressure reached of 44GPa, the cell type, culet size and gasket material are not mentioned. The need for avoidance of sample contamination was overcome by Dmitriev through DAC loading under an inert, dry argon atmosphere, or under mineral oil, however, as with the previous studies contamination remains present in diffraction patterns.

3.4 Contaminants

It is important to note that lanthanide metals are extremely reactive, freshly cleaved lustrous surfaces quickly tarnish in air, react with water at low temperature and rapidly oxidise in moist air [Cotton 91]. It is noted that lanthanides typically react with oxygen at room temperature, whilst at higher temperatures the reaction occurs more vigorously, tending towards ignition at 150-200°C [Cotton 91]. In order to limit the exposure of lanthanides to oxygen and moisture, lanthanides are typically stored under oil (“mineral oil” or “silicon oil”) within sealed glass jars containing an inert atmosphere [Akella 86, Grosshans 92] or prepared under oil [Grosshans 82] (in the absence of a glovebox).

A problem common to studies performed on praseodymium (and indeed other lanthanides) is the presence of contaminants within collected diffraction patterns. Authors of previous studies note [Mao 81, Chesnut 00b, Syassen 00] the presence of one or two contaminant phases in their studies of Pr. There is no solid consensus on the identity of the contaminants present throughout the studies published, indeed some authors fail to comment on observed and unaccounted for peaks present in their data, suggesting an inability to ascertain the identity of the contaminant. Table 3.1 summarises the findings of previous studies on contaminant phases.

Given the differing pressure transmitting media used and potential for different methods of loading of samples mentioned by the authors in Table 3.1, which has little effect on the presence of contaminants in the observed data. Samples for this body of work were loaded with mineral oil pressure medium and without pressure transmitting medium; in an inert argon atmosphere (glovebox) or under oil.

Baer *et al.* [Baer 03] describe the formation of a hydride, PrH_{2+x} (x between 0 and 1) within their DAC at pressures above 14GPa and temperatures exceeding 715K [Baer 03]. Baer determined the contaminant, present as *fcc* diffraction lines in integrated patterns, to be PrH_{2+x} by back extrapolation of the lattice parameter a_0 to

Author	No. Contam'	Lattice parameter, a_x	Comment
Johansson and Rosengren [Johansson 75]	Not stated	Not stated	No mention of contaminants.
Mao <i>et al.</i> [Mao 81]	2	Not stated	2 peaks stated as not being indexed.
Grosshans <i>et al.</i> [Grosshans 82]	1	Not stated	Comments on avoiding oxidation
Hamaya [Hamaya 96]	2	$a_{13.4}=4.9593\text{\AA}$	One attributed to PrO (4 peaks), other unattributed (2 peaks).
Chesnut [Chesnut 00b]	1	Not stated	One contaminant seen, referred to as "oxide".
Errandonea [Errandonea 00]	Not stated	Not stated	No comment.
Dmitriev <i>et al.</i> [Dmitriev 03]	1	$a_0=5.029\text{\AA}$	Attributed to PrO
Baer [Baer 03]	1	$a_0=5.4856\text{\AA}$	Seen at high-T, attributed to PrH_{2+x}
Cunningham <i>et al.</i> [Cunningham 05]	2	Not stated	PrO_2

Table 3.1: Summary of a selection of papers on Pr comments regarding presence of contaminant within their data.

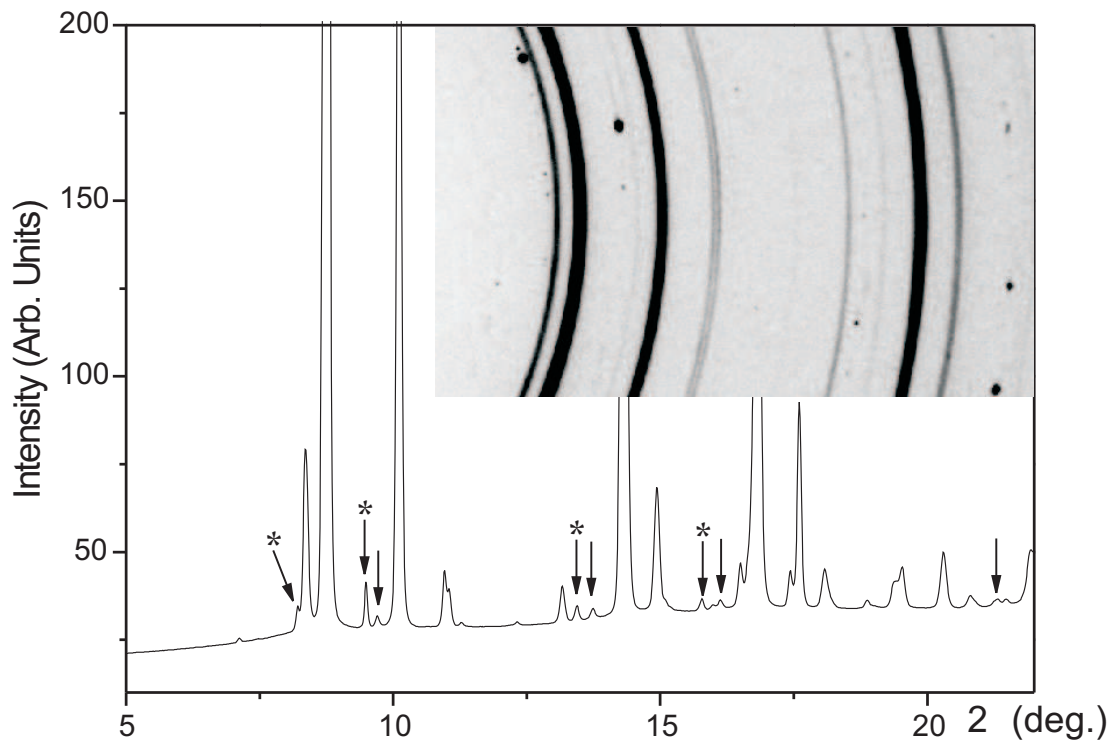


Figure 3.6: Diffraction pattern from the *d-fcc* phase of Pr, collected at 10.4GPa. Additional peaks arising from contamination are identified with arrows. Inset shows an enlarged segment of the 2D diffraction image, with contrast adjusted to illustrate the texture (spottiness) of the contaminant rings, which are identified with arrows. These peaks do not correspond to gasket peaks.

ambient pressure. Baer *et al.* observe an increase in intensity of the peaks they attribute to PrH_{2+x} as temperature is raised, remain at high-pressure and temperature, later decreasing in intensity when the pressure is lowered at room-temperature [Baer 03]. A reaction with the H content of the mineral oil pressure medium used for some of their experiments at high-temperature is cited as the origin of the hydride, which is not observed when Ar is used as a pressure medium [Baer 03].

Dmitriev *et al.* [Dmitriev 00] comment that the diffraction rings arising due to contaminants appear “spotty” on 2D diffraction images. Figure 3.6 (inset) shows how textured the rings appear on a 2D diffraction image collected at 10.4GPa at Daresbury SRS. Given the pronounced difference in texture of the rings arising due to contaminant(s) and sample, identification of the contaminant is straight forward when considering the 2D diffraction image.

3.5 Conclusions

The review presented in this chapter on the lanthanide series, and the more detailed review of Pr, clearly highlight the following problems with the body of work that exists to date in the literature. Significant disagreement remains in the structure of the *d-fcc* phase, a phase accessible in Pr at relatively low pressures. Indeed, disagreement persists over the number of structures required to model the *d-fcc* phase over the entirety of the pressure range it is observed to exist within, with one [Mao 81] or two [Dmitriev 00] structures being proposed. Following the numerous reports of similarities in the phase transition sequence of the regular lanthanides, it appears odd that the *d-fcc* phase has yet to be confirmed within the regular phase transition sequence of the lanthanides, further, if the *d-fcc* phase is found to be a member of the transition sequence, will it be observed to have the same structure(s) as Pr? The identity of contaminant peaks found within diffraction studies of Pr [Mao 81, Syassen 00] remains elusive, with none [Errandonea 00], one [Grosshans 82, Dmitriev 00, Chesnut 00b] or two [Mao 81, Hamaya 96, Cunningham 05] contaminants being observed, which, when present have cubic diffraction patterns.

Studies of Praseodymium

4.1 Introduction

As was shown in Section 3.3, Pr is a key member of the lanthanide series. Being of low- Z , it has been widely studied and used as a high-pressure analogue of the higher- Z members of the lanthanide series. It was the first lanthanide shown to exhibit a large volume collapse upon the transition to the α -U phase, the mechanism of which was shown to be electronically driven [Gschneider 68]. In this chapter the author aims to resolve the outstanding issues pertaining to the structure of the d - fcc phase of Pr, before, in the following chapter, turning attention to Nd, the following member of the lanthanide series.

To recap, the known structural transition sequence of Pr is $dhcp \rightarrow fcc \rightarrow d$ - $fcc \rightarrow \alpha$ -Uranium, with the phase transitions reported to occur at 4, 7 and 20GPa (Section 3.3). Here, the d - fcc phase has attracted a large amount of interest both experimentally [Wittig 80, Mao 81, Vohra 81, Grosshans 82] and theoretically [Johansson 75, Duthie 77], owing to the nature of the transition to the α -U phase that follows ($4f$ electron delocalisation, as observed in Ce) and numerous [Mao 81, Akella 99, Holzapfel 95, Syassen 00, Dmitriev 00] conflicting structural solutions proposed for the d - fcc phase itself. Section 4.4 will cover the phase transitions in Pr up to the d - fcc phase at 7GPa, whereas the bulk of this chapter, Sections 4.5 - 4.8, will be devoted to resolving the ambiguity in the Pr d - fcc structure. The transition from d - fcc to α -U will be covered in Section 4.9, where the author will resolve disagreements in the degree of volume collapse at this transition.

4.2 Experimental Details

The praseodymium used was sourced either from the Aldrich Chemical Company, as powdered chunks with a stated purity of 99.9%, or kindly provided by Dr. Ulrich

Schwarz (MPI, Dresden), as a single crystal, with a stated purity in excess of 99.99%. In each case the Pr was stored in a protective atmosphere for transportation. From Aldrich it came packaged in sealed plastic containers within a sealed glass jar containing an inert atmosphere. Samples from Dresden arrived in sealed tantalum ampoules, containing an inert argon atmosphere and a piece of metal from a single crystal of refined Pr. The samples used were cleaved from a clean, exposed, lustrous surface of one of the larger chunks received from suppliers. Due to praseodymium's propensity to oxidise upon exposure to oxygen and water, care was taken to ensure the samples used were not tarnished (the surface of the tarnished metal appeared dull and matt on exposure to small concentrations of oxygen, on exposure to larger concentrations it appears matt yellow/green).

Cleaved chunks of Pr, with exposed, lustrous surfaces were loaded into the sample chamber of a diamond anvil cell (DAC), within a tungsten gasket. Gaskets were pre-indented to approximately $30\mu\text{m}$, with a spark eroded sample chamber of diameter $75\mu\text{m}$ or $100\mu\text{m}$. Ruby spheres sourced from J. P. Chevrin, of approximate diameter $5\mu\text{m}$, were placed on the opposing diamond culet at off-central locations so as to avoid the diffraction pattern contamination (as the sample will be placed in the centre of the sample chamber). In the cases where mineral oil pressure transmitting media were used (the majority of the experiments performed), the remainder of the sample chamber was filled with dry mineral oil. When no pressure transmitting media was used, the sample chamber was filled only with Pr and a ruby manometer. The use of no pressure transmitting media was likely to introduce deviatoric stresses within the sample, caused by pressure not being applied hydrostatically to the sample.

DACs of DXR6 and Merrill-Basset (MB) design were used, in conjunction with a diamond culet size of 300 and $200\mu\text{m}$, respectively. This combination of culet size, cell design, pressure transmitting media and gasket preindentation is capable of reaching the 20GPa pressure required for the investigation of the *d-fcc* phase.

Care was taken during sample cutting and loading to prevent oxidation of the sample, and, when available, both operations were performed in a glovebox environment with an inert dry argon atmosphere. However, in some cases, such as when new reloadings needed to be made at Daresbury SRS, and where glovebox loading was not possible, loading was performed under mineral oil. In such cases the sample was cut and prepared in excess mineral oil in a petri dish. Performing the preparation (cutting) and loading under oil ensures the praseodymium is always coated in a protective film, preventing direct contact with the surrounding atmosphere, and thus oxidation of the sample.

The prepared cells were closed, mechanically pressurised, allowed to equilibrate and their pressures measured using the ruby fluorescence method, before being aligned on the beamline, as explained in Section 2.5.3.1. 2D powder diffraction data were collected on the IP system (Station 9.1) or Mar345 (Station 9.5) as outlined in Section 2.5.1, then integrated using the appropriate software (EDIPUS [Belmonte 98] and Fit2D [Hammersley 98]).

4.3 Contaminant Phases

4.3.1 Introduction

Noting that the contaminants' diffraction pattern appears as pairs of peaks, which are easily identifiable on 2D images, with, in some cases, one of the pair obscured beneath a sample reflection, leads one to the conclusion that 2 contaminants appear in the data collected, as noted in Mao *et al.* [Mao 81], Hamaya *et al.* [Hamaya 96]. For the 10.4GPa pattern shown in Figure 4.1, the d-spacings of the contaminant peaks can be used to determine a lattice type by using the indexing program DicVol [Louer 04]. A cubic, *fcc*, lattice type is proposed as the simplest solution by DicVol, supporting claims made by Mao *et al.* [Mao 81] and Dmitriev *et al.* [Dmitriev 00], who state viewing a cubic contaminant. The evolution of the peaks identified as contaminants differs notably from that of the sample, having a markedly lower compressibility and remaining in the same phase throughout the pressure range studied. The pressure evolution of the contaminant phases' cubic lattice parameters are shown in Figure 4.2, which were collected on both pressure increase and decrease. Shown for comparison are the lattice parameters measured by Hamaya *et al.* (and derived from their paper), those from Chesnut and Vohra [Chesnut 00b] and ambient pressure lattice parameter for likely contaminants.

Using EOSFIT [Angel 01], a second order Birch-Murnaghan equation of state is fitted to the first contaminant phase, allowing the back extrapolation of lattice parameter of this phase to ambient pressure. A resultant ambient pressure lattice parameter of $a_0 = 5.03\text{\AA}$ is determined. As shown in Figure 4.3, the variation of lattice parameter with pressure for both contaminant phases present in this work, in the range studied. Note the absence of data in the 0-5GPa region of Figure 4.3, this corresponds to an overlap of the sample and contaminant peaks in this pressure range. As noted on this figure, extrapolation to ambient pressure yields values of 5.03 and 4.88Å for the contaminants. One of the contaminants observed has an a_0 that is in excellent agreement to the accepted value for PrO (5.031 Å) at ambient pressure, and distinct from the ambient

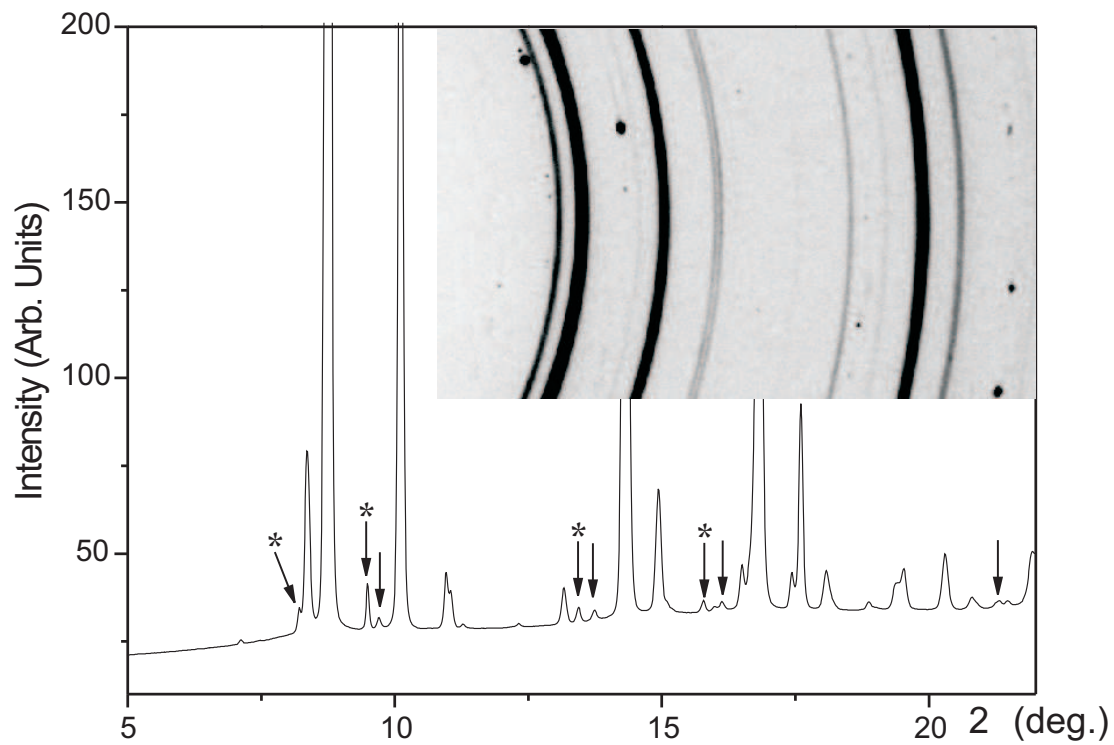


Figure 4.1: Diffraction pattern from the *d-fcc* phase of Pr, collected at 10.4GPa on Station 9.5 of Daresbury SRS, using a wavelength of $\lambda=0.44397\text{\AA}$. Additional peaks arising from contamination are identified with arrows. Inset shows an enlarged segment of the 2D diffraction image, with contrast adjusted to illustrate the texture (spottiness) of the contaminant rings, which are identified with arrows. These peaks do not correspond to gasket peaks. Reproduced from Figure 3.6.

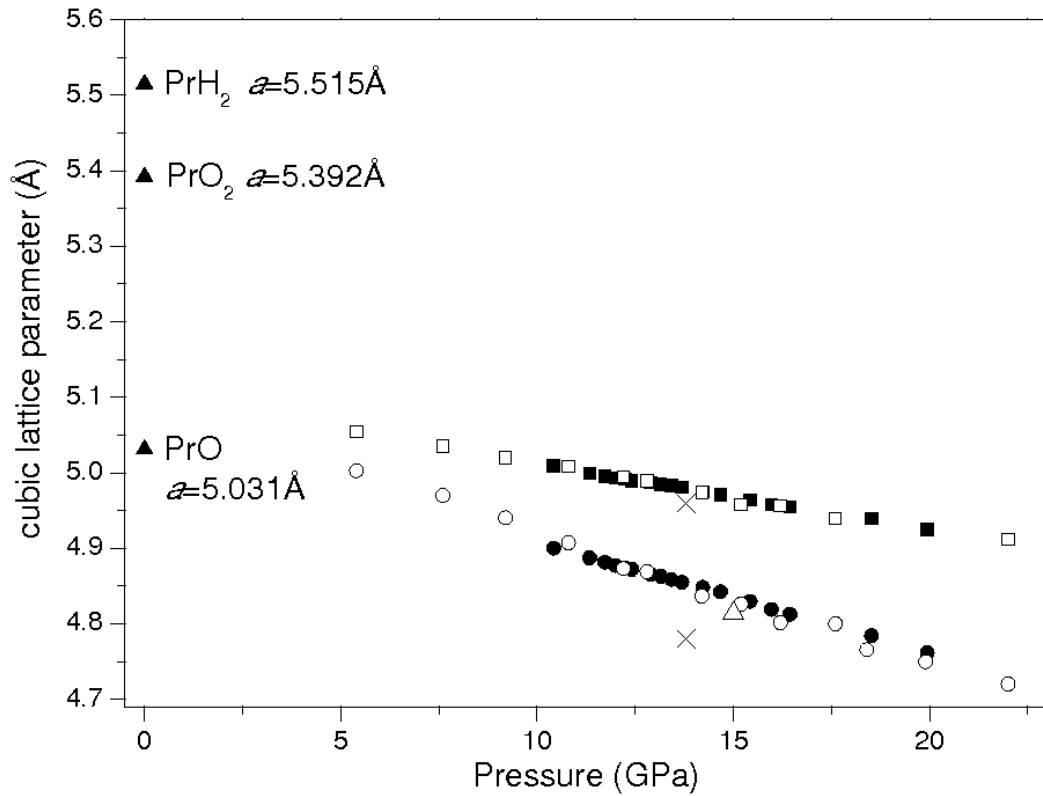


Figure 4.2: Plot of the lattice parameters (\AA) with respect to pressure (GPa) for the contaminant phases. Open symbols represent data collected on pressure decrease, and solid on pressure increase. Shown for comparison are the ambient pressure lattice parameters for PrO, PrO₂ and PrH₂, along with the measured and calculated contaminant lattice parameters from Hamaya *et al.* [Hamaya 96] (\times and $+$). The calculated lattice parameter from the study of Chesnut and Vohra [Chesnut 00b], which was incorrectly identified as a sample reflection is denoted with a \triangle . Figure modified from Evans *et al.* [Evans 09].

pressure lattice parameters of other Pr containing oxides and hydrides (PrO₂ has $a_0 = 5.392\text{\AA}$ and PrH₂ has $a_0 = 5.415\text{\AA}$ [Baer 03]).

The identity of the second contaminant, which has a back-extrapolated lattice parameter of $a_0 \approx 5.1\text{\AA}$ remains unknown, as the determined a_0 does not correspond to the ambient pressure lattice parameter values for PrO₂, PrH₂ and PrOH.

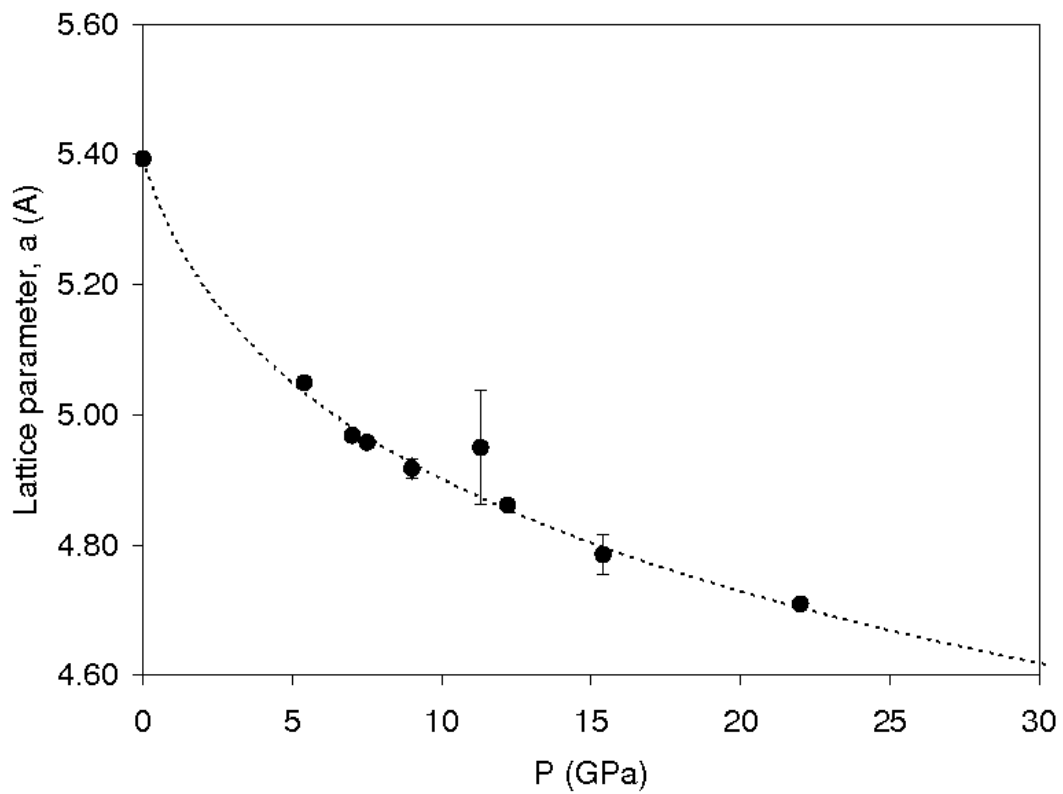


Figure 4.3: Plot of cubic lattice parameter (\AA) with respect to pressure (GPa) for the first contaminant phase. Shown for comparison is the dashed line, which represents the fitted EoS for the contaminant. Error bars are plotted on all points, but only visible for three, the size of the symbols use to plot the data points obscure the error bars for the other points.

4.4 Praseodymium at relatively low pressures (0 - 7GPa)

Although the *d-fcc* phase is of primary importance in this study, diffraction data must be collected from the phases prior to the *d-fcc* phase so that the behaviour of these phases can be confirmed, and the pressure evolution of the contaminant and the transition pressures compared to the literature. A waterfall plot of integrated patterns, representative of the data collected in this range (0-7GPa), is displayed in Figure 4.6, Figure 4.4 shows a waterfall plot of integrated diffraction patterns from Pr over a broader pressure range (0-23GPa).

At ambient-pressure the sample is observed to be in the *dhcp* phase, space group $P6_3/mmc$, as expected. This *dhcp* phase was Rietveld refined using initial unit cell parameters present in the literature (unit cell parameters taken from literature at pressures approximately equal to those of collected data). These refinements are exemplified by the Rietveld refinement shown in Figure 4.5, the data for which was collected at 1GPa. At 1GPa Pr has $a = 3.607\text{\AA}$, $c = 11.624\text{\AA}$. Unit cell parameters are restated, with atomic volume and $\frac{c}{a}$ ratio, in Table 4.1. The relatively flat residuals plot (lower line) in Figure 4.5 indicates the quality of the fit, a $R_{wp} = 4.71\%$ is given by Jana2000 [Petricek 00].

The atomic displacement parameters, ADPs, (occasionally referred to in the past as thermal parameters) from each of the Rietveld refinements made are presented in the associated tables for each refinement (quoted as U_{iso} , the isotropic ADP). The mean square displacement of an atom about its equilibrium position (in addition to static displacive disorder) are accounted for by ADPs, which are modelled in various approximations using Gaussian functions [Trueblood 96]. The validity of the ADPs is suggested by the author as being questionable, as evidenced by the negative values of some ADPs observed in the data collected for this work. Negative ADPs are non physical, implying the Gaussian function which approximates them has negative width. The ADPs, in these cases can be viewed merely as additional refinable parameters which compensate for errors in other refinable parameters, such as preferred orientation (texture in diffraction pattern) or microstructure in the sample.

On pressure increase, the *dhcp* phase was observed as a pure phase at 1.7GPa, limited diffraction data were collected before transition to the *fcc* phase, the *dhcp* phase is seen to co-exist with the *fcc* phase up to 5.1GPa. The transition to the *fcc* phase is completed by 5.4GPa, on pressure increase above 5.4GPa, collected diffraction patterns

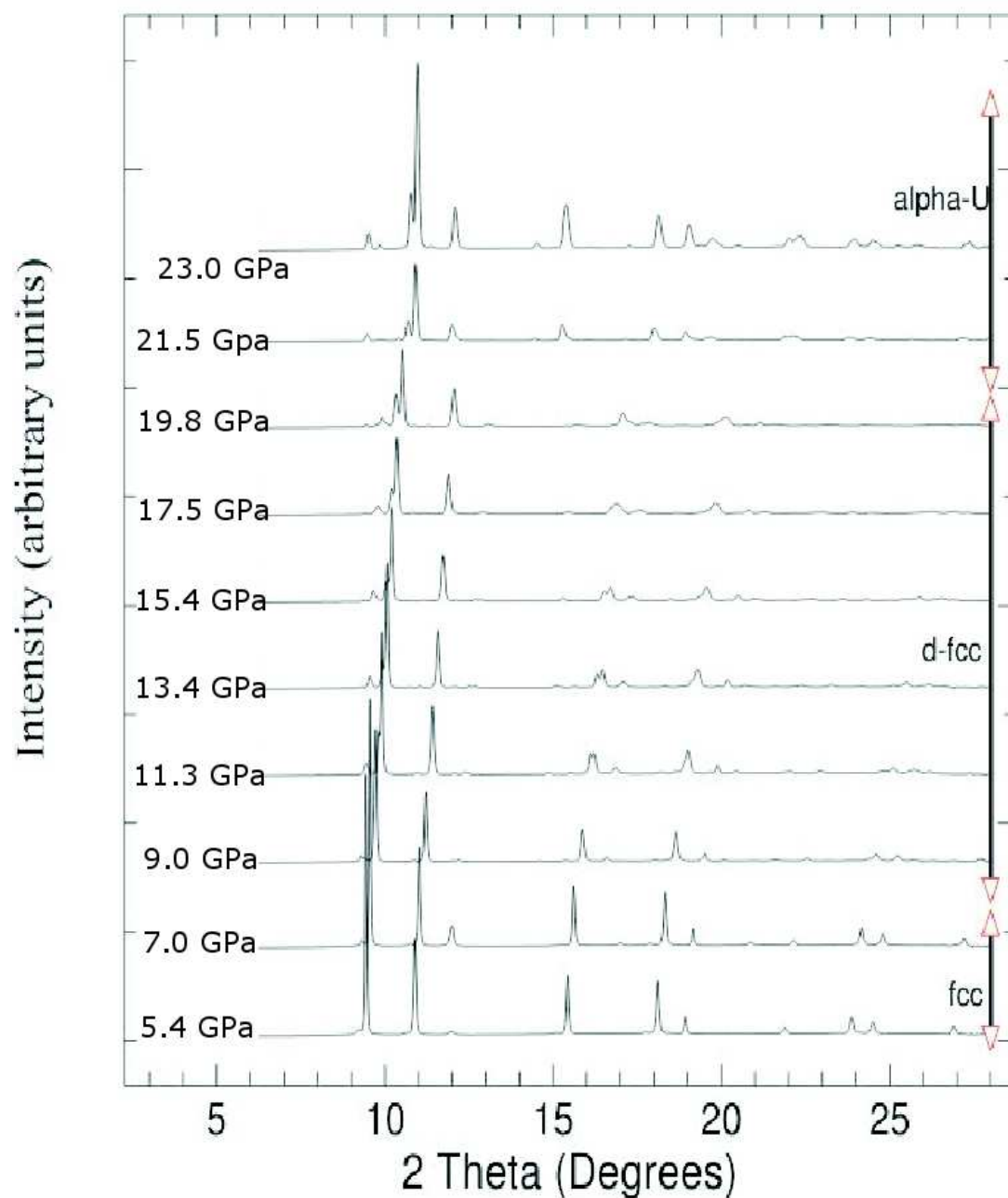


Figure 4.4: Integrated diffraction patterns collected from Pr loaded in a MB DAC, with dry mineral oil pressure medium, plotted as I vs. 2θ . Diffraction patterns are stacked in increasing pressure, with pressures indicated on the left hand side of each plot, the phase name is displayed on the right hand side of the figure, with arrow heads indicating where the transition occurs (on pressure increase). Data were collected using MB DACs with culets of $300\mu\text{m}$ on Station 9.5 of Daresbury SRS, using a wavelength of $\lambda=0.44397\text{\AA}$.

Parameter	Value
a	3.607Å
c	11.624Å
Volume	32.743Å ³
$\frac{c}{a}$	3.223

Table 4.1: Table showing the Rietveld refined unit cell parameters for the *dhcp* phase of Pr, data corresponds to the refinement shown in Figure 4.5 at a pressure of 1GPa, collected using a wavelength of $\lambda = 0.4654\text{\AA}$ on Station 9.1 of Daresbury SRS.

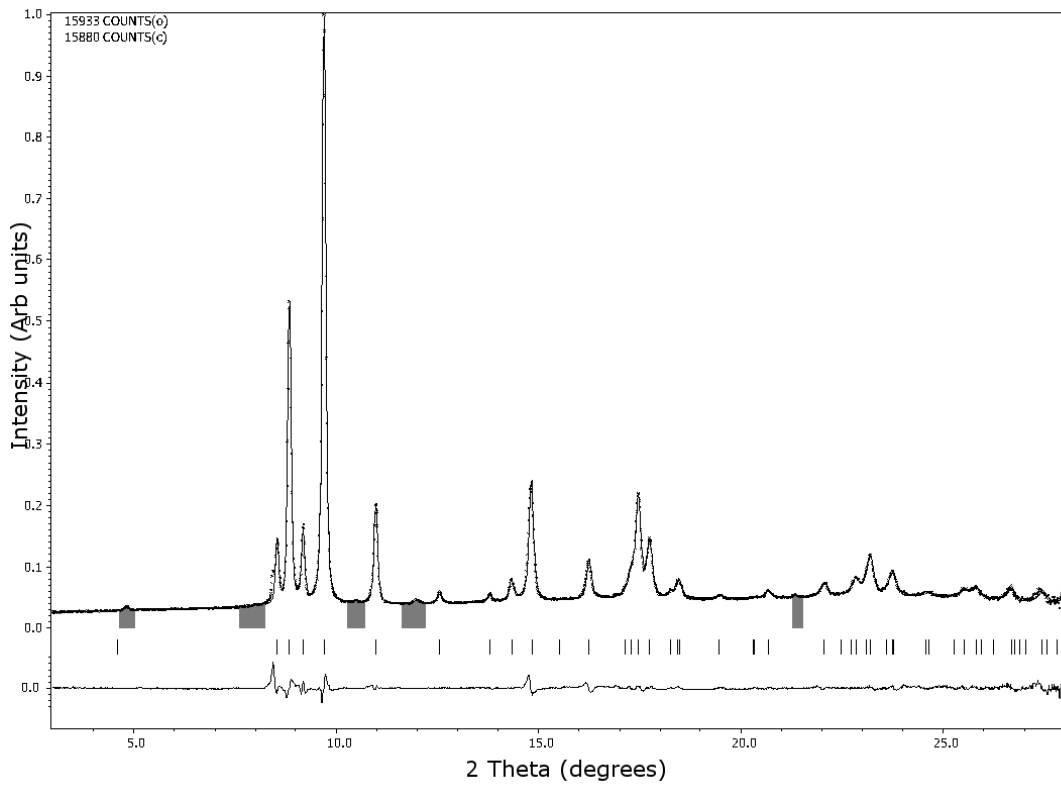


Figure 4.5: Example refinement of Pr in the *dhcp* phase, collected at 1GPa on Station 9.1 of Daresbury SRS using $\lambda = 0.4654\text{\AA}$, mineral oil pressure transmitting media. A MB DAC with $300\mu\text{m}$ culets was used to collect the data.

Parameter	Value
a	4.8220(1) Å
Volume	28.02933(11) Å ³
$\frac{c}{a}$	1 (2.449 in hexagonal setting)
U _{iso1}	0.0443
U _{iso2}	0.0252

Table 4.2: Table showing the Rietveld refined unit cell parameters for the *fcc* phase of Pr, data corresponds to the refinement shown in Figure 4.7 at a pressure of 7GPa, collected using a wavelength of $\lambda = 0.44397\text{Å}$ on Station 9.5 of Daresbury SRS. Atomic positions refined, but round to regular *fcc* values.

contain only peaks originating from the *fcc* (and contaminant) phase. The transition from *dhcp* to *fcc* can be said to occur between 1.7 and 5.1GPa, in agreement with the reported transition pressures of 4GPa [Tonkov 05] and 3.9GPa [Gschneider 68]. Observed however, is a larger degree of co-existence between the *dhcp* and *fcc* phases than is noted in the literature.

A plot of diffraction patterns for the pressure range 1.7 to 7GPa is shown in Figure 4.6. Data for this plot comes from angle dispersive x-ray diffraction experiments made at successive pressure points within this range over a number of experiments at Stations 9.5 and Station 9.1 of Daresbury SRS, on pressure increase.

The *fcc* phase is observed to co-exist with the pre-cursor *dhcp* phase up to 5.1GPa, and seen to be a pure phase from 5.4GPa (with contaminant peaks). Upon further pressure increase the *fcc* phase is observed, with evidence of the following phase, the *d-fcc* phase, from 7.0GPa (with asymmetry observed in the (111) and (200) reflections) which appears completed by 7.4(2)GPa (additional peaks observable in integrated diffraction patterns). The transition from the *fcc* phase to *d-fcc* phase will be considered in greater detail in the following section, Section 4.5.

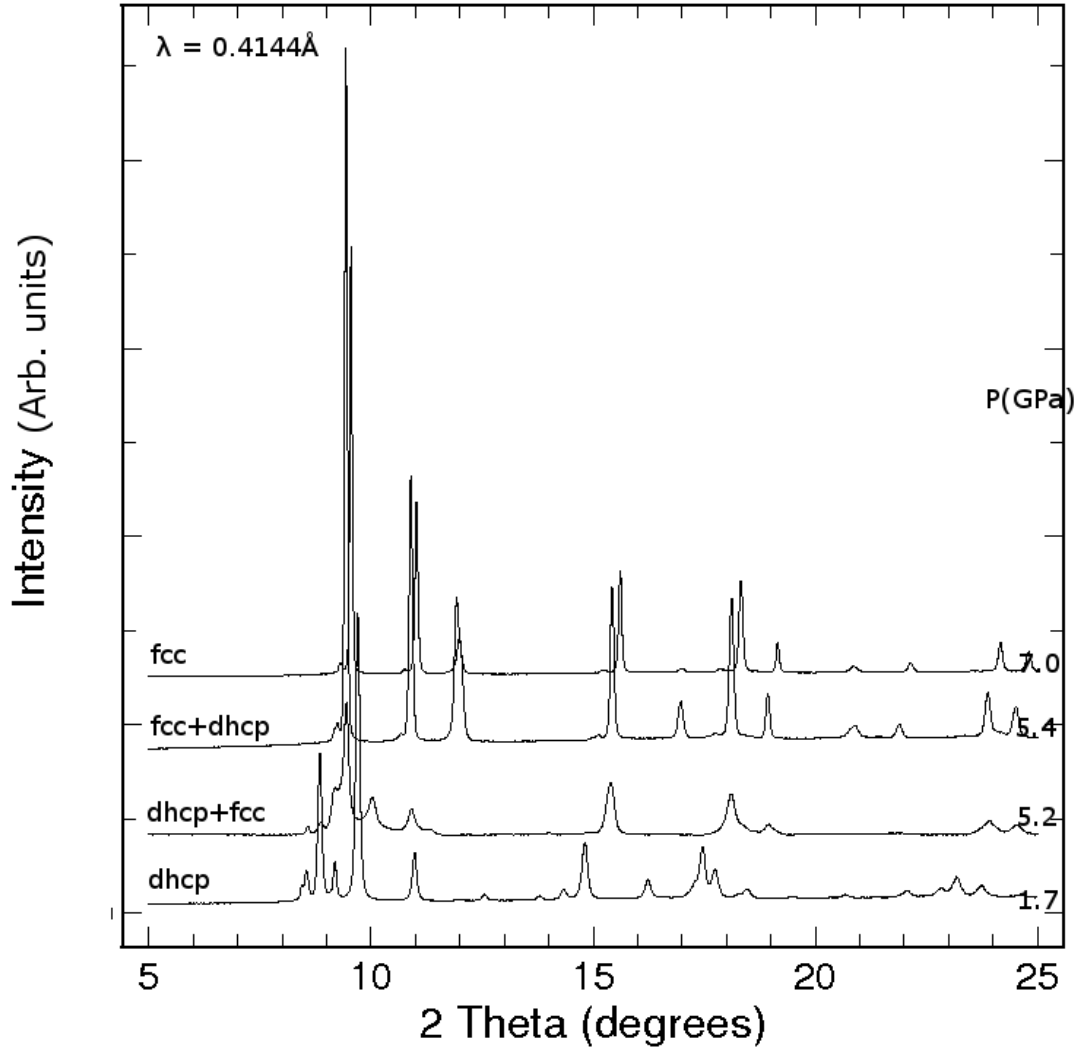


Figure 4.6: Plot of diffraction patterns for Pr between 1.7 and 7.0GPa. The transition pressure from *dhcp* to *fcc* is shown to occur between 1.7 and 5.4 GPa, with the shown intermediary pressure (5.2GPa) showing a mixed phase. The phase of each integrated diffraction pattern is noted on the left of the figure.

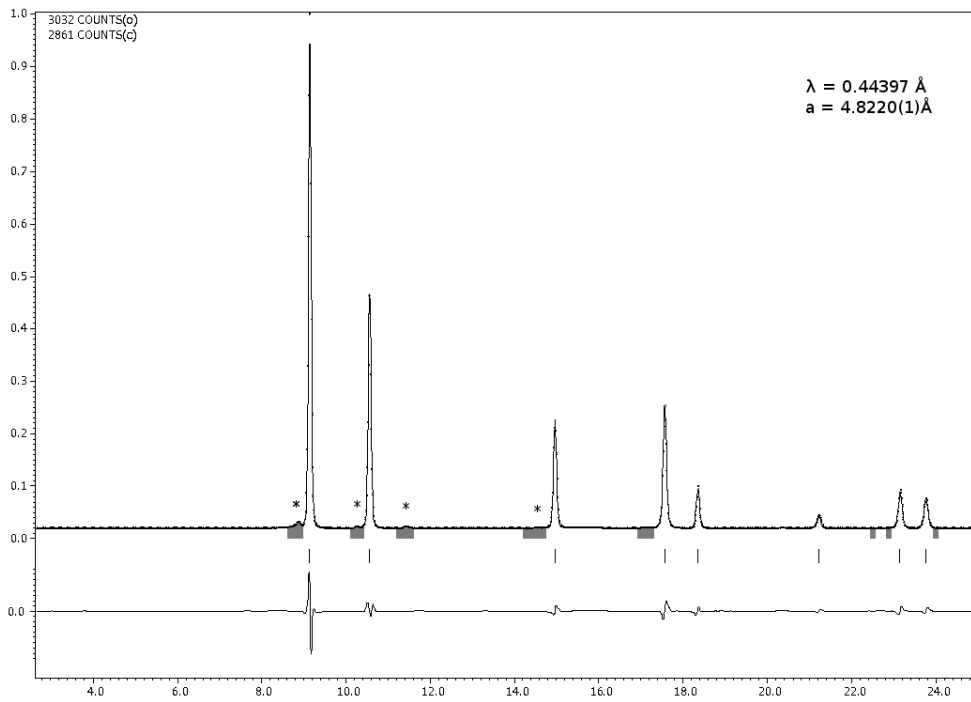


Figure 4.7: Example Rietveld refinement of Pr in the *fcc* phase. The sample pressure is 7.1(2)GPa, diffraction pattern was collected on Station 9.5 of Daresbury SRS using $\lambda = 0.44397 \text{ \AA}$ at room temperature. A MB-type cell with culets of size $300 \mu\text{m}$, ruby sphere manometer and mineral oil pressure medium were used. Peaks labeled with asterisks correspond to contaminant peaks.

4.5 *d-fcc* of Praseodymium from 7-14GPa

At 7.4(2)GPa the first indications of a transition to the *d-fcc* phase are observed in the splitting of the (111) and (200) *fcc* reflections. Slight asymmetry can be observed in these peaks from 7.0GPa, and at 7.4(2)GPa appearing as a resolvable shoulder, as shown in Figure 4.8. In addition to the splitting of *fcc* reflections, peaks appear at the transition pressure at 15.45, 19.21, 13.98 and 20.65° in 2θ , leaving no doubt that the symmetry of the precursor *fcc* phase has been lowered, indicating a change in phase of the sample. As the pressure increases above 7.4(2)GPa, the angular separation of the shoulders from the *fcc* increases to a maximum of 0.12°, and the intensity of the additional reflections increases.

The observed transition pressure of 7.4(2)GPa (average of compression and decompression cycles, due to large hysteresis in observed transition pressures) from *fcc* \rightarrow *d-fcc* is in excellent agreement with the value of 7.0GPa reported in the literature [Mao 81, Dmitriev 00, Holzapfel 95]

Plotting the Pr diffraction data on a succession of waterfall plots, it seems plausible that, as suggested by a number of authors [Mao 81, Dmitriev 00], a transition occurs within the *d-fcc* region at approximately 14GPa. It is at 14GPa that a number of subtle changes occur to the diffraction pattern (see Figure 4.17), suggesting a transition between two closely-related structures. For this reason, the structure of Pr from 7-14GPa will be considered first. The structure from 14-20GPa, along with a more detailed explanation of the evidence for the transition, will be presented in Sections 4.7 and 4.8.

In order to ascertain a structure for the lower region (7-14GPa) of the *d-fcc* phase, attempts were made to fit the collected data using all structures proposed in the literature, these structures are the *hP6* (space group $P3_121$), *hR24* (space group $R\bar{3}m$) and *mC4* (space group $C2/m$). These structures are shown, in relation to the precursor *fcc* phase (as the transition from *fcc* to *d-fcc* is a transition between two structures related by a static distortion) in Figure 4.9. Starting with the *hP6* (*thcp*, or triple-*hcp*) structure, proposed as a model for the *d-fcc* phase of Pr through association with Ce by Smith and Akella [Akella 86], and closely related to the *hP3* proposed by Grosshans *et al.* [Grosshans 82].

The *hR24* structure (hexagonal unit cell equivalent of the $R\bar{3}m$ structure) proposed

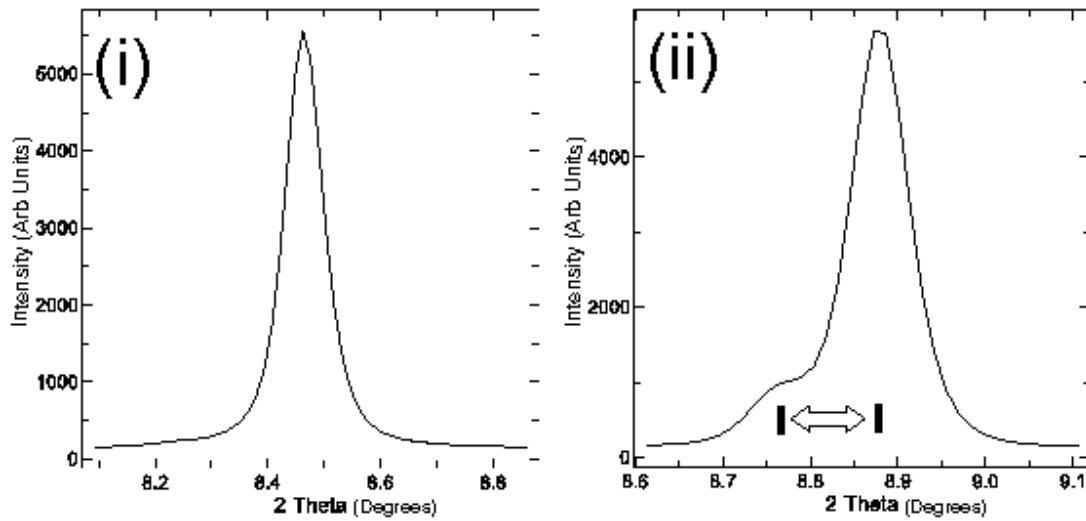


Figure 4.8: Comparison of the (111) reflection from (i) *fcc* pattern, collected at 6GPa and (ii) *d-fcc* pattern collected at 7.4GPa. Shown in (ii) is the reflection that splits from the (111) *fcc* upon pressurisation into the *d-fcc* phase, the maximal splitting is shown here, which is approximately 0.1° . Both patterns were collected from the same sample on pressure increase, at Station 9.5HPT of Daresbury SRS with a wavelength of $\lambda=0.44397\text{\AA}$.

by Hamaya *et al.* [Hamaya 93] and others [Chesnut 00b, Baer 03, Dmitriev 03], is stated as having unit cell parameters of 6.466 and 16.085\AA at 7GPa. Re-examining collected data at an equivalent pressure, using these values as a starting model for Rietveld refinements yields Figure 4.10. Atomic positions provided by Hamaya *et al.* [Hamaya 96], who stated atoms occupy the $6c$ and $18h$ positions. The group-subgroup relation of the $hR24$ solution to the *fcc* precursor phase enabled the construction of a transformation matrix relating the two phases. Using the transformation matrix

$$\begin{pmatrix} a' \\ b' \\ c' \end{pmatrix} = \begin{pmatrix} -\frac{1}{2} & 0 & 1 \\ \frac{1}{2} & -\frac{1}{2} & 1 \\ 0 & \frac{1}{2} & 1 \end{pmatrix} \begin{pmatrix} a \\ b \\ c \end{pmatrix}$$

it was determined that the atoms in the $hR24$ unit cell lay in the $6c$ and $18h$ sites. Use of the Bilbao Crystallographic Server's WYKSPLIT application [Kroumova 98] confirms this calculation and Hamaya *et al.*'s stated atomic positions, by showing atoms from the $4a$ atomic sites in *fcc* go to the $6c$ and $18h$ sites upon transformation to the $hR24$ unit cell. At 7.4GPa this yields atomic positions of $(0, 0, \frac{1}{4})$ and $(\frac{1}{2}, -\frac{1}{2}, \frac{1}{4})$ respectively for the $6c$ and $18h$ sites.

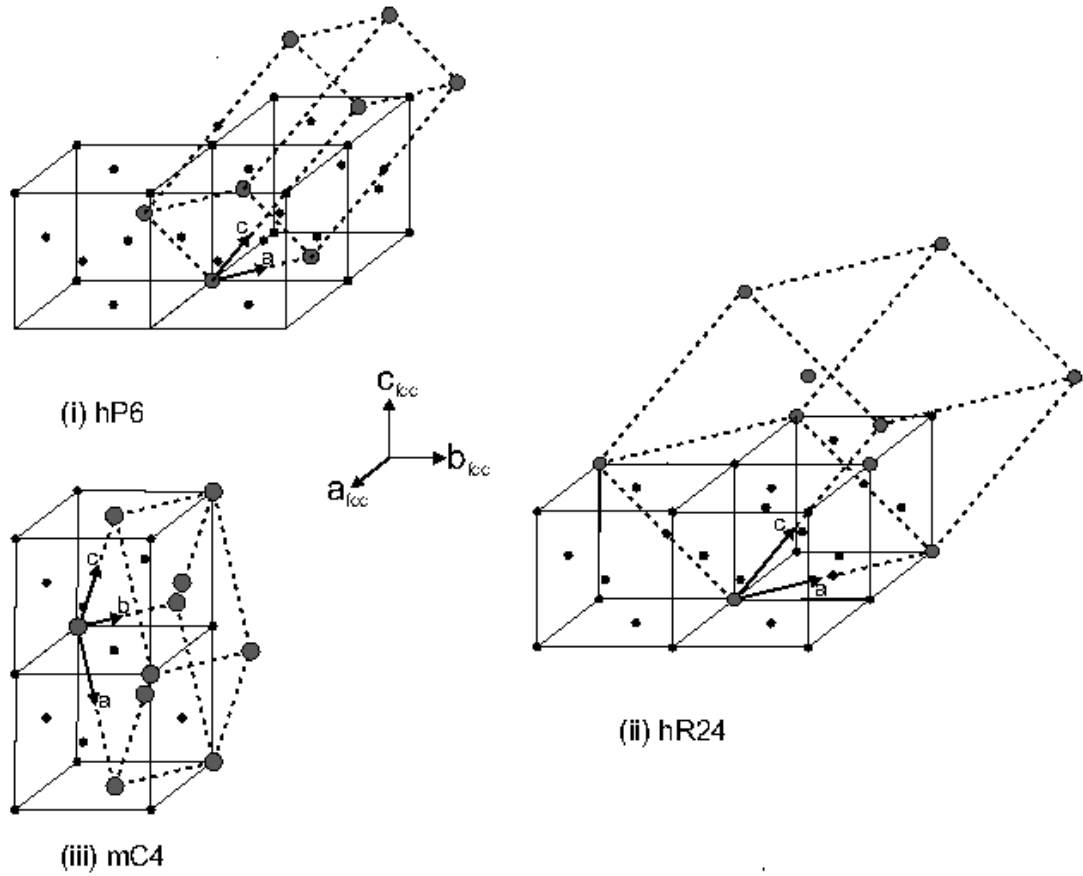


Figure 4.9: Comparison of the *hP6*, *hR24* and *mC4* structures which have been suggested as solutions for the *d-fcc* phase with the precursor *fcc* phase. Shown in (i) is the *hP6* structure, in (ii) the *hR24* structure and in (iii) the *mC4* structure. The *fcc* unit cells are shown with smaller, black circles joined by solid black lines, the respective proposed *d-fcc* solutions have atoms in their unit cell shown with larger, grey circles, joined by dashed lines. The crystallographic axes (*a*, *b* and *c*) for the *fcc* and *d-fcc* are noted on each diagram.

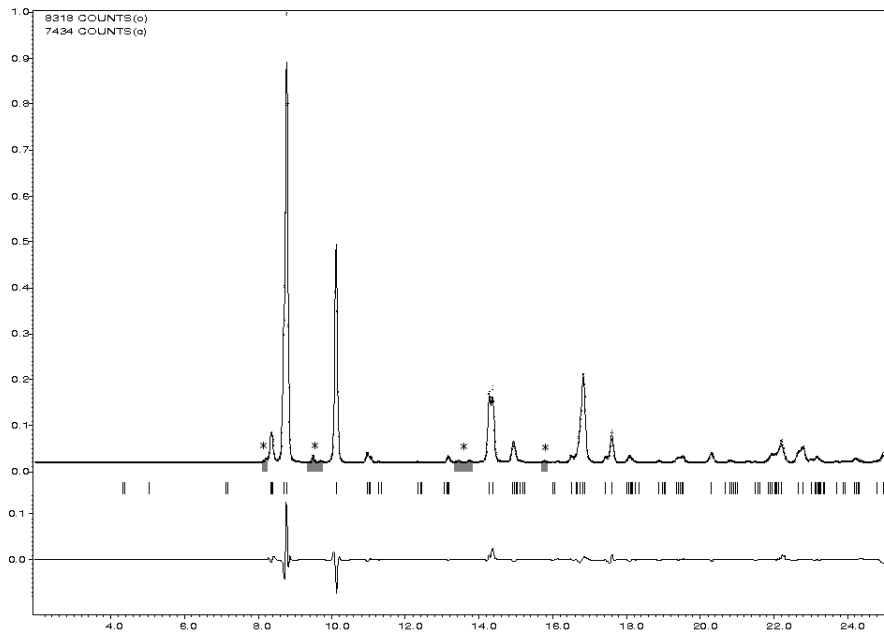


Figure 4.10: Rietveld refinement of Pr in *d-fcc* phase at 10GPa using the *hR24* structure. From Rietveld refinement, the unit cell parameters are given as: $a=6.6284(1)$, $c=16.3991(6)\text{\AA}$, $\text{Vol./atom}=25.9990(11)\text{\AA}^3$. Atomic positions: $z_1=0.2698(3)$, $x_2=0.5053(3)$, $y_2=-x_2$, $z_2=0.2444(4)$. Data was collected on Station ID09A of ESRF using a wavelength of $\lambda=0.414412\text{\AA}$.

Using the above atomic positions, and accounting for the position of contamination peaks (labelled with asterix), the quality of the fit, indicated by the difference plot beneath the profile (Figure 4.10), is excellent, with all peaks accounted for and only minor discrepancies in the intensities of peaks. For this refinement (Figure 4.10), Jana2000 [Petricek 00] quotes the refinement to have $R_{wp}=6.41\%$ and $\chi^2=0.21$.

It can be seen how the *hP6* structure, while being able to account for all of the peaks observed, has a high degree of peak overlap, and zero intensity reflections, which account for the main features of the diffraction pattern, but suggest a higher symmetry solution is possible. Given the study of Grosshans *et al.* did not have access to the resolution or intensity currently afforded to science at synchrotron radiation sources, it is surprising that Grosshans model is a substructure of the lower pressure *d-fcc* structural solution, *hR24*.

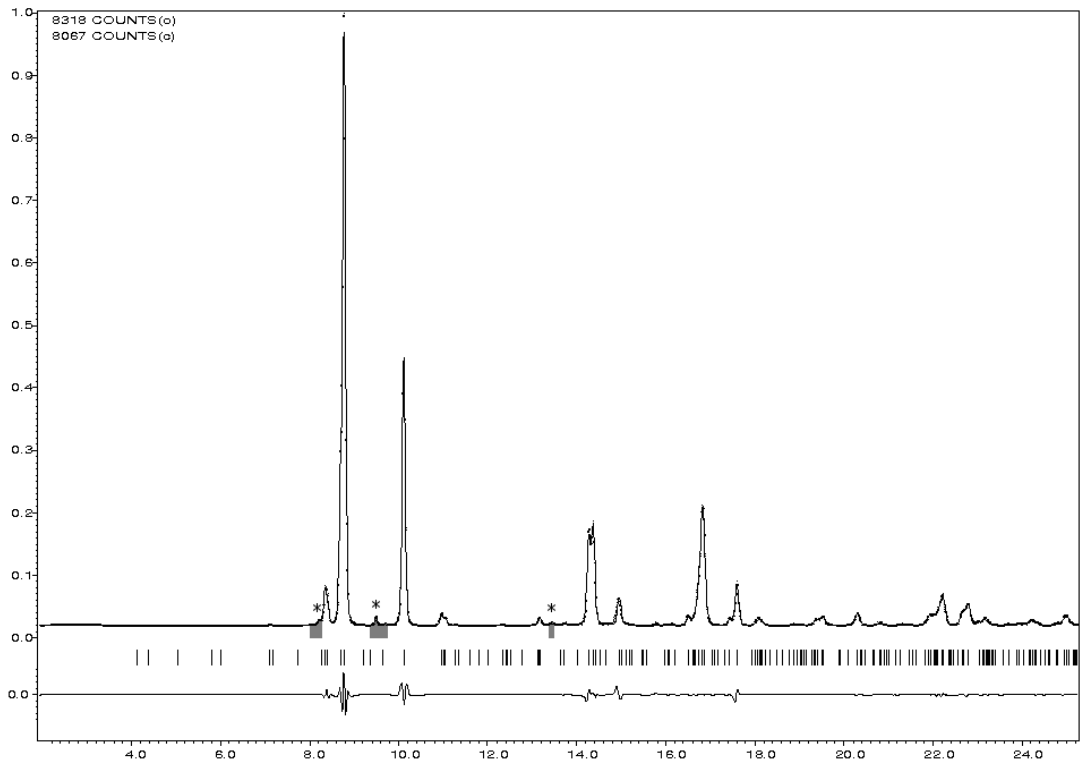


Figure 4.11: Refinement of Pr in *d-fcc* phase at 10GPa using the *hP6* structure. From the refinement the unit cell parameters are given as: $a=6.6295(8)\text{\AA}$ and $c=16.4045(5)\text{\AA}$. Data collected on ID09A of ESRF, Grenoble using a wavelength of $\lambda=0.414412\text{\AA}$. Contaminant peaks are observed and labelled in the figure with asterisks.

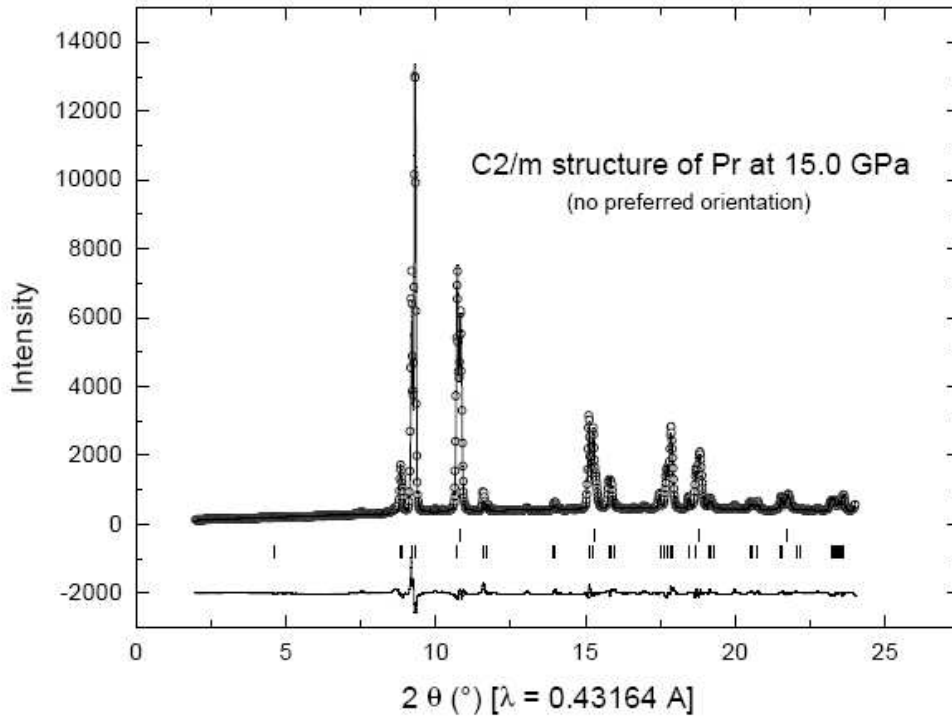


Figure 4.12: Figure showing a refinement of $C2/m$ to a sample of Pr collected at 15GPa on ID09a of the ESRF, Grenoble. Upper tick marks correspond to the refined peak positions from Ta (pressure calibrant), the lower tick marks to refined peak positions from Pr. Figure is reproduced from Syassen *et al.* [Syassen 00].

The validity of the $C2/m$ structure proposed by Syassen *et al.* [Syassen 00] as a solution for the d - fcc phase of Pr was also investigated. Syassen *et al.* observe the transition from fcc to d - fcc to occur at 7.5GPa (in agreement with this work), and suggest the $C2/m$ structure, based on observation of a triplet becoming resolved at 13GPa in the (111) equivalent fcc reflection and from relation to Ce (which exhibits a $C2/m$ structure). Presented in Syassen *et al.* [Syassen 00] is a Figure showing a diffraction pattern of Pr collected at 15GPa (reproduced in Figure 4.12), stated to have a $R(F^2) = 11.4\%$. It is, however, evident from this figure that a peak at 20° is unaccounted for by the $C2/m$ structure. A refinement using the $C2/m$ structure, to a pattern of Pr collected at 10GPa is shown in Figure 4.13, evident from the refined diffraction pattern is a high degree of peak overlap, most of which have zero intensity, suggesting a higher symmetry solution can be found for the d - fcc structure of Pr below 14GPa.

The $hR24$ structure can thus be considered as the structure that best describes the

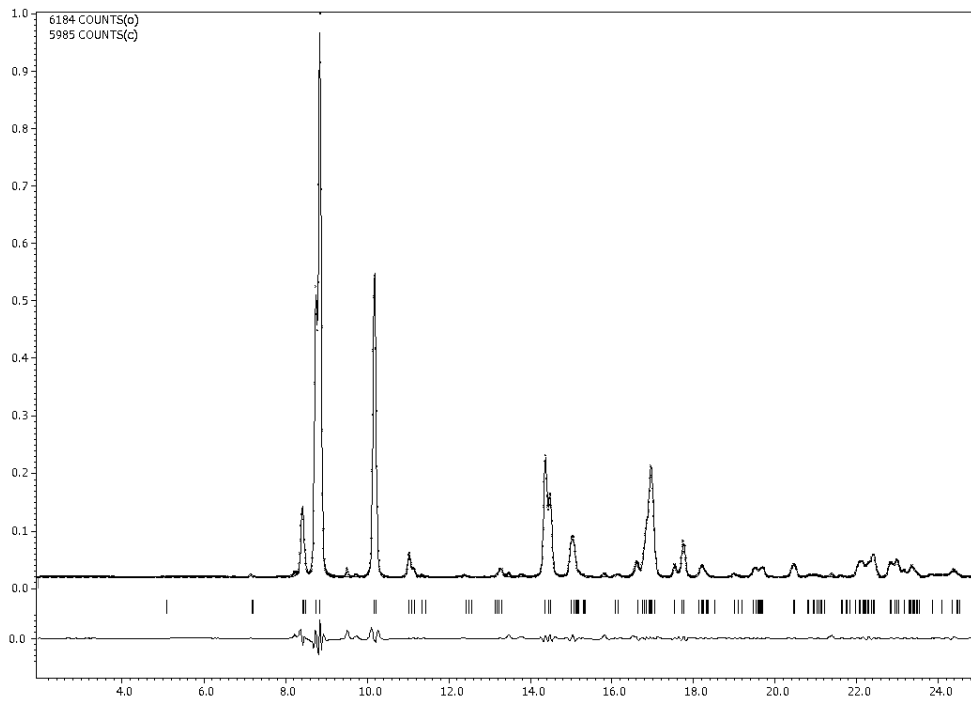


Figure 4.13: Refinement of Pr at 10GPa using the $C2/m$ structure. Unit cells parameters are given as: $a = 5.7510(2)$, $b = 3.2924(2)$ and $c = 5.6817(3)\text{\AA}$. Data was collected on Station 9.5 of Daresbusy SRS using a wavelength of $\lambda=0.44397\text{\AA}$

Parameter	Value
a	6.6284(1) Å
c	16.3991(6) Å
Volume	25.9990(11) Å ³
$\frac{c}{a}$	2.4741
z ₁	0.2698(3)
x ₂	0.5053(3)
z ₂	0.2444(4)
U _{iso1}	0.0186
U _{iso2}	0.0195

Table 4.3: Table showing the Rietveld refined unit cell parameters for the $hR24$ phase of Pr, data corresponds to the refinement shown in Figure 4.10 at a pressure of 10GPa, collected using a wavelength of $\lambda = 0.414412\text{Å}$ on Station ID09A of ESRF.

d - fcc phase for the pressure range 7-14GPa. The structural parameters refined from Figure 4.10 for the $hR24$ phase are summarised in Table 4.3.

4.6 Pressure dependence of $hR24$ 7-14GPa

Having established that the $hR24$ structure best describes the lower range of the d - fcc phase in Pr, 7-14GPa, the pressure dependence of this structure will be presented in this subsection.

Rietveld refinements were performed on each integrated diffraction pattern collected within the 7-14GPa pressure range to ensure the quality of fit does not significantly degrade with increasing pressure (as measured using the internal fitting parameters, R_{wp} and χ^2 in Jana2000). A plot of atomic volume vs. pressure is presented in Figure 4.14, which shows a smooth, non-linear decrease in atomic volume, indicating a decrease in the compressibility of the $hR24$ phase with increasing pressure.

The c/a ratio (axial ratio) for the $hR24$ structure is plotted for increasing pressure in Figure 4.15. The datapoint at 7GPa is shaded in a different colour, corresponds to the c/a ratio of the fcc unit cell at 7GPa transformed into the $hR24$ unit cell using the relations from earlier (Equation 4.5). For the fcc phase, the c/a ratio is constant at $\sqrt{6}$. Upon transformation to the $hR24$ unit cell, as can be seen in Figure 4.15, there is a sharp increase in c/a away from the ideal $\sqrt{6}$ fcc value at the $fcc \rightarrow d$ - fcc transition, this ratio levels off as the pressure approaches 14GPa, approaching a value of 2.485 at 13.5GPa.

In the precursor fcc phase, atoms are located on the $4a$ site, with atomic positions fixed at $(0, 0, 0)$ from Rietveld refinement of the collected fcc patterns. Transformation of these atomic coordinates to the $hR24$ setting (using the transformation matrix from Equation 4.5) yields atomic positions of $(0, 0, \frac{1}{4})$ and $(\frac{1}{2}, -\frac{1}{2}, \frac{1}{4})$. The $6c$ and $18h$ sites have positional freedom in $(0, 0, z)$ and $(x, -x, z)$ respectively. Thus deviation of the atomic position within the $hR24$ relative to the fcc positional values, which provides a measure of the distortion of the fcc lattice, can be determined. These deviations are plotted in Figure 4.16, and correspond to the displacement parameters presented by Hamaya *et al.* in [Hamaya 93] who uses the notation ϵ , δ_1 and δ_2 to represent the static displacements ($\epsilon = x - \frac{1}{2}$), z_1 ($\delta_1 = z_1 - \frac{1}{4}$) and z_2 ($\delta_2 = z_2 - \frac{1}{4}$). It can be seen from Figure 4.16 that the distortions away from the fcc phase are approximately 3x larger for the displacement parameter δ_1 than for δ_2 and ϵ (the latter two share approximately equal values). This is, as stated by Hamaya *et al.*, because of “interrelations between the amplitudes of atomic displacements given by a linear combination of three, zone-boundary TA phonon modes”. These phonons can be expressed with the following

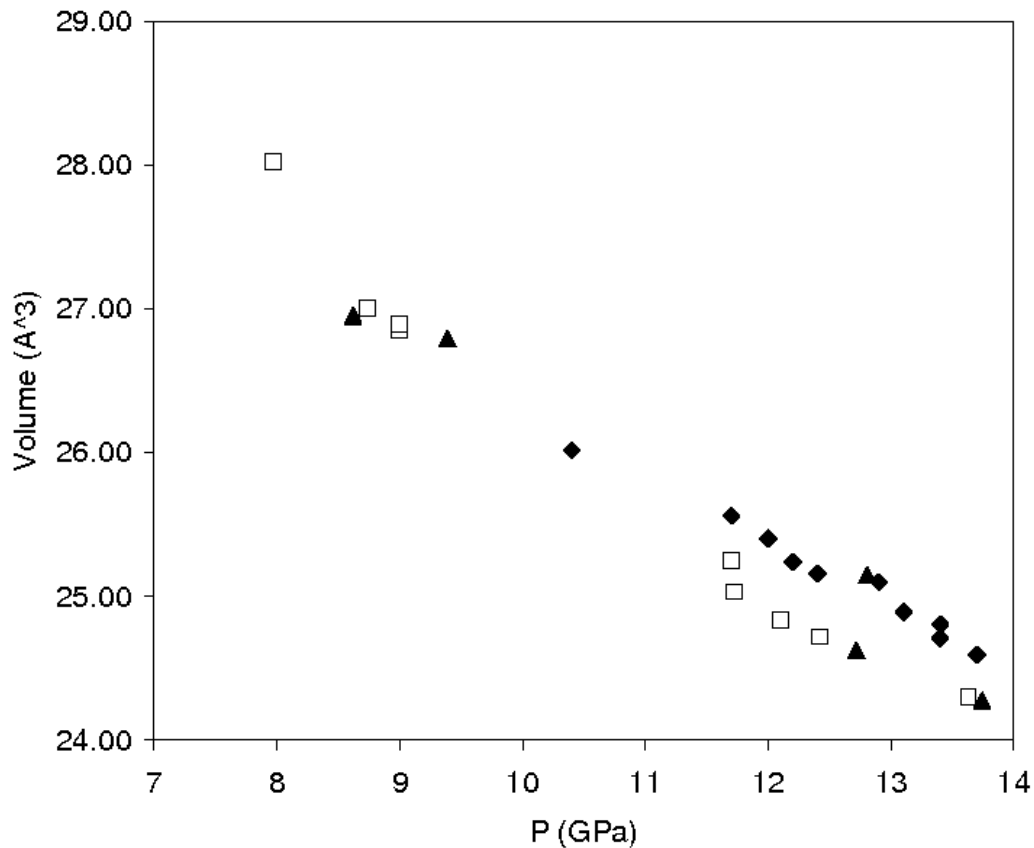


Figure 4.14: Plot showing variation of atomic volume vs. pressure for the stability range of the $hR24$ d - fcc structure of Pr. Errors bars corresponding to errors in volume and pressure (estimated) are omitted, as they are obscured by the symbols used to plot the data. Filled symbols represent data collected on pressure increase, open symbols represent data collected on pressure decrease. Different symbol shapes represent data collected during different experiments at Station 9.5 HPT of Daresbury SRS. A wavelength of $\lambda=0.44397\text{\AA}$ was used for collection of this data.

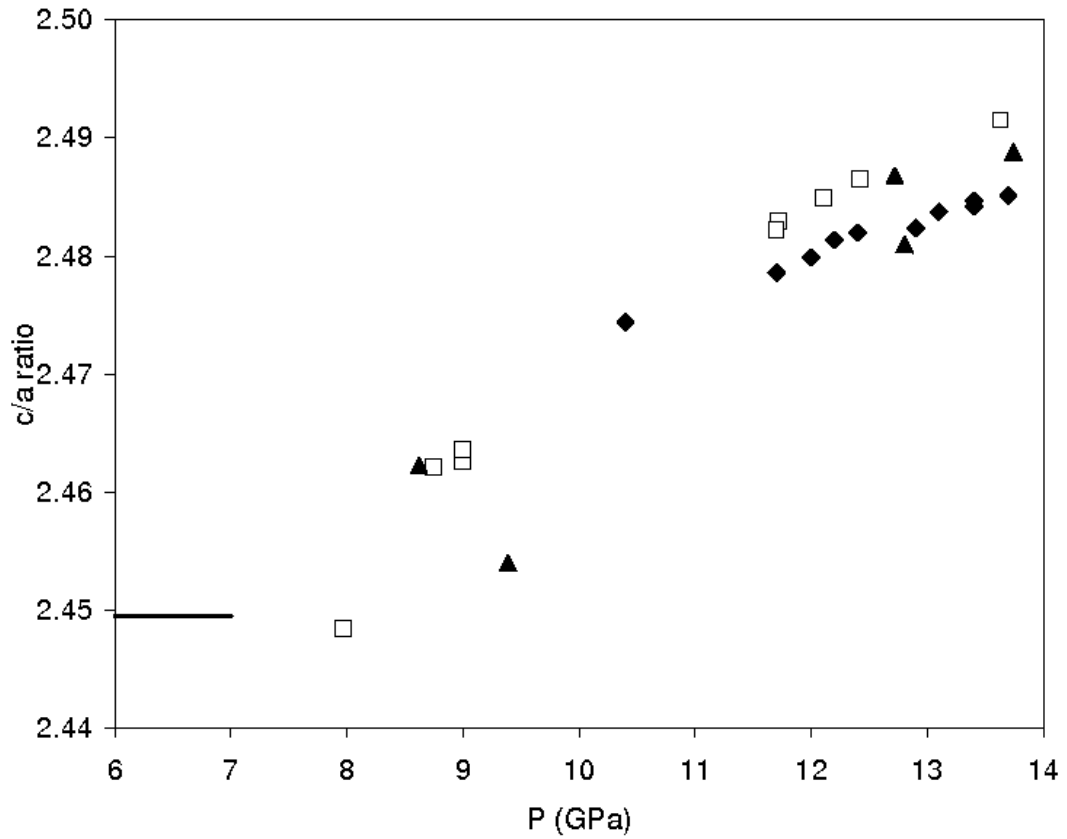


Figure 4.15: Axial ratio, c/a , plotted as a function of pressure for the $hR24$ structure between 7 and 14GPa in Pr. Datapoints for this graph originate from multiple datasets, collected at different times on different beamlines. Error bars are plotted on this figure, but are obscured by the size of the data points. The straight line represents the c/a ratio for the fcc unit cell transformed into the hexagonal setting. Open symbols represent data collected on pressure decrease, filled symbols represent data collected on pressure increase with the different filled symbols corresponding to data collected during different experiments.

wavevectors, in the *fcc* structure:

$$(4.1) \quad \mathbf{q}_1 = \frac{2\pi}{a_0} \left(\frac{1}{2}, \frac{1}{2}, -\frac{1}{2} \right), \quad \mathbf{q}_2 = \frac{2\pi}{a_0} \left(-\frac{1}{2}, \frac{1}{2}, \frac{1}{2} \right), \quad \mathbf{q}_3 = \frac{2\pi}{a_0} \left(\frac{1}{2}, -\frac{1}{2}, \frac{1}{2} \right)$$

Each of these curves (Figure 4.16), as in Hamaya *et al.* [Hamaya 93], can be modelled using a least squares refined power law, $A(P - P_c)^\beta$ with A and β being refinable parameters and P_c fixed at the transition pressure of 7.4 GPa.

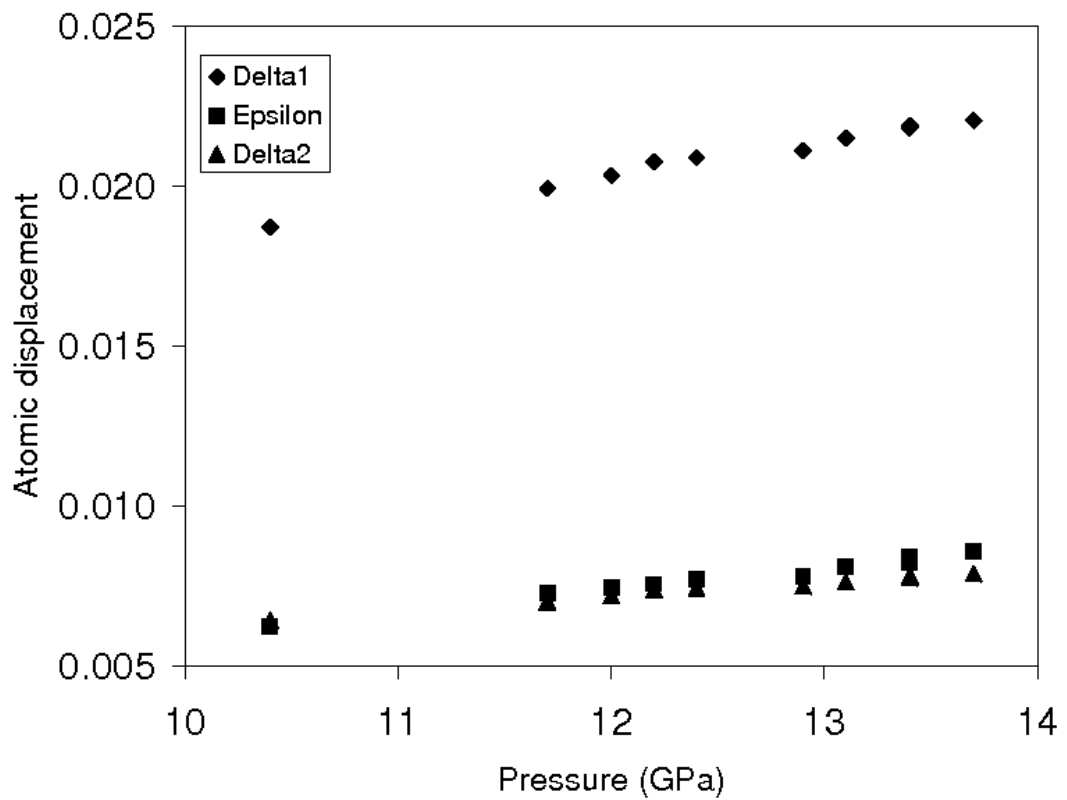


Figure 4.16: Plot of relative displacements of atomic positions in hR24 away from fcc positions as a function of pressure. Labels ϵ , δ_1 and δ_2 are used, as from Hamaya *et al.* [Hamaya 93]. Error bars are too small to be seen.

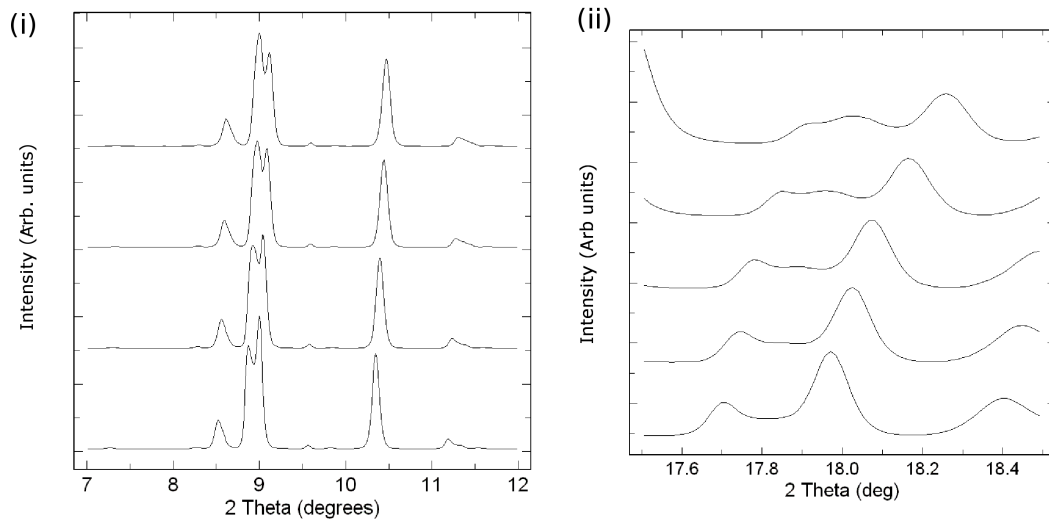


Figure 4.17: Waterfall plot showing the switching in relative intensities of (i) the 8-10° doublet, and (ii) the doublet around 17-18°, between which an additional peak appears. Data for (i) and (ii) were collected on pressure increase at Station 9.5 of Daresbury SRS, using a wavelength of $\lambda=0.44397\text{\AA}$

4.7 Transition at 14GPa

A subtle but noticeable change occurs in the integrated 1D diffraction profiles of *d-fcc* Pr at 14GPa, as noted by Dmitriev et al. [Dmitriev 00]. A doublet, containing the (0 0 6) and (2 0 2) highest-intensity peaks, located at $2\theta \approx 9^\circ$ on diffraction profiles from the *d-fcc* phase, exhibits the most pronounced evidence of a transition. Below 14GPa, the intensity of the first reflection of this main doublet is greater than that of the second peak of that doublet. After 14 GPa the relative intensities of these two peaks switches, so that the second peak ((2 0 2) in $R\bar{3}m$) has the greater intensity, as shown in Figure 4.17 (i). Evidence for a transition is also found at higher 2θ for a transition, shown in (ii) of Figure 4.17, whereby a new peak appears between the Bragg peaks located at 17.6° and 17.95° on the 13.9GPa diffraction profile. A higher-than-background intensity between these two peaks (17.6° and 17.95°) is indicative of the presence of a broad peak. Indeed, attempting to model this region using the peak fitting routines in Matlab requires an additional peak, at 17.5° , to account for the intensity observed. Baer *et al.* [Baer 03] have commented on a drop in the quality of fits around 14GPa, using this as evidence for a transition to a related, but new, structure. Further evidence is found at higher angles, with the intensities of peaks at $\approx 9^\circ$ and $\approx 19^\circ$ being observed to undergo the same switching of relative intensity, which is to be expected, as this is the $d/2$ analogue.

Initial attempts were made to fit data collected in the 14-20 GPa pressure range for Pr using the structures stated to be solutions for this pressure range in the literature. It was expected that, after comments made in the literature by Baer *et al.* [Baer 03], Syassen *et al.* [Syassen 00] and Dmitriev *et al.* [Dmitriev 00], that some difficulty would be encountered fitting patterns above 17GPa. This statement alone warrants detailed examination of the *d-fcc* phase above 14GPa.

As pressure is increased towards 14GPa (above 13.5GPa) the quality of the $R\bar{3}m$ refinements, as measured by comparison of Jana2000's R factors (R_{wp}) and χ^2 worsens. Tending from (examples taken from Rietveld refinements made on data collected at Station 9.5HPT of Daresbury SRS) values of $R_{wp}=0.16$ at 8GPa to $R_{wp}=0.6$ at 13GPa. This loss of fit quality approaching the transition suggests the transition to be gradual, indeed, evidence for this can be seen by the rising in intensity of the (2 0 2) reflection over a 2GPa range. Given the $R\bar{3}m$ phase has (0 0 6) with highest intensity, and the subsequent phase has the (2 0 2) as the highest intensity of the doublet (using $R\bar{3}m$ indexing), the process of the switching between these can be viewed as evidence of the coexistence of the two phases. To accurately fit the data at pressures within this 2GPa range will require modelling of the system as a mixture of both phases.

Rietveld refinements using the *mC16* structure given by Dmitriev *et al.* [Dmitriev 00] gave a good fit to the data collected above 14GPa. At 19GPa refined values for the lattice parameters are $a=10.951(1)\text{\AA}$, $b=6.2012(3)\text{\AA}$, $c=6.3817(4)\text{\AA}$ and $\beta=125.71(2)^\circ$. This refinement is shown in Figure 4.18. However, unlike the unit cell reported by Dmitriev *et al.*, which at 19GPa has lattice parameters of $a=10.984(2)\text{\AA}$, $b=6.3810(2)\text{\AA}$, $c=6.275(3)\text{\AA}$, and $\beta=126.12(1)^\circ$, the *b* and *c* lattice parameter values are reversed. Using the structure suggested by Dmitriev *et al.* [Dmitriev 00] exactly as described, with the *b* and *c* lattice parameters in reverse order to those obtained through refinement of the Station 9.5 HPT data, resulted in poor Rietveld refinements. No scientific reason for the Dmitriev *et al.*'s lattice parameter difference can be found, a typographical error is suggested as a likely cause. The obtained R factors, when the lattice parameters used in the order Dmitriev *et al.* state, are much greater than those found from direct refinement of the Station 9.5 HPT data, further, more substantial misfits arise in the difference plot. This is shown in Figure 4.19.

Even though switching the *b* and *c* lattice parameters in Dmitriev *et al.*'s model improves the quality of the Rietveld refinements, with closer agreement between the

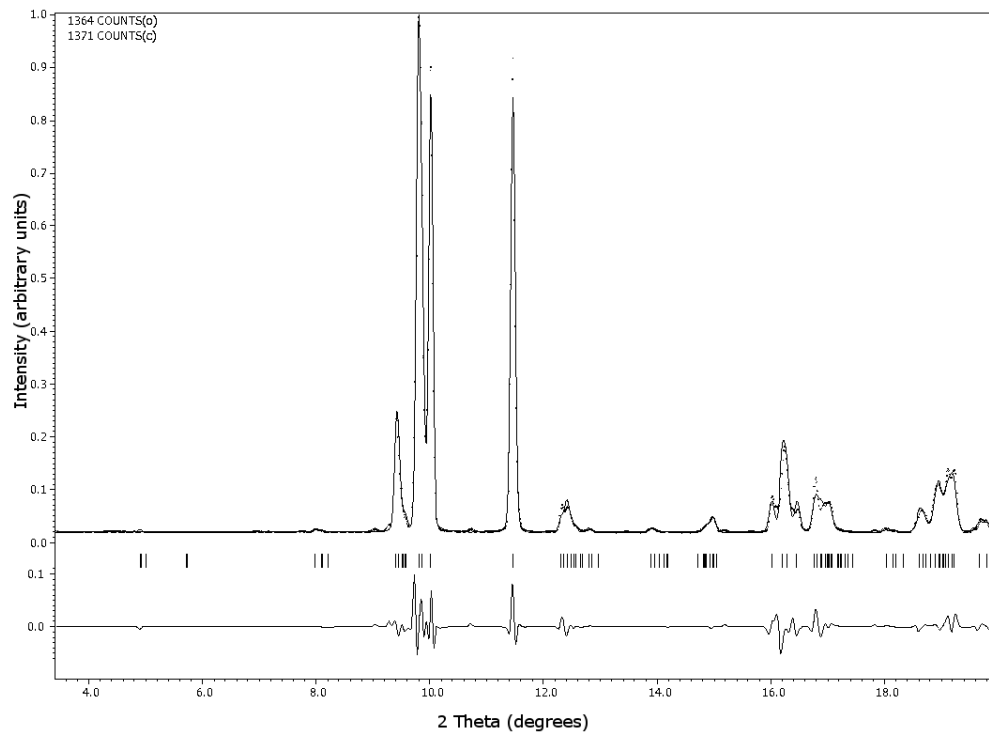


Figure 4.18: Rietveld refinement made to Pr diffraction pattern collected at 19GPa on Station 9.5HPT of Daresbury SRS using the *mC16* structure reported as the solution to the *d-fcc* phase by Dmitriev *et al.* Dots are experimental points, upper line is calculated diffraction pattern, lower line is the difference plot between calculated and observed data and tick marks are the locations of peaks in the model structure. [Dmitriev 00]. A wavelength of $\lambda=0.44397\text{\AA}$ was used for the collection of this data.

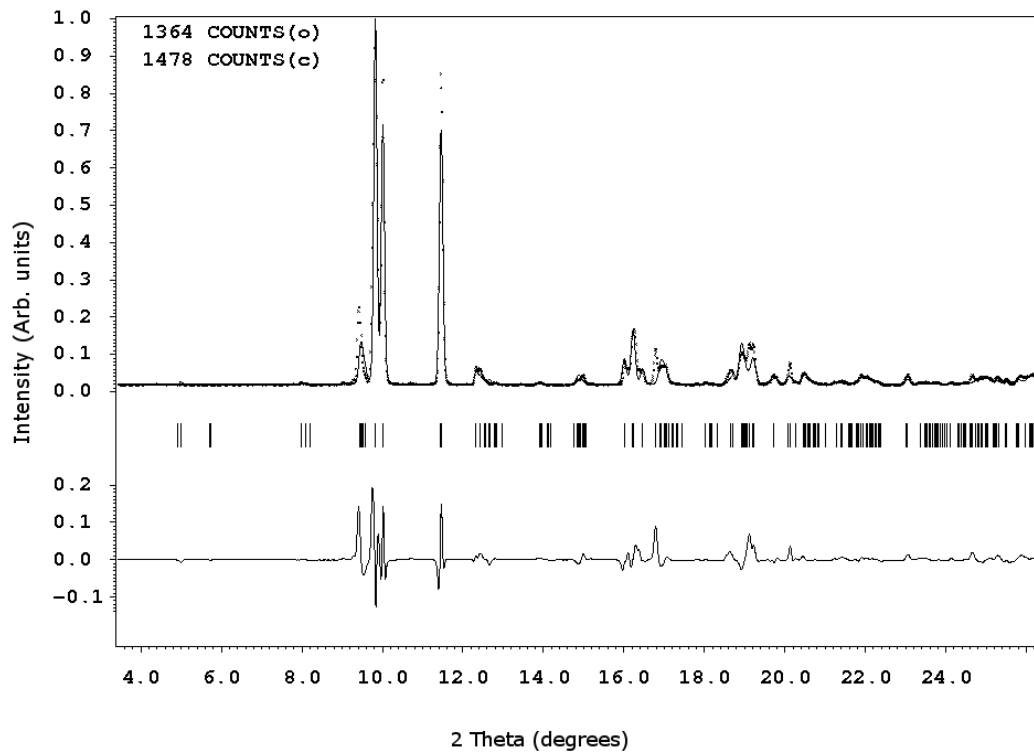


Figure 4.19: Rietveld refinement made to Pr diffraction pattern collected at 19GPa on Station 9.5HPT of Daresbury SRS using the *mC16* structure reported as the solution to the *d-fcc* phase by Dmitriev *et al.* [Dmitriev 00] with the *b* and *c* lattice parameters switched relative to those refined in Figure 4.18. A wavelength of $\lambda=0.44397\text{\AA}$ was used for the collection of this data.

2θ	<i>Index</i>
13.5740	-6 0 1
13.6363	-6 0 3
13.6391	5 1 0
13.6919	3 3 0
13.7208	4 0 1
13.7228	-3 3 2
13.7504	-4 2 3
13.7810	-1 3 2
13.8375	-2 2 3
13.8982	0 0 3

Table 4.4: Table showing the degree of overlap encountered in the structure proposed by Dmitriev [Dmitriev 00] for a peak at 13° in 2θ . Locations of the peak in 2θ and index assigned by Jana2000 during refinement. Values from a Rietveld refinement made to data collected at 13GPa at Station 9.5 HPT of Daresbury SRS using a wavelength of $\lambda=0.44397\text{\AA}$.

observed and calculated peak positions (shown in the difference plot in Figure 4.18) there remains a striking number of overlapping peaks predicted by this model. A closer inspection of Figure 4.18, tabulated in Table 4.4, reveals the 13° Bragg peak (used as an example, as the degree of peak overlap for this reflection is representative of a number of other peaks in the diffraction pattern) to be the superposition of numerous peaks. This extraordinary degree of peak overlap for what appears to be a single peak in integrated 1D diffraction profiles, with many of the constituent peaks having zero or low (approximately background) intensity (evident using the “Info” function in Jana2000’s “Profile Viewer” and from viewing the .m91 file created by Jana2000 during the refinement), which is representative of a majority of the peaks in the refined pattern in Figure 4.18 suggests that a structural solution with higher symmetry than monoclinic can be found. Further, a problem exists with the structure reported by Dmitriev *et al.* [Dmitriev 00], the volume reported in this paper for the *d-fcc* phase is $V_{reported}=21.969 \text{\AA}^3$, whereas, when using the unit cell parameters stated in the paper for this pressure one arrives at a volume of $V_{derived}=22.204 \text{\AA}^3$.

4.8 Structure of Praseodymium from 14-20GPa

Using the indexing software DicVol [Louer 04], a new structure was sought to account for all the observed peaks and intensity distributions with a higher symmetry than the monoclinic $C2/m$ structure proposed by Dmitriev *et al.*

2θ	$\delta 2\theta$
9.1082	0.001
9.2851	0.001
10.6192	0.001
14.8315	0.001
15.0490	0.001
15.2590	0.001

Table 4.5: Subset of the peaks from a diffraction pattern of Pr, used for indexing the *d-fcc* phase. Data was collected on Station 9.5 of Daresbury SRS using a wavelength of $\lambda=0.44397\text{\AA}$

For the indexing, a sharp (small FWHM, unaffected by strain broadening), well defined (minimal peak overlap, with well resolved peaks), clean (minimal amount of contamination) and single-phase pattern is required. Sharp, well-resolved peaks were obtained in a sample through a process of raising the sample pressure such that the single (post 14GPa) phase is observed, annealing the sample (within the DAC) in a furnace with temperature set at 200°C for 4 hours, and then adjusting the pressure to the required value. Annealing of the Pr sample at high temperature sharpens the diffraction pattern (i.e. reduces the FWHM of integrated peaks), by promoting recrystallisation of the sample and pressure transmitting media, thus relieving strain on the sample. This allows additional structural detail to be seen, as peaks become better resolved. An image taken during at ID09A of the ESRF, Grenoble, using a sample which was annealed prior to the experiment, fulfilled these criterion. Peak positions for each of the singlets and well resolved doublets belonging to Pr in the integrated 1D diffraction pattern were modelled and 2θ values extracted using the pseudo-Voigt peak fitting routine in Matlab.

Attempts to index using all of the extracted peaks in DicVol yielded no usable solutions, even when attempting to index over small ranges in volume (searching in 0-100 \AA^3 , 100–200 \AA^3 , 200–300 \AA^3 ranges, etc.) whilst systematically searching through structure types (monoclinic, orthorhombic, triclinic) sequentially.

A subset of the total number of peaks, which are shown in Table 4.5, and comprising of the 6 most intense, well-resolved peaks in the 0-15° 2θ region of the aforementioned data collected at ID09A of the ESRF, were supplied as the input to DicVol [Louer 04]. This subset of peaks might be expected to find a sub-cell of the structure solution for this phase, requiring the application of some multiplicative factors to each unit cell

Parameter	Value
a	4.4486Å
b	3.18967Å
c	3.10067Å
Volume	43.96Å ³
$\frac{a}{\text{average}(b,c)}$	1.41323

Table 4.6: Table showing the orthorhombic trial cell found by DicVol when indexing the peaks from Table 4.5.

dimension to account for all of the peaks present in this phase. The same systematic procedure mentioned above was adopted to search for solutions, although, a number of solutions presented by this method had to be discounted for being too general (triclinic) or not of sufficiently high symmetry (tetragonal). Monoclinic solutions were discarded at this stage as a higher symmetry structure than that proposed by Dmitriev was being searched for (as the large degree of peak overlap found when using the solution proposed by Dmitriev *et al.* suggests a higher-symmetry spacegroup). In the 0-100Å³ volume interval, with upper limits of 25Å on unit cell parameters, a single orthorhombic subcell was found with unit cell parameters listed in Table 4.6. This subcell represents the simplest, highest-symmetry solution which fits the subset of peaks provided to DicVol with an average difference between 2θ calculated and observed of $-1.3 \times 10^{-3}^\circ$.

The orthorhombic subcell found by DicVol (Table 4.6) can be related to the *fcc* phase when the two shorter axis, *b* and *c*, are averaged. Note the larger unit cell parameter for this orthorhombic subcell is the *a* axis, in contrast to the $R\bar{3}m$ phase where the *c* axis is longer. Dividing the *a* unit cell parameter in the orthorhombic cell by the average of *a* and *b* yields a value of $\sqrt{2}$ (to 1 part in 1000), the face diagonal length in a cubic system. A diagram showing the relationship of this structure to the *fcc* phase is shown in Figure 4.20.

$$\begin{pmatrix} a' \\ b' \\ c' \end{pmatrix} = \begin{pmatrix} \frac{2}{3} & -\frac{1}{2} & \frac{2}{3} \\ \frac{1}{3} & 0 & \frac{7}{3} \\ -\frac{1}{3} & \frac{1}{2} & -\frac{4}{3} \end{pmatrix} \begin{pmatrix} a \\ b \\ c \end{pmatrix}$$

In attempting to determine the spacegroup for the orthorhombic cell proposed by DicVol, an analysis of the symmetry relations and systematic absences within this

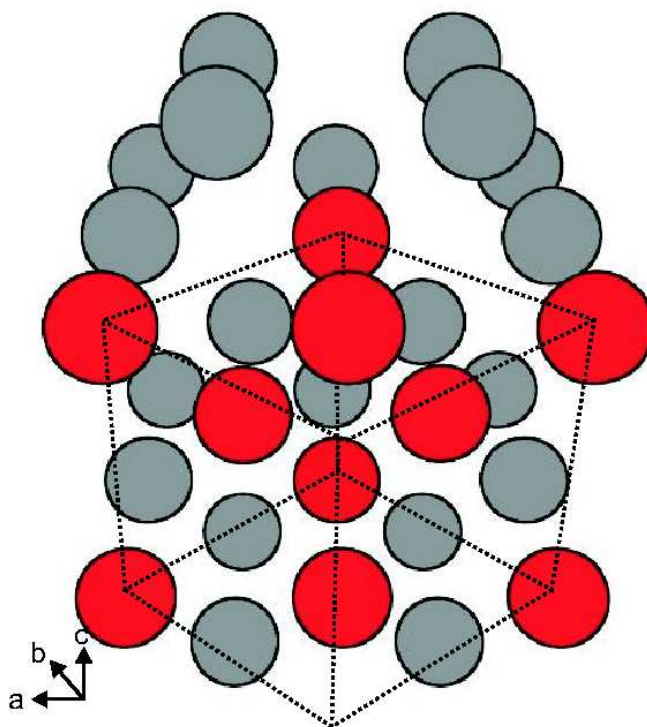


Figure 4.20: Diagram showing the relationship between the *fcc* and *Ibam* structures. In this 3D view a single *Ibam* unit cell is drawn (comprises of all atoms, with basis vectors, *a*, *b* and *c* shown). Atoms within the *Ibam* unit cell are shown as grey circles, atoms within the *fcc* unit cell are shown by red circles, with the *fcc* unit cell shown by dashed black lines, the *Ibam* unit cell is not drawn.

pattern must be made. Choosing the lowest symmetry orthorhombic spacegroup with I centering, the *Immm* spacegroup as a starting model, a refinement was made in Jana2000. Using the cell as proposed by DicVol in refinements it was evident that only the strongest peaks were modelled, with few other peaks in the observed data accounted for. By close inspection of the files created by Jana2000 during the refinement process, a list of the indices and associated fitted intensities assigned to each observed and predicted reflection can be made.

Looking for patterns in the absent/zero intensity reflections and comparing these with the reflection conditions from Table 3.1.4.1 of International Tables A [Hahn (Editor) 02], allows the spacegroup of this *d-fcc* phase to be determined. It is evident from the reflection conditions $h+k+l=2n$; $k,l=2n$; $h,l=2n$; $h+k=2n$ and $h00$, $0k0$, $00l=2n$ that the spacegroup is either *Iba2* or *Ibam*. As both of these spacegroups is capable of describing the observed data equally well in LeBial fits, and further are indistinguishable by x-ray diffraction, as they are both belonging to the same Laue class. To decide between the two structures the number of refinable structural parameters was considered. *Ibam* has 6 refinable parameters (a, b, c, x_1 , y_1 , and y_2). *Iba2* has 8 refinable parameters (a, b, c, x_1 , y_1 , z_1 , z_2 and z_3) owing to reduced multiplicity at the atomic positions within the structure. As *Ibam* requires fewer parameters to model a diffraction pattern, it can be viewed as the simplest and highest symmetry solution. *Ibam* is thus the logical choice for spacegroup of the 14-19GPa *d-fcc* phase. A refined fit (Rietveld) using the *Ibam* structure to data collected at 19GPa on ID09 of the ESRF is presented in Figure 4.21.

The positions of atoms in the *Ibam* structure were determined using the web-based WYCKSPLIT [Kroumova 98] program on the Bilbao Crystallographic Server [Aroyo 06]. Providing the *fcc* structure as a basis, the atoms in the *Ibam* structure are given at the $8j$ (atoms located at $(x, y, 0)$, $(-x, -y, 0)$, $(-x + \frac{1}{2}, y + \frac{1}{2}, 0)$, $(x + \frac{1}{2}, -y + \frac{1}{2}, 0)$ within the *Ibam* unit cell) and $8g$ (atoms located at $(0, y, \frac{1}{4})$, $(0, -y, \frac{1}{4})$, $(0, -y, \frac{3}{4})$, $(0, y, \frac{3}{4})$ within the *Ibam* unit cell) positions. Knowing the atomic positions at transition to the structure, Rietveld refinements can be made of the 19GPa ID09A dataset. This is shown in Figure 4.21. The structural information is summarised in Table 4.7.

Analysis of the symmetry relationships between the $R\bar{3}m$ structure and the *Ibam* structure shows no direct subgroup-supergroup relationship. The $R\bar{3}m$ and *Ibam* structures can be related through an intermediary structure, the $C2/m$ structure that was originally proposed as a solution to the 14-20GPa region of the *d-fcc* stability-range.

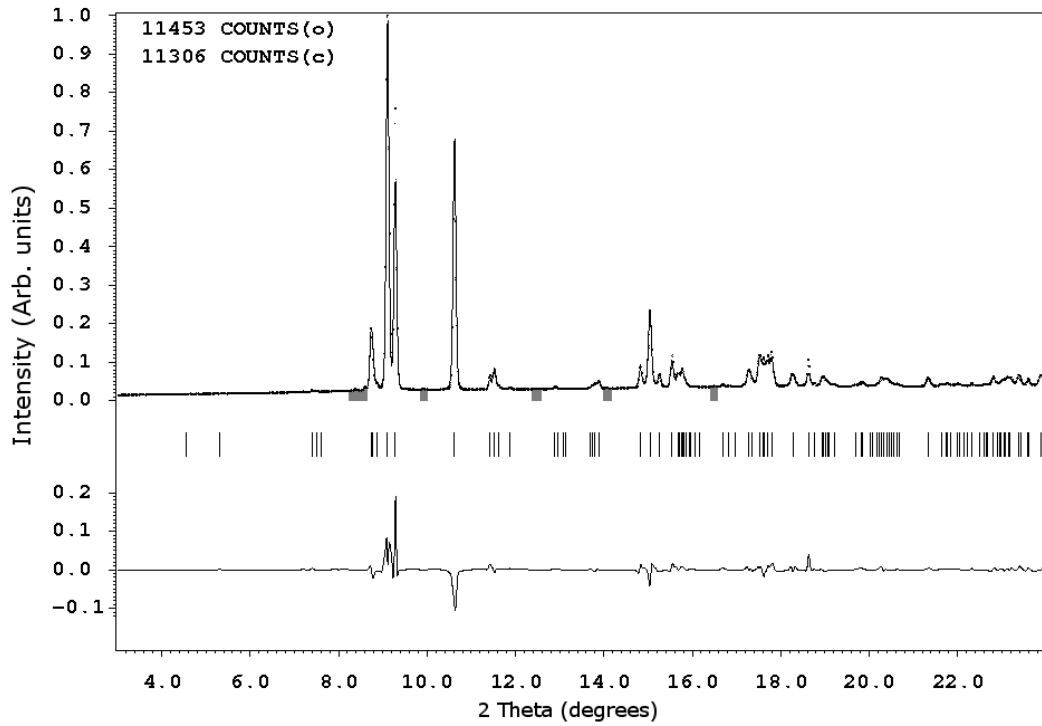


Figure 4.21: Rietveld refinement of Pr using the *Ibam*, the 1D integrated pattern made from file 260 of the HS3109 run, collected at Station ID09A of the ESRF, Grenoble. Where $\lambda=0.41146\text{\AA}$, pressure= 19GPa. Fit parameters are as follows $a=8.8955\text{\AA}$, $b=6.3809\text{\AA}$; $c=6.2011\text{\AA}$. $x_1=0.2673(5)$; $y_1=0.0405(6)$; $y_2=0.2310(6)$.

Parameter	Value
a	8.8955(6) \AA
b	6.3809(3) \AA
c	6.2011(4) \AA
Volume	21.99 \AA^3
$\frac{c}{a}$	0.6971
x_1	0.2673(5)
y_1	0.0405(6)
y_2	0.2310(6)
U_{iso1}	0.0179
U_{iso2}	0.0025

Table 4.7: Structural information gained from a Rietveld refinement of Pr diffraction data collected at 19.0GPa using the *Ibam* structure. Data collected at Station ID09A of the ESRF, Grenoble with a wavelength of $\lambda=0.41146\text{\AA}$.

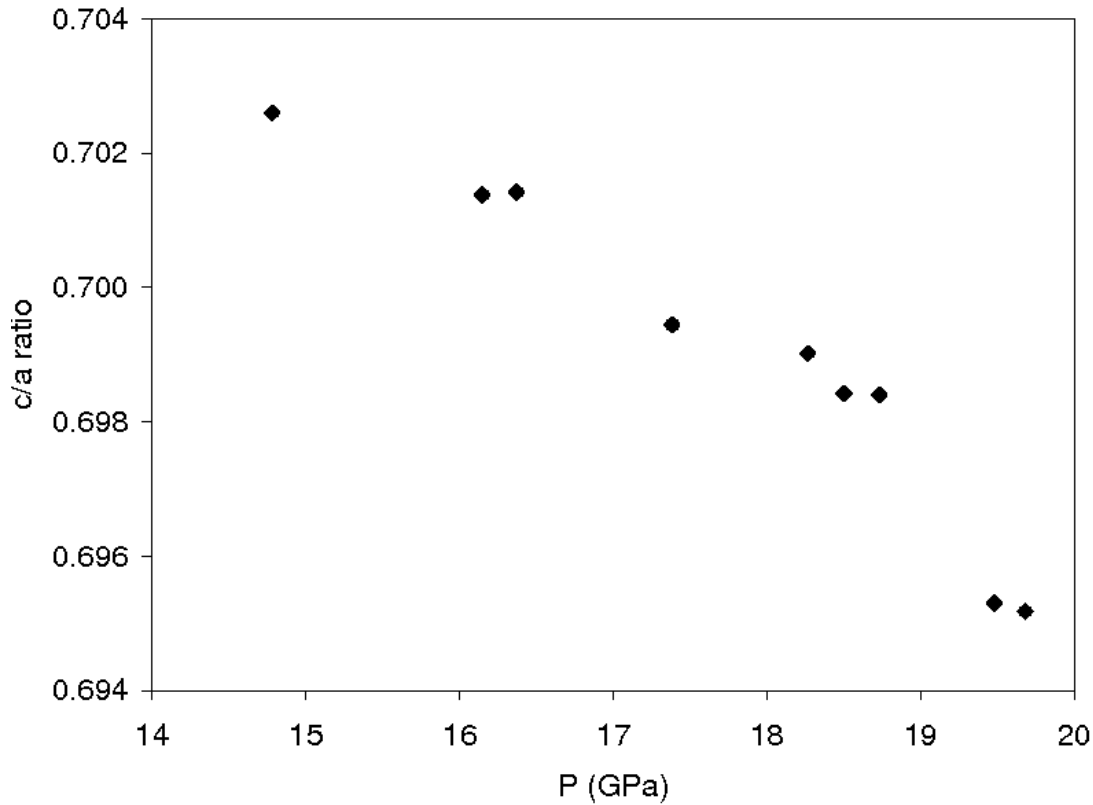


Figure 4.22: Plot of variation of the *Ibam* c/a ratio with respect to pressure. Error bars are plotted, but are obscured by the plotted symbols.

Refinements were made of all patterns collected from Pr in the 14-19 GPa pressure range, this encompassed data collected from Station 9.5 of Daresbury SRS and ID09A of ESRF. When using the *Ibam* structure the difficulty in fitting and refining integrated Pr powder diffraction data from pressures greater than 16GPa, as mentioned by previous authors [Baer 03, Holzapfel 95], was not observed. The *Ibam* structure provided low R_{wp} ($\approx 4\%$) and χ^2 values and no significantly large misfits (on the refinement difference plots) in Jana2000. Figure 4.21 is representative of the quality of refinements made using the *Ibam* structure, the small misfits here are likely due to preferred orientation effects, all observed resolvable peaks are accounted for.

Plots of the variation of unit cell parameters ($\frac{a}{\text{average}(b,c)}$) and volume with pressure are shown in Figures 4.22 and 4.23 respectively.

In relating the *Ibam* structure to the precursor phase, *hR24*, there is no direct group-sub/super group relation shown by International Tables (or Bilbao Crystallographic

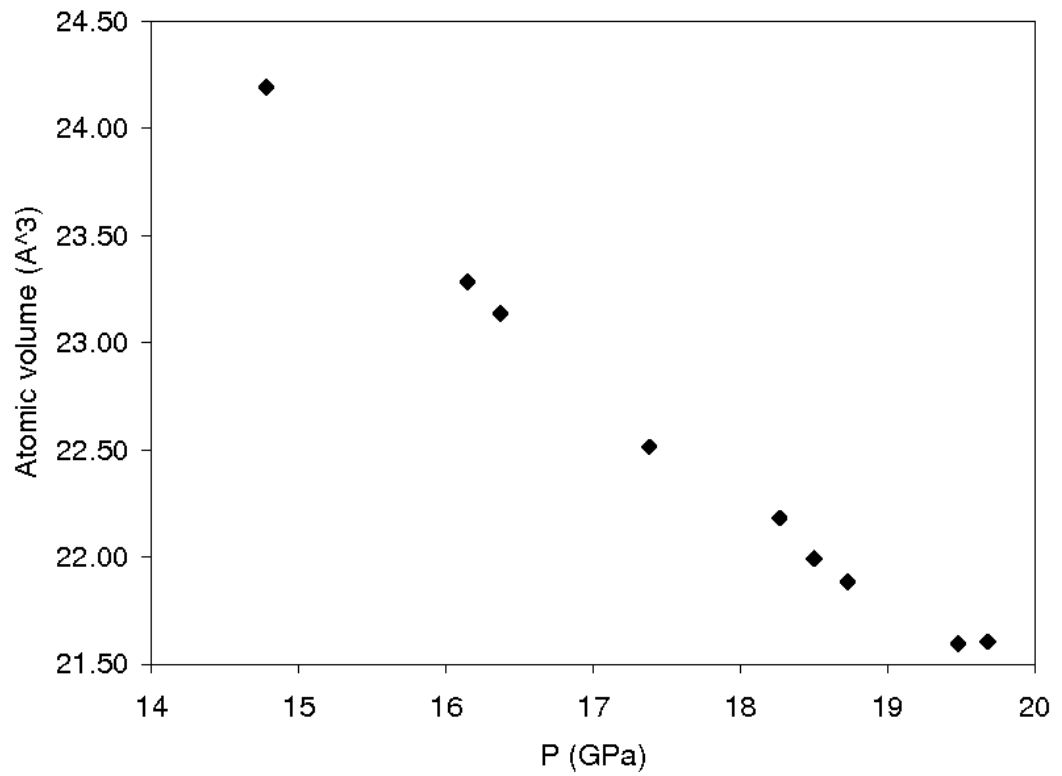


Figure 4.23: Plot of of the *Ibam* atomic volume with respect to pressure. Error bars are plotted, but are obscured by the plotted symbols.

Server). A direct relationship to the *fcc* structure can be formed, of which the *hR24* is a minor distortion. Following this reasoning, distortions to the *hR24* could yield the *Ibam* structure using *fcc* relations as an intermediary step. It is interesting to note that the previous reported structure solution for the *d-fcc* phases, *C2/m*, is also capable of acting as an intermediary phase between the *hR24* and *Ibam* structures. Transformation matrices quantifying the relationship between the *Ibam* and *fcc* cells are presented near the start of this section, and pictorially in Figure 4.20.

A small, but notable misfit occurs with the *Ibam* structure (which is also unexplained by the other previously suggested structures in the literature [Mao 81, Dmitriev 00, Baer 03, Syassen 00]) at $\approx 18^\circ$. Here, it is observed that the (440) reflection is resolved to a doublet in patterns collected on ID09a (ESRF), which used a sample that was annealed prior to the experiment. There is a separation of $\approx 0.05^\circ$ between peaks (measured from fitting each peak in Datlab). Figure 4.24 depicts this splitting. The (440) reflection is predicted by the *Ibam* structure to be a singlet, thus the observed splitting is not accounted for. No other splittings were observed in the data. Further, this splitting was only observed in the highest resolution datasets (collected on ID09a at the ESRF) that had been previously annealed. While the author notes this suggests a slight distortion to the *Ibam* structure, there is not enough data to ascertain, with certainty, if the structure of Pr is indeed distorted from the orthorhombic *Ibam* solution proposed here. *Ibam* represents the best found solution to the observed data.

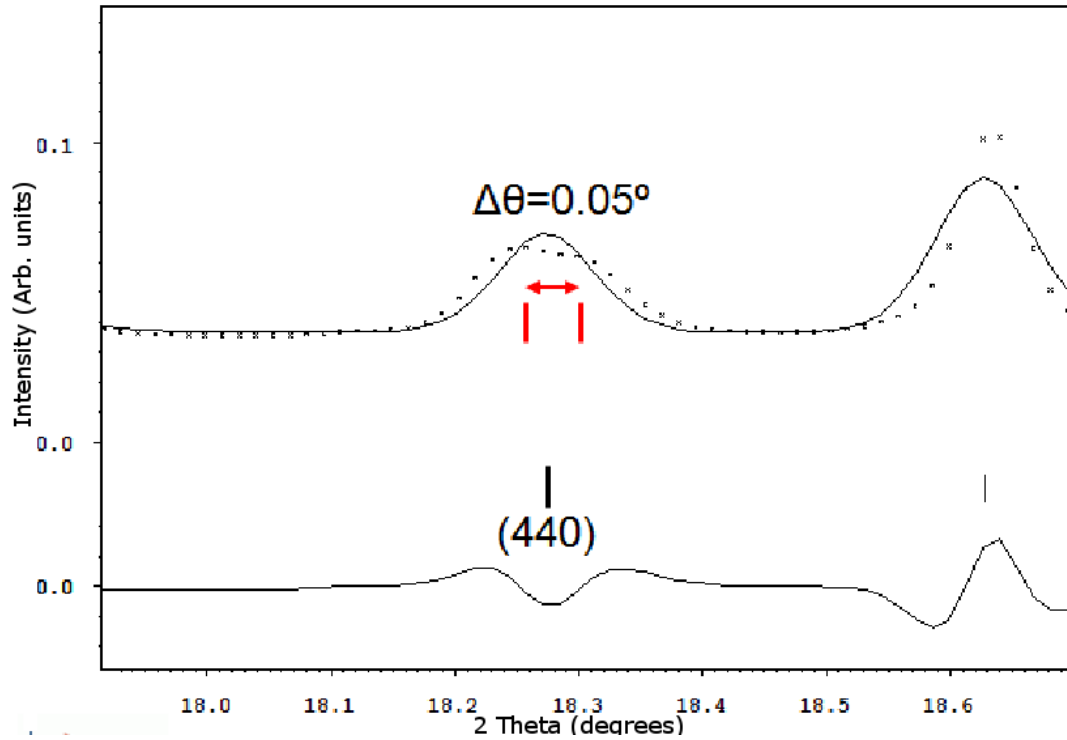


Figure 4.24: Diagram how the *Ibam* structure fails to account for the splitting of a peak (440) located at 18.27° . Here, dots represent the observed data, the upper line represents the refined model, the lower line is the difference plot between the observed and refined data. Lower tick marks are the peak positions as predicted by the *Ibam* model, the upper tick marks were added to highlight the positions of the observed peak centroids. The small peak splitting, 0.05° was only observed in the x-ray diffraction data collected at beamline ID09a of the ESRF, which offered both higher resolution and higher flux compared to Station 9.5 of Daresbury SRS. $\lambda = 0.414412\text{\AA}$, $P = 19\text{GPa}$.

4.9 Structure of the α -Uranium phase

A transition from the high-pressure (*Ibam*) *d-fcc* phase to the α -U phase is observed to occur in Pr at 20.5(5)GPa, determined through averaging the pressure at which the α -U phase is first observed (19GPa, in a mixed phase with *d-fcc*) to occur and at which it is completed (21GPa). On pressure increase beyond 19GPa the *d-fcc* phase is observed to contain weak peaks originating from the *Cmcm* α -U structure reported in the literature [Mao 81, Dmitriev 00, Baer 03]. These α -U peaks can be seen to increase in intensity with increasing pressure, with peaks originating from the *d-fcc* phase decreasing in intensity as the pressure is raised further above 19GPa, up to 21GPa, where the α -U diffraction pattern dominates as the applied pressure increases. At 21GPa, the α -U diffraction pattern is the sole phase present in the sample. Integrated 2D diffraction patterns collected from Station ID09A of the ESRF are shown in Figure 4.25. The patterns in this figure highlight the differences between the clean, single-phase patterns from within the *d-fcc* and α -U phase, in stark contrast to the subtle changes to the diffraction profiles which accompanied the transition from $R\bar{3}m$ to *Ibam* within the *d-fcc* phase at 14GPa.

As noted by Dmitriev *et al.* [Dmitriev 00] and Chesnut *et al.* [Chesnut 00b] the onset of this transition is apparent on 2D diffraction patterns from the appearance and tendency of additional Debye-Scherrer rings to appear and become highly textured (spotty) on the 2D diffraction image. The appearance of textured rings is in contrast to the smooth Debye-Scherrer rings observed within the *d-fcc* phase, and indicates evidence of recrystallisation of the sample upon the entering the α -U phase. This appearance of spotty diffraction rings is observed in all patterns collected within the α -U pressure range reported by Baer *et al.* [Baer 03], an example of a 2D diffraction image, collected at Station 9.5 of Daresbury SRS, is presented in Figure 4.26, which shows an enlarged section of the Debye-Scherrer ring from the α -U and *d-fcc* phases.

Patterns in the α -U phase were collected, as for the *d-fcc* phase, in a multitude of separate experiments, which encompassed using Station 9.1, Station 9.5 HPT of Daresbury SRS and ID09A of the ESRF, with samples loaded in mineral oil or dry. Little ambiguity persists in the literature to date pertaining to the structure of the α -U phase, only a study by Mao *et al.* [Mao 81] misreported the structure for this phase (which lead to a large volume change being noted at the *d-fcc* to α -U transition). Successive investigations on the α -U stability range in Pr have revised the upper pressure limit of the phase, which was noted by Chesnut *et al.* [Chesnut 00b] as being stable up to 103GPa. Velisavljevic and Vohra [Velisavljevic 04a] performed

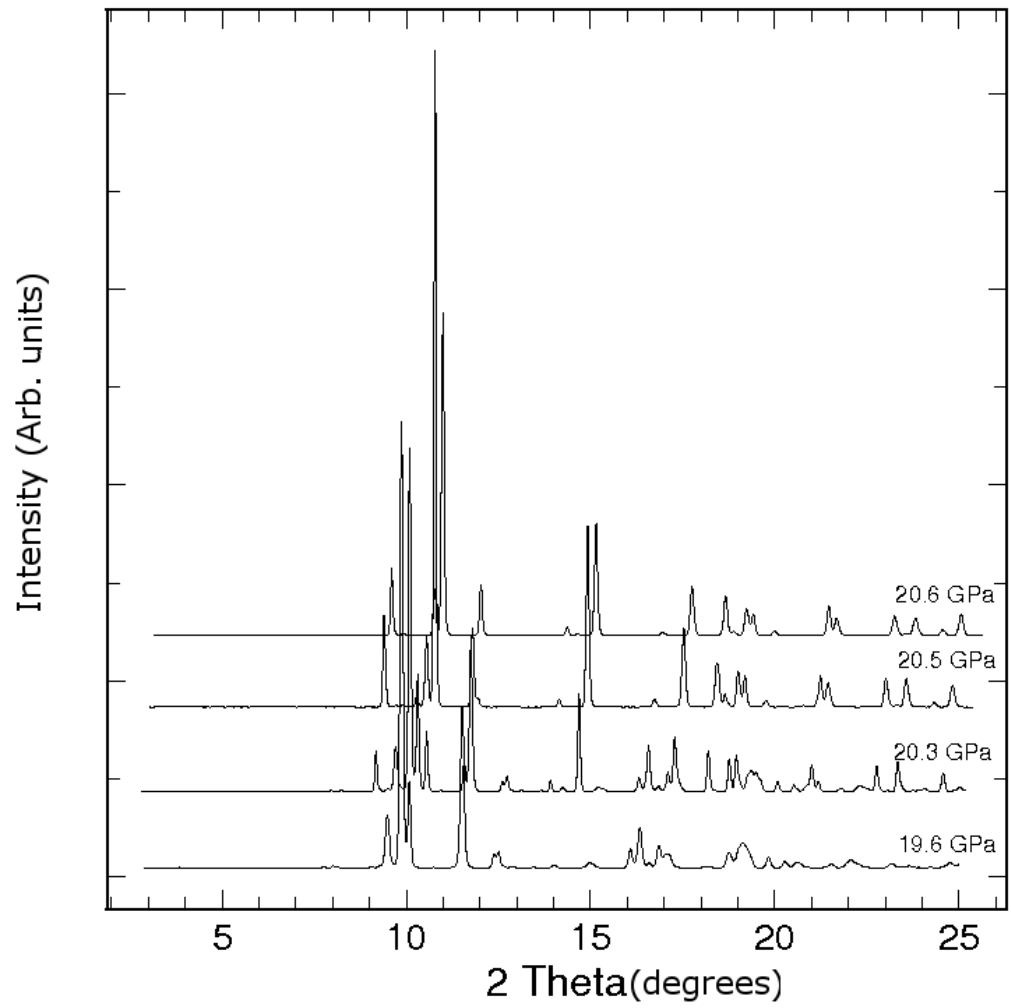


Figure 4.25: Waterfall plot showing the transition from the *Ibam* *d-fcc* phase to the α -U phase in Pr. Pressures of each data set are noted on the right side of the diffraction pattern. The pattern at 19.6GPa is predominantly *Ibam*, 20.3 and 20.5GPa are mixed-phase patterns, 20.6GPa is a predominantly α -U pattern.

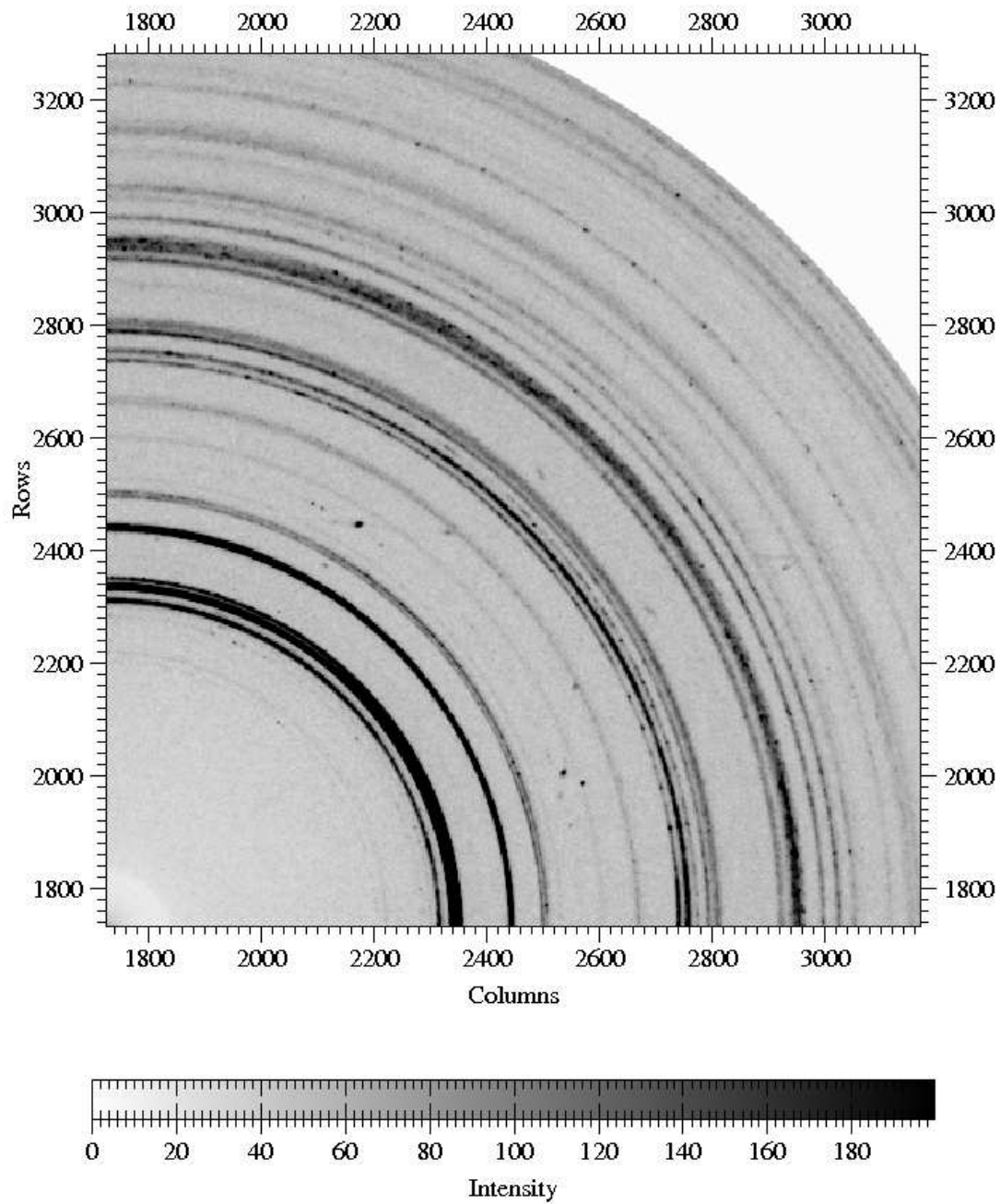


Figure 4.26: Part of a 2D diffraction image of Pr at 21GPa taken at beamline ID09a of the ESRF. This figure highlights the pronounced texture visible in the diffraction rings, which is observed in all samples upon transition to the α -Uranium phase.

x-ray diffraction studies at room-temperature up to 311GPa, but did not observe a transition from α -U to another phase. Indeed, using the MB DACs with a highest attainable pressure of 40GPa, and for the DXR6 cells the highest attainable pressure of 50GPa (using the diamonds available) falls well below the upper stability pressure for this phase. For these reasons the α -U phase was not systematically studied through its pressure stability range. Instead, studies were made up to a maximum of 25GPa, based on Vohra's [Vohra 81] claim of the *d-fcc* stability extending to 25GPa. This statement can be disproved, as shown in Figure 4.25, which clearly shows the α -U phase's stability above 20.5(5)GPa, in agreement with work published later [Mao 81, Grosshans 92, Chesnut 00b, Dmitriev 03, Baer 03].

Using the spacegroup for α -U reported in the literature by numerous authors as the post *d-fcc* phase in lanthanides [Chesnut 00b, Dmitriev 03, Baer 03], *Cmcm*, Rietveld refinements were made to the data collected above 20.5GPa for Pr. Values for the unit cell dimensions given by Baer *et al.* [Baer 03] at 27GPa (and a temperature of 718K) using energy dispersive techniques ($a = 2.7330$, $b = 5.4665$ and $c = 4.8769\text{\AA}$) provide excellent starting values for refinements when (the 4) atoms are located in the $4c$ atomic positions within the unit cell ($(0, y, \frac{1}{4})$ and $(0, -y, \frac{3}{4})$ with $y = 0.1$ (as stated by Chesnut [Chesnut 00b]). Excellent quality fits can be produced to the data collected above 20.5GPa, as demonstrated by Figure 4.27. Close inspection of this figure reveals no significant misfits to the observed data. Refined lattice parameters for the Rietveld refinement (on a pattern collected at 21GPa) shown in Figure 4.27 are given in Table 4.8. Discrepancies between the values quoted by Baer *et al.* and those refined here originate from the difference in pressure and temperature (27GPa, 718K vs. 21GPa, 300K). Using the reindexed values from Grosshans *et al.* [Grosshans 83] to Mao *et al.*'s data [Mao 81], which states lattice parameters of $a = 2.761$, $b = 5.618$ and $c = 4.877\text{\AA}$ ($V = 18.91\text{\AA}^3$) at 21GPa yields a different value to the volume collapse than that reported.

The volume/atom at this pressure of 21GPa (where the α -U pattern has no remaining *d-fcc* peaks) is markedly lower than that of the highest pure *d-fcc* phase refined pattern, $\approx 8\%$ lower, in agreement with the reported volume collapse of $\approx 14\%$ stated in [McMahan 98] as arising from the delocalisation of the $4f$ electrons. This large volume collapse signifies a 1st order transition. This measured volume difference upon transition to the α -U structure is somewhat lower than the value originally reported by Mao *et al.* [Mao 81], but in close agreement with Grosshans's [Grosshans 83], which states the volume change to be 9.3%.

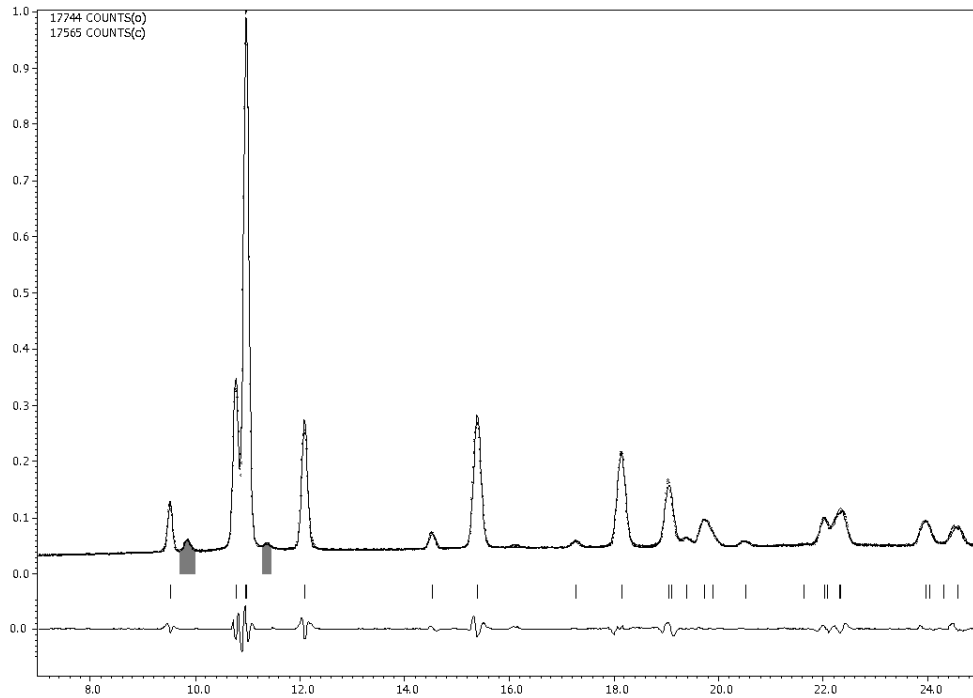


Figure 4.27: Rietveld refinement made to a sample of Pr, at 21GPa, in the α -Uranium phase. Data collected on Station 9.5 of Daresbury SRS using a wavelength of $\lambda = 0.44397\text{\AA}$. Refined lattice parameters are given in Table 4.8 $R_{wp}=4.79\%$

Parameter	Value
a	2.7743(1) \AA
b	5.6165(2) \AA
c	4.8924(3) \AA
Volume	76.2326(4) \AA^3
Volume/atom	19.0582(4) \AA^3
$\frac{a}{c}$	0.56710(4)
y	0.1
U_{iso}	0.0197

Table 4.8: Table showing the structural parameters of the α -U phase of Pr, as refined from patterns collected at 21GPa

4.9.1 Single Crystal Growth Attempts

Attempts were made to resolve the ambiguity encountered in determining the structure of the *d-fcc* phase by growing a single crystal in both the high and low pressure ranges previously referred to as the *d-fcc* phase (7-14 GPa and 14-20GPa). The method of annealing at low-moderate temperatures (compared to the melting point of Pr at the relevant pressures), 200-300°C, whilst resulting in integrated patterns with smaller FWHM, showed no evidence which suggested the recrystallisation of Pr from a powder into a single crystal crystal. This method of annealing the DAC in an oven suffered a major limitation, in that limitations are imposed on the temperatures that can be used. These limitations are imposed by the design of the DAC and safety concerns related to components used in the DACs. Heating a substantial amount above 300° risked loosening of the support structure around the diamond anvils and/or introducing an excessive amount of strain upon the Be backing discs used in the MB DACs employed for the majority of this study.

Laser heating was used to overcome safety concerns, and the heating limitations when using the DACs in conjunction with regular (resistive heating) collars (which enclose the DAC within a metal ring which is resistively heated upon application of an electric current) or furnace heating. Laser heating thus allows access to temperatures in the region of the melting curve for Pr at high pressures (at 19GPa the melting point is $\approx 1100^\circ\text{C}$ and *d-fcc* \rightarrow *fcc* is at $\approx 200^\circ\text{C}$ [Tonkov 05]). Efforts were made to grow a single crystal of Pr from the melt by laser annealing, using a 150W CO₂ laser, capable of heating to temperatures in excess of 6000°C. Laser heating required a different sample preparation (loading) method, to ensure thermal insulation of the diamonds from the laser heated sample (to prevent damage to the diamond culets). A schematic diagram of the loading is shown in Figure 4.28, with thermal isolation achieved by using a thin layer of dry, ultra-pure NaCl atop the diamond culet and atop the sample, effectively sandwiching a freshly cleaved chip of Pr between layers of NaCl. The NaCl acted as a thermal barrier and a pressure transmitting media, albeit an extremely stiff media, likely to introduce a large degree of strain within the sample. A 200 μm thick tungsten gasket, preindented to 40 μm , with a laser-cut sample hole of 100 μm diameter was used to form the sample chamber. NaCl was pressed into a disc within the empty sample chamber (prior to loading of the sample and ruby manometer), this disc was approximately halved in height, the sample and ruby sphere were placed atop one half within the sample chamber and NaCl positioned on top of this layer. A schematic of this loading is shown in Figure 4.28, the DAC was then closed within the glovebox and initially pressurised.

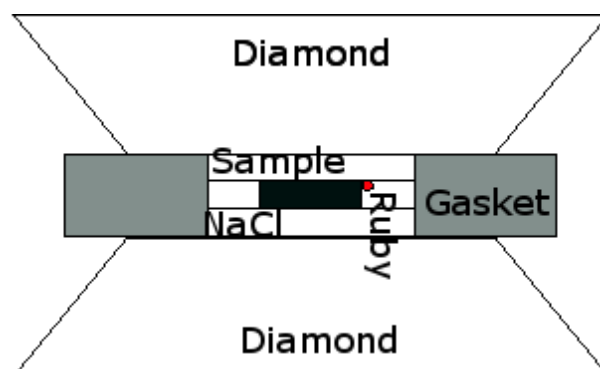


Figure 4.28: Schematic diagram of the sample chamber used for laser annealing trials. A thin NaCl barrier is highlighted. Location of Pr sample, ruby sphere pressure calibrant and tungsten gasket are labeled.

An initial attempt at loading a sample in this manner was made in a MB type DAC, a number of failed loading attempts in this DAC were made before a Boehler-Almax DAC became available for use. The Boehler-Almax design represented the most sensible choice for DAC to house a single crystal, having larger opening angle than a MB cell, granting access to a broader region of reciprocal space, and without contamination of the 2D diffraction image from Be (from the backing discs of “standard” MB DACs) at high rotation angles.

The Centre for Science at Extreme Conditions (CSEC, an inter-disciplinary centre at the University of Edinburgh) IR laser source produces light of λ of 1064nm, within the near-IR spectrum, readily absorbed by metallic elements, but not by the other components within the sample chamber, as shown in Figure 4.28 as for Boehler *et al.* [Boehler 01]. A focused laser spot size of $10\mu\text{m}$ impinges on the sample of approximate size $70 \times 20\mu\text{m}$, and requires the sample to be rastered across to effectively heat the sample. Normally, the temperature of the heated sample during the laser annealing is measured indirectly, by fitting a black body radiation spectrum to the incandescent light collected from the sample during the annealing process. However, the fitting of black body radiation spectra was not available at the time the annealing was carried out. As such, the temperature was estimated based on the power output settings of the laser. Large thermal gradients within the chamber were avoided by ensuring the temperature did not greatly exceed the intended value, nor the temperature of the sample remain elevated for prolonged periods of time. The intention of these considerations is to allow heat to dissipate from the system between heatings, without the highly (thermally) conductive diamonds being endangered. The DAC was pressurised to 19GPa, a

pressure close to the $d\text{-}fcc \rightarrow \alpha\text{-U}$ phase boundary, at which heating is shown earlier to increase the quality of patterns and create pronounced texture in diffraction rings ([Dmitriev 00]). Heating occurred in ≈ 5 second intervals, separated by ≈ 2 minute pauses. Initially the laser was used on 3% power, ramped up with successive exposures to 10% power ($\approx 750^\circ\text{C}$). The DAC was rotated and the opposite side of the sample exposed. Coupling of the laser to the metallic sample at 10% power is suspected to be weak.

Data collected from the laser-annealed Pr sample on Station 9.5 of Daresbury SRS showed tentative suggestions of recrystallisation, with powder diffraction rings tending to “clump” (becomes polycrystalline) exhibiting regions where the diffracted intensity is markedly at background and regions where it is markedly higher, but did not become a single crystal. Figure 4.29 shows a section of the 2D diffraction pattern from this sample. An increased number of contaminant peaks were evident from the 1D diffraction profile which arose from the NaCl present as a pressure medium and thermal barrier. It is promising that the sample became more textured after laser annealing, suggesting that further heating at a higher temperature (into the melt) and cooling would encourage the growth of a single crystal. It is not known what effect the immediate cessation of heating (if any) has upon the crystallisation process here. If perhaps gradual cooling from HT would encourage the formation of a single crystal. Further investigation, unfortunately not permissible within the timescale of this research, would be required to ascertain the conditions required to grow a single crystal of Pr within a DAC.

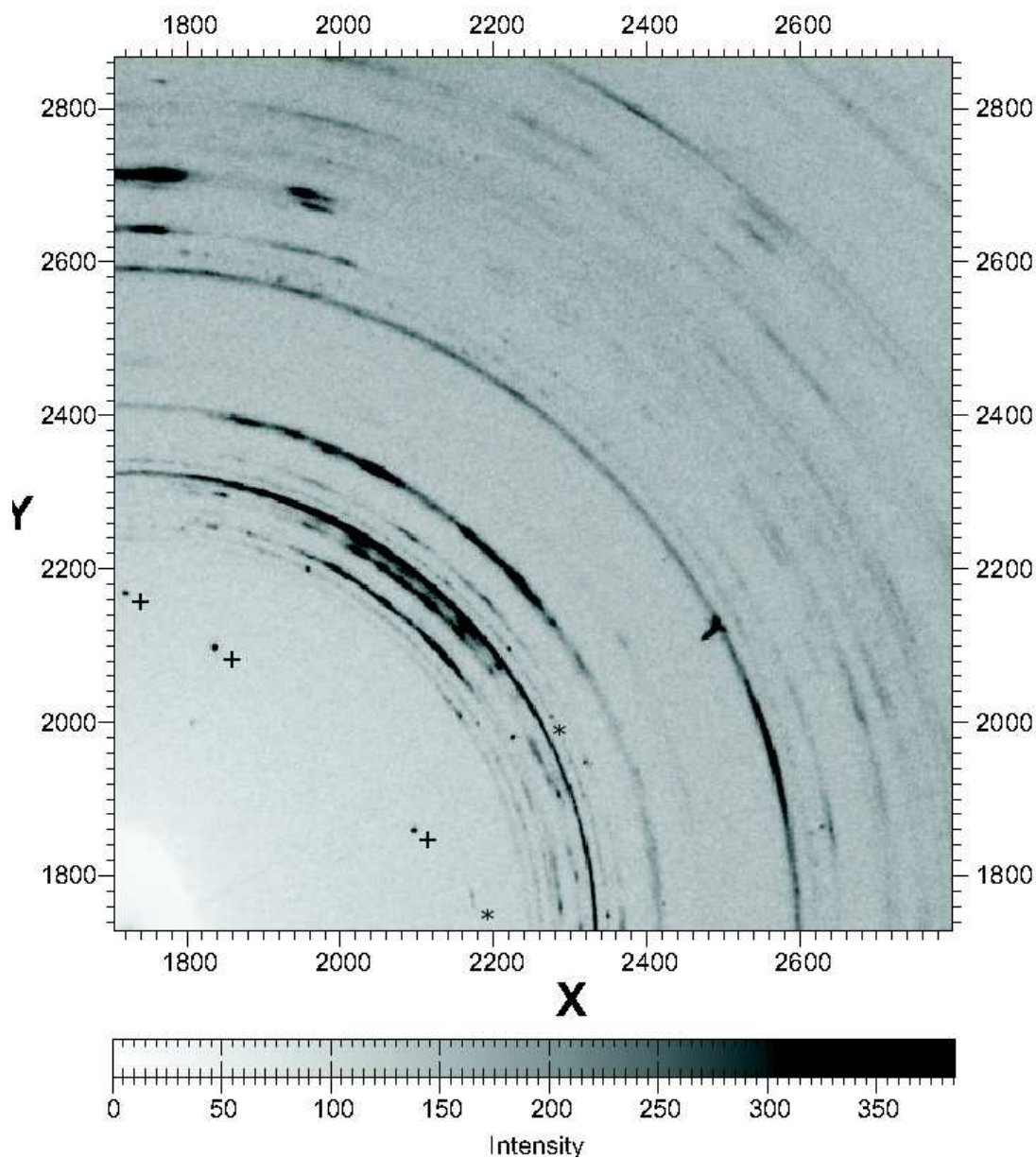


Figure 4.29: Section of 2D diffraction image from the laser annealed Pr sample in Bohler-Almax style DAC. Diffraction pattern collected on Station 9.5 HPT at Daresbury SRS, with a wavelength of $\lambda = 0.44397\text{\AA}$, $P = 19\text{GPa}$. Spots originating from contaminants are labelled with (*), from ruby manometer with (+), remaining diffraction rings originate from the laser annealed Pr sample.

4.10 Discussion and conclusions

Contaminants observed during the course of this study can be considered equivalent to those observed in previous studies [Mao 81, Dmitriev 00, Chesnut 00b]. Observed are two cubic (*fcc*) contaminants, one of ambient pressure lattice parameter $a = 5.03\text{\AA}$ attributable to the praseodymium monoxide, PrO. From comparison with a materials data sheet provided with the commercially sample of Pr, the highest impurity concentration is stated as being oxygen. The proclivity of Pr to oxidise in air is observed in the formation of a tarnished green coating, observed to form over extended periods of time in a low oxygen concentration environment (glovebox). The other contaminant's identity, also *fcc*, of ambient pressure unit cell size $a = 4.88\text{\AA}$ remains elusive. It is observed in the literature by only a small number of authors (shown in Table 3.1), who neither commented on or speculated as to its origin. An EOS for the contaminants has been prepared, shown in Figure 4.3, although it should be noted the lack of data in the region 0 to 5GPa arises from overlap of sample reflections with contaminant peaks (the ambient pressure point is back extrapolated using the fitted EoS). Where possible lattice parameters were extracted using a single *fcc* peak (of known hkl).

At 7GPa Pr has been shown to transform from an *fcc* unit cell to the *hR24* structure (Section 4.5). Determining the *d-fcc* phase between 7 and 14GPa required close examination of the misfits that occurred during the refinements made in Jana2000 for each structure reported in the literature. The *hR24* structure yielded the simplest, best fitting solution able to account for all of the peaks observed in integrated diffraction profiles collected. Atoms are located in the *18h* and *6c* sites, with 24 atoms comprising a unit cell. A direct group-subgroup relationship exists between the precursor *fcc* phase and the *hR24*, as expected for a continuous 2nd order transition. Indeed minor displacements of the atoms away from their *fcc* positions, caused by a stretching along the body diagonal (geometric relation of *fcc* to *hR24*, 4x bigger unit cell, stretched along body diagonal) which gives rise to the “distortion” reflections from which the phase is named.

A transition is observed at 14GPa which accounts for the difficulty Baer *et al.* [Baer 03] had in fitting what was once considered a single phase spanning 7-20GPa. A smooth, sluggish 2nd order transition, is observed to occur over a pressure range of 4GPa from a *hR24* structure to what the author has shown in Section 4.7 to be a body-centered orthorhombic cell (*oC16*, *Ibam*) discounting previous suggestions (which failed to adequately account for all of the observed peaks in the integrated diffraction profiles, without having a large degree of peak overlap). This solution has limitations, being

unable to account for the observed splitting of the peak indexed as (440), suggesting a further slight distortion to the structure. With the data collected, it was not possible to find a better fitting solution.

Above 20GPa the author was able to confirm the observations of the majority of previous studies, a 1st order transition to an closed-packed α -U structure. The discrepancy over the transition pressure from the d -fcc to α -U phase (Chesnut *et al.* [Chesnut 00b]), which differs from the consensus within the literature, having reported a transition pressure from d -fcc to α -U of 25GPa has been resolved. The stability and structure of the α -U phase has not been questioned in the literature, as such detailed studies were not made of this phase.

A plot of the variation of atomic volume with pressure for the pressure range studied in Pr is shown in Figure 4.30. Evident is the lack of volume discontinuity for the transitions in the regular lanthanide phase transition sequence ($dhcp \rightarrow fcc \rightarrow d$ -fcc). A volume discontinuity of $\approx 11\%$ is observed upon transition from the $Ibam$ (d -fcc) phase to the α -U phase.

A fitted 3rd order Birch-Murnaghan equation of state (EoS) is shown in Figure 4.31 to measured atomic volume for the pressure range 0-20GPa in Pr. A datapoint from the α -U phase is shown at 21GPa for comparison (but not fitted, owing to the volume discontinuity which occurs at the 20GPa d -fcc to α -U transition). Fitted k_0 , k' , k'' and v_0 are noted on the Figure. A discrepancy exists between the plotted (34.56\AA^3) and EoS fitted (33.83\AA^3) value for v_0 , a percentage difference of 2.11%, a small but non negligible difference. The zero pressure data-point corresponded to a value not measured, instead this data was taken from the literature [?]. Refinement of the zero pressure value was allowed by the author to improve the quality of the EoS fit, and because this value was not measured by the author. The determined bulk modulus, $k_0 = 31.818\text{GPa}$ is in close agreement, within 9.5%, of the expected value of $k_0 = 28.8\text{GPa}$.

Attempts were made to crystallise a single crystal of Pr from a powder sample (using the Pr supplied by Ulrich Schwartz of the MPI, Dresden) using laser annealing to heat the sample to the melting point of Pr near the α -U phase transition. These attempts were however unsuccessful, with prepared, laser annealed samples remaining a powder, albeit with what appears to be larger grain size, showing promise for the technique. Further attempts at laser annealing were not possible. The author suspects (after discussion with colleagues, Dr. J Proctor and Dr. E. Gregoryanz) that the exposure

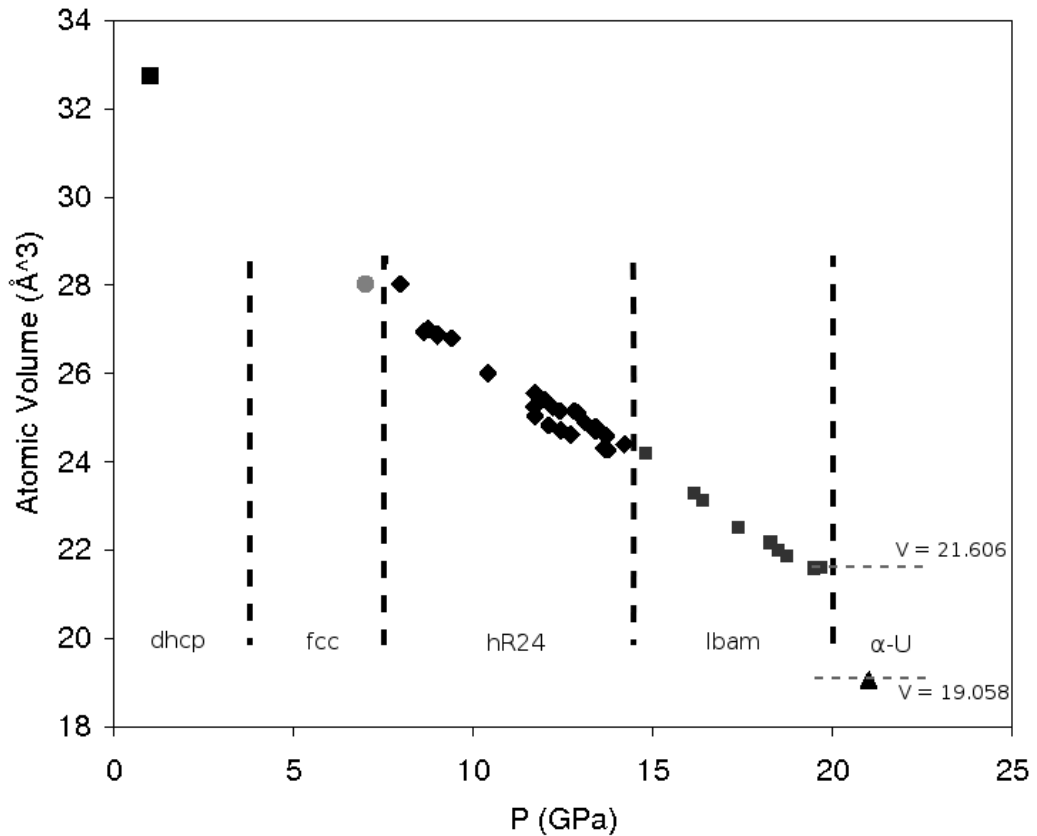


Figure 4.30: Plot of the atomic volume vs. pressure for the pressure range investigated in Pr. Alternating black and grey points are used to differentiate between data collected in different phases. The determined phase transition pressures are represented on the figure with dashed vertical lines, phases are labelled. The *d-fcc* phase is labelled as *hR24* and *lbam*, representing the respective solutions for the structure of the phase. On the right of the figure the volumes before and after the transition to the α -U phase are noted, a volume difference of 11% is observed at this transition. Data was collected on Station 9.5 of Daresbury SRS using a wavelength of $\lambda=0.44397\text{\AA}$.

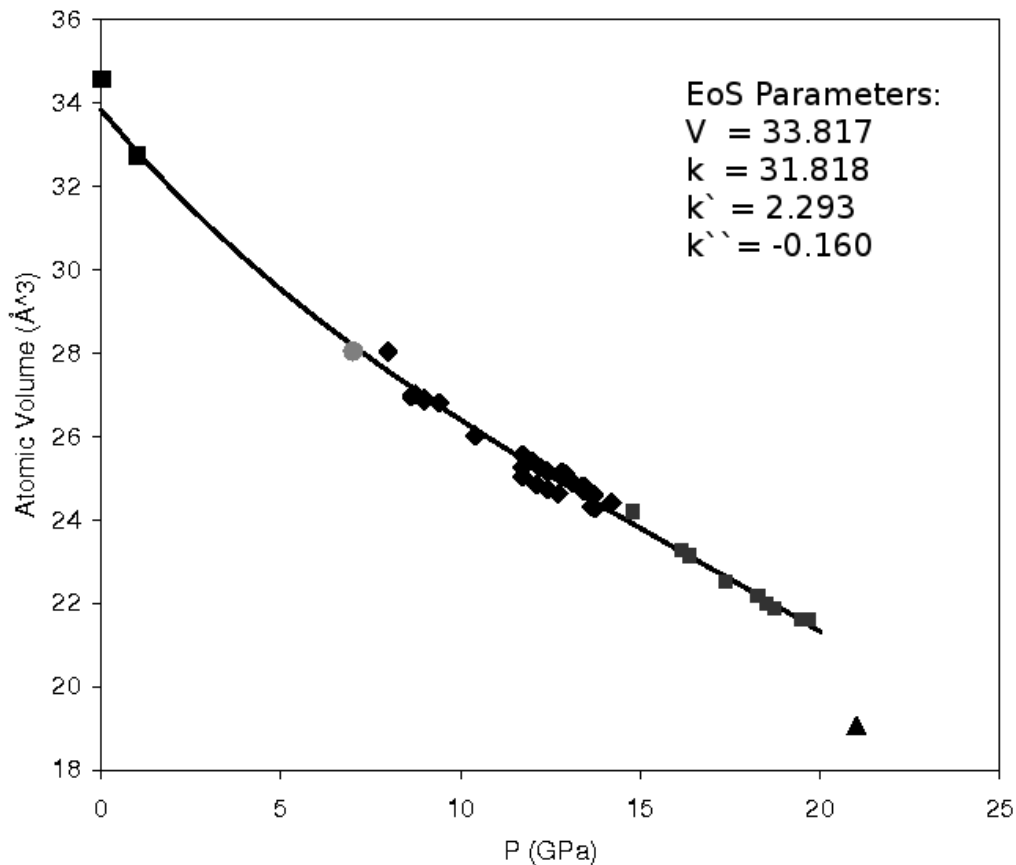


Figure 4.31: Plot of the atomic volume vs. pressure for the pressure range investigated in Pr with a fitted 3rd order Birch-Murnaghan equation of state (EoS) shown in black. The EoS, fitted using EOSFIT [Angel 01], has least-squares refined values of $k_0=31.81761$ GPa, $k'=2.29268$, $k''=-0.16018$ and $V_0=33.81656$ \AA^3 . The EoS was fitted from zero (ambient pressure) to 20GPa, owing to the volume discontinuity which occurs at 20GPa. Data collected from Station 9.5 of Daresbury SRS using a wavelength of $\lambda=0.44397\text{\AA}$. Errors plotted, but obscured by the size of the datapoints.

time of the Pr to IR laser may not have been sufficiently long to have completely melted the $30 \times 30 \mu\text{m}$ sample.

Chapter 5

Studies of Neodymium and Lanthanum

5.1 Introduction

A marked similarity can be observed in the high-pressure structural transition sequence of the lanthanides. Thus, it is expected that the behaviour which occurs in Nd is similar to that which was observed in Pr, as described in the previous Chapter.

This Chapter will take the form of a brief recap of the information presented in Chapter 3.2, which presents in greater detail a literature review of the Lanthanide series. Relevant studies from the literature, performed on Nd and La will be summarised in Section 5.2. The experimental details for work carried out in preparation for this Thesis are presented in 5.3. Having solved the structure of the Pr *d-fcc* phase in the previous chapter (Chapter 4), similar reasoning will be applied to solving the *d-fcc* phase of Nd in Section 5.6 and Section 5.8, as the author ascertains if the Pr and Nd *d-fcc* phases share common structures.

5.2 Brief review of Neodymium and Lanthanum

Nd shares the generalised lanthanide phase-transition sequence shown to exist throughout the lanthanides [Baer 03] as shown in Figure 3.2 [Johansson 75]. The phase diagram of Nd is reproduced from Tonkov [Tonkov 05] in Figure 5.1. Starting at ambient pressure and temperature Nd exhibits a *dhcp* structure (labeled as Phase II in Figure 5.1), reported as stable to ≈ 6 GPa, at which point a transition to *fcc* (Phase III) occurs. The *fcc* phase is stable to 12-18 GPa (depending on the source of reference in the literature) [Akella 99, Chesnut 00a], when the *fcc* (Phase III) \rightarrow *d-fcc* (Phase IV) transition occurs. Similar to reported structures in the literature for Pr, Nd is stated to have a *hR24* structure [Porsch 94a, Chesnut 00a, Velisavljevic 05] (which is denoted *thcp* in the work of [Akella 86]) for the *d-fcc* phase. Upon further compression to 40 GPa, the *d-fcc* phase is reported to transform to a *hP3* structure (Phase V) [Chesnut 00a]

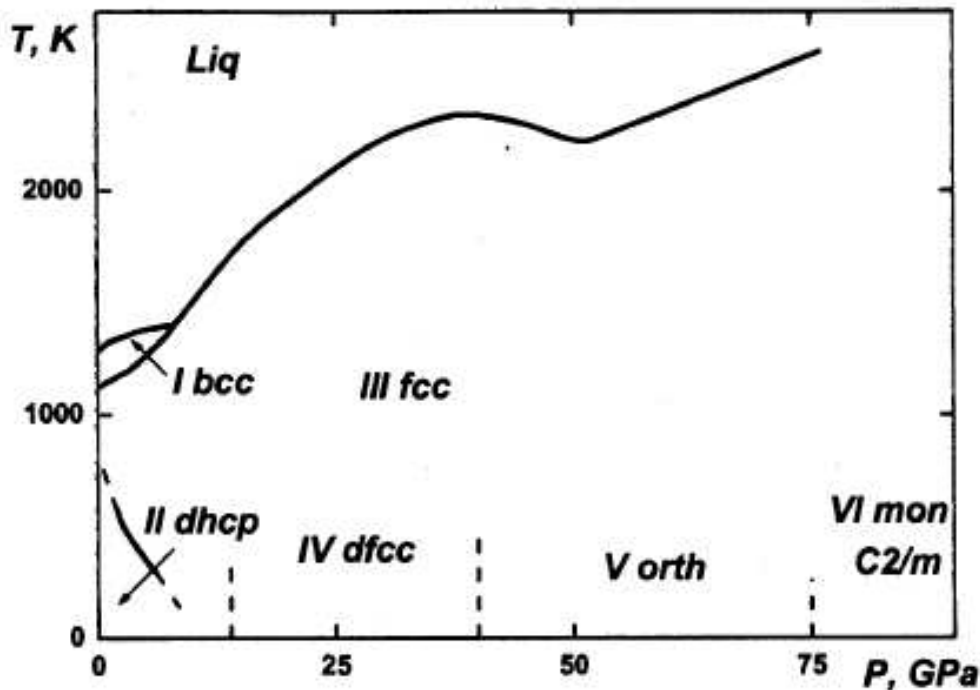


Figure 5.1: High-pressure and high-temperature phase diagram of Nd, reproduced from Tonkov [Tonkov 05].

structure. Following the transition to $hP3$ at 40GPa, there is a second-order transition to a $C2/m$ (Phase VI) structure at 75(5)GPa [Akella 99, Velisavljevic 05] before the $4f$ -delocalisation transition to a closed-packed, α -Uranium structure [Chesnut 00a] at 113(6)GPa (with no volume discontinuity). Velisavljevic *et al.* state the onset of α -U transition is observed at 118GPa by x-ray diffraction, but note that electrical resistivity measurements place the onset of the transition at 100GPa [Velisavljevic 05]. Velisavljevic *et al.* state the first pressure a single-phase diffraction pattern of the α -U phase is observed, is at 152GPa. Interestingly, Akella *et al.* [Akella 99], in their study (to 153GPa), did not observe a transition to the α -U phase.

This is intriguing, as studies of a high-pressure analogue, Pr, reported the $hP3$ and $C2/m$ structures as candidates for the Pr d -fcc phase (see Chapter 4.5). Both structures have, however, been shown to be incorrect structures for describing the d -fcc phase, by the author in Section 4. This begs the question as to whether the structural sequence in Nd and La possesses the same phases discovered in Chapter 4 to exist in Pr.

5.3 Experimental Details

5.3.1 Loadings

The neodymium used for this study was sourced from a commercial vendor, Alfa-Aesar (stated purity of 99.9%) and through colleagues (Ulrich Schwarz) at the Max Plank Institute (MPI), Dresden (stated purity of 99.99%). Nd, like Pr, has a high propensity to discolour (tarnish) in air, upon its surface an oxide coating rapidly forms, which is attributable to Nd_2O_3 [Winter 09, McCullough 50] and necessitating preparation of samples in an oxygen-free environment, be it under oil in a laboratory, or in a glovebox in an inert Ar atmosphere. This is the same procedure adopted for the loading of Pr (Chapter 4).

Samples were loaded into a MB or DXR6 type pressure cells with either 250 μm or 300 μm diamond culets; prepared with a 200 μm tungsten gasket, preindented to approximately 30 μm with a spark eroded sample chamber hole, 75 μm in diameter. Two ruby spheres of approximate size 5 μm enable the pressure to be measured using the ruby fluorescence method [Mao 86]. Mineral oil was used in all cells as a pressure transmitting medium. Where possible, samples were loaded within a glove box to prevent the contamination of samples upon exposure to air. Where this was not possible, for example, when reloadings needed to be made in Daresbury SRS without access to a glovebox, the loadings were performed under oil (as for Pr, described in Section 4.2).

Data from the cells loaded with Nd and La were collected by angle-dispersive x-ray diffraction methods on Station 9.5 of Daresbury SRS, using the In K-edge, giving $\lambda = 0.44396\text{\AA}$. Pressure cells were mounted on the motorised stage, as described in Section 2.5.3.1, with the sample-to-detector distance set at approximately 300mm. This distance was calibrated exactly using a Si reference sample, as noted in Section 2.5.3.1, the use of which also allows the tilt (of the detector surface away from the vertical) to be refined in the software package Fit2D [Hammersley 98].

5.4 Contaminants

As noted earlier in Chapter 3, the high reactivity of the lanthanides leads to a propensity to react upon exposure to moisture or air. Curiously, however, comments within the literature pertaining to the presence of contaminants within samples are not present

(for both Nd and La). Citing the work of Akella *et al.* as an example, the diffraction pattern shown in Figure 3 of [Akella 99], Nd at 89 GPa (collected as an EDX pattern as opposed to the ADX methods employed during this thesis), has an unlabelled peak at approximately 31 keV which the authors attribute to neither sample, gasket, “escape peak”, pressure medium, or to the pressure calibrant used. The origin of this peak can be postulated to arise either from an unidentified contaminant, as Akella ascertains the structure at this pressure is $C2/m$ (yet fails to provide an adequate means of assessing the quality of the $C2/m$ structure as a model for Nd at this pressure), or that the peak originates from the sample and (like in the case for Pr) it is indicative of a poorly-chosen structural model for Nd at this pressure.

In all data collected for this thesis from Nd (from multiple experiments at Station 9.5 of Daresbury SRS), on both compression and decompression, contaminant peaks are observed. Precautions were taken to minimise the appearance of contaminants through exposure to air and moisture during the sample preparation and loading stage of each experiment, as discussed in Section 5.3.1. Observed in the data are contaminant peaks, as highlighted in Figure 5.2, which occur in pairs, with distinct d-spacings, which are consistent with two *fcc* lattices, suggesting, as with Pr, that two cubic contaminants are present.

As observed in Pr, contaminant peaks are readily identifiable in 2D diffraction patterns collected with the Mar345 detector. That is, the contaminants have diffraction rings which are weak in intensity, and appear textured (whereas diffraction rings originating from the sample have a more uniform intensity distribution around the diffraction ring). Also, from observing the evolution of the contaminant peaks upon pressure increase, it can be seen that the contaminant has a lower compressibility than the sample, as also observed for the contaminants present in Pr (see Section 4.3).

However, overlap between the sample and contaminant peaks obscures the weak contaminant peaks in many of the diffraction patterns, preventing more than 2 or 3 of them from being observed. As such, the author speculates from comparison to the Pr contaminants that the contaminant has an *fcc* structure.

The structure of Nd was not studied below 1.6GPa during the experiments performed for this thesis. The ambient-pressure values for the lattice parameters of the contaminant(s) cannot therefore be provided from direct measurement. Extrapolation

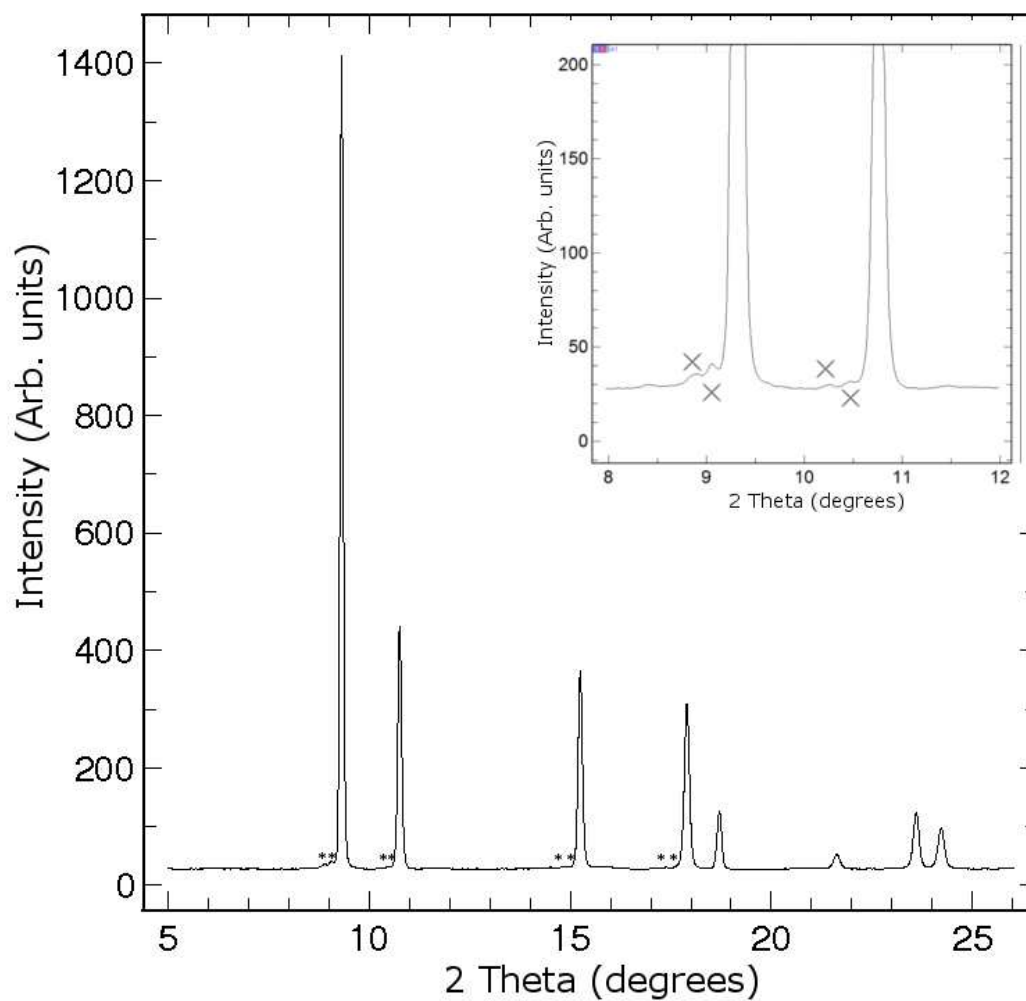


Figure 5.2: Integrated 1D diffraction profile of Nd collected at 11.6 GPa from a sample in a DXR6 type DAC on Station 9.5 of Daresbury SRS, using a wavelength of $\lambda=0.44397\text{\AA}$. Contaminant peaks are highlighted with asterisks in the main diffraction profile. The inset shows an enlarged region of the diffraction profile, between 8 and 12° in 2θ , with contaminant peaks indicated by crosses.

of the lattice parameters to zero pressure has instead been made by the fitting of a 3rd order Birch-Murnaghan equation of state [Birch 47] using EOSFIT [Angel 01] to measured values of the contaminant's lattice parameters.

Parameter	Value
a	3.5394(2)Å
c	11.5867(1)Å
Volume	129.5846(3)Å ³
Volume/atom	32.3961(3)Å ³
$\frac{a}{c}$	0.3101(1)
U_{iso1}	0.0237(13)
U_{iso1}	0.0247(12)

Table 5.1: Table showing the structural parameters of the *dhcp* phase of Nd, as refined from a pattern collected at 1.7GPa on Station 9.5 of Daresbury SRS, using a wavelength of $\lambda=0.44397\text{\AA}$. Reitveld refinement is shown in Figure 5.4.

5.5 Structures of Neodymium below 16GPa

Figure 5.3 shows a waterfall plot of a subset of the data collected from Nd. Patterns from this figure are chosen to be representative of the phases observed, and were collected during two experiments on pressure increase. Evident from Figure 5.3 are three distinct regions, each attributable to a different high-pressure phase of Nd.

The ambient-pressure, room-temperature structure observed in Nd is *dhcp*, with $a = 3.657\text{\AA}$, and $c = 11.799\text{\AA}$. Like the other lanthanides, the *dhcp* phase in Nd has a $P6_3/mmc$ spacegroup with 4 atoms on the $2a$ ($(0, 0, 0)$ and $(0, 0, \frac{1}{2})$) and $2c$ ($(\frac{1}{3}, \frac{2}{3}, \frac{1}{4})$ and $(\frac{2}{3}, \frac{1}{3}, \frac{3}{4})$) positions within the unit cell as reported by previous authors [Tonkov 05, Akella 86]. A Rietveld refinement of a *dhcp* diffraction pattern collected at 1.7GPa is presented in Figure 5.4. It can be seen that the *dhcp* structure yields an excellent fit ($R_{wp}=11.16\%$) to the data, the refined lattice parameters are presented in Table 5.1.

On pressure increase from ambient pressure (at room temperature), Nd is observed to undergo a second-order phase transition at 3.8(10)GPa from the ambient-pressure *dhcp* structure to *fcc* (shown in Figure 5.3). The transition pressure is determined as the mid-point of the pressures of the highest-pressure single-phase example of the precursor phase and the lowest pressure single-phase example of the new phase as observed on pressure increase. Thus, a number of distinct transition pressures taken in this way during six separate experiments can be averaged to give a transition pressure of 3.9(2)GPa. Comparing this determined transition pressure with that reported in the literature, 3.8GPa [Akella 86] shows a close agreement, with the measured value lying within errors bounds of the literature value.

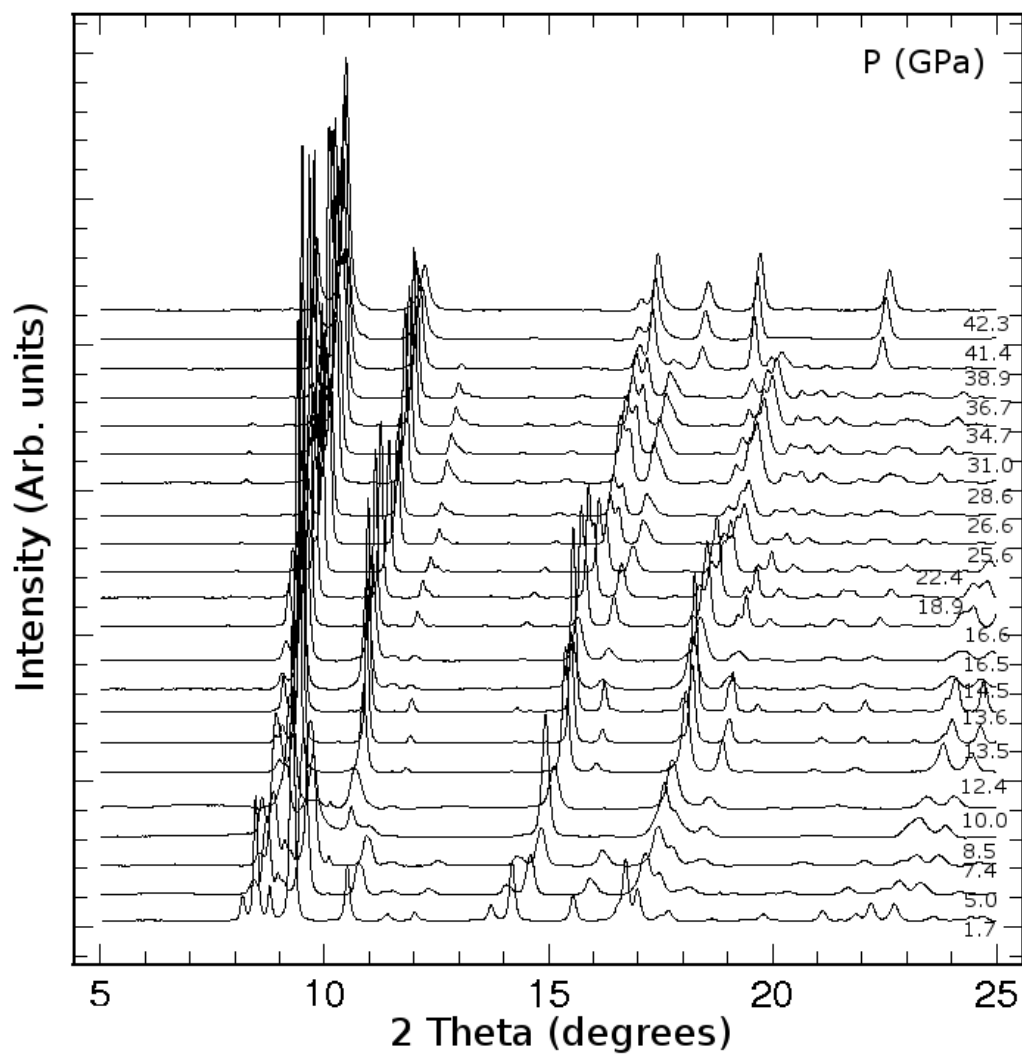


Figure 5.3: Waterfall plot of integrated 1D diffraction profile representative of the phases observed on compression of Nd from 1.7-42GPa. Pressures of the individual patterns are listed to the right of each diffraction pattern. Data were collected on Station 9.5 of Daresbusy SRS using a wavelength of $\lambda=0.44397\text{\AA}$.

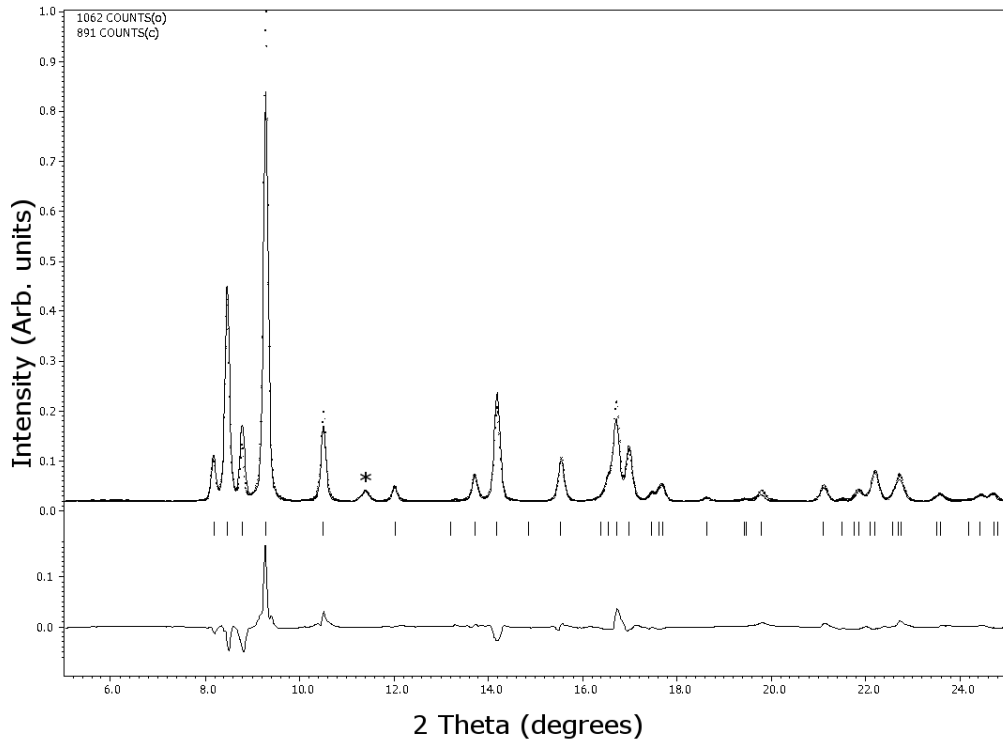


Figure 5.4: Rietveld refinement of a Nd *dhcp* pattern collected at 1.7GPa on Station 9.5 of Daresbury SRS, using a wavelength of $\lambda=0.44397\text{\AA}$. A mineral oil pressure transmitting medium was used. $R_{wp} = 11.16\%$. The unit cell parameters are: $a = 3.5394(2)\text{\AA}$ and $c = 11.5867(1)\text{\AA}$. An asterisk indicates the position of the contaminant peak within the sample.

Parameter	Value
a	4.7431(1)Å
Volume	106.7194(10)Å ³
Volume/atom	26.6798(10)Å ³
$\frac{a}{c}$	1 (or 2.4495 in hexagonal setting)
U _{iso1}	0.0538(7)
U _{iso1}	-0.0119(20)

Table 5.2: Table showing the structural parameters of the *fcc* phase of Nd, as refined from a pattern collected at 12.3GPa on Station 9.5 of Daresbury SRS, using a wavelength of $\lambda=0.44397\text{\AA}$. Reitveld refinement is shown in Figure 5.5.

The pressure-evolution of the *dhcp* structure, while not of primary importance in this study, was observed through to the transition to *fcc*. The *dhcp* phase changes continuously with pressure increase, with some peaks decreasing in intensity until 3.8GPa, at which point a *fcc* pattern remains. No measurable volume change is observed at the transition from the *dhcp* to the *fcc* phase.

The *fcc* phase of Nd has atoms located in the $4a$ site, and Rietveld refinement of patterns collected above 4GPa confirm the structure to be *fcc*. An example of such a Rietveld refinement is shown in Figure 5.5. Note the excellent quality of the fit, which results in the low R_{wp} of 4%. The lattice parameters at 12.3GPa are $a=b=c=4.7431(1)\text{\AA}$. This data is summarised in Table 5.2. As shown in Figure 5.6, the volume of the *fcc* phase decreases steadily (approximately linearly) from 27.0589(40) to 24.4574(3)Å³ over its stability range.

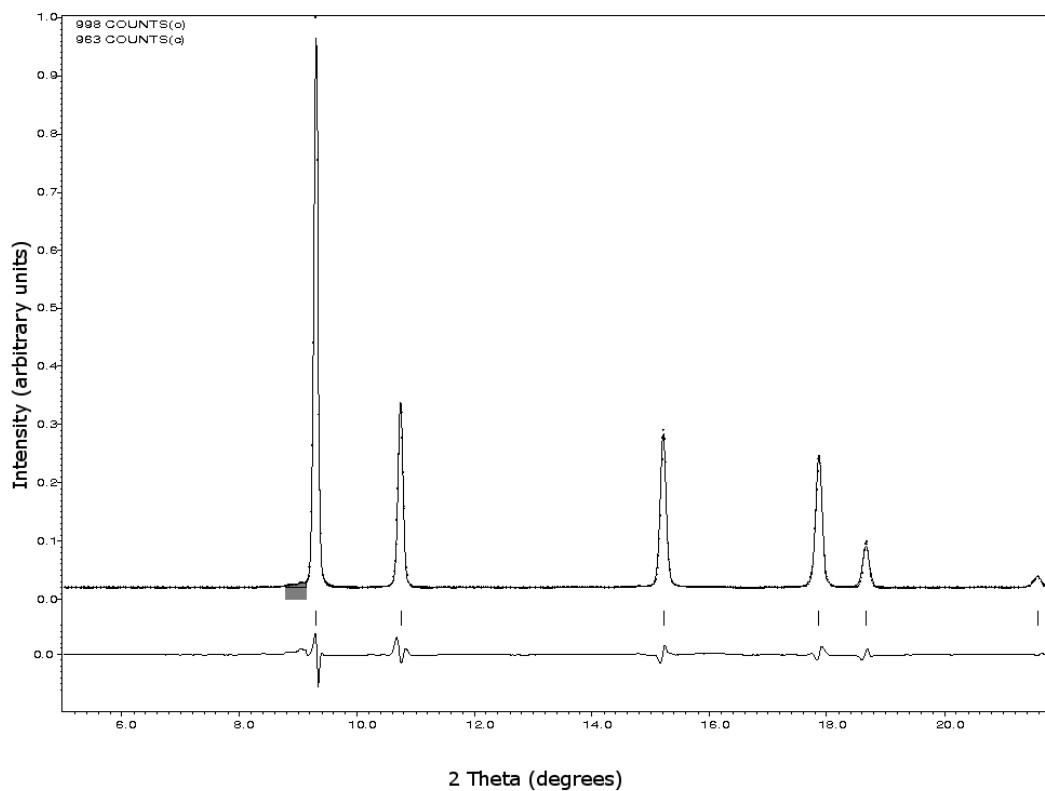


Figure 5.5: Rietveld refinement of the *fcc* phase of Nd collected at 12.3GPa on Station 9.5 of Daresbury SRS, using a wavelength of $\lambda=0.44397\text{\AA}$. A mineral oil pressure medium was used, with ruby spheres as a pressure manometer within the sample chamber. The unit cell parameters are $a = b = c = 4.74309(5)\text{\AA}$, $R_{wp}=4\%$.

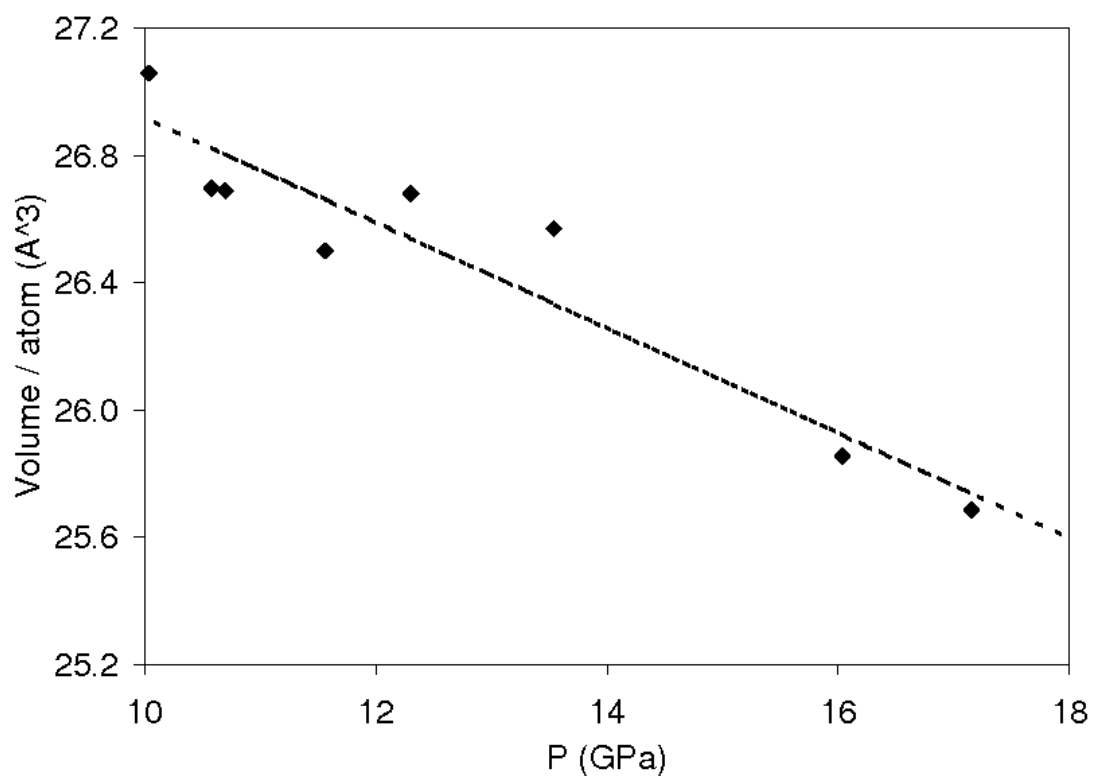


Figure 5.6: Plot showing the atomic volume plotted against pressure for the *fcc* phase of Nd. Data were collected on Station 9.5 of Daresbury SRS, on both pressure increase and pressure decrease, during different experiments. Errors in the volume at each pressure are of the order $\times 10^{-4} \text{ \AA}^3$ and as such are not visible on the plot. A guide to the eye (fitted using a linear least squares routine) is also shown.

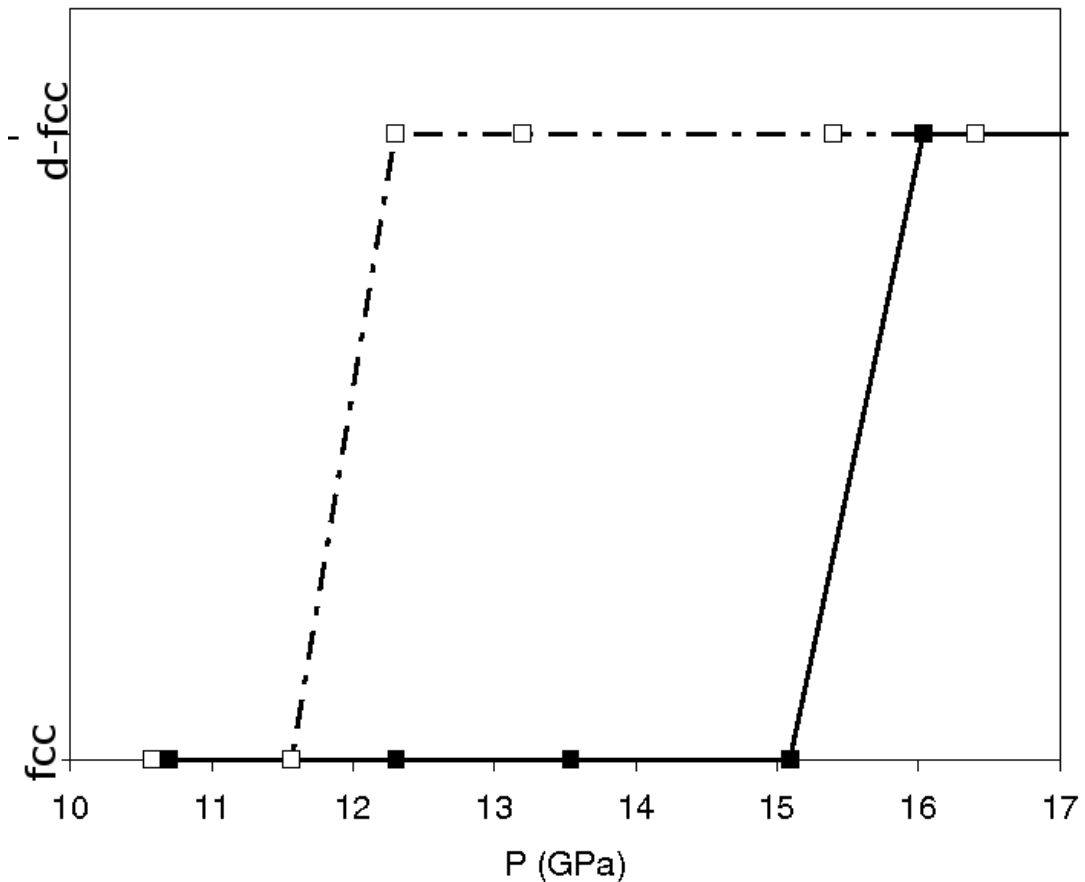


Figure 5.7: Diagram illustrating the hysteresis observed in the *fcc* to *d-fcc* transition on pressure increase and decrease. The data shown were collected from a single sample during an experiment on Station 9.5 of Daresbury SRS, using a wavelength of $\lambda=0.44397\text{\AA}$. Open squares represent data collected on pressure decrease, filled squares represent data collected on pressure increase.

5.6 Structure of *d-fcc* Neodymium

The *fcc* phase remains stable up to 16.6GPa on pressure increase, as shown in Figure 5.8. Above 16.6GPa a number of additional peaks appear and the *fcc* (111) and (200) peaks split. Observation of the transition back to the *fcc* phase of Nd upon decompression reveals a large degree of hysteresis in the transition pressure, with Figure 5.8 highlighting the splitting of the (111) peak from the *fcc* structure, and presence of superlattice reflections originating from the *d-fcc* phase until 11.5GPa on pressure decrease. The transition from *fcc* \rightarrow *d-fcc* on increasing pressure is measured

to be 18(1)GPa, in agreement with previous work [Akella 99, Chesnut 00a] who report a transition pressure to *d-fcc* at 18 and 17GPa, respectively. The observation of hysteresis in the transition from *fcc* \rightarrow *d-fcc* is surprising, as Porsch and Holzapfel [Porsch 94b] state that all transitions in the regular lanthanide sequence, *excluding* the *fcc* \rightarrow *d-fcc* transition, are “accompanied by a perceptible hysteresis”. It was noted in Chapter 4 that similar hysteresis in this transition is observed for Pr.

Peaks identifiable as strong intensity singlets, or obviously-resolvable doublets from the *d-fcc* profile shown in Figure 5.9 were indexed in DicVol [Louer 04]. Prior to indexing, the locations of the peaks to be used for indexing were determined by profile fitting in DatLab [Syassen 08b]. Suggested by DicVol are a number of monoclinic and hexagonal structures, as for Pr (described earlier). These structures correspond to those previously reported as solutions for the *d-fcc* phase of Pr, the *C2/m* [Syassen 00], *P2/m* [Dmitriev 00] and *R $\bar{3}m$* [Hamaya 93] structures.

Attempts were made to refine the a pattern collected in shown in Figure 5.9 using the *hR24*, *C2/m* and *P2/m* models suggested by [Velisavljevic 05, Chesnut 00a] and [Dmitriev 00] (for Pr) and [Syassen 00] (for Pr) respectively. Reports in the literature for Nd, however, consistently state that the *hR24* (*R $\bar{3}m$*) structure is the solution to the *d-fcc* phase for Nd.

Using a LeBail refinement (to gauge the best possible fit to be expected using this structure, as at this model-testing stage, misfits, peak overlap and unexplained peaks are of primary interest) of the *C2/m* structure to a *d-fcc* pattern of Nd collected at a pressure of 22.4GPa is shown in Figure 5.10, with refined lattice parameters given in the figure caption. The refinement, whilst having a low $R_{wp} = 5.69\%$, fails to account for a number of low-intensity reflections found in the diffraction pattern, examples of which are the peaks located at $\approx 13.9^\circ$ and 21.5° as highlighted in Figure 5.10. This inability to account for low-intensity peaks (in similar relative locations) was observed in Pr.

Lowering the symmetry of the *C2/m* structure by removing the C-centering condition gives the *P2/m* structure, which was also given as a solution for Pr [Syassen 00]. A LeBail refinement using this structure to the same 22.4GPa Nd pattern as used for the *C2/m* refinement is shown in Figure 5.11. Lattice parameters are noted in the figure caption. The lower symmetry *P2/m* structure displays a lower R_{wp} , $R_{wp} = 4.28\%$, and is able to account for all of the observed sample reflections. However, as was the

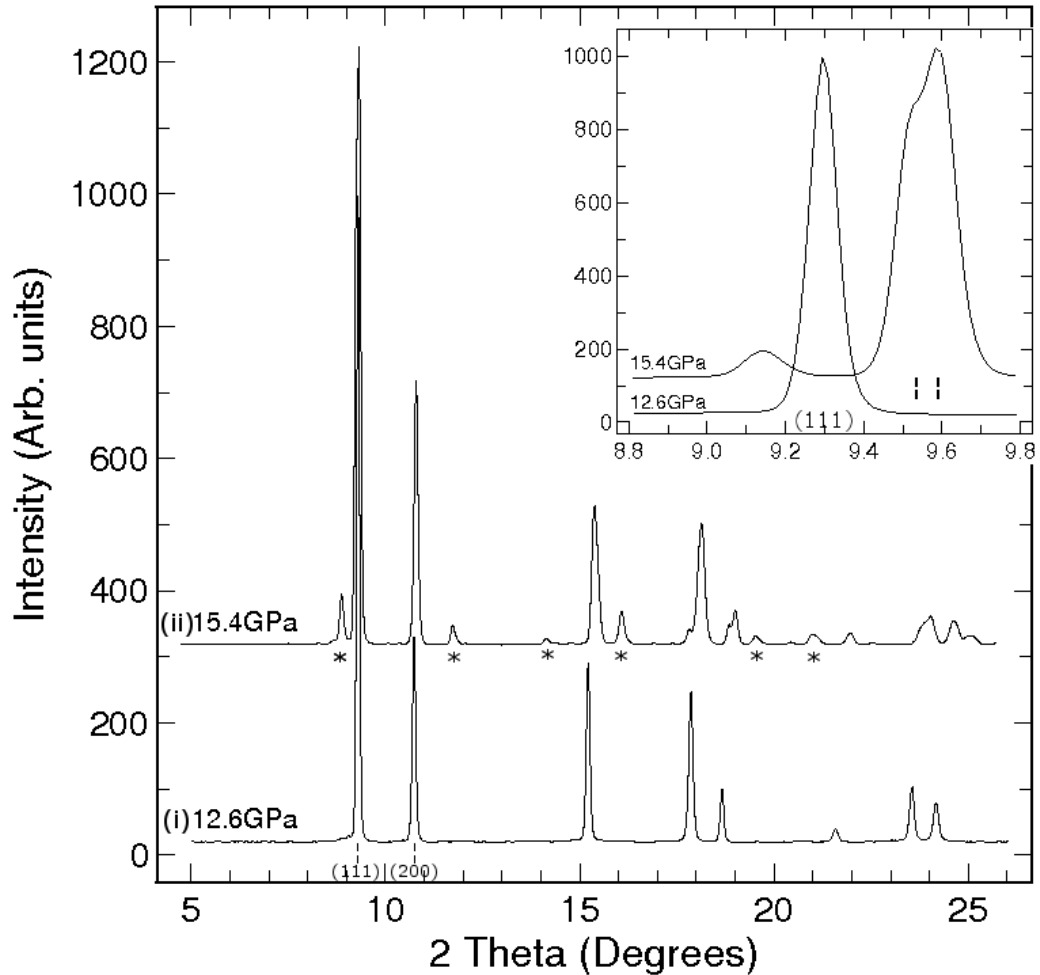


Figure 5.8: Two integrated diffraction patterns from Nd, collected at (i) 12.6GPa and (ii) 15.4GPa. The pattern in (i) is within the *fcc* phase, while that of (ii) is in the *d*-*fcc* phase. Note the splitting of the *fcc* (111) and (200) peaks and additional peaks appearing in (ii). This splitting is highlighted (by tick marks below the diffraction patterns) in the inset, which shows an the region around the *fcc* (111) reflection for both the 12.6GPa and 15.4GPa diffraction pattern shown in main body of the figure. The pattern presented in (ii) is shifted by -0.27° in 2θ , such that the main peaks are approximately aligned in both patterns. Data for this figure were collected on Station 9.5 of Daresbury SRS, using a wavelength of $\lambda=0.44397\text{\AA}$

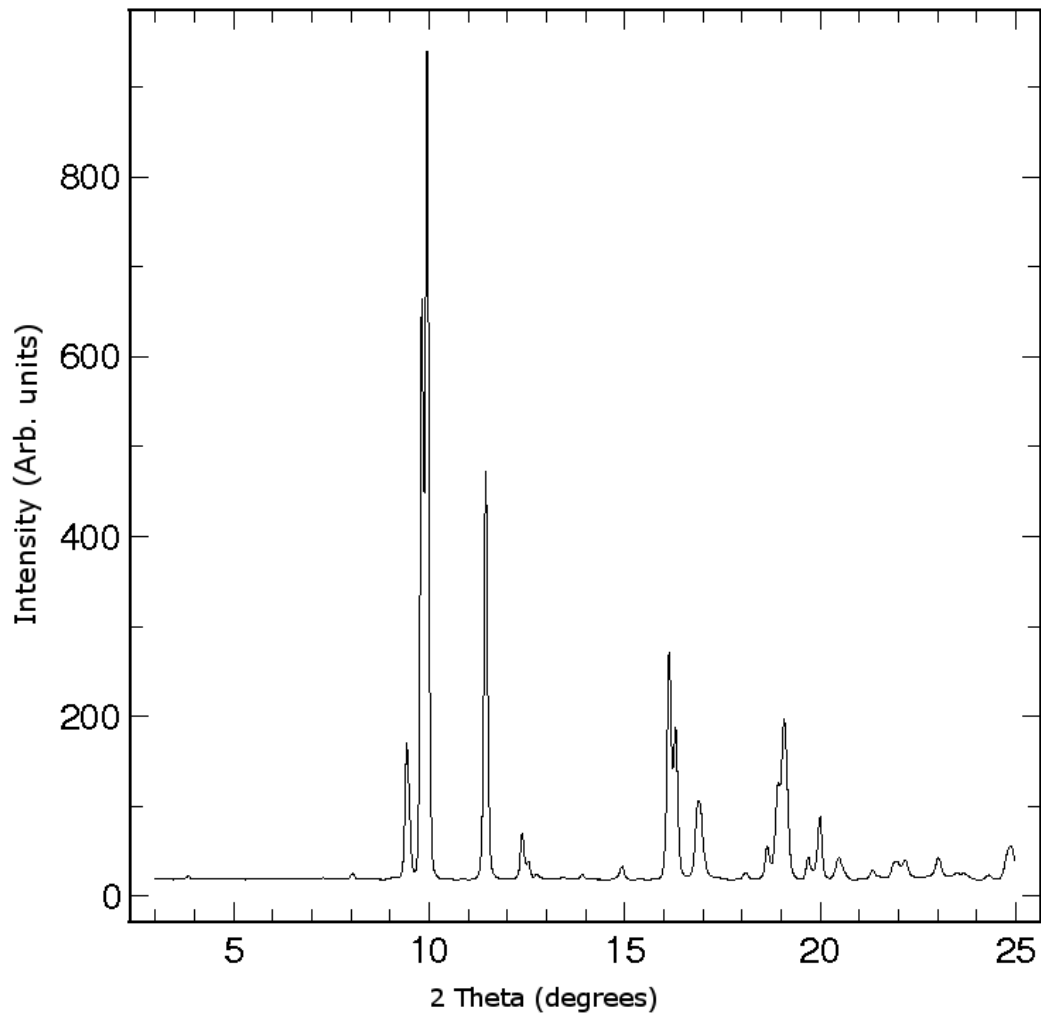


Figure 5.9: Background-corrected *d-fcc* Nd pattern collected at 22.4GPa on Station 9.5 of Daresbury SRS, using a wavelength of $\lambda=0.44397\text{\AA}$.

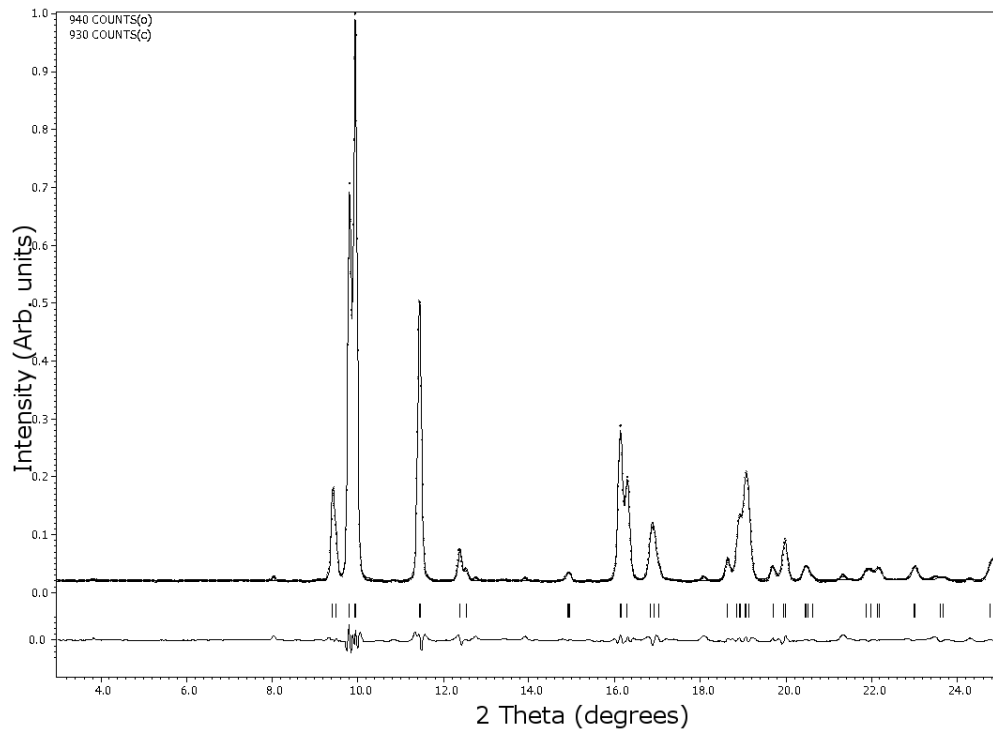


Figure 5.10: LeBial refinement of a Nd *d*-fcc pattern collected at 22.4GPa on Station 9.5 of Daresbury SRS using the $C2/m$ structural solution. Refined lattice parameters are $a = 5.5010(2)\text{\AA}$, $b = 3.1328(2)\text{\AA}$, $c = 5.4232(3)\text{\AA}$, and $\beta = 109.295(5)^\circ$. $R_{wp} = 5.69\%$ for this LeBial refinement. A wavelength of $\lambda=0.44397\text{\AA}$ was used to collect this data.

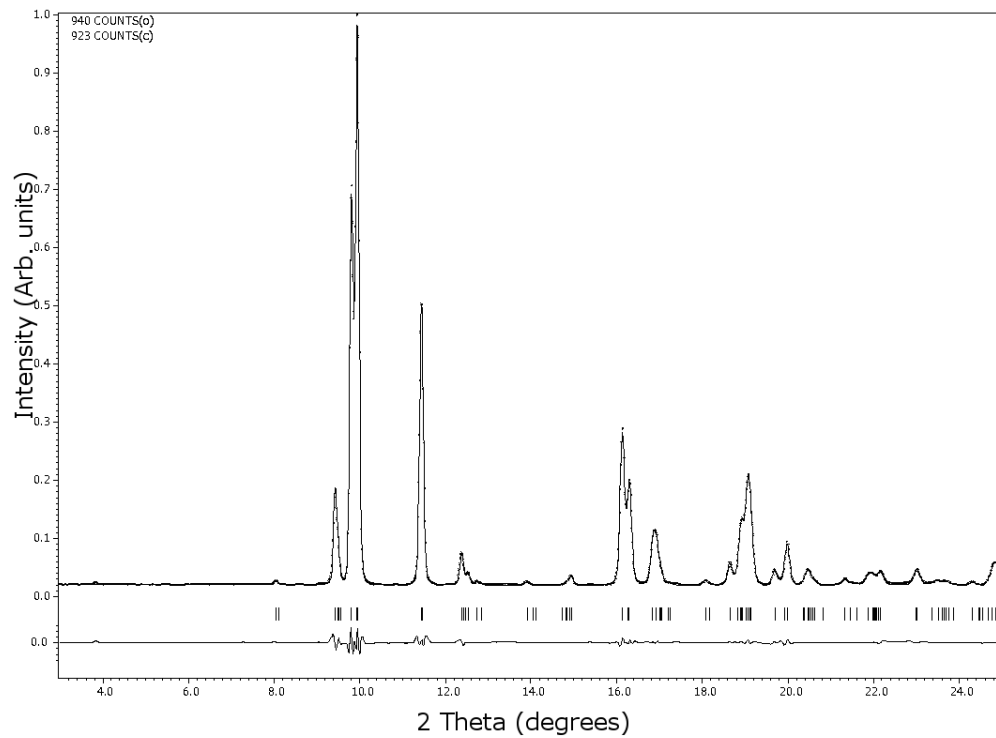


Figure 5.11: Refinement made to a Nd *d-fcc* pattern collected at 22.4GPa from Station 9.5 of Daresbury SRS using the *P2/m* structural solution. Refined lattice parameters are $a = 5.4988(2)\text{\AA}$, $b = 3.1373(2)\text{\AA}$, $c = 5.4198(2)\text{\AA}$, and $\beta = 109.217(4)^\circ$. $R_{wp} = 4.28\%$ for this LeBial refinement. A wavelength of $\lambda=0.44397\text{\AA}$ was used to collect this data.

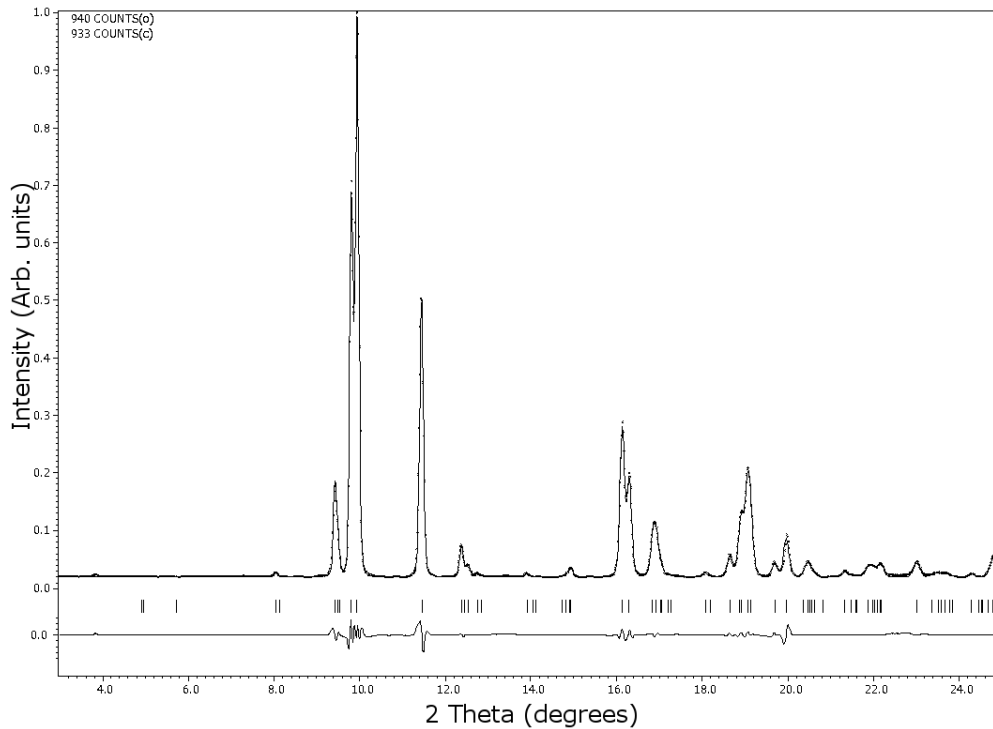


Figure 5.12: Refinement made to a Nd *d*-fcc pattern collected at 22.4GPa from Station 9.5 of Daresbury SRS using the *hR24* structural solution. Refined lattice parameters are $a = b = 6.2640(1)\text{\AA}$, $c = 15.5776(3)\text{\AA}$. $R_{wp} = 5.14\%$ for this LeBial refinement. A wavelength of $\lambda=0.44397\text{\AA}$ was used to collect this data.

case for Pr, this lower-symmetry solution predicts a majority of the observed peaks to be doublets or triplets, and no evidence of this is seen. Furthermore, most of these multiplets are comprised of zero intensity reflections.

A LeBail refinement using the *hR24* structure to the same 22.4GPa diffraction pattern used for the *C2/m* and *P2/m* is shown in Figure 5.12. Refined lattice parameters are given in the figure caption. It can be seen from this refinement that the *hR24* structure is able to account for all of the peaks present from the sample. Unlike the *P2/m* structure, this is possible without making a majority of the observed peaks into multiplets and necessitating many zero-intensity reflections. In describing the *d*-fcc phase, the *hR24* structure requires fewer refinable parameters (2 in a Lebial fit, 5 in a Rietveld refinement. The *P2/m* requires 4 refinable parameters in a Lebial, 8 in a Rietveld refinement), as such it offers a simpler and higher symmetry solution to the observed data. Thus, the *d*-fcc phase of Nd is best described using the *hR24* structure as described in the literature [Velisavljevic 05], [Chesnut 00a].

Parameter	Value
a	6.2639(2)Å
c	15.5773(5)Å
Volume/atom	22.0508(15)Å ³
$\frac{c}{a}$	2.4871
x ₁	0.4909(2)
z ₁	0.2575(2)
z ₂	0.2277(2)
U _{iso1}	0.0037(8)
U _{iso1}	0.0087(15)

Table 5.3: Table showing the structural parameters of the *fcc* phase of Nd, as refined from a pattern collected at 12.3GPa on Station 9.5 of Daresbury SRS, using a wavelength of $\lambda=0.44397\text{\AA}$. Reitveld refinement is shown in Figure 5.5.

5.7 Pressure Dependence of *hR24* Neodymium

A Rietveld refinement of *d-fcc* Nd, using the *hR24* structure is shown in Figure 5.13, with structural parameters summarised in Table 5.3. As stated in the previous section, the *hR24* structure represents the best-fitting, simplest structure to the data, while also remaining consistent with observations made in the literature and accounting for all of the observed peaks.

The *hR24* structure was used as the structure model for Rietveld refinements made of all of the patterns collected within the *d-fcc* pressure range. Figure 5.14 shows the pressure variation of the *c/a* ratio for Nd over the stability range of the *hR24* phase on pressure increase ($\approx 14\text{GPa}$ to 22.4GPa), and pressure decrease (22.4GPa to 12GPa). Evident from this plot is a non-linear increase of the *c/a* ratio from 2.449 ($\sqrt{6}$) from the *fcc* phase to a maxima of 2.487 at 22.4GPa ; the shape of this graph is comparable to the behaviour of the *c/a* ratio of Pr (shown in Figure 4.15).

The atomic volume of Nd in the *hR24* phase decreases approximately linearly (to first order), as shown in Figure 5.15, from a maxima of $26.0812(6)\text{\AA}^3$ (at 12.3 GPa) to $22.0508(15)\text{\AA}^3$ (at 22.4 GPa). The maximum value here was measured on pressure decrease from the *hR24* phase to the *fcc* phase, in a pressure cell which had been cycled in pressure. The volume minima was observed on pressure increase in a different loading. There is a degree of scatter amongst the recorded data, in Figure 5.15, where different-shaped symbols are used to identify different loadings, each with

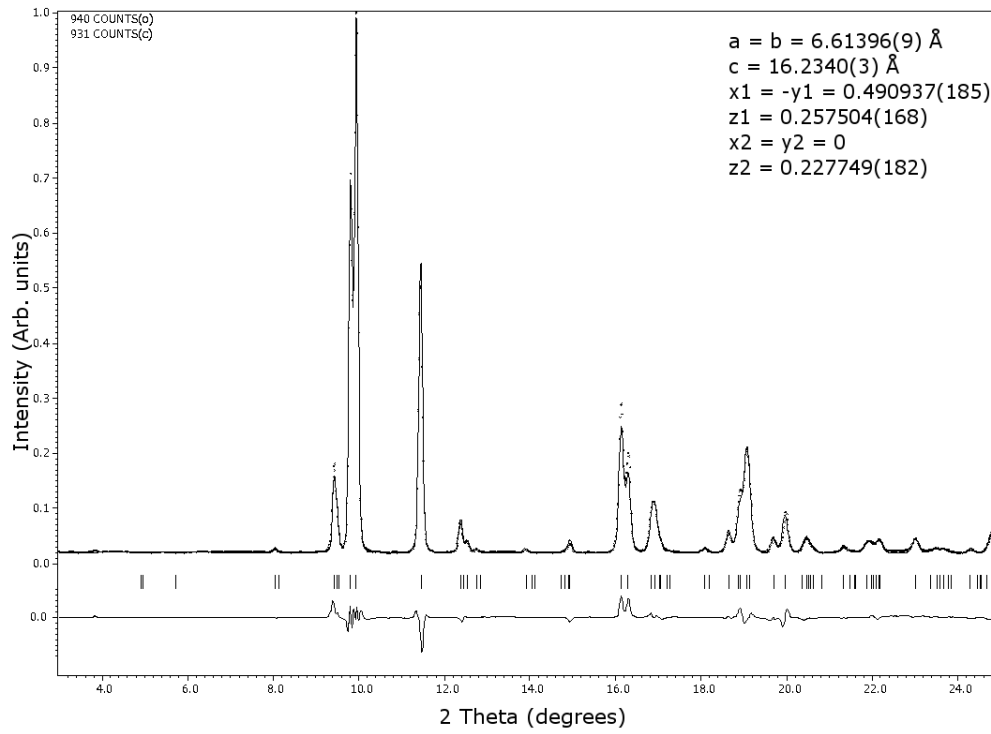


Figure 5.13: Rietveld refinement of Nd d - fcc phase using the $hR24$ structure to an x-ray diffraction pattern collected at 22.4GPa at Station 9.5 of Daresbury SRS, with a wavelength of $\lambda=0.44397\text{\AA}$. Refined lattice parameters are $a = b = 6.61396(9) \text{ \AA}$, $c = 16.2340(3)\text{\AA}$. Atomic positions are $x_1 = -y_1 = 0.4909(2)$, $z_1 = 0.2575(2)$, $x_2 = y_2 = 0$, $z_2 = 0.2277(2)$. $R_{wp} = 7.63\%$ for this refinement.

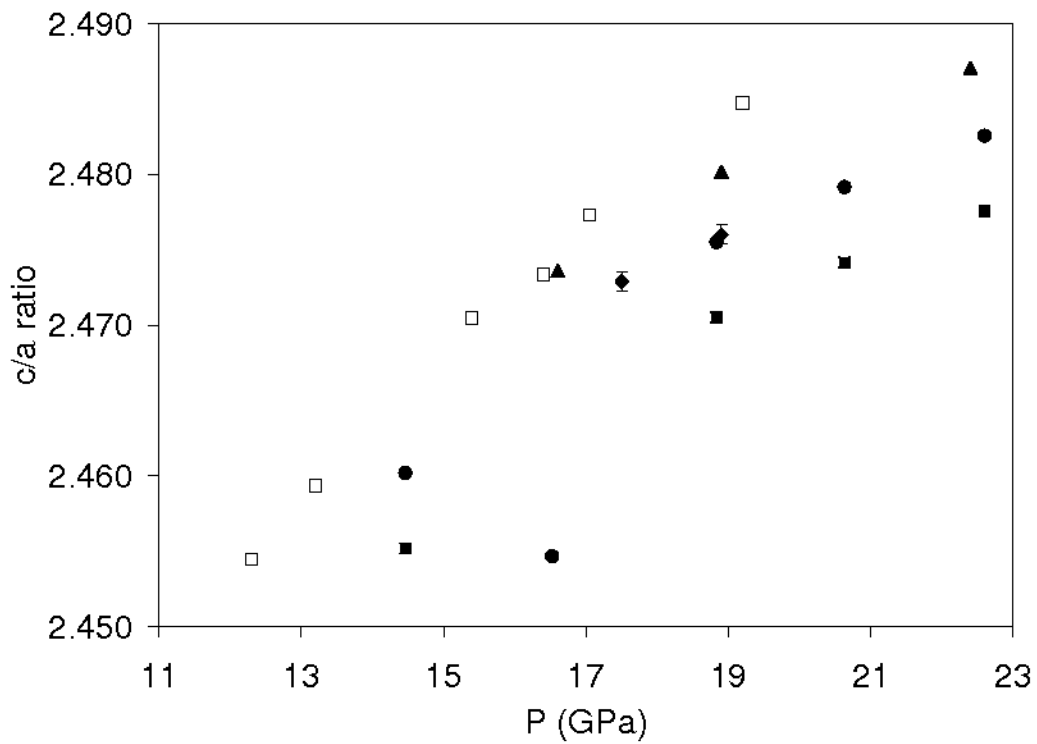


Figure 5.14: Variation of the c/a ratio for the $hR24$ phase of Nd, between 12.3 and 22.4GPa on both pressure decrease (open squares) and pressure increase (all filled symbols). The c/a ratio of the precursor fcc phase for comparison is $\sqrt{6}$, or 2.449. Data were collected on Station 9.5 of Daresbury SRS using a wavelength of $\lambda=0.44397\text{\AA}$.

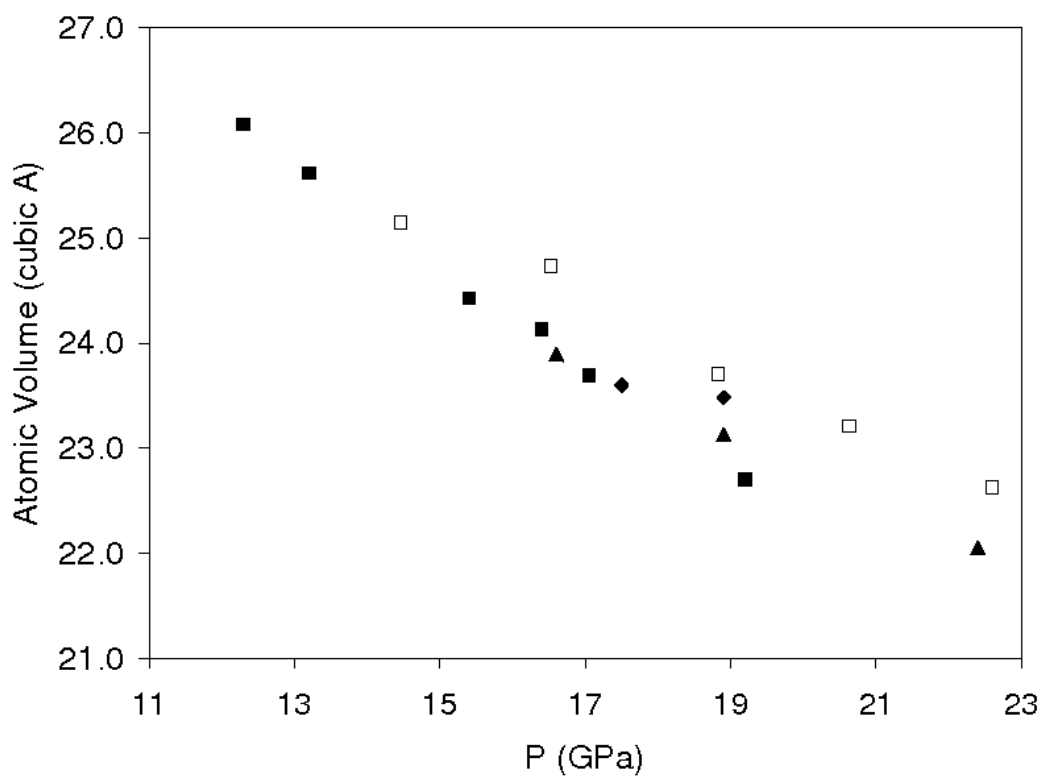


Figure 5.15: Variation of the atomic volume Nd in the stability range of the $hR24$ phase (between 12.3 and 22.4GPa), on both pressure decrease (open squares) and pressure increase (all filled symbols). Different filled symbols correspond to data collected from different loadings of Nd. Data was collected on Station 9.5 of Daresbury SRS using a wavelength of $\lambda=0.44397\text{\AA}$.

mineral oil pressure transmitting medium, and $300\mu\text{m}$ diamond culets. The open-square datapoint at 16.5GPa in Figure 5.15 is considered by the author as an outlier, as the pressure measured before and after the exposure to the x-ray beam for this point differed considerably ($\approx 5\text{GPa}$), possibly due to rapid pressurisation with insufficient time allowed for the pressure inside the sample chamber to equilibrate.

A plot of the variation of the atomic positions x_1 , z_1 and z_2 with pressure is shown in Figure 5.16, which plots data collected on pressure increase (filled square and triangle symbols) and pressure decrease (open square symbols). For x_1 , as pressure increases the atomic position decreases continuously away from the *fcc* position (0.5) in the *hR24* setting, towards a minima of 0.4918 at 23.8GPa (the atomic position in the following phase). z_1 increases steadily away from the *fcc* position of 0.25, while z_2 decreases away from the *fcc* atomic position of 0.25. For z_1 and z_2 , the triangular (increasing pressure) data points show a marked deviation from the other data sets. The data for these points were collected before annealing the sample, and on rapid pressurisation, and this could explain their departure from the trend established by the other data points. Hysteresis is evident on this figure from the separation of the data points collected on increasing and decreasing pressure.

The structure of the *d-fcc* phase of Nd has been widely reported in the literature as *hR24*, which this author confirms up to $\approx 23\text{GPa}$. Above this pressure distinct changes occur in the integrated diffraction patterns, as will be discussed in Section 5.8, along with a reduction in the observed quality of the *hR24* Rietveld refinements.

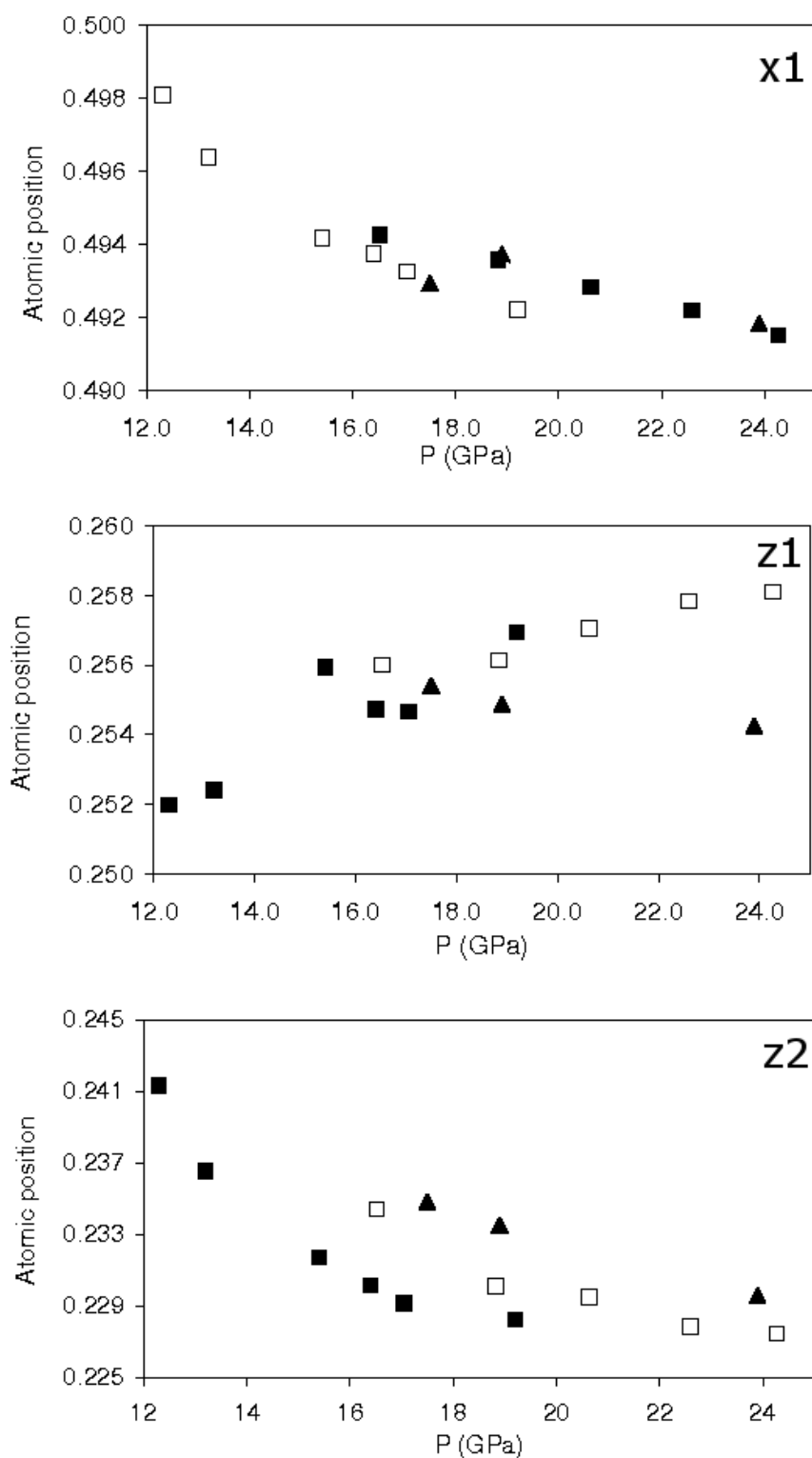


Figure 5.16: Variation of the refinable atomic positions Nd in the stability range of the $hR24$ phase, between 12.3 and 22.4 GPa (a data point at 24 GPa is shown for comparison of the atomic position in the following phase). The refinable atomic position x_1 , z_1 and z_2 are shown in different plots, for clarity. Filled square and triangle data points are collected on pressure increase, open squares on pressure decrease. Data was collected on Station 9.5 of Daresbury SRS using a wavelength of $\lambda=0.44397\text{\AA}$.

5.7.1 Comparison to Praseodymium

The structure adopted in the low pressure region, 16 to ≈ 22 GPa of the *d-fcc* phase of Nd has been shown to be the same as for Pr, a $hR24$ structure (spacegroup $R\bar{3}m$ with atoms on $6c$ and $18h$ sites). The pressure dependence of the lattice parameters and c/a ratio are shown to follow a similar trend to that shown previously in Pr, increasing away from the $\sqrt{6}$ value of the *fcc* precursor phase. The pressure dependence of the refinable atomic co-ordinates (x_1 , z_1 and z_2) are shown in Figure 5.16. The steady decrease (increase for z_1) away from the *fcc* atomic positions (transformed to the $hR24$ unit cell) of 0.5, 0.25 and 0.25, confirms reports of the $hR24$ structure arising from a distortion of the *fcc* unit cell along the body diagonal, which increases in magnitude with pressure.

5.7.2 Comment on quality of collected data

During the course of the experiments performed on Nd, samples were loaded as described in Section 5.3.1 with either no pressure-transmitting medium or mineral oil as pressure-transmitting medium. Above ≈ 30 GPa, the integrated 1D diffraction patterns collected from Nd in the DXR pressure cells, when mineral oil was used as a pressure-transmitting medium, show pronounced broadening in Bragg peak width (FWHM). This broadening, illustrated in Figure 5.17, can be attributed to uniaxial compression of the sample, caused by the loss of hydrostaticity of the pressure-transmitting medium. When no pressure-transmitting medium was used the diffraction patterns exhibited broadening of the Bragg peaks at much earlier pressures. The presence and intensity of contaminant reflections was unaffected by the choice to use, or not use pressure-transmitting media.

Mineral-oil loses hydrostaticity (above ≈ 25 GPa, stated in Section 2.4.2) when used as a pressure transmitting medium. To minimise the effects of strain-induced Bragg peak broadening at pressures greater than ≈ 25 GPa, samples were annealed in a furnace when their pressure was raised above that pressure. As stated in Section 4.8, when annealing a sample within a DAC at a temperature below the melting point of the sample, there is insufficient thermal energy being transferred to the sample to melt the polycrystalline sample and allow regrowth of the (poly) crystal. Instead, this gentle heating supplied enough energy to thermally excite the lattice, with the heating and subsequent slow cooling acting to relax inhomogeneous strain within the samples crystal lattice.

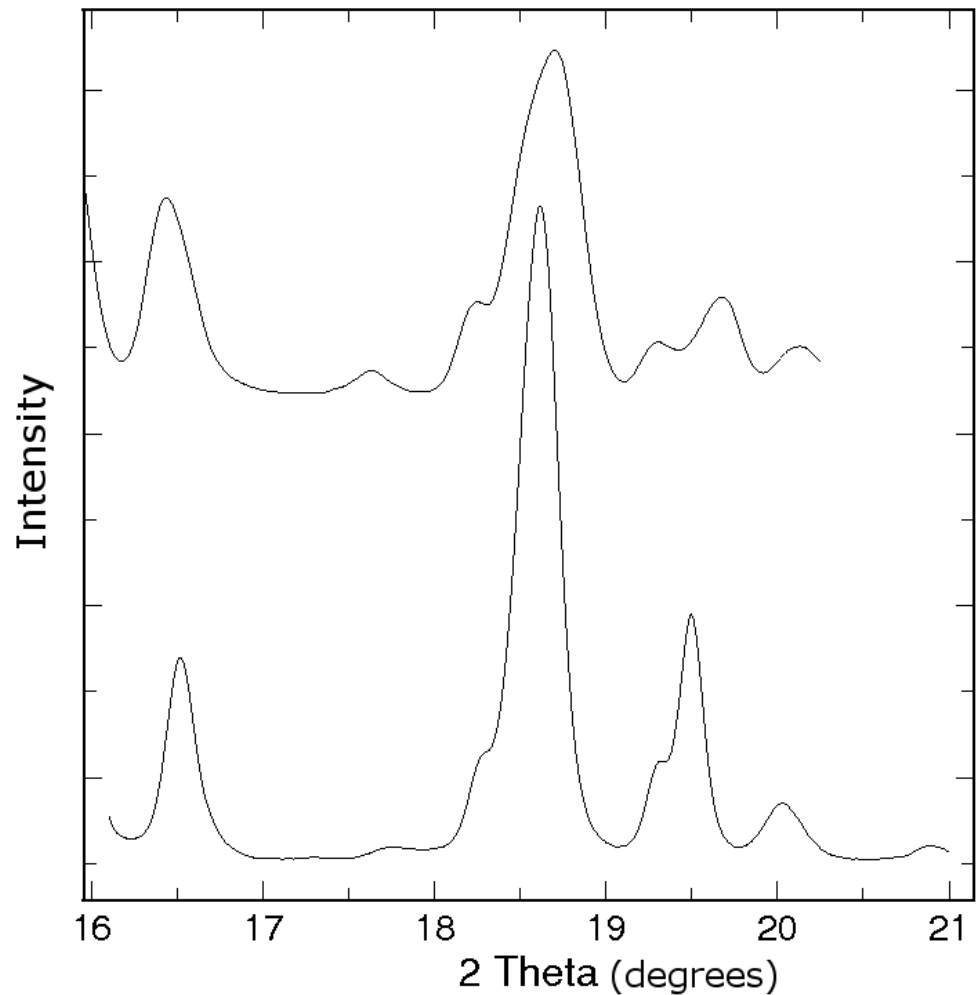


Figure 5.17: Comparison of a section of two datasets, collected from a DAC containing Nd and a mineral-oil pressure medium at 17.5 GPa (lower diffraction pattern) and 22.4 GPa (upper diffraction pattern). The upper pattern has been offset in 2θ to better illustrate the effect of pressure on the observed peak widths. Some additional peak separation is evident in the upper diffraction pattern, which is expected from the pressure dependence of the lattice parameters. Data was collected on Station 9.5 of Daresbury SRS using a wavelength of $\lambda=0.44397\text{\AA}$.

Annealing of Nd was carried out at 200°C for 4 hours by placing the DAC in a pre-heated furnace. Once removed from the furnace, the DAC was allowed to cool to room temperature before the pressure in the sample chamber was measured and experiments could continue. Figure 5.18 illustrates the affect that annealing on Bragg peak width for a Nd sample at 23.9GPa. Taking the (006) and (202) reflections as examples, the FWHM (full width at half of maximum intensity) decreased by 8 and 12% respectively after annealing. This reduction in FWHM of $\approx 10\%$ in these peaks is indicative of the decrease throughout the diffraction pattern, and enables the resolving of broad asymmetric peaks at $2\theta > 18^\circ$ into distinct peaks, as shown in the inset to Figure 5.18. Figure 5.19 shows the effect of annealing on the 2D diffraction image.

5.8 New phase of Neodymium?

The $hR2_4$ structure adopted by Nd above 16 GPa shows a reduction in the quality of its refinements, above 20GPa. Between 22.4 and 25.6 GPa the intensity distribution within the major doublet (006)-(202) switches from $I_{(006)} \gg I_{(202)}$ to $I_{(006)} \ll I_{(202)}$, as shown in Figure 5.20, which compares the 9.0° - 11.0° region in 2θ of patterns collected between 22.4 and 25.6 GPa.

Akella *et al.* [Akella 86] reported a post d -fcc phase that has a $hP3$ structure, and which is stable above 40.5GPa on pressure increase. This phase then undergoes a first-order transition to a monoclinic $C2/m$ structure at 75(5)GPa, and a first-order transition to the α -Uranium (open packed) structure at 113(6)GPa [Chesnut 00a]. The suggestion of $hP3$ and $C2/m$ phases as precursors to the open packed α -Uranium structure is interesting, as both of these structures were proposed by numerous authors ([Velisavljevic 05] and [Dmitriev 00]) as different solutions to the d -fcc phase in Pr, and which have been shown to be incorrect (Chapter 4.7). The authors of [Chesnut 00a] state each of these three phases to be present in Nd, before the transition to the α -U phase.

Using the $hP3$ structure, with lattice parameters derived from Chesnut *et al.*'s paper [Chesnut 00a] (who state the $hP3$ to be the post $hR2_4$ d -fcc phase), LeBial refinements were made to Nd data collected above 25.6GPa. Using these derived values yielded discrepancies in difference plots of observed and calculated data, with a number of peaks accounted for, as illustrated in Figure 5.26. This rules out the $hP3$ phase as a solution to this data around 25GPa.

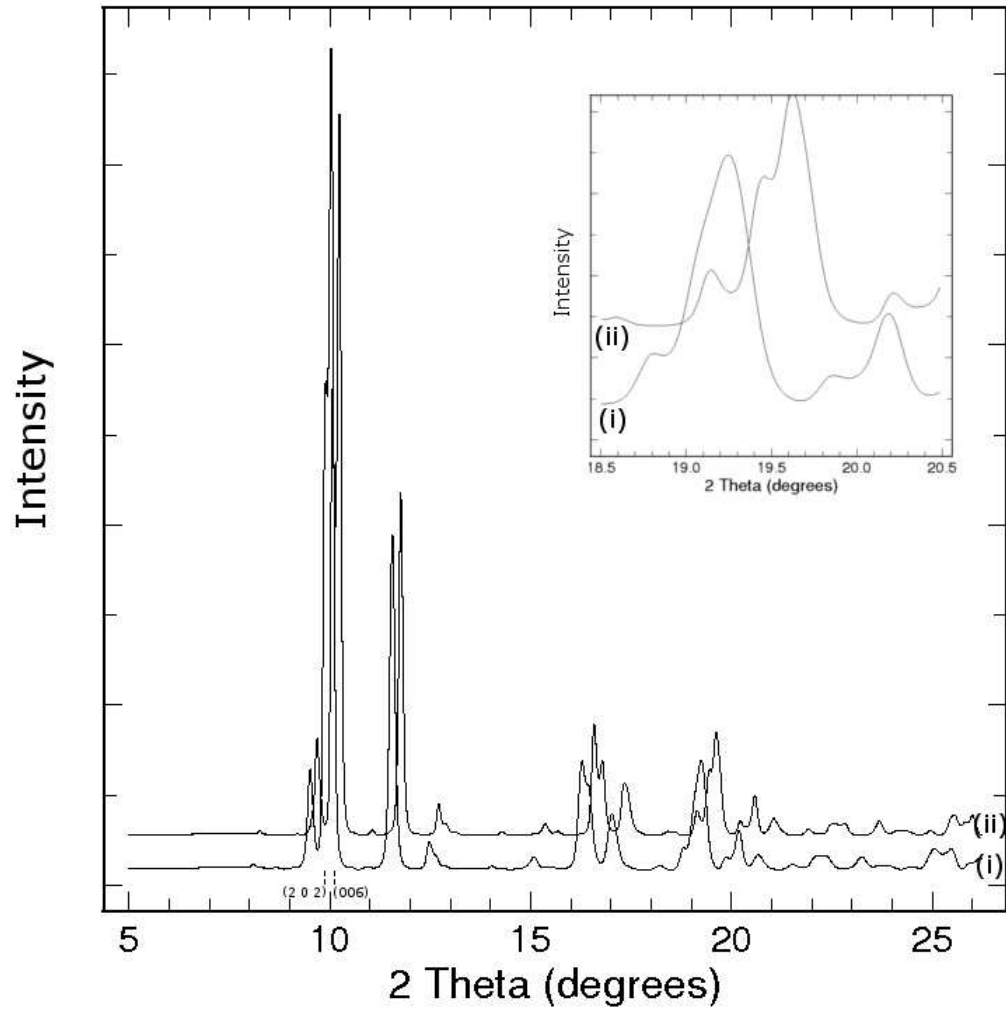


Figure 5.18: Comparison of a sample of Nd within a DXR6 DAC before (i), and after (ii) annealing in a furnace for 4 hours at 200°C. Diffraction patterns collected on Station 9.5 of Daresbury SRS. $\lambda = 0.44397\text{\AA}$, $P = 23.9\text{ GPa}$. Insert shows an enlarged section of the diffraction pattern, which illustrates the increase in resolution gained from annealing. Patterns are offset in 2θ for clarity.

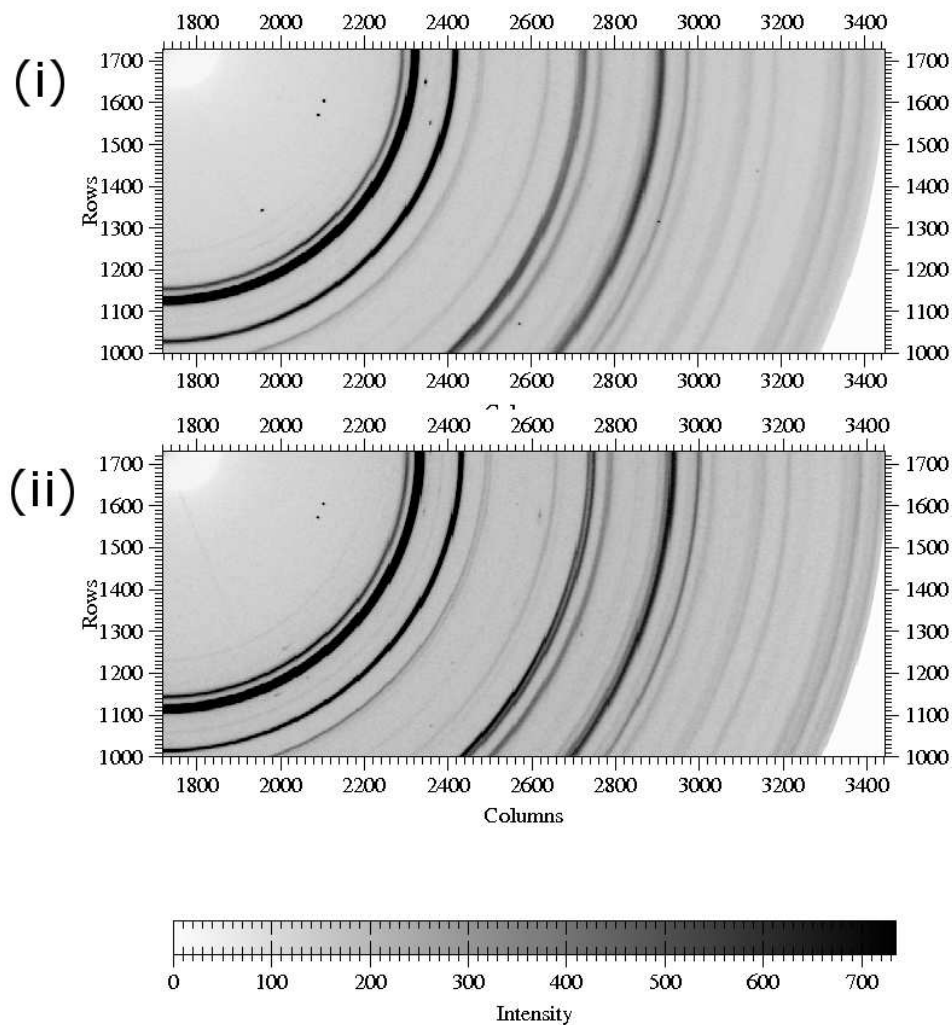


Figure 5.19: Comparison of diffraction patterns obtained from a sample of Nd within a DXR6 DAC (i) before, and (ii) after annealing in a furnace for 4 hours at 200°C. Diffraction patterns are the same as those used in Figure 5.18, but focused on a section of the 2D diffraction pattern, exemplifying how “fuzzy” diffraction rings become sharper and resolved into distinct rings.

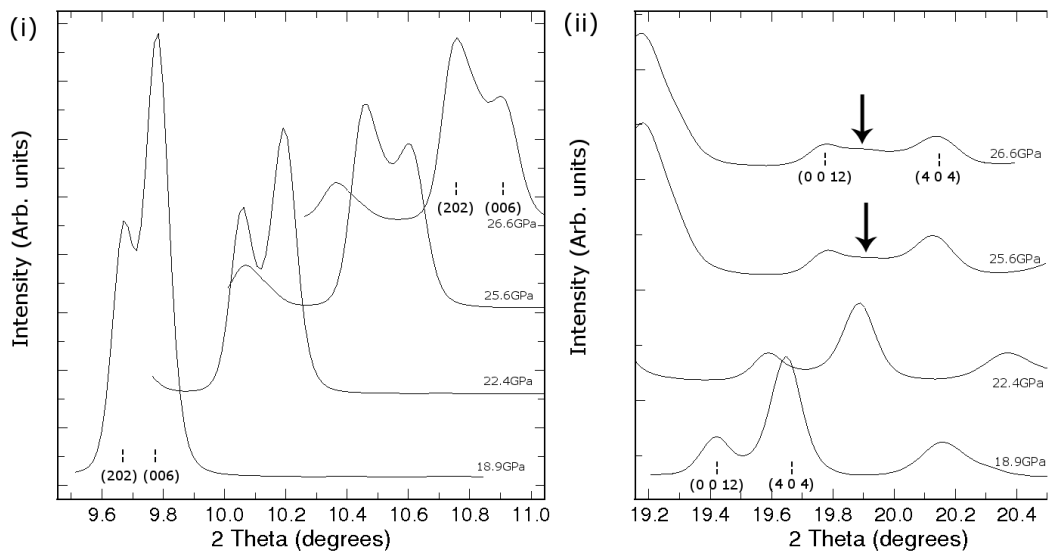


Figure 5.20: Comparison of the (i) $9.0 - 11.0^\circ$ and (ii) $19.2 - 20.4^\circ 2\theta$ range for patterns collected from Nd in a DXR6 DAC at 18.9, 22.4, 25.6 and 26.6 GPa at Station 9.5 of Daresbury SRS during a single experiment. In (i) the (202) and (006) peaks are visible, in (ii) the (0 0 12) and (404) are seen. The appearance of a peak between the (0 0 12) and (404) peaks on pressure increase is highlighted in (ii) with an arrow. Data were collected using a DXR6 type DAC, $\lambda = 0.44397\text{\AA}$, and a mineral-oil pressure-transmitting medium.

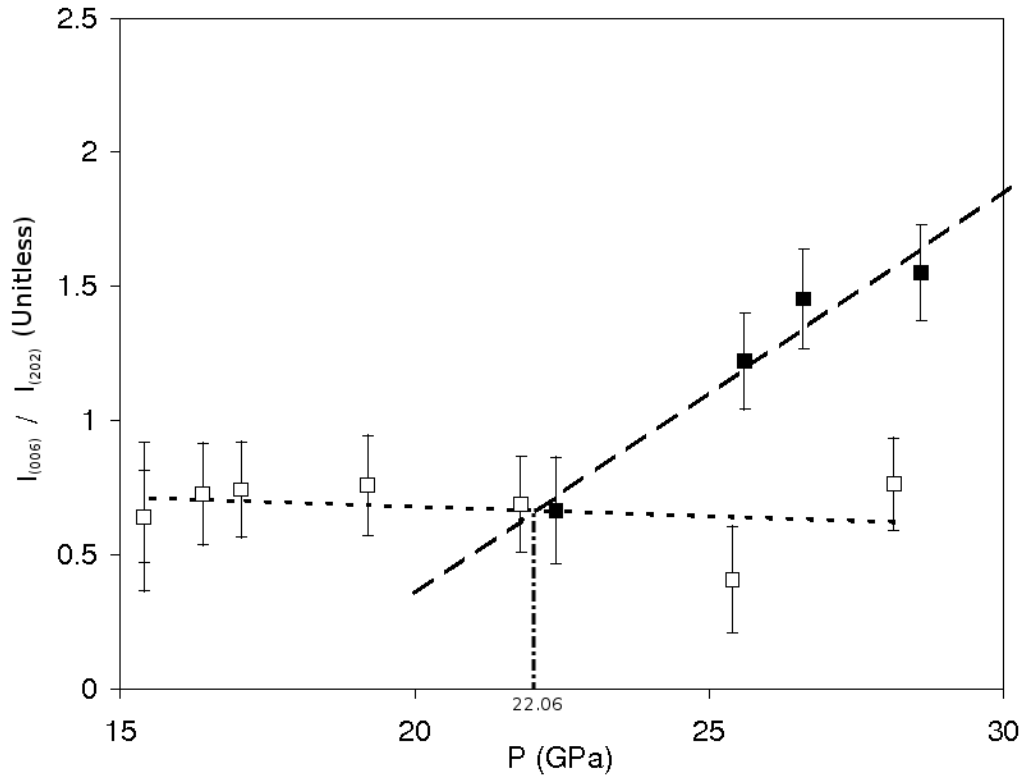


Figure 5.21: Graph of relative intensities of the (006) and (202) reflections for the *d*-fcc phase of Nd between 15 and 27 GPa. Open squares represent data collected on pressure decrease, filled squares represent data collected on pressure increase. Dashed lines represent linear least-squares fits made to the data, in the case of increasing pressure, back extrapolated to 20 GPa to better highlight the intersection point at 22.06 GPa. The data were collected on Station 9.5 of Daresbury SRS, a wavelength of $\lambda=0.44397\text{\AA}$ was used.

In addition to the switching of the intensity of the (006) and (202) peaks around 10° in 2θ in the patterns shown in Figure 5.20, there are peaks raising and peaks splitting (at approximately 19° in 2θ). These peaks can be considered as the $d/2$ (where d here represents the d -spacing of the peak, see Chapter 2.2.2) analogues to the (006) and (202) reflections. A peak appears between the peaks indexed as (0 0 12) and (404) in the $hR24$ structure indicating a transition to a different structure, as, this peak cannot be indexed using the $hR24$ spacegroup.

Figure 5.21 shows the variation of relative intensity, $\frac{I_{(006)}}{I_{(202)}}$ as a function of pressure (collected on pressure increase), clearly indicated on this figure is a crossover point at

≈ 22 GPa. The exact location of this crossover point has been determined through linear (non-weighted) least squares regression fitting to each of the data series in Figure 5.21 (shown as a dashed line in Figure 5.21) to be 22.06 GPa.

22 GPa can be considered as the midpoint of the broad transition from $hR24$ to a second phase within the $d-fcc$ pressure range. Gradual switching of the intensities of these (006) and (202) peaks is indicative of a sluggish, second-order transition and the coexistence of the two phases over a pressure range of ≈ 5 GPa.

5.9 Structure of Neodymium from 25-40GPa

Using Pr as an analogue to the behaviour of Nd, during which a transition to the $Ibam$ structure was preceded by a gradual switching of intensities in the main doublet ((006)/(202)), a splitting of higher-angle reflections, and the rising of peaks (notably the peak located between the (0 0 12) and (404) $hR24$ peaks (see earlier), observation of a similar occurrence in Nd suggests the same process to be occurring. Using DicVol [Louer 04] to index the main reflections of a pattern above 25.6 GPa, trial cells were made, and structural solutions tested, as described earlier (Section 4.8). Note that this process was more challenging in Nd owing to the lower quality of diffraction patterns above 26 GPa (caused by broadening of peaks), due to non-hydrostatic effects within the sample chamber (loss of quasi-hydrostaticity of the pressure medium used). Ruby luminescence profiles were noted to broaden above 30 GPa for samples of Nd.

Fitting the $Ibam$ structure to the observed data yields Rietveld refinements, a typical example of which is presented in Figure 5.22. Refined lattice parameters for this diffraction pattern (collected on Station 9.5 of Daresbury SRS) are $a = 8.7511(26)$, $b = 6.2325(9)$, $c = 6.1036(11)$ Å. Atoms are located on the $8g$ ($(0, y, \frac{1}{4}), (0, -y, \frac{1}{4}), (0, -y, \frac{3}{4}), (0, y, \frac{3}{4})$ with $y_1 = 0.2338(11)$) and $8j$ positions ($(x_2, y_2, 0), (-x_2, -y_2, 0), (-x_2 + \frac{1}{2}, y_2 + \frac{1}{2}, 0), (x_2 + \frac{1}{2}, -y_2 + \frac{1}{2}, 0)$ with $x_2 = 0.2299(10)$ and $y_2 = -0.4600(8)$), and the atomic volume, at 26.6(2) GPa is $20.806(4)$ Å³ and c/a ratio is 0.6975(3). This data is summarised in Table 5.4.

The pressure evolution of the atomic volume of this phase, modelled using the $Ibam$ structure, is shown in Figure 5.23. The plot in Figure 5.23 is an extension of the plot shown in Figure 5.15, and data points obtained below 25 GPa are modelled using the $hR24$ structure, while data points above 25 GPa are modelled using the $Ibam$ structure. It is expected, for a second order transition between the two phases, that there will

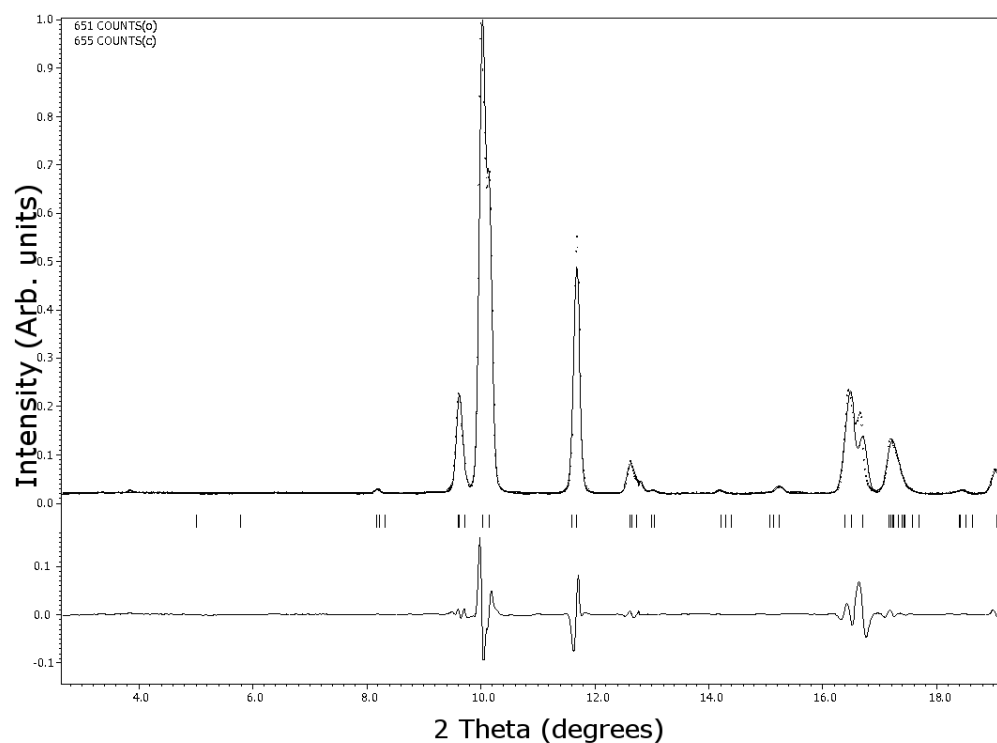


Figure 5.22: Rietveld refinement of a sample of Nd collected at 26.6(2) GPa on Station 9.5 of Daresbury SRS using a wavelength of $\lambda=0.44397\text{\AA}$. Refinement made using the *Ibam* structure in Jana2000, refined lattice parameters are $a = 8.7511(26)$, $b = 6.2325(9)$, $c = 6.1036(11)\text{\AA}$. Preferred orientation effects are present in the sample and account for the difference in intensity of observed and predicted diffraction pattern.

Parameter	Value
a	$8.7511(26)\text{\AA}$
b	$6.2325(9)\text{\AA}$
c	$6.1036(11)\text{\AA}$
Volume/atom	$26.6798(10)\text{\AA}^3$
$\frac{a}{c}$	1
y_1	$0.2338(11)$
x_2	$0.2299(10)$
y_2	$-0.4600(8)$
U_{iso1}	$0.0048(1)$
U_{iso2}	$0.0060(2)$

Table 5.4: Table showing the structural parameters of the *Ibam* phase of Nd, as refined from a pattern collected at 26.6GPa on Station 9.5 of Daresbury SRS, using a wavelength of $\lambda=0.44397\text{\AA}$. Reitveld refinement is shown in Figure 5.22.

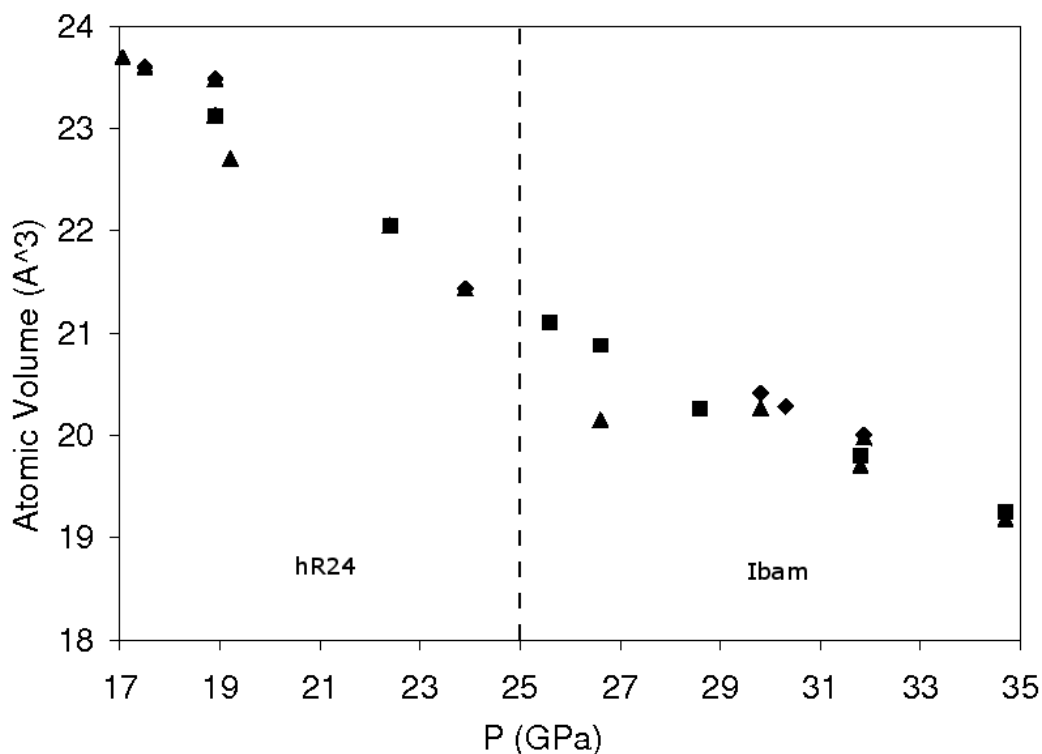


Figure 5.23: Plot of the pressure-dependence of the atomic volume for the $hR24$ and $Ibam$ solutions to the $d-fcc$ phase of Nd. Points below 25 GPa (which correspond to the atomic volume of the $hR24$ solution) are shown for comparison. A dashed vertical line indicates the boundary of the two phases on pressure increase. The lack of discontinuity in the plot indicates a 2nd-order transition between the two structures. Different symbols represent data collected from different loadings of Nd, all on pressure-increase.

be no discontinuity in a volume vs. pressure plot across the transition pressure. As shown, there is a smooth decrease in atomic volume with pressure, from 26 GPa until ≈ 38 GPa, at which point the following phase (the $hP3$ phase) dominates the observed diffraction patterns.

A plot of the c/a ratio against pressure for the $Ibam$ structure is shown in Figure 5.24. As pressure increases, the c/a ratio increases approximately linearly from a minima of 0.6975(3) towards a maxima of 0.7021(24), a percentage increase of 1%.

As in Pr, for Nd, the $Ibam$ solution to the $d-fcc$ phase has a notable misfit located at high angles. Located at approximately 20.01° , the (440) peak splits upon pressurisation into the $Ibam$ phase, with the intensity of the “shoulder” increasing, but retaining a

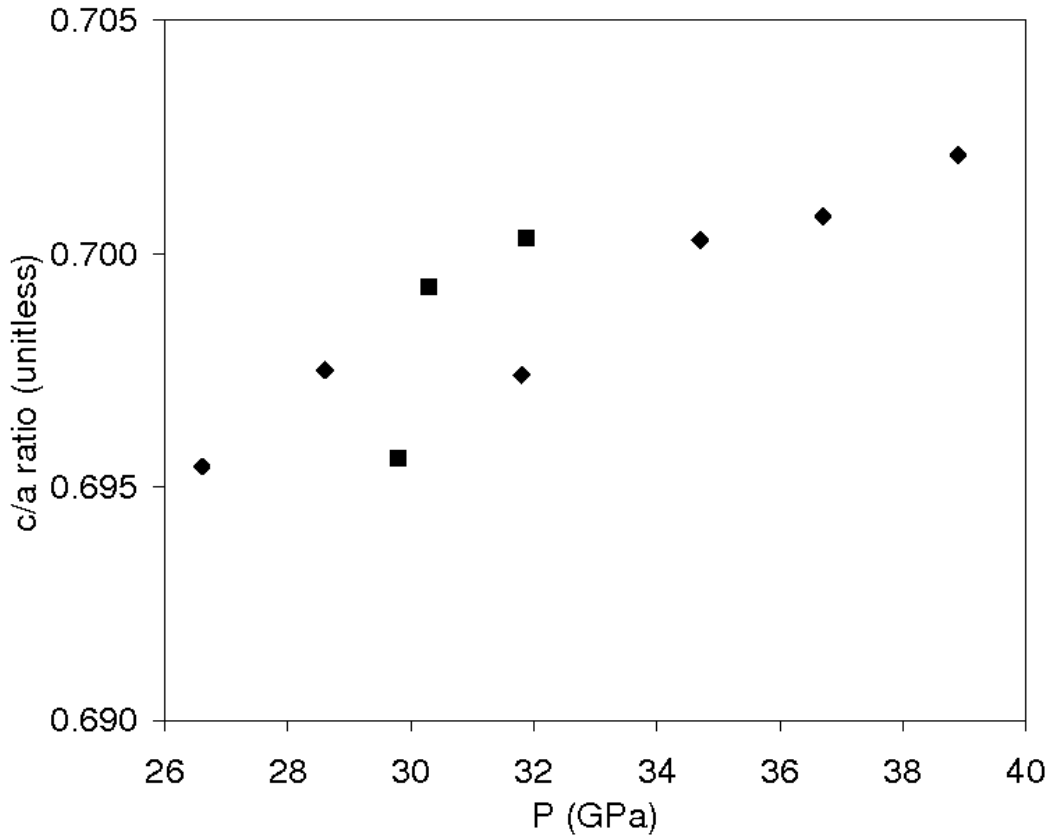


Figure 5.24: Plot of the pressure-dependence of c/a ratio for the *Ibam* solution to the *d-fcc* phase of Nd. Errors are too small to be seen with the plotted symbol size. Different symbols represent data collected from different loadings of Nd, all on pressure-increase. Data was collected on Station 9.5 of Daresbury SRS using a wavelength of $\lambda=0.44397\text{\AA}$.

constant angular separation of 0.099° from the (440) reflection. Figure 5.25 shows this split peak.

5.9.1 Comparison to Praseodymium

In Pr the *Ibam* structure affords a number of distinct advantages over the other structures proposed in the literature for the 14-20GPa region of the *d-fcc* phase. In Nd, however, the distinction is less well defined, owing to broader diffraction patterns (including after annealing). The *Ibam* structure accounts for the switching in intensities

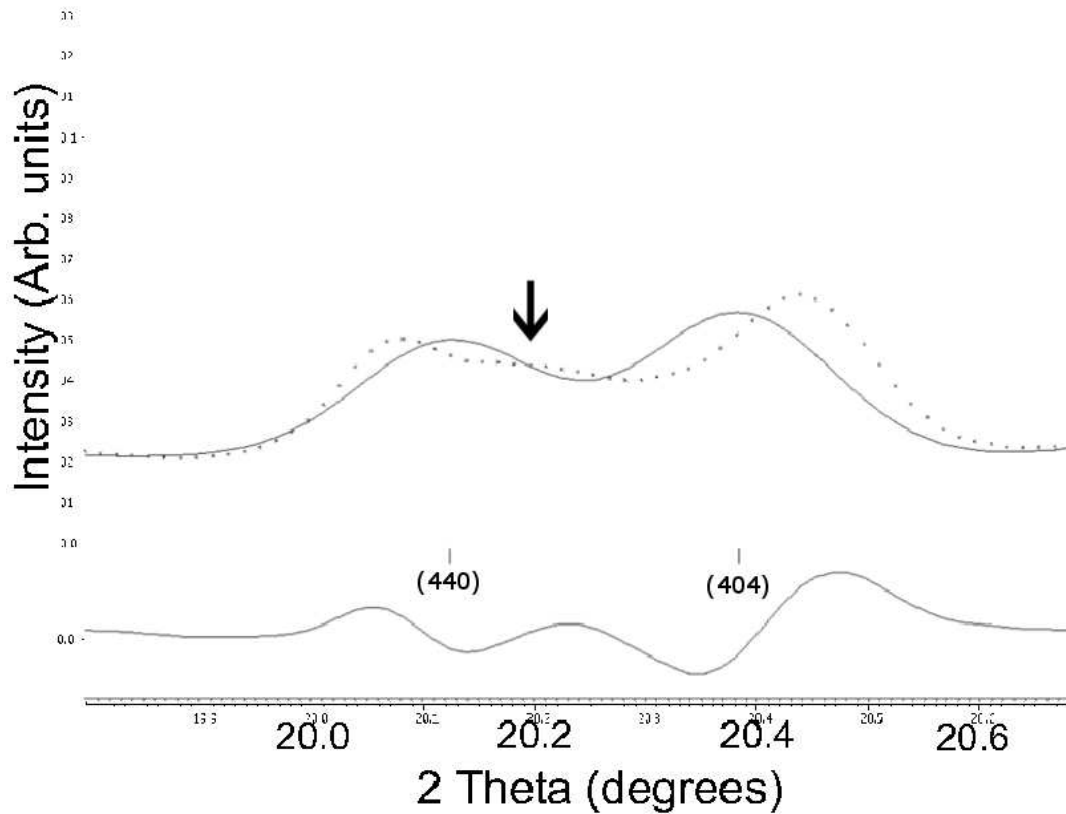


Figure 5.25: Figure showing the splitting of the (440) *Ibam* reflection, into the (440) and the peak identified with an arrow above it. The data for this integrated diffraction pattern was collected at 26.6(2)GPa on Station 9.5 of Daresbury SRS with a wavelength of $\lambda=0.44397\text{\AA}$. Dots correspond to the observed (integrated) data, the upper line to the refined *Ibam* model, the lower line is the difference plot between observed and modelled data. Tick marks represent the positions of peaks in the refined model.

of the (006) and (202) peaks, and explains some of the additional peaks observed, yet, as for Pr, is unable to account for a slight misfit at high angles. It is worth repeating that the $hR24$ phase also fails to account for this. Due to the broad FWHM and difficulty in resolving some of the peaks (as slight asymmetries are, in cases, the only suggestion of doublets), the $hR24$ solution is observed in the refinement software Jana2000 to provide solutions of similar quality.

5.10 $hP3$ Phase of Neodymium

Up to 40GPa the structural transition sequence of Nd has been shown, in this body of work, to be $dhcp \rightarrow d\text{-fcc} (hR24) \rightarrow d\text{-fcc} (Ibam)$. Above 40GPa it is reported that Nd transforms from the $d\text{-fcc}$ phase to a $hP3$ phase [Akella 99] [Chesnut 00a]. Akella *et al.* further report that the $hP3$ phase stable until 75(5) GPa, at which point a transformation to a $C2/m$ phase is observed, with a labelled diffraction pattern and peak locations presented as figures in [Akella 99].

Evidence is seen for the occurrence of a transition at pressures approaching 40GPa in Figure 5.3, a section of which is re-shown in Figure 5.27 with a before-and-after comparison of integrated 1D diffraction profiles collected on a single sample of Nd during pressure increase. It can be seen that peaks associated with a new phase appear at approximately 18.4° in 2θ , as the peaks located at approximately 17.8° and 20.0° , from the $d\text{-fcc} (Ibam)$ phase diminish in intensity, this is shown in greater detail in Figure 5.28.

Using the profile shown in the upper portion of Figure 5.27, peaks that are distinct singlets were fitted using pseudo-Voigt functions in Datlab [Syassen 08b] to precisely determine the location of these peaks in 2θ . These peaks, 8 in total, are listed in Table 5.5, and were indexed using DicVol [Louer 04] in an exhaustive, progressive search regime in which successive, incremental volume bounds are used as the search space for each symmetry type. This process is the same as used in Section 4.8 for the indexing of Pr's $d\text{-fcc}$ phase.

DicVol presented a number of possible solutions that account for the peaks supplied to it (5.5) for indexing. Monoclinic and tetragonal solutions dominated the solution results from DicVol, yet, were of low FoM.

Searching within the trigonal solutions, attempts were made to find the spacegroup

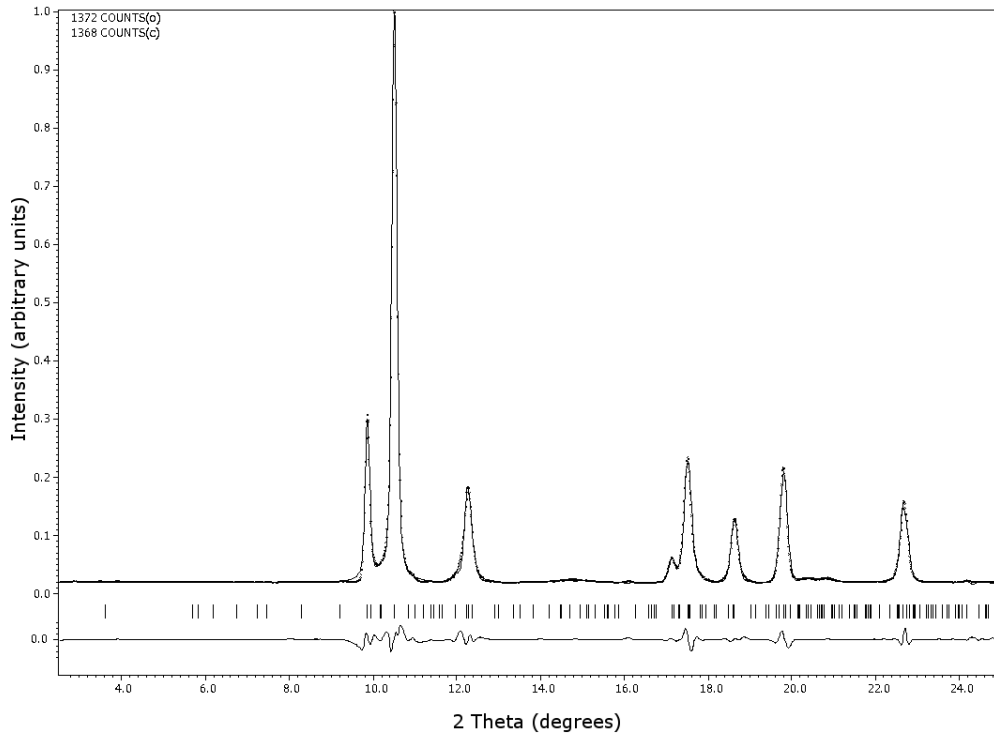


Figure 5.26: LeBail fit of a *hP3* model to the post-*Ibam* phase, using unit cell values derived from the *hP3* structure reported by Akella *et al.* ([Akella 99]) as the solution to the structure of Nd before transformation to α -Uranium structure. Data was collected on Station 9.5 of Daresbury SRS using a wavelength of $\lambda=0.44397\text{\AA}$.

2θ	Intensity
9.7940	286.79
10.4496	881.06
12.2035	193.61
17.0205	61.45
17.4098	227.62
18.5046	115.08
19.6719	233.87
22.5501	163.19

Table 5.5: Table of peak positions extracted from a 40GPa pattern of Nd run on Station 9.5 of Daresbury SRS, using a wavelength of $\lambda=0.44397\text{\AA}$. Peaks location, together with associated intensity were extracted using DatLab [Syassen 08b], then indexed using DicVol [Louer 04].

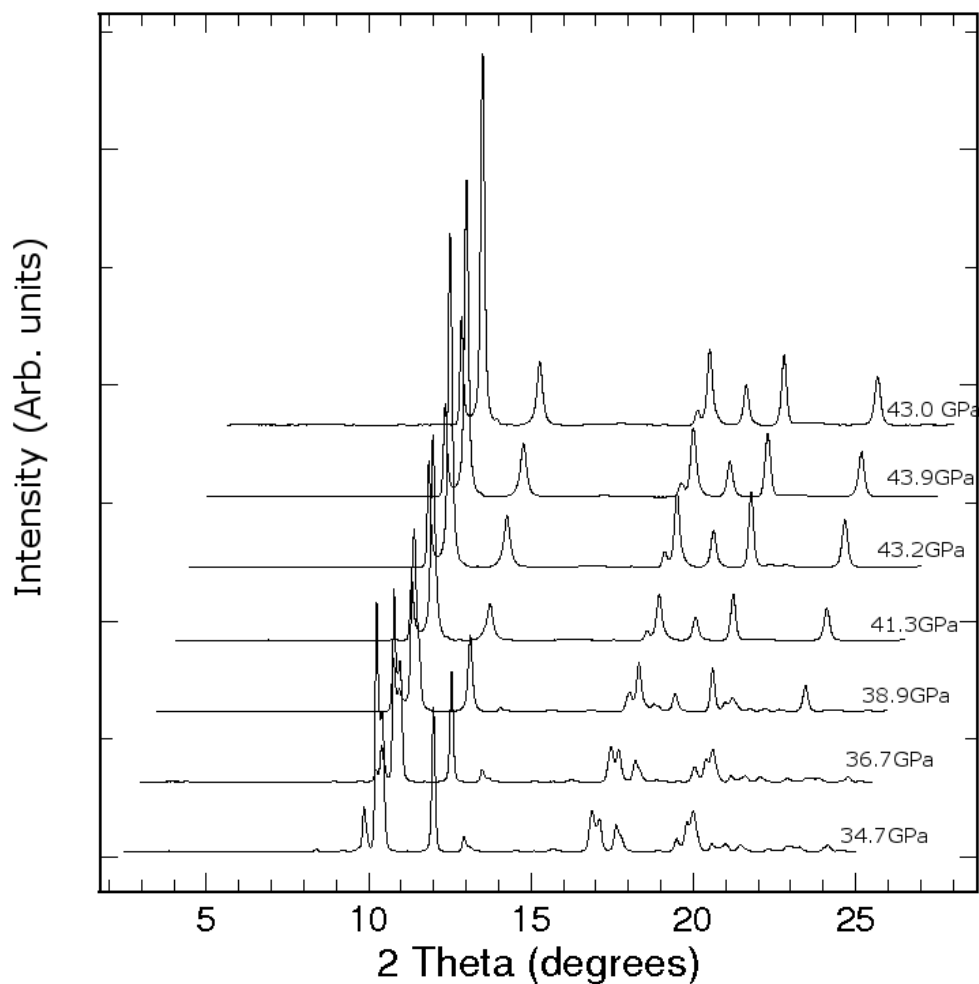


Figure 5.27: Waterfall-plot of integrated diffraction profiles collected from Nd on pressure increase from 34.7 to 43.1 GPa during a single experiment at Station 9.5 of Daresbury SRS, using a wavelength of $\lambda=0.44397\text{\AA}$. For clarity, successive patterns are shifted by 0.5° in 2θ . The pressure of each dataset is indicated at the right of each plot.

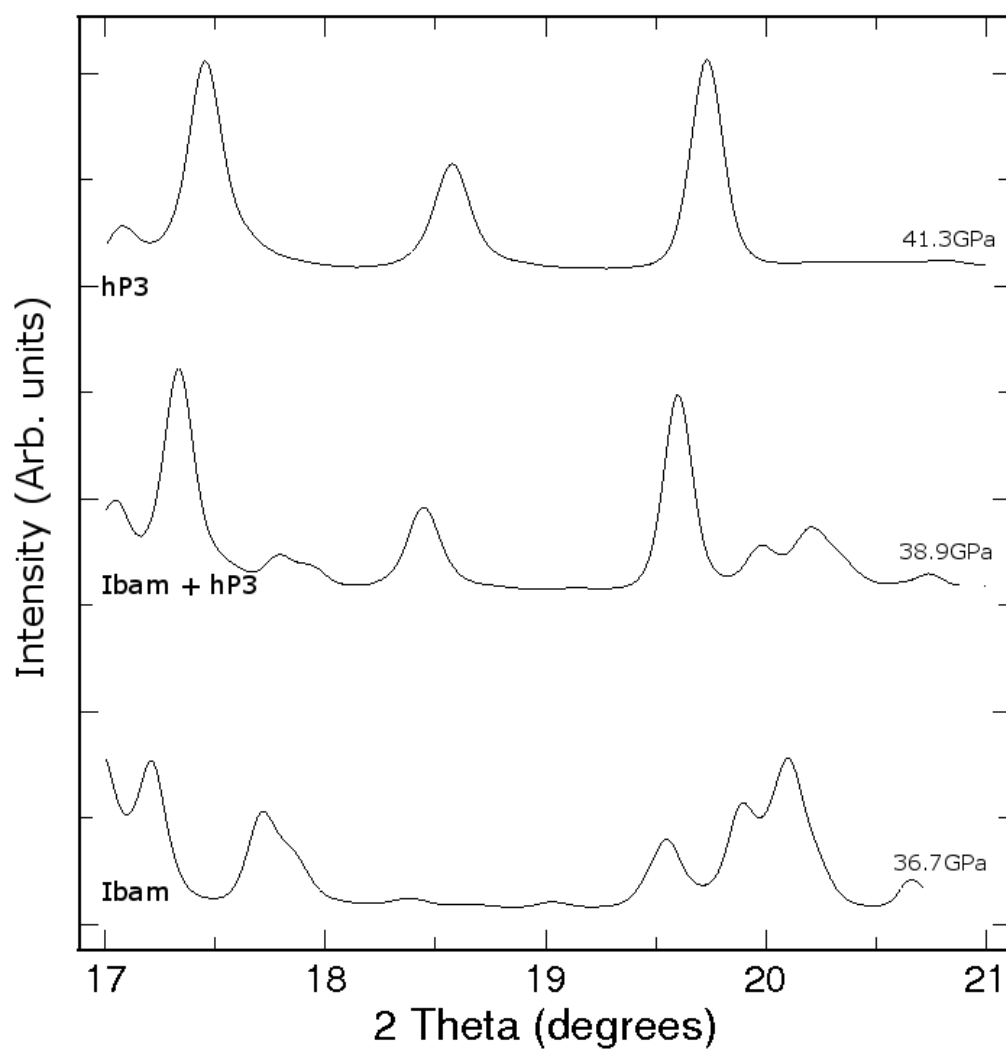


Figure 5.28: Enlarged section of the 17-21° region in 2θ of Figure 5.27 for the patterns collected at 36.7, 38.9 and 41.3 GPa, thus illustrating the changes occurring during the transition from an *Ibam* structure (36.7 GPa), a mixed (*hP3*+*Ibam*) phase (38.9 GPa), to a *hP3* phase (41.3 GPa). Data was collected on Station 9.5 of Daresbury SRS using a wavelength of $\lambda=0.44397\text{\AA}$.

of this phase, starting with the most general of trigonal spacegroups, $P\bar{3}$ (Spacegroup number 143 [Hahn (Editor) 02]). Refinement of the diffraction pattern from which the peaks are extracted, using a Lebial fit (pattern matching only) with lattice parameters given by DicVol ($a = 5.16553\text{\AA}$, $c = 21.11400\text{\AA}$ in the hexagonal setting) was performed in Jana2000 [Petricek 00]. Refinements were made to the data in Jana2000, allowing for background intensity, peak shape and a limited freedom to refine lattice parameters (a , c), until a stable minima in R_{wp} (Jana2000's internal GoF parameter) was reached. Viewing of the files created by Jana2000, which contains a list of indices assigned to fitted peaks, along with the corresponding intensity of the fitted peak. Thus, each possible reflection within the $P\bar{3}$ spacegroup is present.

Careful analysis of the reflection conditions [Hahn (Editor) 02, pp. 44–54] limits the spacegroup to those with $l=3n$, that is l must be a multiple of 3, for $(00l)$ reflections. Further to this constraint on $(00l)$ reflections, peaks are observed only for $-h + k + l = 3n$, which suggests the spacegroup to be $P\bar{3}$ or $\bar{P}3$. Reflections are however observed of the type $l = 2n$, which violates the reflection condition $l = 3n$ (for $hh\bar{2}hl$ reflections) imposed by spacegroups of $R\bar{3}$ type. Violation of this reflection condition leads the author to deduce, that the structure of Nd, must, as reported by Akella *et al*, be $P\bar{3}_1$, or an enantiomorphic spacegroup (such as $P\bar{3}_121$) [Akella 99].

5.10.1 Comparison to Praseodymium

Unlike Pr (where the post d -*fcc* phase is a “collapsed”, open-packed structure) the post d -*fcc* phases in Nd go through two additional close-packed structural transitions (to $hP\bar{3}$, then $C2/m$) before the $4f$ electronic collapse to an α -Uranium structure. Drawing comparisons within the literature to other Lanthanides, the “post d -*fcc*” phase of Nd can be seen as similar to that of Sm [Zhao 94], which the authors observe as a $hP\bar{3}$ phase, indexed as $P\bar{3}_121$ or the corresponding enantiomorphic spacegroup $P\bar{3}_221$.

5.11 Preliminary Studies of Lanthanum

Having shown the presence of a new phase in Nd, and, having solved the structure of Pr between 14 and 20 GPa, it was decided to investigate the d -*fcc* phase of La. The d -*fcc* phase is reported to be stable between 8 and 60 GPa, and is unique in that on further compression beyond 60 GPa, La transforms back to a *fcc* phase. The re-entrant *fcc* phase is not observed in other lanthanides upon compression at room-temperature.

Lanthanum is reported to crystallise at ambient-pressure and temperature in the *dhcp* phase [Tonkov 05], with lattice parameters of $a=3.770\text{\AA}$ and $c=12.159\text{\AA}$. This phase was not observed, due to no data being collected below 4GPa. Following the lanthanide transition sequence La is reported to transform to a *fcc* structure at $\approx 2\text{GPa}$. Data collected is in agreement with these reported transition pressures.

The *fcc* structure is reported by Seipel *et al.* [Seipel 97] to transform to the *d-fcc* structure at around 8GPa. This transition pressure cannot be confirmed due to insufficient data, the *fcc* structure was observed to be present up to 6GPa, and the *d-fcc* to be present above 12.3GPa.

Modelling the *d-fcc* phase of La with *hR24* yields excellent fits, as evident from Figure 5.31, which has a $R_{wp}=11.2\%$ in Jana2000.

Observed within the *d-fcc* patterns collected is the characteristic intensity switching of the (006) (202) doublet, in La situated at about 9° in 2θ at a pressure between 21 and 28GPa, this is shown in Figure 5.30. This intensity switching is accompanied by the associated raising of a peak around 19.5° . From the conclusions drawn on Pr and Nd, this is seen to be indicative of a transition from the *hR24* to *Ibam* structure. Refinements were made to data above 28GPa, an example of such a refinement is shown in Figure 5.32. Patterns collected above 31GPa showed a noticeable increase in the FWHM of peaks in the diffraction patterns, as such refinements are of a poor quality above this pressure. The refinement presented in Figure 5.32 confirms the *Ibam* structure to be present in La.

The maximum pressure reached during the experiments on La was 40GPa. This pressure was not sufficiently high to observe the re-entrant *fcc* phase transition, which is reported to occur at 60GPa. This pressure limitation was imposed by the DACs available for use.

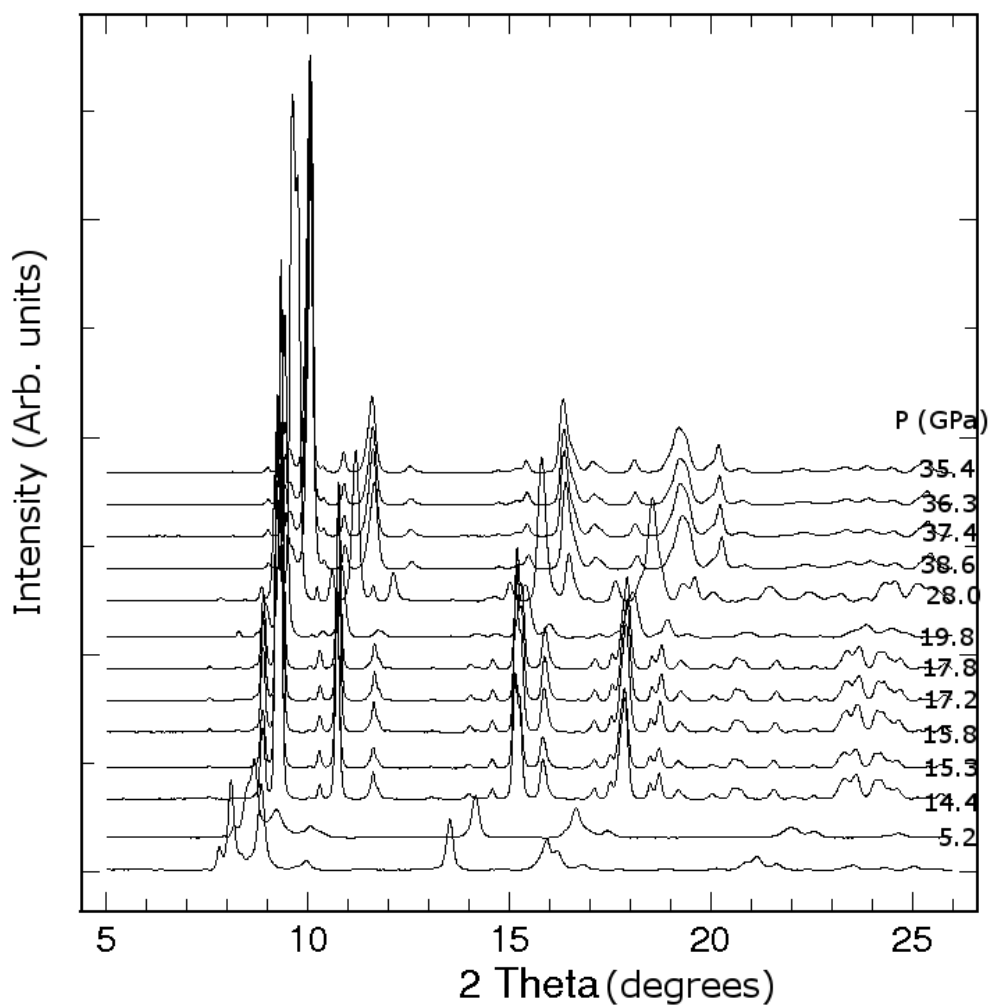


Figure 5.29: Waterfall plot showing data collected on La at Station 9.5 of Daresbury SRS using monochromatic x-rays of wavelength $\lambda=0.44397\text{\AA}$. The sample pressure, measured by ruby fluorescence, is displayed on the right hand side of each diffraction pattern. Pressures shown are from 5.2 to 38.6GPa in uneven steps.

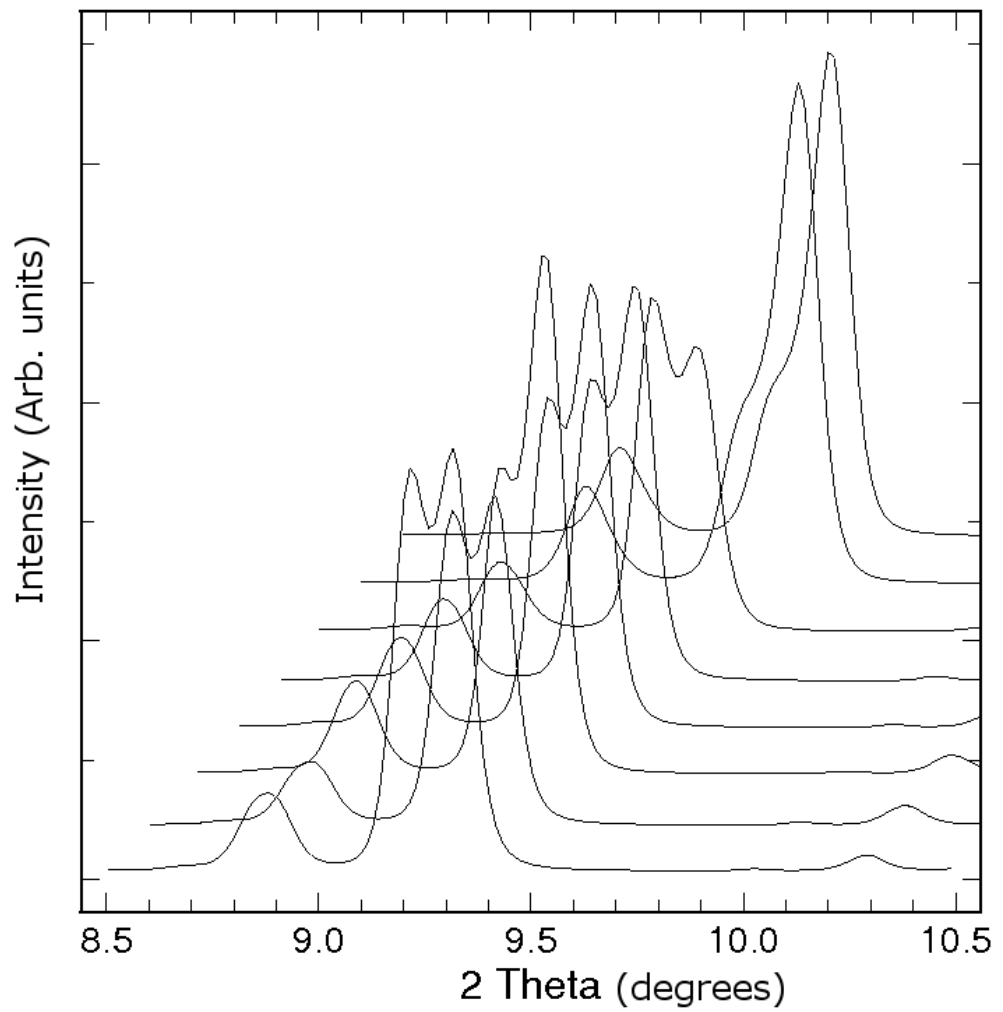


Figure 5.30: Waterfall plot showing data collected on La at Station 9.5 HPT of Daresbury SRS using monochromatic x-rays of $\lambda=0.44397\text{\AA}$. Successive plots are shifted by 0.1° in 2θ for clarity. A switching in the relative intensities of the first (006) and second (202) peaks in the doublet occurs at about 16GPa on pressure increase.

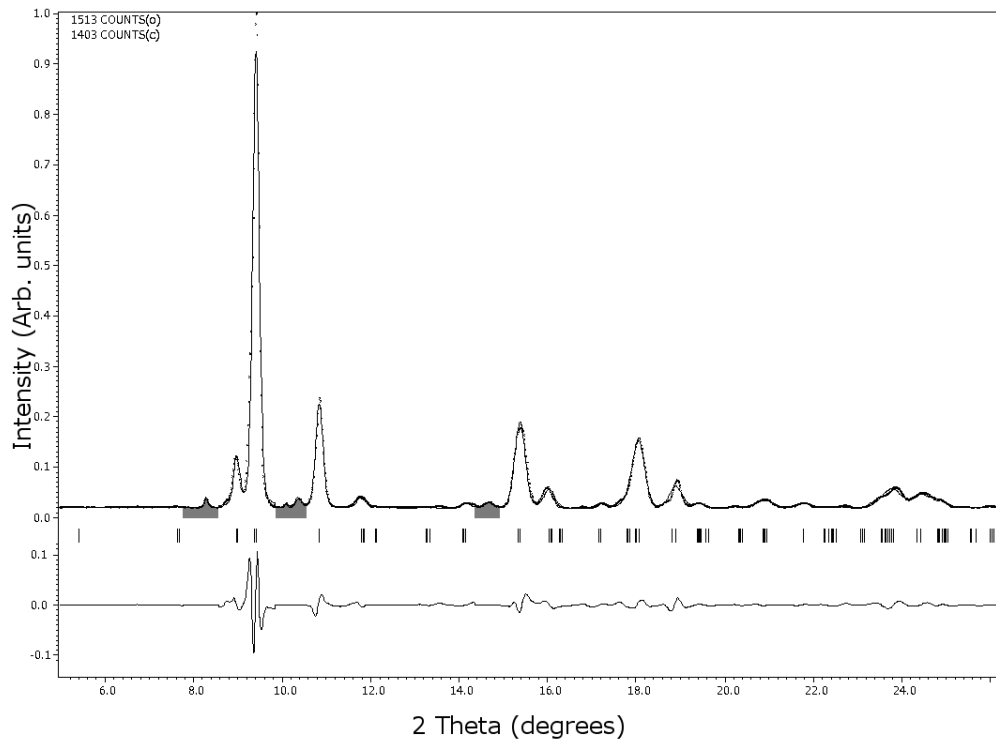


Figure 5.31: Refinement of La with $hR24$ structure made to a d -fcc diffraction pattern collected at 19.8GPa from Station 9.5 of Daresbury SRS. Refined lattice parameters are $a = 6.66112(9)\text{\AA}$, and $c = 16.2280(1)\text{\AA}$.

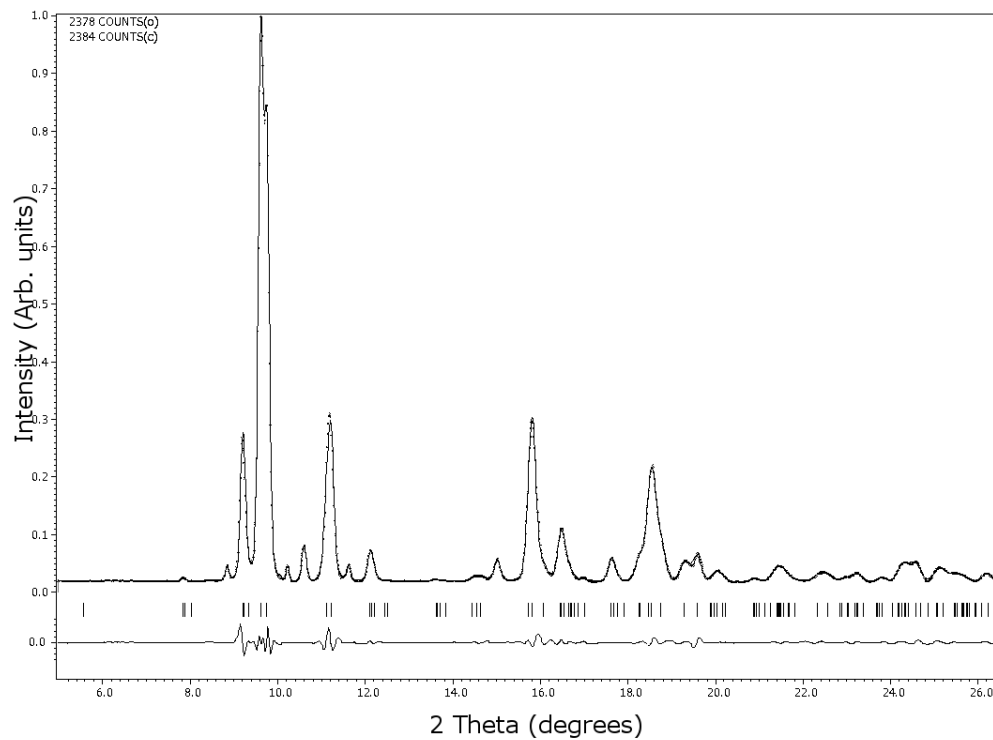


Figure 5.32: Refinement of La with *Ibam* structure made to a *d-fcc* diffraction pattern collected at 28GPa from Station 9.5 of Daresbury SRS, using a wavelength of $\lambda=0.44397\text{\AA}$. Refined lattice parameters are $a = 9.1734(4)\text{\AA}$, $b = 6.4914(3)\text{\AA}$ and $c = 6.3557(3)\text{\AA}$. $R_{wp} = 4.65\%$.

5.12 Discussion and Conclusions

The $dhcp \rightarrow fcc$ transition in Nd as reported [Tonkov 05, Chesnut 00a, Velisavljevic 05] is observed to occur at a pressure of 3.8GPa, in agreement with earlier reports in the literature. The fcc phase is confirmed to be stable to a pressure of 18GPa on pressure increase.

Above 18GPa the transformation to the $d-fcc$ phase is evidenced by the raising of superlattice reflection and splitting of the (111) and (200) fcc reflections. Up to 25.6(10)GPa this phase is best described using a $hR24$ structure (spacegroup $R\bar{3}m$). This $hR24$ structure, reported in the literature to be stable between 18-40GPa, the $d-fcc$ phase, is shown to not be the clear solution above 26GPa, where numerous changes occur in the observed data. As for Pr, there is a switching in the relative intensities of the peaks indexed as (006) and (202) in the $hR24$ solution accompanied by the splitting of some high-angled peaks into a poorly-resolved doublets (asymmetric peaks) and raising of a peak between the (0 0 12) and (404) reflections. Re-indexing and analogy to Pr suggests the $Ibam$ structure to be the solution to this new phase, although, with the quality of data collected, it is not possible to definitively state if this is truly the solution. Higher-resolution diffraction data, with a hydrostatic medium better suited to pressures above 30GPa, would be required to definitively determine the solution.

The behaviour of Nd above the $d-fcc$ phase is a departure from the behaviour of Pr, in which no $hP3$ phase is observed. Above the $hP3$ phase, it is stated in the literature [Chesnut 00a, Velisavljevic 05] that Nd undergoes a further transition to a monoclinic, $C2/m$ structure before reaching the α -U phase. This is of note, as the $C2/m$ structure was a candidate for the 14-20GPa pressure region of the $d-fcc$ phase in Pr. This work shows the $C2/m$ structure to poorly describe the 14-20GPa region of Pr's $d-fcc$ phase, which leads the author to ponder if the $C2/m$ phase in Nd is also the best solution to structure. Velisavljevic's work [Velisavljevic 05], carried out using EDX would unlikely be able to distinguish between the $C2/m$ and $Ibam$ structures. Unfortunately, this region of Nd's phase diagram was out of the pressure range attainable using equipment at the authors disposal. Further experiments, with DACs capable of reaching \approx 1Mbar and high resolution ADX synchrotron radiation would be required to investigate the validity of the $C2/m$ structure.

In Figure 5.33 the atomic volume over the phases studied of Nd is presented, evident is a lack of discontinuities upon transition between the high pressure phases.

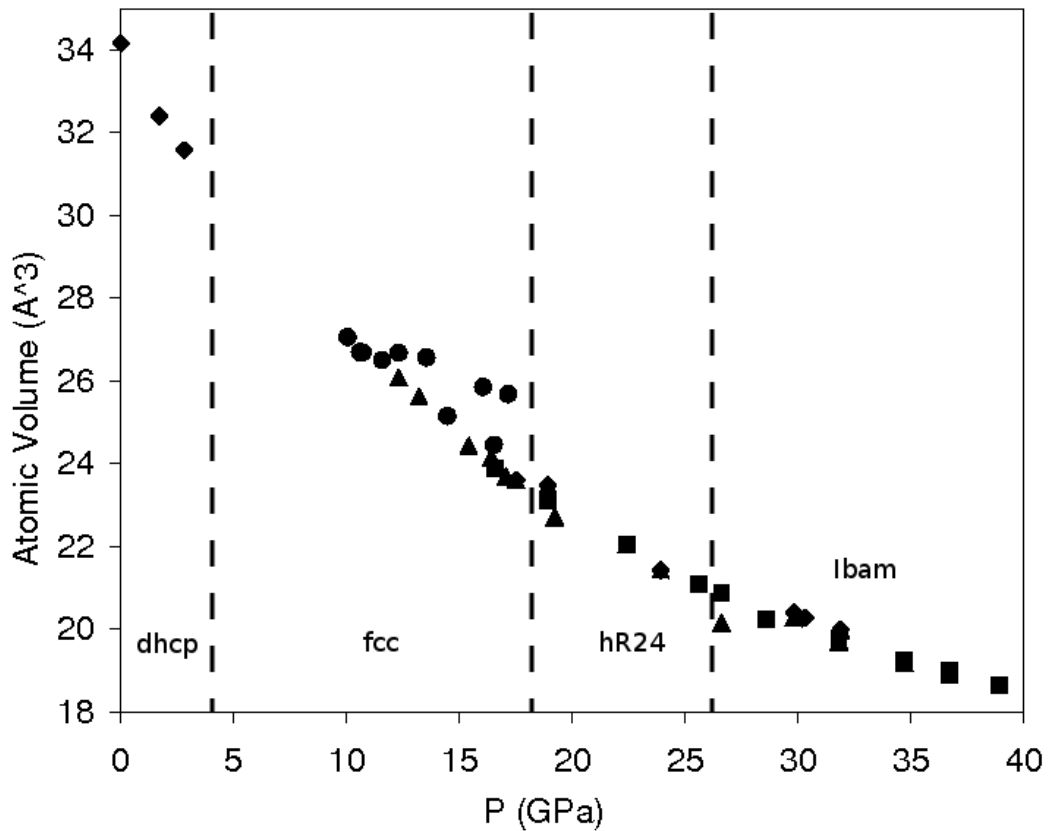


Figure 5.33: A plot of the variation of atomic volume with pressure for the entirety of the pressure range studied within Nd. Transition pressures between structures are indicated by dashed vertical lines, the respective phases are labelled on the diagram. Data were collected on multiple separate experiments on Station 9.5 of Daresbury SRS, using a wavelength of $\lambda=0.44397\text{\AA}$. Some scatter exists on within the *fcc* region due to a mixture of data collected on pressure increase and decrease being plotted. Atomic volume derived from volume calculated using Rietveld refined lattice parameters for patterns at each pressure point.

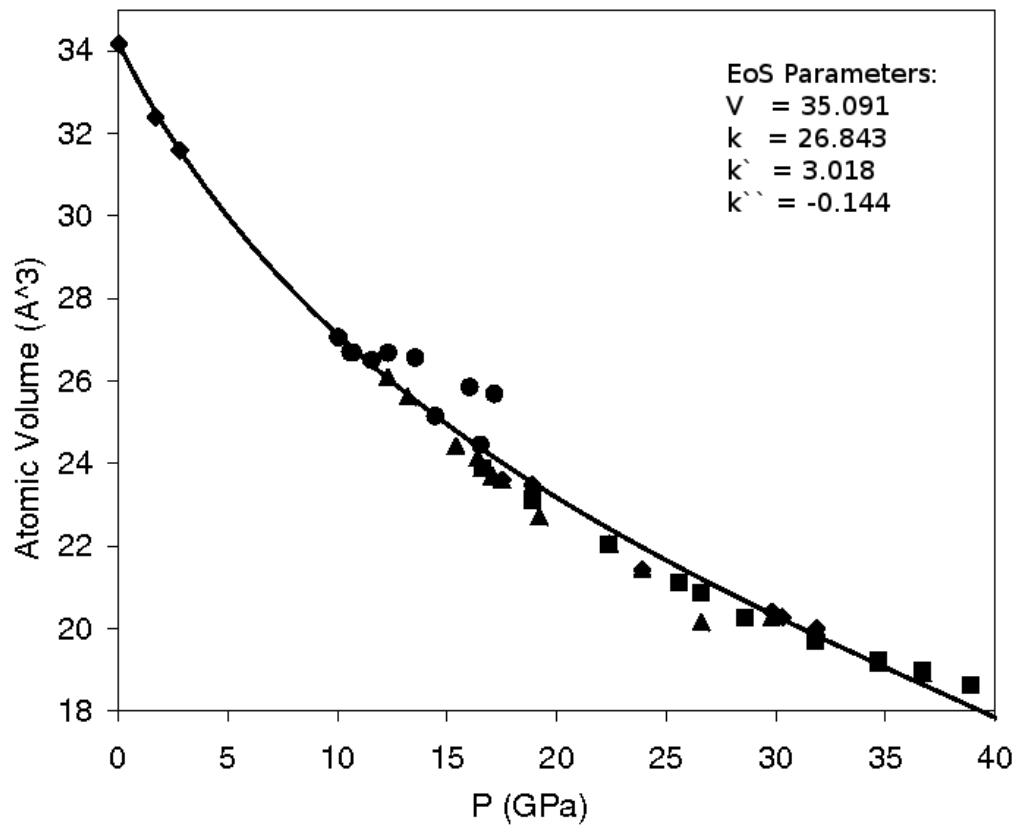


Figure 5.34: Plot of the atomic volume vs. pressure for the pressure range investigated in Nd (0-40GPa) with a fitted 3rd order Birch-Murnaghan equation of state (EoS) shown in black. The EoS, fitted using EOSFit[Angel 01], has least-squares refined values of $k_0=31.96464$ GPa, $k'=2.82263$, $k''=-0.12820$ and $V_0=34.16375$ Å³. The EoS was fitted from zero (ambient pressure) to 40GPa. Data collected from Station 9.5 of Daresbury SRS using a wavelength of $\lambda=0.44397$ Å. Errors plotted, but obscured by the size of the datapoints.

A fitted 3rd order Birch-Murnaghan equation of state (EoS) is shown in Figure 5.34 to measured atomic volume for the pressure range 0-40GPa in Nd. Fitted k_0 , k' , k'' and v_0 are noted on the Figure. Datapoints used for this plot are the same used for the atomic volume plot in Figure 5.33, the (circular) outlying data points between 12 and 16GPa were removed from the least squares refinement (but left on the figure for continuity with the Figure 5.33). Refinement of the zero-pressure atomic volume value was not made as data measured close to zero was available. The determined bulk modulus, $k_0 = 31.965\text{GPa}$ is in close agreement, within 0.5%, of the expected value of $k_0 = 31.8\text{GPa}$.

A preliminary study of La was performed, insufficient data was collected to observe the low pressure transitions, from the ambient pressure (*dhcp*) phase to the *fcc* phase. The *fcc* phase was observed from 4GPa to 6.6GPa, the transition from *fcc* to *d-fcc*, reported to occur at 8GPa was not observed due to a lack of data between 6.6 and 12.3GPa. Data was collected to a maximum of 40.7GPa, which was insufficiently high to observe the re-entrant transition to *fcc*, which is stated to occur at about 60GPa at room temperature [Seipel 97].

The *d-fcc* phase of La was confirmed to be comprised of 2 structures, with a transition occurring between 21 and 28GPa. Evidence for this transition, as for Pr and Nd, is the observation of the intensity switching of the (006) and (202) reflections, with associated rising of peaks. Like with Pr and Nd, the lower pressure region is described using a *hR24* structure, and higher pressure region with *Ibam* structure. However, data was only collected up to 40.7GPa for La, as such, it is unknown if a further transition will be discovered before the re-entrant *fcc* phase. Further experiments will be required to investigate if there is another transition before the *d-fcc* \rightarrow *fcc* phase transition at 60GPa.

Conclusions

6.1 Conclusions

As presented in the previous chapters, detailed investigation of the high-pressure behaviour of the *d-fcc* phase of Pr and Nd have been made; along with a preliminary investigation into the behaviour of La in the *d-fcc* phase. The results of these studies will be summarised in this chapter, and conclusions drawn.

The high-pressure behaviour of the lanthanides has been studied extensively owing to the similarity exhibited by trivalent members of the series in their adopted high-pressure crystal structures [Grosshans 83]. A transition from an close to open-packed structure driven by delocalisation of *4-f* electrons and ambiguity in the structure of one of the high pressure phases. Upon pressurisation, lanthanides display the same sequence of phases shown as one traverses through the series (from low to high Z), namely the sequence: *hcp* → *dhcp* → *fcc* → *d-fcc* → collapsed.

The questions posed in Section 1.3, which provided the motivation for this study, were as follows: Is there a transition between two similar structures occurring within the *d-fcc* stability range (7-20GPa) in Pr? What is (are) the structure(s) of the *d-fcc* phase in Pr? What is the degree of volume collapse at the *d-fcc* to α -Uranium phase transition in Pr?

These questions relate to the high-pressure structure of the *d-fcc* phase of Pr, which, prior to the work performed in this thesis, was a source of persistent disagreement within the literature, as discussed in Section 3.3.

The *d-fcc* phase of Pr has been extensively studied during this thesis, to resolve the ambiguity which persisted up to this study concerning the identity of the structure. The *d-fcc* is stable over the pressure range 7 - 20 GPa in Pr on pressure-increase. Further pressurisation causes a transition to the α -U open-packed structure, a transition previously shown to be driven by delocalisation of the *4-f* valence electrons, with an

associated volume collapse, the size of which is ambiguous in the literature [Mao 81, Chesnut 00b]. Data were collected from Station 9.1 and Station 9.5 HPT of Daresbury SRS, and ID09A of ESRF.

Within the *d-fcc* phase of Pr, two distinct phases are observed, in the low-pressure region (7-14 GPa) the structure of the *d-fcc* phase is $hR24$ ($R\bar{3}m$), with atoms located in the $18h$ and $6c$ sites. The pressure-dependance of this phase was studied, atomic displacement parameters are seen to increase from the *fcc* value as the structure becomes more “distorted” with increasing pressure, eventually approaching steady values at 18GPa. The c/a ratio of the $hR24$ phase increases from the *fcc* ($c/a = \sqrt{6}$) to a maxima of 2.738. Above 14GPa evidence is seen of a transition to a different unit cell, as noted by Dmitriev *et al.* [Dmitriev 00]. However, the structure suggested by Dmitriev fails to account for a number of observed peaks. Subsequent re-indexing of diffraction patterns above 14GPa yields a trial orthorhombic cell (supercell) which, upon doubling in each direction gives a solution which accounts for each observed reflection, analysis of systematic absences yields the structural solution *Ibam*, a solution with less refinable variables than the solution proposed by Dmitriev *et al.*. The pressure-dependance of this newly discovered solution over the 14-20GPa stability range was investigated.

The *d-fcc* phase (*Ibam* structure) was observed to transform to the α -U phase at 20.5(5) GPa upon the application of pressure. Upon transformation a loss of volume of 7.6% was seen, in agreement with [Dmitriev 00] (8%), but differing from the observation of [Mao 81] (14%). This smaller volume collapse at the transition from *d-fcc* to α -U structure implies the $4-f$ electrons role in the previously suggested structure [Mao 81] was overestimated.

A plot of the atomic volume against pressure for Pr, over the pressure range studied is presented in Figure 6.1 (repeated from Figure 4.30), which highlights the observed transition pressures and volume collapse at the *d-fcc* \rightarrow α -U transition. An equation of state (3^{rd} order BirchMurnaghan) was fitted to this atomic volume data collected on Pr up to the volume collapse transition between the *d-fcc* and α -U phases (shown in Figure 4.31). Least squares fitted k_0 , k' and k'' were presented, the fitted value for k_0 , the bulk modulus, of Pr (31.82GPa) differs from the value reported in the literature of 28.8GPa by 9.5%. The author acknowledges this discrepancy, and suggests the requirement to refine the zero pressure atomic volume whilst fitting the EoS within EOSFIT [Angel 01] due to the lack of an ambient pressure datapoint and sparse low pressure data as the cause for this discrepancy.

Following the investigation of the *d-fcc* phase of Pr, and driven by known similarities in the structures adopted by lanthanides upon the application of pressure [Holzapfel 95, Baer 03], the neighbouring, higher-Z lanthanide, Nd was studied. An investigation of the *d-fcc* phase of Nd was made, with the aim to determine the structure(s) adopted by Nd within the *d-fcc* phase stability range.

The high-pressure structure of Nd has been studied to a maximum of 43GPa. Previously reported transitions from *dhcp* \rightarrow *fcc* \rightarrow *d-fcc* (*hR24*), are observed to occur at the pressures noted in the literature (3.8GPa and 18GPa). The structure of the *d-fcc* (*hR24*) phase is confirmed to a pressure of 25.6(10)GPa, using angle-dispersive x-ray diffraction from powder samples in Merrill-Bassett and DXR6 type DACs. The atomic volume, *c/a* ratio and lattice parameter reduction are observed to follow continuous trends, similar to those observed in Pr. At around 25 GPa, diffraction patterns from Nd undergo a number of subtle changes; switching in intensity of the (110) and (200) relative intensities; raising of addition peaks and broadening (splitting) of others at high angles, indicative of a phase transition to a closely-related structure. The *Ibam* (*oC16*) structure is proposed by this author as a solution to the *d-fcc* phase above 25GPa until a pressure of 40GPa is reached on pressure increase. No volume change is observed at the transition between *hR24* and *oC16* (as seen from Figures 6.2 and 5.34), indicating a second-order transition driven by small displacements of the atoms within the *hR24* unit cell further away from their *fcc*-equivalent positions. The transition to the following *hP3* phase begins to occur at around 38GPa and is completed at around 41GPa. Such a pressure range for this transition is observed in other work [Velisavljevic 05], the authors of which note the coexistence of phases over a broad pressure range. Difficulties were encountered in the fitting of Nd data above 30GPa owing to the broadening of observed peaks, and subsequent inability to ascertain if observed peaks are the superposition of multiple Bragg peaks, a problem likely caused by non-hydrostaticity within the sample chamber.

A plot of the atomic volume against pressure for Nd, over the pressure range studied is presented in Figure 6.2 (repeated from Figure 5.33), which highlights the observed transition pressures up to the *hP3* phase transition. This data was used for the fitting of a 3rd order BirchMurnaghan EoS, shown in Figure 5.34, in which least squares fitted k_0 , k' and k'' are presented. The determined value (31.96GPa) for the bulk modulus, k_0 , is in close agreement (within 0.5%) to the value reported in the literature of 31.8GPa. This compares more favourably than the difference between the expected and determined k_0 for Pr (9.5%), likely due to clusters of measured data points at low pressure (including close to ambient pressure).

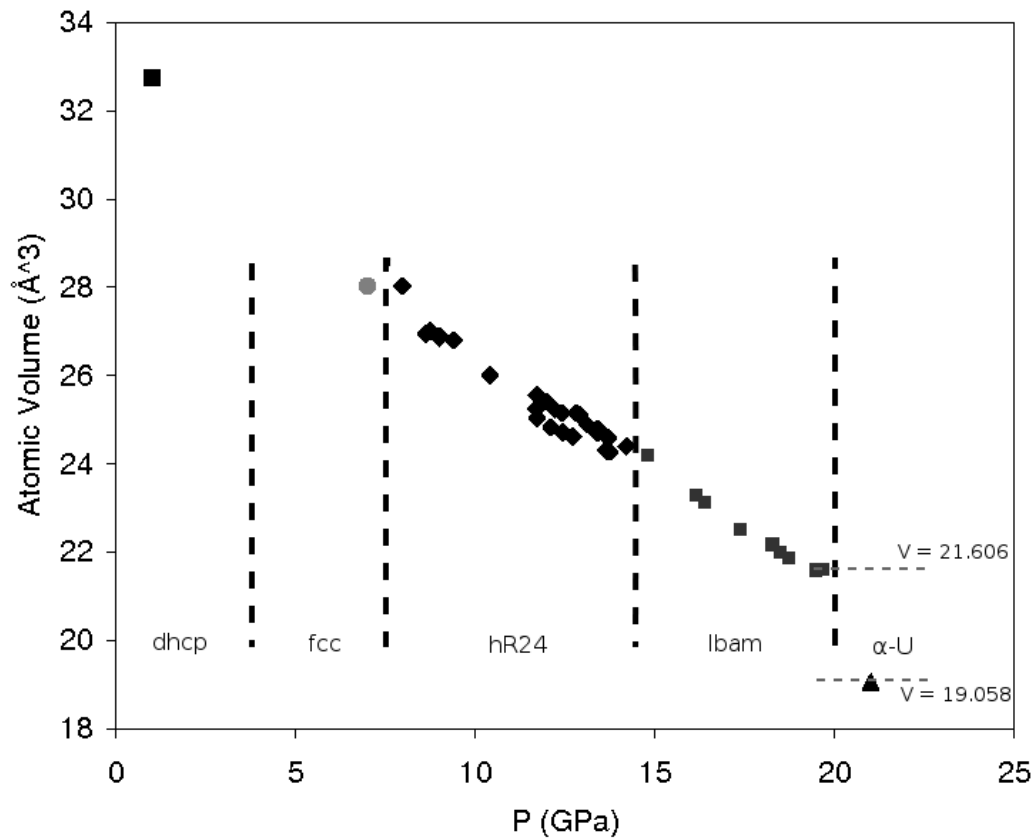


Figure 6.1: Plot of the atomic volume vs. pressure for the pressure range investigated in Pr. Alternating black and grey points are used to differentiate between data collected in different phases. The determined phase transition pressures are represented on the figure with dashed vertical lines, phases are labelled. The *d-fcc* phase is labelled as *hR24* and *lbam*, representing the respective solutions for the structure of the phase. On the right of the figure the volumes before and after the transition to the α -U phase are noted, a volume difference of 11% is observed at this transition.

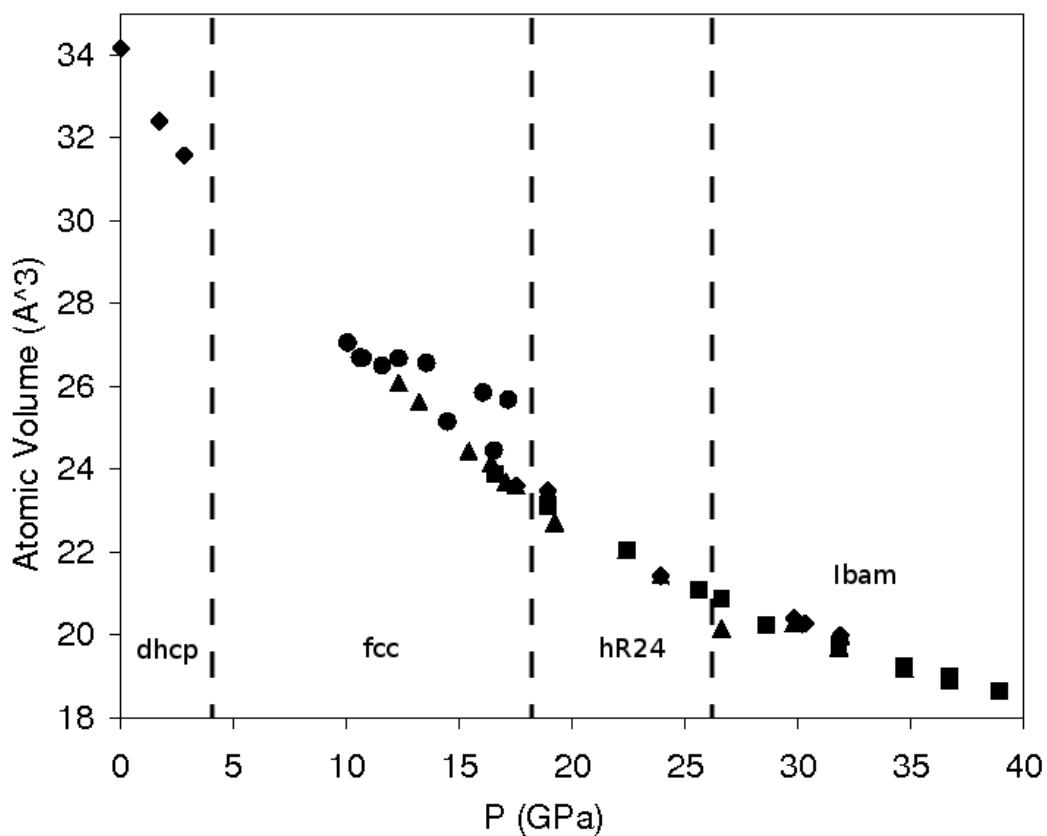


Figure 6.2: Plot of the atomic volume vs. pressure for the pressure range investigated in Nd. Alternating black and grey points are used to differentiate between data collected in different phases. The determined phase transition pressures are represented on the figure with dashed vertical lines, phases are labelled. The *d-fcc* phase is labelled as *hR24* and *Ibam*, representing the respective solutions for the structure of the phase. The maxima of pressure included in this diagram is 40GPa.

Similarly, a preliminary study of La has provided evidence for the occurrence of the *Ibam* structure, with a transition between 21 and 28GPa. The lower region of the *d-fcc* phase in La, in agreement with previous authors [Seipel 97], is best described using a $hR24$ ($R\bar{3}m$ structure. As for Nd, for pressures above ≈ 30 GPa, difficulties were encountered in fitting the data, which was likely caused by non-hydrostatic conditions within the sample chamber. Further experiments would be required, using an inert gas pressure transmitting medium, to study the *d-fcc* phase of La.

The work presented in this thesis was aimed at understanding the *d-fcc* phase of the low-Z lanthanides Pr, Nd and La. In each of these low-Z lanthanides the *d-fcc* phase is readily accessible using the MB and DXR6 DACs, pressure media, and equipment available. The use of mineral oil pressure transmitting media. Investigation of the *d-fcc* phase of higher-Z lanthanides would require the use of a pressure medium capable of maintaining a hydrostaticity (or quasi-hydrostatic) at pressures in excess of 40GPa. Gaseous loadings of an inert gas, such as He, would be required to fulfil the requirements of pressure transmitting medium that would remain quasi-hydrostatic at pressures greater than 50GPa.

Single-crystal growth attempts were made during the course of this work, at first through heating the DAC in a furnace and later by heating the sample directly using an IR laser. Results of these heatings yielded a decrease in FWHM of Bragg reflections and a tendency towards (although not full) re-crystallisation, evident in 2D diffraction images taken at synchrotron light sources. Partial re-crystallisation is seen by intensity around debye-scherrer rings clumping at discrete, but many, locations around diffraction rings. The growth of a single-crystal was not observed when the sample was heated in a furnace, or using an IR laser. The author suggests a higher sample temperature would be required, approaching the melting point of the sample, which would necessitate the use of an IR laser.

Synchrotron radiation was used for all of the experiments performed for this study. For the majority of the experiments, Station 9.5 HPT of Daresbury SRS was used ($\lambda = 0.44397\text{\AA}$), the remaining data were collected from ID09A of the ESRF ($\lambda = 0.414509\text{\AA}$). Both of these synchrotrons used Mar345 detectors, although, ID09A affords a higher resolution in measured diffraction patterns (evidenced from a reduction in FWHM of peaks from the same sample at comparable pressures). Synchrotron radiation was necessitated by the observed intensity of the weak superlattice reflections which differentiate between the solutions proposed in the literature [Mao 81, Chesnut 00b, Dmitriev 00, Syassen 00, Baer 03] and the solution found during the course of this work.

Further studies on lanthanides would also require the use of synchrotron radiation, however, as Daresbury SRS has been decommissioned, the UK successor, Diamond Light Source or ID09A of ESRF would need to be used.

Evidence has thus been found for the existence of a new structure within the *d-fcc* phase, the *oC16*, *Ibam* structure, within 3 members of the Lanthanide series. The author tentatively suggests this *Ibam* structure to be a new member of the Lanthanide transition sequence, but acknowledges that further study, of the higher-*Z* lanthanides would be required to definitively state if this is the case. To investigate the *d-fcc* phase of the higher-*Z* lanthanides would require DACs capable of reaching the Mbar pressure range, a pressure-transmitting medium that would remain (quasi-)hydrostatic in this pressure range and access to high purity lanthanide metals and a synchrotron radiation source.

Appendix A

Appendix Title

Bibliography

- [Akella 86] J. Akella, J. Xu & G. S. Smith. *Static High Pressure Studies On Nd and Sc*. Physica, vol. 139 140B, pages 285–288, 1986.
- [Akella 99] J. Akella, S. T. Weir & V. H. *et al.* Vohra. *High pressure phase transformations in neodymium studied in a diamond anvil cell using diamond-coated rhenium gaskets*. J.Phys.: Condens. Matter, vol. 11, pages 6515–6520, 1999.
- [Angel 01] R.J Angel. *Equations of State*. In Hazen, R.M., Downs, R.T. (Eds.) Reviews in Mineralogy and Geochemistry, vol. 41, pages 35–60, 2001.
- [Angel 07] Ross J. Angel, Maciej Bujak, Jing Zhao, G. Diego Gatta & Steven D. Jacobsen. *Effective hydrostatic limits of pressure media for high-pressure crystallographic studies*. Journal of Applied Crystallography, vol. 40, no. 1, pages 26–32, Feb 2007.
- [Anurag Sharma 02] George D. Cody Marilyn L. Fogel Robert M. Hazen Russell J. Hemley Wesley T. Huntress Anurag Sharma James H. Scott. *Microbial Activity at Gigapascal Pressures*. Science, vol. 295, pages 1514 – 1516, 2002.
- [Aroyo 06] M. I. Aroyo, J. M. Perez-Mato, C. Capillas, E. Kroumova, S. Ivantchev, G. Madariaga & H. Kirov A. Wondratschek. *Bilbao Crystallographic Server I: Databases and crystallographic computing programs*. Zeitschrift fuer Kristallographie, vol. 1, pages 15–27, 2006.
- [Baer 03] Bruce J. Baer, Hyunchoe Cynn, Valentin Iota, Choong-Shik Yoo & Guoyin Shen. *Phase diagram and equation of state of praseodymium at high pressures and temperatures*. Phys. Rev. B, vol. 67, page 134115, 2003.
- [Belmonte 98] S.A. Belmonte. *PhD. Thesis*. PhD thesis, The University of Edinburgh, 1998.
- [Birch 47] Francis Birch. *Finite Elastic Strain of Cubic Crystals*. Phys. Rev., vol. 71, no. 11, pages 809–824, Jun 1947.
- [Boehler 01] R. Boehler. *Laser heating in the diamond cell: techniques and applications*. Hyperfine Interactions, vol. 128, pages 307–321, 2001.
- [Bovornratanaraks 01] T. Bovornratanaraks. *High-Pressure Structural Studies of Strontium*. PhD thesis, The University of Edinburgh, 2001.
- [Bucher 69] E. Bucher, C. W. Chu, J. P. Maita, K. Andres, A. S. Cooper, E. Buehler & K. Nassau. *Electronic Properties of Two New Elemental Ferromagnets: fcc Pr and Nd*. Phys. Rev. Lett., vol. 22, no. 23, pages 1260–1263, Jun 1969.

- [Cavazzoni 99] C. Cavazzoni, G.L. Chiarotti, S. Scandolo, E. Tosatti, M. Bernasconi & M. Parrinello. *Superionic and Metallic states of Water and Ammonia at Giant Planet Conditions*. Science, vol. 283, page 44, 1999.
- [Chesnut 00a] G. N. Chesnut & Y. K. Vohra. *α -uranium phase in compressed neodymium metal*. Phys. Rev. B, vol. 61, page R3768, 2000.
- [Chesnut 00b] Gary N. Chesnut & Yogesh K. Vohra. *Phase transformations and equations of state of praseodymium metal to 103 GPa*. Phys. Rev. B, vol. 62, page 2965, 2000.
- [Cotton 91] Simon Cotton. *Lanthanides and actinides*. Macmillan Education, 1991.
- [Cullity 78] B.D Cullity. *Elements of x-ray diffraction - 2nd edition*. Addison-Wesley, 1978.
- [Cunningham 05] Nicholas C. Cunningham, Nenad Velisavljevic & Yogesh K. Vohra. *Crystal grain growth at the α -uranium phase transformation in praseodymium*. Phys. Rev. B, vol. 71, no. 1, page 012108, Jan 2005.
- [Datchi 97] F. Datchi, R. LeToullec & P. Loubeyre. *Improved calibration of the SrB₄O₇:Sm²⁺ optical pressure gauge: Advantages at very high pressures and high temperatures*. Journal of Applied Physics, vol. 81, no. 8, pages 3333–3339, 1997.
- [Davidson 07] Alistair J. Davidson, Iain D. H. Oswald, Duncan J. Francis, Alistair R. Lennie, William G. Marshall, David I. A. Millar, Colin R. Pulham, John E. Warren & Adam S. Cumming. *Explosives under pressure the crystal structure of gamma-RDX determined by high-pressure X-ray and neutron diffraction*. CrystEngComm, vol. 10, pages 162–165, 2007.
- [Davis 64] B. L. Davis. *X-ray Diffraction Data on Two High-Pressure Phases of Calcium Carbonate*. Science, vol. 145, no. 3631, pages 489–491, 1964.
- [de Wolff 85] P. M. de Wolff, N. V. Belov, E. F. Bertaut, M. J. Buerger, J. D. H. Donnay, W. Fischer, Th. Hahn, V. A. Koptsik, A. L. Mackay, H. Wondratschek, A. J. C. Wilson & S. C. Abrahams. *Nomenclature for crystal families, Bravais-lattice types and arithmetic classes. Report of the International Union of Crystallography Ad-Hoc Committee on the Nomenclature of Symmetry*. Acta Crystallographica Section A, vol. 41, no. 3, pages 278–280, 1985.
- [Dewaele 04] Agnès Dewaele, Paul Loubeyre & Mohamed Mezouar. *Equations of state of six metals above 94 GPa*. Phys. Rev. B, vol. 70, no. 9, page 094112, 2004.
- [Dmitriev 00] V. P. Dmitriev. *Stability of the high-pressure monoclinic phases in Ce and Pr metals: Comparative diffraction study and phenomenological theory*. Phys. Rev. B, vol. 70, page 014104, 2000.
- [Dmitriev 03] V. P. Dmitriev, A. Yu. Kuznetsov, D. Machon, H. P. Weber & P. Toldano. *Phase transition mechanisms in lanthanide elemental crystals*. Euro. Phys Lett, vol. 61, page 783, 2003.
- [Duthie 77] J.C. Duthie & D.G. Pettifor. *Correlation between d-Band Occupancy and Crystal Structure in the Rare Earths*. Phys. Rev. Lett., vol. 38, pages 564–566, 1977.

- [Errandonea 00] Daniel Errandonea, Reinhard Boehler & Marvin Ross. *Melting of the Rare Earth Metals and f-Electron Delocalization*. Phys. Rev. Lett., vol. 85, no. 16, pages 3444–3447, Oct 2000.
- [ESRF 10] ESRF. <http://www.esrf.fr/aboutus/guidedtour/beamline>. April 2010.
- [Evans 09] S. R. Evans, I. Loa, L. F. Lundegaard & M. I. McMahon. *Phase transitions in praseodymium up to 23 GPa: An x-ray powder diffraction study*. Phys. Rev. B, vol. 80, no. 13, page 134105, Oct 2009.
- [Gregoryanz 03] Alexander F. Matsuishi Kiyoto Mao Ho-kwang Hemley Russell J. Gregoryanz Eugene Goncharov. *Raman Spectroscopy of Hot Dense Hydrogen*. Phys. Rev. Lett., vol. 90, no. 17, page 175701, Apr 2003.
- [Grosshans 82] W. A. Grosshans, Y. K. Vohra & W. B. Holzapfel. *Evidence for a Soft Phonon Mode and a New Structure in Rare-Earth Metals under Pressure*. Phys. Rev. Lett, vol. 49, pages 1572–1575, 1982.
- [Grosshans 83] W. A. Grosshans, Y. K. Vorah & W. B. Holzapfel. *F bonding in praseodymium under high pressure*. J. Phys. F: Met. Phys, vol. 13, page L147, 1983.
- [Grosshans 92] W. A. Grosshans & W. B. Holzapfel. *Atomic volumes of rare-earth metals under pressures to 40GPa and above*. Phys. Rev. B, vol. 45, pages 5171–5178, 1992.
- [Gschneider 68] K. A. Jr. Gschneider & R. M. Valletta. *Concerning the crystal structure sequence in the lanthanide metals and alloys; evidence for 4f contribution to the bonding*. Acta. Metallurgica, vol. 16, pages 477–484, 1968.
- [Hahn (Editor) 02] Th. Hahn (Editor). *International tables for Crystallography - Volume A: Space-group symmetry (Fifth Edition)*. Kluwer Academic Publishers, 2002.
- [Hamaya 93] N. Hamaya, Y. Sakamoto, H. Fujii, K. Takemura, T. Kikegawa & O. Shimomura. *Crystal Structure of the distorted FCC high-pressure phase of praseodymium*. J. Phys Condens. Matter, vol. 5, page L369, 1993.
- [Hamaya 96] N Hamaya. *Performance of different types of detectors in a high-pressure X-ray study of phase transition*. High Pressure Research, vol. 14, page 287, 1996.
- [Hammersley 98] A. P. Hammersley. *FIT2D V9.129 Reference Manual V3.1*. Rapport technique ESRF Internal Report, ESRF98HA01T, ESRF, 1998.
- [Hanfland 02] M. Hanfland, K. Syassen & J. Kohler. *Pressure-volume relationship of Ta*. Journal of Applied Physics, vol. 91, no. 7, pages 4143–4148, 2002.
- [Hofmann 04] Albert Hofmann. *The physics of synchrotron radiation*. Cambridge University Press, 2004.
- [Holzapfel 95] W. B. Holzapfel. *Structural systematics of 4f and 5f elements under pressure*. J. Alloys Comp., vol. 223, pages 170–173, 1995.
- [Ingo Loa 07] Malcolm McMahon Ingo Loa. Poster presented at royal society summer of science exhibit. April 2007.

- [Jayaraman 64] A. Jayaraman & R. C. Sherwood. *Static High Pressure Studies on Nd and Sc*. Phys. Rev. Lett, vol. 12, pages 22–23, 1964.
- [Johansson B. 81] Andersen O. K. Johansson B. Skriver H. L. *Electronic Structure of the Actinide Metals*. In Int. Symposium on the PHYSICS OF SOLIDS UNDER HIGH PRESSURE, Bad Honnef, West Germany, 1981.
- [Johansson 75] Borje Johansson & Anders Rosengren. *Generalised phase diagram for the rare-earth elements: Calculations and correlations of bulk properties*. Phys. Rev. B, vol. 11, pages 2836–2857, 1975.
- [Klotz 09] S Klotz, J-C Chervin, P Munsch & G Le Marchand. *Hydrostatic limits of 11 pressure transmitting media*. Journal of Physics D: Applied Physics, vol. 42, no. 7, page 075413, 2009.
- [Kroumova 98] E. Kroumova, J. M. Perez-Mato & M. I. Aroyo. *WYCKSPLIT: a computer program for determination of the relations of Wyckoff positions for a group-subgroup pair*. Journal of Applied Crystallography, vol. 31, no. 4, page 646, Aug 1998.
- [Lennie 07] A.R. et. al. Lennie. *A novel facility using a Laue focusing monochromator for high-pressure diffraction at the SRS, Daresbury, UK*. Journal of Synchrotron Radiation, vol. 14, pages 433–438, 2007.
- [Lienert 98] U. Lienert, C. Schulze, V. Honkimäki, Th. Tschentscher, S. Garbe, O. Hignette, A. Horsewell, M. Lingham, H. F. Poulsen, N. B. Thomsen & E. Ziegler. *Focusing Optics for High-Energy X-ray Diffraction*. Journal of Synchrotron Radiation, vol. 5, no. 3, pages 226–231, 1998.
- [Loa 07] I. Loa, L. F. Lundegaard, M. I. McMahon, S. R. Evans, A. Bossak & M. Krisch. Phys. Rev. Lett., vol. 99, no. 3, page 035501, 2007.
- [Louer 04] A. Boulouf D. Louer. *Powder pattern indexing with the dichotomy method*. J. Appl. Cryst., vol. 37, pages 724–731, 2004.
- [Lundegaard 06] Lars F et. al. Lundegaard. *Observation of an O8 molecular lattice in the [epsiv] phase of solid oxygen*. Nature, vol. 443, pages 201–204, 2006.
- [Mao 81] H. K. Mao. *Evidence for 4f-shell delocalisation in praeodymium under pressure*. J. Appl. Phys., vol. 52, page 4572, 1981.
- [Mao 86] H. K Mao, J Xu & P. M. Bell. *Calibration of the Ruby Pressure Gauge to 800kbar Under Quasi-Hydrostatic Conditions*. J. Geophysical Res., vol. 91, pages 4673–4676, 1986.
- [McCullough 50] J. D McCullough. *An X-Ray Study of the Rare-earth Oxide Systems: CeIVNdIII, CrIVPrIII, CeIVPrIV and PrIVNdIII*. Journal of the American Chemical Society, vol. 72, page 1386, 1950.
- [McMahan 84] A.K. McMahan & D.A. Young. *Is there a missing rare earth crystal structure?* Physics Letters, vol. 105A, pages 129–131, 1984.
- [McMahan 98] A. K. McMahan, C. Huscroft, R. T. Scalettar & E. L. Pollock. *Volume-collapse transitions in rare earth metals*. J Comp Aided Mat, vol. 5, page 131, 1998.
- [McMahon 94] M. I. McMahon & R. J. Nelmes. *High-pressure powder diffraction on synchrotron sources*. J. Synch. Radiat., vol. 1, pages 69–73, 1994.

- [McWhan 65] D. B. McWhan & A. L. Stevens. *Effect of Pressure on the Magnetic Properties and Crystal Structure of Gd, Tb, Dy, and Ho*. Phys. Rev., vol. 139, no. 3A, pages A682–A689, Aug 1965.
- [McWhan 67] D. B. McWhan & A. L. Stevens. *Magnetic Properties of Some Rare-Earth Alloys at High Pressures*. Phys. Rev., vol. 154, page 438, 1967.
- [McWhan 72] D. B. McWhan. *The Pressure Variable in Materials Research*. Science, vol. 176, no. 4063, pages 751–758, 1972.
- [mim]
- [Momma 08] Koichi Momma & Fujio Izumi. *VESTA: a three-dimensional visualization system for electronic and structural analysis*. Journal of Applied Crystallography, vol. 41, no. 3, pages 653–658, Jun 2008.
- [Oliveira 09] C. L. P. Oliveira, T. Vorup-Jensen, C. B. F. Andersen, G. R. Andersen & J. S. Pedersen. *Applications of synchrotron light to scattering and diffraction in materials and life sciences*. Springer Berlin / Heidelberg, 2009.
- [Perez-Albuerne 66] R. L. Lynch R. W. Perez-Albuerne E. A. Clendenen & Drickamer H. G. *Effect of Very High Pressure on the Structure of Some hcp Metals and Alloys*. Phys. Rev., vol. 142, pages 392–399, 1966.
- [Petricek 00] M. Petricek V. Dusek. Jana2000. the crystallographic computing system. 2000.
- [Porsch 94a] F. Porsch & W. B. Holzapfel. *Symmetry change at the fcc distorted-fcc phase transition of lanthanides under pressure*. Phys. Rev. B, vol. 50, page 16212, 1994.
- [Porsch 94b] F. Porsch & W. B. Holzapfel. *Symmetry change at the fcc–distorted-fcc phase transition of lanthanides under pressure*. Phys. Rev. B, vol. 50, no. 22, pages 16212–16218, Dec 1994.
- [Rietveld 69] H.M. Rietveld. *A Profile Refinement Method for Nuclear and Magnetic Structures*. J. Appl. Cryst., vol. 2, pages 65–71, 1969.
- [Seipel 97] M. Seipel, F. Porsch & W. B. Holzapfel. *Characterization of the fcc-distorted fcc-structural transition in lanthanum in an extended pressure and temperature range*. High Pressure Research, vol. 15, page 321, 1997.
- [Shimomura 92] O. Shimomura & K. et al. Takemura. *Application of an imaging plate to high-pressure x-ray study with a diamond anvil cell*. Rev. Sci. Instrum., vol. 63, pages 967–973, 1992.
- [Smith 84] G. S. Smith & J. Akella. *On the possibility of Pr-III having a thcp structure*. Physics Letters, vol. 105A, pages 132–133, 1984.
- [Source 10] Diamond Light Source. <http://www.diamond.ac.uk/home/beamlines/mx/i04/schematic> April 2010.
- [Stager 64] A. Stager R & H. G. Drickamer. *Effect of Pressure and Temperature on the Electrical Resistance of Eleven Rare-Earth Metals*. Phys. Rev., vol. 133, pages A830–A834, 1964.
- [Syassen 00] Karl Syassen, Andrzej Grzechnik, Jrgen Khler & Ingo Loa. Esrf report on experiment hs1132. February 2000.

- [Syassen 08a] K. Syassen. *Ruby under pressure*. High Pressure Research, vol. 28, pages 75–126, 2008.
- [Syassen 08b] Karl Syassen. Software developed for internal use at mpi kfk. v 1.40e 2008.
- [tay]
- [Tonkov 05] E. Yu. Tonkov & E. G. Ponyatovsky. Phase transformations of elements under high pressure. CRC Press, 2005.
- [Trueblood 96] K. N. Trueblood, H.-B. Bürgi, H. Burzlaff, J. D. Dunitz, C. M. Gramaccioli, H. H. Schulz, U. Shmueli & S. C. Abrahams. *Atomic Displacement Parameter Nomenclature. Report of a Subcommittee on Atomic Displacement Parameter Nomenclature*. Acta Crystallographica Section A, vol. 52, no. 5, pages 770–781, 1996.
- [Velisavljevic 04a] N Velisavljevic & Y. K. Vohra. *Distortion of alpha-uranium structure in praseodymium metal to 311 GPa*. High Pressure Research, vol. 24, page 295, 2004.
- [Velisavljevic 04b] Nenad Velisavljevic, Kirkland M. MacMinn, Yogesh K. Vohra & Samuel T. Weir. *Electrical measurements on praseodymium metal to 179 GPa using designer diamond anvils*. Applied Physics Letters, vol. 84, no. 6, pages 927–929, 2004.
- [Velisavljevic 05] N Velisavljevic, Y. K. Vohra & S. T Weir. *Simultaneous electrical and X-ray diffraction studies on neodymium metal to 152 GPa*. High Pressure Research, vol. 25, pages 137–144, 2005.
- [Villars 91] P. Villars & L.D. Calvert. Pearsons handbook of crystallographic data for intermetallic phases. Am. Soc. Microbiol, 1991.
- [Vohra 81] Y. K. Vohra, H. Olijnik, W. Grosshans & W. B. Holzapfel. *Structural Phase Transitions in Yttrium under Pressure*. Phys. Rev. Lett, vol. 47, pages 1065–1067, 1981.
- [Warren 90] B.E Warren. X-ray diffraction. Dover Publications, 1990.
- [Website 10] Edinburgh University Chemical Crystallography Group Website. <http://www.crystal.chem.ed.ac.uk/>. January 2010.
- [Weir] C. E. Weir, E. R. Lippincott, A. Van Valkenburg & E. N. Bunting. *Symmetry change at the fcc-distorted-fcc phase transition of lanthanides under pressure*. J. Res. Natl. Bur. Stand. 63A, 5562., volume = 63A, pages = 55-62, numpages = 7, year = 1959.
- [Wigner 34] Wigner. *On the Interaction of Electrons in Metals*. Phys. Rev., vol. 46, pages 1002–1011, 1934.
- [Winter 09] Dr. Mark Winter. http://www.webelements.com/compounds/neodymium/dineodymium_trioxide. September 2009.
- [Wittig 80] J. Wittig. *Possible observation of localized 4f shell breakdown in praseodymium under pressure*. Z. Phys. B, vol. 38, pages 11–20, 1980.
- [Woolfson 97] Michael. M Woolfson. An introduction to x-ray crystallography - 2nd edition. Cambridge University Press, 1997.
- [XFEL 09] European XFEL. <http://www.xfel.eu/en/in-comparison/>. September 2009.

- [Zhao 94] Y.C. Zhao, F. Porsch & W. B. Holzapfel. *Intermediate 4f bonding structure for samarium under pressure*. Physical Review B, vol. 50, no. 10, pages 6603–6609, 1994.

Publications

Evans, Shaun and McMahon Malcolm. Phase Transitions in Praesodymium to 25GPa.
In *Phys. Rev. B*. Submitted April 2008. Published October 2009.